

Transition to elastic turbulence in channel flows

A DISSERTATION
SUBMITTED TO THE FACULTY OF THE GRADUATE SCHOOL
OF THE UNIVERSITY OF MINNESOTA
BY

Gokul Hariharan

IN PARTIAL FULFILLMENT OF THE REQUIREMENTS
FOR THE DEGREE OF
DOCTOR OF PHILOSOPHY

Advisors: Satish Kumar and Mihailo R. Jovanović

April, 2020

© Gokul Hariharan 2020
ALL RIGHTS RESERVED

Acknowledgments

I would like to thank Satish and Mihailo for being great advisors, mentors, and friends. Satish's care to detail and openness to explore new possibilities in research, and Mihailo's hands-on approach and vision to not stop at "good", but to go toward "great" have brought the best out of me in this thesis.

My motivation to work on this project came from attending David Morse's course on Linear Algebra. I am grateful to Yousef Saad for his class on Matrix Theory, to Satish for his course on Fluid Mechanics, Eray for Thermodynamics, and Mihailo for Nonlinear Systems and his fantastic website with course notes on Distributed Systems Analysis.

Armin and Binh helped me get familiar with the systems theoretical point of view I use in this dissertation. Weihua, Chen-Yu, Chung-Hsuan, Jyun-Ting, Truong, Chance, Vasileos, and Panos helped me present complex ideas in a simple manner. I must also acknowledge Wentao and Matt for their inputs on linear systems and optimization whenever needed.

Great friends and their inspiring company were an indispensable part of this endeavor - Sanyam, Raghav, Shashank, Saket, Ashish, and Ankit. I am very grateful to Pallavi for her unconditional love and support, and not to miss, her unprecedented culinary skills.

Abstract

Materials processing operations such as extrusion and coating often involve the low-inertia flow of viscoelastic fluids through straight channels. Experimental evidence suggest that such flows can transition from a laminar to a disordered flow-state, resulting in defective end-products. On the other hand, such a transition with low inertia is useful for enhancing transport in microfluidic flows where good mixing is hard to achieve. Therefore a fundamental understanding of such a transition is important.

Chapter 2 of this thesis considers external disturbances in the form of small-amplitude localized body forces (impulses). They provide a good approximation of the external disturbances that can be realized relatively easily in laboratory experiments. Localized body forces are used to identify the optimal location in a channel that induces the largest kinetic energy growth. A disturbance in the channel that generates the largest kinetic energy growth has a high potential to trigger a transition to a disordered flow-state.

Chapter 3 presents tools to accurately resolve steep stress gradients encountered in frequency response calculations of the linearized equations governing channel flow of a viscoelastic fluid. Recently reported well-conditioned spectral methods in conjunction with a reflection technique enable frequency response computations of channel flows of viscoelastic fluids with large elasticity.

Applying the methods developed in Chapter 3 to 2D channel flow of a viscoelastic fluid, it is found that the stress can develop large magnitudes even when the velocity has negligible growth. A stress of large magnitude generated by small-amplitude disturbances may provide a new route to a transition to a disordered flow-state observed in recent experiments. Chapter 4 studies stress amplification and conditions in which they become prominent.

A first step to perform direct numerical simulations (DNS) of channel flows of viscoelastic fluids using tools developed in Chapter 3 is to develop an algorithm for DNS of channel flows of Newtonian fluids. Chapter 5 extends tools discussed in Chapter 3 to perform direct numerical simulations of channel flows of a Newtonian fluid.

Analyzing transition to turbulence in viscoelastic channel flows is a challenging problem that needs a multi-faceted approach involving linear and nonlinear systems theory,

robust numerical methods, and complementary experiments. We believe that this dissertation provides new insights into possible mechanisms that may govern the initial stages of a transition to elastic turbulence using linear systems theory and recent numerical methods. We further hope that the numerical methods studied in this dissertation will open new avenues to simulate and analyze flow transition in complex fluids.

Contents

Acknowledgments	i
Abstract	ii
List of Tables	viii
List of Figures	ix
1 Introduction	1
1.1 Preliminaries	3
1.1.1 Stability and sensitivity	3
1.1.2 Spectral methods and their well-conditioned variants	5
1.2 Main topics of the dissertation	7
1.2.1 Amplification of localized body forces in channel flows of viscoelastic fluids	7
1.2.2 Well-conditioned ultraspherical and spectral integration methods for resolvent analysis of Newtonian and viscoelastic channel flows	8
1.2.3 Stress amplification in inertialess channel flows of viscoelastic fluids	9
1.2.4 An integral reformulation of the influence-matrix algorithm for direct numerical simulations of channel flows	9
2 Amplification of localized body forces in channel flows of viscoelastic fluids	11
2.1 Introduction	11
2.2 Problem formulation	14

2.2.1	Evolution form of governing equations	14
2.2.2	Numerical method	18
2.2.3	Model parameters	19
2.2.4	Energy of velocity fluctuations	21
2.3	Flow sensitivity to the location of the impulse	22
2.4	Energy evolution	26
2.5	Spatio-temporal evolution of flow structures	30
2.6	Concluding remarks	34

3 Well-conditioned ultraspherical and spectral integration methods for resolvent analysis of Newtonian and viscoelastic channel flows 38

3.1	Introduction	38
3.2	Problem formulation and motivating examples	41
3.2.1	Problem formulation	41
3.2.2	Reaction-diffusion equation: Ill-conditioning arising from operator	43
3.2.3	Channel flow of viscoelastic fluids: Ill-conditioning arising from spatial discretization	45
3.2.4	The linearized Navier-Stokes equations: A model in the descriptor form	47
3.3	SVD via feedback interconnection	49
3.3.1	The feedback interconnection	51
3.3.2	Numerical approximation of spatial differential operators	55
3.3.3	Boundary conditions for linearized NS equations in the descriptor form	61
3.3.4	Frequency response analysis of 3D channel flow of a viscoelastic fluid	64
3.4	Computational examples	65
3.4.1	Reaction-diffusion equation	65
3.4.2	2D viscoelastic channel flow	66
3.4.3	Frequency response analysis of systems in the descriptor form	71
3.5	Concluding remarks	75

4	Stress amplification in inertialess channel flows of viscoelastic fluids	76
4.1	Introduction	76
4.1.1	Experimental observations on elastic turbulence	76
4.1.2	Linear analysis	78
4.1.3	Localized amplification	79
4.2	Problem formulation	81
4.2.1	Governing equations	81
4.2.2	Recasting the governing equations	83
4.2.3	The resolvent norm	86
4.2.4	Localized amplification	88
4.3	Numerical methods	89
4.4	Localized and square-integrated amplification of the stress	92
4.4.1	Square-integrated amplification	92
4.4.2	Localized amplification	94
4.4.3	A potential mechanism: Flow transition via localized amplification	99
4.5	Mechanisms for localized amplification	100
4.5.1	The role of the continuous spectrum	100
4.5.2	Locations of localized amplification	105
4.6	Summary and conclusions	107
5	An integral reformulation of the influence-matrix algorithm for direct numerical simulations of channel flows	109
5.1	Introduction	109
5.2	Governing equations	111
5.3	Numerical method	113
5.3.1	Kleiser and Schumann’s influence-matrix method	115
5.3.2	An integral reformulation of the influence-matrix method	118
5.4	Computational experiments	120
5.4.1	The impulse response of the linearized NS equations	120
5.4.2	Simulating a sustained turbulent flow state of plane Couette flow	122
5.5	Summary and conclusions	125
6	Summary	126

7	Future directions	129
7.1	Complementary experiments on effects of localized body forces in channel flows of viscoelastic fluids	129
7.2	Well-conditioned spectral methods to study effects of impulsive body forces in channel flows	130
7.3	DNS of elastic turbulence using well-conditioned spectral methods . . .	131
7.4	Control of elastic turbulence	132
7.5	Concluding remarks	132
	References	134
	Appendix	144
A	Operators in Poiseuille flow of FENE-CR fluids	144
B	Inner product that determines the kinetic energy	149
C	Operators governing 2D channel flow of an Oldroyd-B fluid	151
D	Operators governing 3D channel flow of an Oldroyd-B fluid	153
D.1	Evolution form	153
D.2	Descriptor form with the stress eliminated	157
E	Operators governing channel flow of an Oldroyd-B fluid	161
E.1	Evolution form	161
E.2	Descriptor form	165
F	Validation	168
G	Additional figures for § 4.5	169
H	Time-stepping schemes for DNS	174
	Supplementary material	177
S1	A Matlab spectral integration suite	177
S1.1	Introduction	177
S1.2	Arbitrary order linear differential equation with non-constant coefficients	184
S1.3	The spectral integration suite	188
S1.4	Recurrence relations	198

List of Tables

H1	Implicit-explicit time-stepping schemes used in DNS, where h is the time step [1, 2]; see Table H2 for values of γ and c . The first name refers the implicit part, e.g., in “Crank-Nicholson, three-stage RK”, quantities treated implicitly use Crank-Nicholson, and quantities treated explicitly use three-stage RK time discretization.	175
H2	Family of second-order time-stepping schemes implemented in DNS (Chapter 5), taken from [2]. The first name refers the implicit part, e.g., in “Crank-Nicholson, Adams-Bashforth”, quantities treated implicitly use Crank-Nicholson, and quantities treated explicitly use Adams-Bashforth time discretization.	176

List of Figures

1.1	Experiments of Groisman and Steinberg [3] illustrating elastic turbulence. (a) The experimental setup to observe a dilute polymer solution subjected to parallel shear, where $R = 38$ mm, $R_2 = 43.6$ mm and $d = 10$ mm. (b) The dispersion of a drop of black ink in a Newtonian fluid and (c) in a dilute polymer solution, at a Reynolds number (in terms of the maximum velocity and d) of 1. The Newtonian fluid shows poor mixing after nine hours of rotation, whereas, the dilute viscoelastic solution shows uniform mixing in two minutes.	2
1.2	Solution to (1.1) by setting $\lambda_1 = -2$, $\lambda_2 = -3$, and $\psi_1(0) = \psi_2(0) = 1$, (a) $R = 0$, and (b) $R = \{5, 7, 9, 11, 13, 15, 17, 19\}$	4
2.1	Flow geometry and the steady-state parabolic velocity profile for Poiseuille flow.	15
2.2	Kinetic energy integrated over the wall-normal direction and time, with an impulsive excitation located at $y_0 = -0.75$. Plots correspond to (a) \bar{E}_x , (b) \bar{E}_y , and (c) \bar{E}_z respectively, calculated from (2.15). Parameters used are $Re = 50$, $We = 50$, $L = 100$, and $\beta = 0.5$. The maximum value of the kinetic energy is marked by the black dots.	23
2.3	Maximum kinetic energy induced by an impulsive excitation in the (a) streamwise, (b) wall-normal, and (c) spanwise directions as a function of y_0 , calculated using (2.15). The Newtonian fluid corresponds to $\mu = 0$, and the viscoelastic fluid to $\mu = 1$ (the parameters are $Re = 50$, $We = 50$, $L = 100$, and $\beta = 0.5$).	24

2.4	Maximum energy induced by an impulsive excitation in the (a) streamwise, (b) wall-normal, and (c) spanwise directions as a function of y_0 , calculated using (2.15). The Newtonian fluid corresponds to $\mu = 0$, and the viscoelastic fluid to $\mu = 0.05$ (the parameters are $Re = 1000$, $We = 50$, $L = 100$, and $\beta = 0.5$).	25
2.5	Kinetic energy integrated over the wall-normal direction and time, with an impulse in the direction i , calculated using (2.15). We consider a viscoelastic fluid with an impulsive excitation in the (a) streamwise, (b) wall-normal, and (c) spanwise directions, and a Newtonian fluid with an impulsive excitation in the (d) streamwise, (e) wall-normal, and (f) spanwise directions. The maximum value of the kinetic energy is marked by the black dots.	28
2.6	Componentwise contributions of (a) streamwise, (b) wall-normal, and (c) spanwise velocities to the total kinetic energy calculated from (2.16b) arising from an impulsive spanwise forcing in a flow with $Re = 50$, $We = 50$, $L = 100$, and $\beta = 0.5$	29
2.7	Transient evolution of kinetic energy of streamwise velocity fluctuations arising from an impulse in the spanwise direction, $E_{uz}(\boldsymbol{\kappa}, t)$ calculated from (2.16a), in a flow with $k_x = 10^{-1}$ and $k_z = 10^0$. Panel (a) shows the effect of increasing the polymer relaxation time by increasing the Weissenberg number. $We = 0$ corresponds to the Newtonian fluid. Panel (b) shows the effect of increasing polymer concentration, $1 - \beta$. For a Newtonian fluid, $\beta = 1$	29
2.8	Isosurface plots of the streamwise velocity at $\pm u_{z,\max}/10$ at $Re = 50$. Red color denotes regions of high velocity and green color denotes regions of low velocity. Panels correspond to a viscoelastic fluid at (a) 0.1, and (c) 1 time units, and a Newtonian fluid at (b) 0.1, and (d) 1 time units, with parameters $L = 100$, $\beta = 0.5$ and $\mu = 1$ for the viscoelastic fluid.	31

2.9	Isosurface plots of the streamwise velocity at $\pm u_{z,\max}/10$ at $Re = 50$. Red color denotes regions of high velocity and green color denotes regions of low velocity. Panels correspond to a viscoelastic fluid at (a) 3.5, and (c) 6 time units, and a Newtonian fluid at (b) 3.5, and (d) 6 time units, with parameters $L = 100$, $\beta = 0.5$ and $\mu = 1$ for the viscoelastic fluid.	32
2.10	Three-dimensional streamtubes of the velocity fluctuation vector that originate from the plane $y = 0.5$ at $Re = 50$ with a spanwise impulsive excitation at $y_0 = -0.75$. Show are (a) top view and (c) isometric view for a viscoelastic fluid and (b) top view and (d) isometric view for a Newtonian fluid at $t = 0.1$. Parameters used for the viscoelastic fluid are $L = 100$, $\beta = 0.5$ and $\mu = 1$	35
2.11	Three-dimensional streamtubes of the velocity fluctuation vector that originate from the plane $y = 0.5$ at $Re = 50$ with a spanwise impulsive excitation at $y_0 = -0.75$. Show are (a) top view and (c) isometric view for a viscoelastic fluid and (b) top view and (d) isometric view for a Newtonian fluid at $t = 6$. Parameters used for the viscoelastic fluid are $L = 100$, $\beta = 0.5$ and $\mu = 1$	36
3.1	Singular values of the frequency response operator of the reaction-diffusion equation (3.3) obtained using Chebfun's spectral scheme with $N = 64$ collocation points. Symbols represent exact values (\times) and the numerical solution resulting from the composite operator $\mathcal{T}(\omega)\mathcal{T}^\dagger(\omega)$ (\circ). The principal singular value is not shown as its value is very large compared to the remaining singular values.	44
3.2	Geometry and steady-state velocity profiles in Poiseuille and Couette flows.	46
3.3	Block diagram of a cascade connection of the operators $\mathcal{T}^\dagger(\omega)$ and $\mathcal{T}(\omega)$. The composite operator, $\mathcal{T}^\dagger(\omega)\mathcal{T}(\omega)$, can be used to compute the singular values of the frequency response operator $\mathcal{T}(\omega)$	51
3.4	Through a sequence of equivalent transformations, the cascade connection of the operators $\mathcal{T}^\dagger(\omega)$ and $\mathcal{T}(\omega)$ shown in Figure 3.3 is cast as a feedback interconnection of the operators $(1/\sigma)\mathcal{T}^\dagger(\omega)$ and $(1/\sigma)\mathcal{T}(\omega)$ [4, Theorem 1].	52

3.5	Singular values of the frequency response operator for reaction-diffusion equation (3.3) with $\epsilon = 10^{-4}$ and $\omega = 0$ resulting from the use of Chebfun's spectral collocation scheme with $N = 64$. Symbols represent analytical solution (\times), and the computations based on the feedback interconnection shown in Figure 3.4 (\circ) and the cascade connection shown in Figure 3.3 (\diamond). The principal singular value (corresponding to $i = 0$) is not shown as its value is significantly larger than the remaining singular values.	66
3.6	Principal singular values of the frequency response operator (3.8a) for inertialess 2D Couette flow of an Oldroyd-B fluid with $\beta = 0.5$, $k_x = 1$, and $\omega = 0$ as a function of fluid elasticity, We , resulting from the use of (a) ultraspherical; (b) spectral integration; and (c) spectral collocation methods. The velocity fluctuations are selected as the output and symbols represent $N = 479$ (\circ) and $N = 511$ (\times).	68
3.7	The left singular function associated with the principal singular value $\sigma_{\max} = 14.936$ of inertialess 2D Couette flow of an Oldroyd-B fluid with $We = 40$, $k_x = 1$, $\omega = 0$, and $\beta = 0.5$. The first normal stress component, τ_{xx} , (a) in the whole domain, $y \in [-1, 1]$; and (b) near $y = 0$ is shown. The stress fluctuations are selected as the output and the lines correspond to $\text{Re}(\tau_{xx})$ (-), and $\text{Im}(\tau_{xx})$ (- -).	69
3.8	The left singular function associated with the principal singular value $\sigma_{\max} = 6.184$ of inertialess 2D Poiseuille flow of an Oldroyd-B fluid with $We = 40$, $k_x = 1$, $\omega = 0$ and $\beta = 0.5$. The first normal stress component, τ_{xx} , (a) in the whole domain, $y \in [-1, 1]$; and (b) near $y = 1$ is shown. The stress fluctuations are selected as the output and the lines correspond to $\text{Re}(\tau_{xx})$ (-), and $\text{Im}(\tau_{xx})$ (- -).	69
3.9	The left singular function associated with the principal singular value $\sigma_{\max} = 5.98$ of inertialess 2D Poiseuille flow of an Oldroyd-B fluid with $We = 500$, $k_x = 1$, $\omega = 0$, and $\beta = 0.5$. The first normal stress component, τ_{xx} , (a) in the whole domain, $y \in [-1, 1]$; and (b) near $y = 1$ is shown. The stress fluctuations are selected as the output and the lines correspond to $\text{Re}(\tau_{xx})$ (-), and $\text{Im}(\tau_{xx})$ (- -).	70

3.10	The linearized NS equations in Poiseuille flow with $Re = 2000$ and $k_x = k_z = 1$. The spectral integration method with $N = 255$ basis functions is used. (a) Spectrum resulting from the use of the evolution form model (\times) and the descriptor formulation (\circ); and (b) two largest singular values of the frequency response operator (evolution form (\times) and descriptor formulation (\circ) results for σ_{\max} ; evolution form (\triangle) and descriptor formulation (∇) results for the second largest singular value).	72
3.11	(a) Real; and (b) imaginary parts of the principal singular value in inertialess Couette flow of an Oldroyd-B fluid with $\beta = 0.5$, $k_x = k_z = 1$, and $\omega = 0$. The velocity fluctuations are selected as the output and the results are obtained using the descriptor formulation (\times) that eliminates stresses (see § 3.3.4) with $N = 383$ basis functions and the evolution form model (\circ) (see § 3.3.4) with $N = 1000$ basis functions.	72
3.12	(a) Real; and (b) imaginary parts of the principal singular value in inertialess Couette flow of an Oldroyd-B fluid with $\beta = 0.5$, $k_x = k_z = 1$, and $\omega = 0$. The first normal stress component, τ_{xx} , is selected as the output and the results are obtained using the descriptor formulations that eliminates stresses (see § 3.3.4) with $N = 863$ basis functions.	73
3.13	The left singular function corresponding to the principal singular value $\sigma_{\max} = 7.434$ in inertialess Poiseuille flow of an Oldroyd-B fluid with $We = 10$, $\beta = 0.5$, $k_x = k_z = 1$, and $\omega = 0$. The first normal stress component, τ_{xx} , is selected as the output and the results are obtained using the descriptor formulations that eliminates stresses with $N = 863$ basis functions. The lines correspond to $\text{Re}(\tau_{xx})$ (-) and $\text{Im}(\tau_{xx})$ (- -) and the results (a) in the entire domain, $y \in [-1, 1]$; and (b) near $y = 1$, are shown.	74
4.1	The Gaussian function (4.1) with (a) $\alpha = 0.01$, and (b) $\alpha = 0.005$	79
4.2	Flow geometry and the steady-state velocity profile for plane Poiseuille flow.	81

4.3	Principal singular values of (a) $\mathcal{T}_{\mathbf{v}}$ in (4.14) and (b) \mathcal{T}_{xx} in (4.17) of 2D3C Poiseuille flow of an Oldroyd-B fluid with $\beta = 0.5$, $k_z = 1$, and $\omega = 0$. The solid lines mark singular values, and the dashed lines show the slope of their scaling with We	93
4.4	Principal singular values of (a) $\mathcal{T}_{\mathbf{v}}$ in (4.14) and (b) \mathcal{T}_{xx} in (4.17) of 2D Poiseuille flow of an Oldroyd-B fluid with $\beta = 0.5$, $k_x = 1$, and $\omega = 0$. The solid lines mark singular values, and the dashed line in (b) shows the magnitude of the singular value when $We = 500$	94
4.5	The quantity $\hat{\tau}_{xx}$ (see (4.18)) corresponding to the principal singular value from the SVD of \mathcal{T}_{xx} in (4.17) of inertialess (a) 2D3C ($k_z = 1$), and (b,c) 2D ($k_x = 1$) Poiseuille flow of an Oldroyd-B fluid with $We = 100$, $\beta = 0.5$, and $\omega = 0$. Solid lines mark the real parts and the dashed lines mark the imaginary parts of $\hat{\tau}_{xx}$. Figure (c) enlarges (b) near $y = 1$	96
4.6	The (a,b) velocity components $\mathbf{v} = [u \ v]^T$ respectively, and (c,d) x - and y -components of the body force \mathbf{d} corresponding to the principal singular value from the SVD of \mathcal{T}_{xx} in (4.17) of 2D Poiseuille flow of an Oldroyd-B fluid with $We = 100$, $\beta = 0.5$, $k_x = 1$, and $\omega = 0$. The solid lines mark the real parts and the dashed lines mark the imaginary parts of the velocity and body force vectors.	97
4.7	The steady-state (a) kinetic energy $u^2 + v^2$ and (b,c,d) squared stress τ_{xx}^2 that result from a persistent body force of the form in (4.5e) with a frequency $\omega = 0$, and a variation in y shown in Figures 4.6c and 4.6d in the 2D system of (4.5), with $We = 100$ and $\beta = 0.5$. Figure (c) enlarges (b) near $y = -1$, and Figure (d) enlarges (b) near $y = 1$. Plots in physical space are obtained by applying an inverse Fourier transform to the velocity and stress by linearly sampling 24 wavenumbers from $k_{x,\min} = -2.5$ to $k_{x,\max} = 2.29$, and using 6000 Chebyshev basis functions in the y -direction.	98
4.8	The function g_1 in (4.31) with $We = 100$, and $\omega = 0$ (a,b) $k_x = 1$, and (c) $k_x = 0$. The solid lines mark the real parts and the dashed lines mark the imaginary parts of g_1 in (4.31). Figure (b) enlarges (a) near $y = 1$. . .	102

4.9	Stress τ_{xx} corresponding to the principal singular value from the SVD of \mathcal{T}_{xx} in (4.17) with $We = 40$, $\beta = 0.5$, and $k_x = 1$, and (a) $y^* = 0$, (b) $y^* = \pm 0.2$, (c) $y^* = \pm 0.4$, (d) $y^* = \pm 0.6$, (e) $y^* = \pm 0.8$, and (f) $y^* = \pm 1$. For a given value of k_x and y^* , ω is calculated from (4.33). The solid lines mark the real parts and the dashed lines mark the imaginary parts of $\hat{\tau}_{xx}$. The dashed-dotted lines mark $y = \pm y^*$. Figure G4 (relegated to Appendix G) shows the region enlarged near $y = y^*$	103
5.1	Flow geometry showing the steady-state laminar velocity profile for plane Poiseuille and Couette flows.	112
5.2	The impulse response (2.9) of a Newtonian fluid with $Re = 2000$, $k_x = 0$, $N_z = 256$, $k_{z,\max} = 5$, $N = 127$, using the matrix-exponential solution from (2.9) (\times) and the DNS algorithm in § 5.3.2 (\square) with the nonlinear term $\mathbf{v} \cdot \nabla \mathbf{v}$ in (5.3) (a) switched off, and (b) switched on. Note that in (b) the impulsive body force is attenuated by a factor of 100 to restrict the nonlinear terms to a maximum frequency $k_{z,\max} = 5$	121
5.3	The velocity profile of plane Couette flow averaged in the x - and z -directions, with $Re = 1250$ ($Re_\tau = 73$), (a) the initial condition at $t = 0$, and (b) the profiles at times 500, 1000, 1500, and 2000 units.	122
5.4	Couette flow with $Re = 1250$ ($Re_\tau = 73$) using the DNS algorithm in § 5.3.2, (a) the streamwise velocity (rescaled with wall-friction velocity, see (5.26)) averaged in the x - and z -directions, conforming with the wall-law (5.27), (b) RMS of the velocity averaged in the x - and z -directions (see (5.28)).	124
F1	Principal singular values of (a) \mathcal{T}_v in (4.14) and (b) \mathcal{T}_{xx} in (4.17) of 2D Couette flow of an Oldroyd-B fluid with $\beta = 0.5$, $k_x = 1$, and $\omega = 0$. Spectral integration 1 uses the descriptor form in § E.2, and Spectral integration 2 uses the evolution form in § E.1. The ultraspherical method uses the evolution form.	168
F2	Principal singular values of (a) \mathcal{T}_v in (4.14) and (b) \mathcal{T}_{xx} in (4.17) of 2D3C Couette flow of an Oldroyd-B fluid with $\beta = 0.5$, $k_z = 1$, and $\omega = 0$. The solid lines mark singular values, and the dashed lines show the slope of their scaling with We [5].	169

G3	Stress τ_{xx} corresponding to the principal singular value from the SVD of \mathcal{T}_{xx} in (4.17) with $We = 40$, $\beta = 0.5$ and $k_x = 3$, and (a) $y^* = 0$, (b) $y^* = \pm 0.2$, (c) $y^* = \pm 0.4$, (d) $y^* = \pm 0.6$, (e) $y^* = \pm 0.8$, and (f) $y^* = \pm 1$. For a given value of k_x and y^* , ω is calculated from (4.33). The solid lines mark the real parts and the dashed lines mark the imaginary parts of $\hat{\tau}_{xx}$. The dashed-dotted lines mark $y = \pm y^*$. Figure G5 shows the region enlarged near $y = y^*$	171
G4	Stress τ_{xx} corresponding to the principal singular value from the SVD of \mathcal{T}_{xx} in (4.17) with $We = 40$, $\beta = 0.5$, and $k_x = 1$, and (a) $y^* = 0$, (b) $y^* = \pm 0.2$, (c) $y^* = \pm 0.4$, (d) $y^* = \pm 0.6$, (e) $y^* = \pm 0.8$, and (f) $y^* = \pm 1$. For a given value of k_x and y^* , ω is calculated from (4.33). The solid lines mark the real parts and the dashed lines mark the imaginary parts of $\hat{\tau}_{xx}$. The dashed-dotted lines mark $y = y^*$. Figure 4.9 shows corresponding plots in the full domain, i.e., $y \in [-1, 1]$	172
G5	Stress τ_{xx} corresponding to the principal singular value from the SVD of \mathcal{T}_{xx} in (4.17) with $We = 40$, $\beta = 0.5$, and $k_x = 3$, and (a) $y^* = 0$, (b) $y^* = \pm 0.2$, (c) $y^* = \pm 0.4$, (d) $y^* = \pm 0.6$, (e) $y^* = \pm 0.8$, and (f) $y^* = \pm 1$. For a given value of k_x and y^* , ω is calculated from (4.33). The solid lines mark the real parts and the dashed lines mark the imaginary parts of $\hat{\tau}_{xx}$. The dashed-dotted lines mark $y = y^*$. Figure G3 shows corresponding plots in the full domain, i.e., $y \in [-1, 1]$	173
S1	Comparing analytical and numerical solutions to (S1-39) from Code 7.2.	194
S2	Eigenvalues and frequency responses of the linearized Navier equations in plane Poiseuille flow with $Re = 2000$ and $k_x = k_z = 1$, generated from Code 7.3. The spectral integration method with $N = 91$ basis functions is used. (a) Spectrum resulting from the use of the descriptor formulation, and (b) two largest singular values of the frequency response operator computed using Code 7.3. A reference for this plot is found in [6, Figure 4.10].	197

Chapter 1

Introduction

Newtonian fluids transition from a structured and ordered (laminar) flow state to a three-dimensional, unstructured, time-dependent (turbulent) flow state when the inertia of the fluid is sufficiently large. In contrast, certain viscoelastic fluids transition to a turbulent-like flow state even with negligible inertia [3, 7, 8, 9].

Figure 1.1 shows experimental observations by Groisman and Steinberg [7]. A dilute polymer solution in a cylindrical cup was subject to shear using a rotating disk resting on its surface (Figure 1.1a). The fluid velocity was measured using laser Doppler velocimetry. Figures 1.1b and 1.1c show the effect of placing a drop of black ink at the center bottom of a Newtonian fluid and a dilute viscoelastic fluid respectively at a Reynolds number of 1. We see poor mixing in the Newtonian fluid (Figure 1.1b) after nine hours of rotation, while the dilute viscoelastic fluid (Figure 1.1c) is nearly uniformly mixed in two minutes due to elastic turbulence.

Elastic turbulence is useful in microfluidic devices where good mixing is difficult to achieve by other means [10]. Elastic turbulence also finds applications in implementing microscale flow-control devices [11, 10] like nonlinear flow resistors and flow memory devices such as flip-flops, which are analogous to their counterparts in electric circuits. Elastic turbulence is sometimes undesired in materials processing operations like coating and polymer processing to avoid defective end-products [12, 13]. However there is a lack of fundamental understanding regarding the origin and the initial stages of a transition to elastic turbulence in straight channels.

This thesis provides insight into mechanisms that may govern the initial stages of

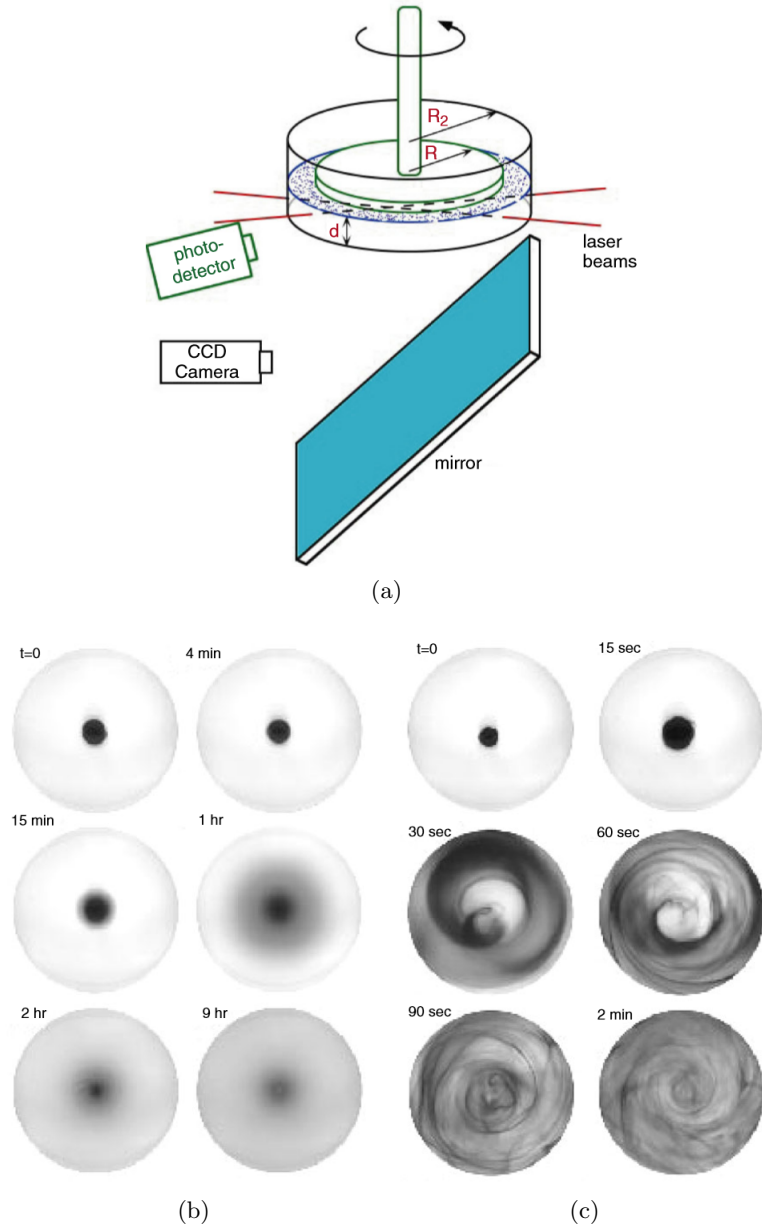


Figure 1.1: Experiments of Groisman and Steinberg [3] illustrating elastic turbulence. (a) The experimental setup to observe a dilute polymer solution subjected to parallel shear, where $R = 38$ mm, $R_2 = 43.6$ mm and $d = 10$ mm. (b) The dispersion of a drop of black ink in a Newtonian fluid and (c) in a dilute polymer solution, at a Reynolds number (in terms of the maximum velocity and d) of 1. The Newtonian fluid shows poor mixing after nine hours of rotation, whereas, the dilute viscoelastic solution shows uniform mixing in two minutes.

a transition to turbulence in viscoelastic channel flows using tools from linear systems theory and recently developed well-conditioned spectral methods. We consider four problems relevant to studying transition to turbulence in viscoelastic channel flows: (a) The effects of localized body forces. (b) Development of tools to carry out linear analysis of high-elasticity fluids in channels, (c) The effects of a persistent body force that is localized in space and is a sinusoidal function of time, and (d) Development of a method to perform direct numerical simulations of Newtonian channel flows that is applicable to a broad class of spectral methods. Such a method may be useful for simulating the nonlinear evolution of the flow of viscoelastic fluids in channels.

In the section to follow, we introduce subjects from linear systems theory and numerical methods that we will use in this dissertation. This is followed by an overview of the projects we consider.

1.1 Preliminaries

1.1.1 Stability and sensitivity

The initial stages of a transition to turbulence is studied by considering effects of small-amplitude perturbations on a dynamical system [14, 15, 16]. This corresponds to analyzing the effect of an initial condition on the linearized equations [15] governing the system. If at the least one initial condition grows exponentially at long times, the system is linearly unstable, and if all initial conditions asymptotically decay at long times, the system is linearly stable [17]. A growing initial condition may actuate the system to a new nonlinear state that is observed as turbulence.

Linear stability analysis only ascertains the long time growth or decay of initial conditions on a system, and provides no information about growth at finite times. A linearly stable system in which a small-amplitude perturbation grows significantly at finite times is said to be sensitive. To understand the notions of stability and sensitivity we repeat an example from [18]. Consider a system of coupled ordinary differential equations (ODE) governing the dynamics of ψ_1 and ψ_2 ,

$$\frac{d}{dt} \begin{bmatrix} \psi_1 \\ \psi_2 \end{bmatrix} = \begin{bmatrix} \lambda_1 & 0 \\ R & \lambda_2 \end{bmatrix} \begin{bmatrix} \psi_1 \\ \psi_2 \end{bmatrix}, \quad (1.1)$$

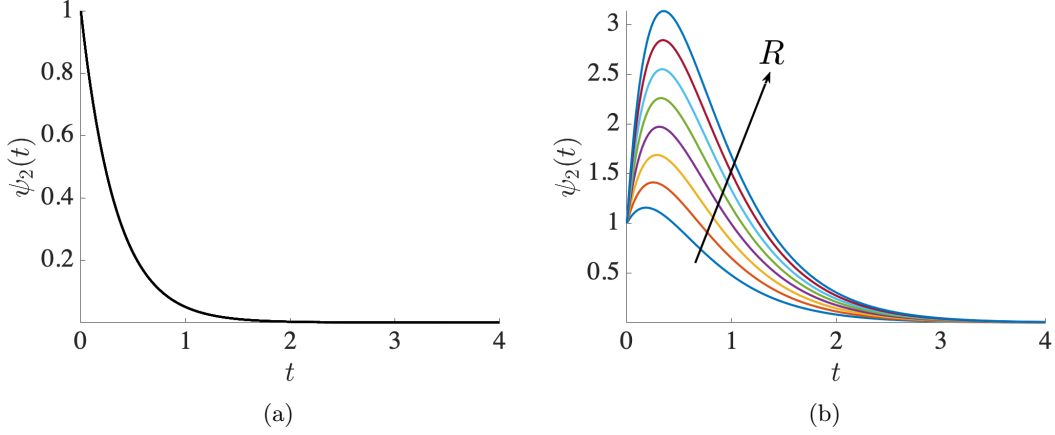


Figure 1.2: Solution to (1.1) by setting $\lambda_1 = -2$, $\lambda_2 = -3$, and $\psi_1(0) = \psi_2(0) = 1$, (a) $R = 0$, and (b) $R = \{5, 7, 9, 11, 13, 15, 17, 19\}$.

where λ_1 and λ_2 are the eigenvalues of this system, and R is a parameter. The solution of system (1.1) assuming that $\lambda_1 \neq \lambda_2$ is

$$\begin{aligned}\psi_1(t) &= e^{\lambda_1 t} \psi_1(0), \\ \psi_2(t) &= e^{\lambda_2 t} \psi_2(0) + \frac{R}{\lambda_1 - \lambda_2} (e^{\lambda_1 t} - e^{\lambda_2 t}) \psi_1(0).\end{aligned}\tag{1.2}$$

We see from (1.2) that if $\lambda_1, \lambda_2 < 0$, then ψ_1 will decay monotonically at long times. However, the solution for ψ_2 in (1.2) has two terms: The first term $e^{\lambda_2 t} \psi_2(0)$ would decay exponentially, whereas the second term has a competition between two exponential terms. We would expect that the second term also decays exponentially at long-times as $\lambda_1, \lambda_2 < 0$. Figure 1.2b shows the solution for ψ_2 by setting $\lambda_1 = -2$, $\lambda_2 = -3$, and $\psi_1(0) = \psi_2(0) = 1$. Notice in Figure 1.2a that when $R = 0$, ψ_2 decays exponentially, whereas with an increase in R (Figure 1.2b), ψ_2 first increases at finite times before it decays at long times.

Furthermore, we observe in Figure 1.2b that the amount of finite-time amplification increases with an increase in R . If (1.1) represents the linearized dynamics of a nonlinear system, such a finite-time amplification as in Figure 1.2b may act as a finite-amplitude perturbation to drive the system to a new nonlinear solution state.

Such finite-time growth (Figure 1.2b) is referred as nonmodal growth (growth that

is not related to unstable modes, i.e., eigenvalues with positive real part). Nonmodal amplification of exogenous disturbances plays a key role in the initial stages of a transition to turbulence in channel flows of Newtonian fluids [19, 15, 16, 14]. The role of nonmodal amplification for a transition to elastic turbulence is not very clear, although it is likely that viscoelastic channel flows are sensitive to small-amplitude perturbations [20, 21, 22, 5, 23].

Although we considered a system of ODEs to illustrate nonmodal amplification in Figure 1.2, the spatio-temporal evolution of the flow of a viscoelastic fluid in a channel is governed by a set of partial differential equations (PDE). In this thesis, PDEs are reduced to ODEs in time (similar to (1.1)) by expressing spatial variations in sets of orthogonal basis functions like the Chebyshev polynomials (i.e., using spectral methods [24, 25]). In particular, we use recently introduced well-conditioned spectral methods [26, 27] whose details can be found in Chapter 3. In the following section we briefly introduce spectral methods and their well-conditioned variants.

1.1.2 Spectral methods and their well-conditioned variants

Spectral methods express a variable of interest in a basis of orthogonal functions such as the Chebyshev polynomials. Consider a function $u(y) \in C^n[-1, 1]$, where $C^n[-1, 1]$ is the set of functions defined in the domain $y \in [-1, 1]$ that are differentiable n times. The spectral expansion of u in a Chebyshev basis is given by

$$u(y) = u_0 \frac{1}{2} T_0(y) + u_1 T_1(y) + u_2 T_2(y) \cdots + u_N T_N(y), \quad (1.3)$$

where u_i are the spectral coefficients, and T_i are the i th Chebyshev polynomials of the first kind. The Chebyshev polynomials are orthogonal with respect to an integration weight $1/\sqrt{1-y^2}$ [28, 29],

$$\frac{2}{\pi} \int_{-1}^1 \frac{T_i(y) T_j(y)}{\sqrt{1-y^2}} dy = \begin{cases} 0, & i \neq j, \\ 1, & i = j \neq 0, \\ 2, & i = j = 0. \end{cases} \quad (1.4)$$

The orthogonality relationship in (1.4) in conjunction with (1.3) yield the relationship of the spectral coefficients u_i in (1.3) with the function $u(y)$,

$$u_i = \frac{2}{\pi} \int_{-1}^1 \frac{u(y) T_i(y)}{\sqrt{1-y^2}} dy. \quad (1.5)$$

To solve the reaction-diffusion equation,

$$\frac{d^2 u}{dy^2} - k^2 u = 0, \quad u(\pm 1) = 0, \quad (1.6)$$

the function u is expressed in a Chebyshev basis with finite N in (1.3), and substituted in (1.6). The action of the second derivative operator in (1.6) is accounted for by using an equation that relates the spectral coefficients of the variable and spectral coefficients of its derivatives (Equation 10 in [28]).

Spectral methods are attractive for solutions to ODEs and PDEs as the remainder from the Chebyshev expansion for finite N in (1.3) is of $\mathcal{O}(1/N^{n-1})$ as $N \rightarrow \infty$, i.e., the spectral coefficients decay as an algebraic power ($n-1$, where n is the number of times u is differentiable) of N [28, 29]. If a function is infinitely differentiable ($n \rightarrow \infty$), then the decay rate of spectral coefficients is super-algebraic, i.e., faster than any finite power of N .

The fast convergence rate of spectral methods has been leveraged extensively to obtain solutions to ODEs and PDEs in physics and mathematics [30, 31]. For many physically motivated problems, about 100-150 basis functions are sufficient to obtain solutions to ODEs and PDEs that are nearly accurate to machine precision [32, 31].

However, the stress in viscoelastic fluids shows steep variations over localized regions which necessitates using a very large number of Chebyshev polynomials (~ 1000). The conventional procedure we discussed with the reaction-diffusion equation (1.6) yields erroneous results in a linear analysis considered here (see Chapter 3), and in [33] when using a very large number of basis functions (~ 1000).

The problem lies with using the differentiation operator that relates the spectral coefficients of a variable (say u in (1.6)) and the spectral coefficients of its derivatives [33, 26]. The differentiation operator yields ill-conditioned matrix approximations to differential equations, and the amount of ill-conditioning increases with an increase

in the number of basis functions.

Well-conditioned methods [28, 26, 27] avoid the differentiation operator. For example, one way to avoid the differentiation operator is to use the integration operator instead; we could express the highest derivative in a basis Chebyshev polynomials, i.e., in the case of (1.6)

$$\frac{d^2 u}{dy^2} = u_0 \frac{1}{2} T_0(y) + u_1 T_1(y) + u_2 T_2(y) \cdots + u_N T_N(y), \quad (1.7)$$

and use the integration operator to obtain expressions for lower derivatives. The discrete approximation obtained in this manner yields well-conditioned matrices that are suitable to use with a large number of Chebyshev basis functions.

Apart from deriving well-conditioned matrix approximations to PDEs, these well-conditioned spectral methods [26, 27] yield matrices that are also sparse and banded. Sparse banded matrices are very efficient both in terms of memory requirements and processing speed compared to dense matrices [34]. This becomes even more important as we use a large number of Chebyshev basis functions (needed in viscoelastic channel flows), which results in large matrices. In contrast, conventional spectral methods almost always produce dense-matrix approximations to PDEs [35]. With this prelude to spectral methods, we now summarize the main topics of this thesis.

1.2 Main topics of the dissertation

1.2.1 Amplification of localized body forces in channel flows of viscoelastic fluids

Nonmodal amplification of distributed body forces in channel flows of viscoelastic fluids has provided useful insights into the mechanisms that may govern the initial stages of transition to elastic turbulence [20, 21, 22, 5, 36]. However, distributed body forces are not easy to implement in experiments and so there is a need to examine amplification of localized body forces. In this first project, we use the linearized governing equations to examine such amplification in Poiseuille flow of FENE-CR fluids. We first identify the wall-normal location at which impulsive excitations experience the largest amplification and then analyze the kinetic energy of the fluctuations and the resulting flow structures.

For both a Newtonian fluid at high Reynolds numbers and a viscoelastic fluid at low Reynolds numbers, the largest amplification occurs for disturbances that are located near the channel wall. Our analysis of the energy evolution shows that a localized body force in the spanwise direction has the largest impact and that the streamwise velocity component is most affected. For viscoelastic fluids we observe the development of vortical structures away from the source of impulsive excitation. This feature is less prominent in Newtonian fluids and it may provide a mechanism for triggering the initial stages of transition to elastic turbulence

1.2.2 Well-conditioned ultraspherical and spectral integration methods for resolvent analysis of Newtonian and viscoelastic channel flows

Linear analyses of hydrodynamic flow problems provide fundamental insight into the early stages of transition to turbulence. Eigenvalues of the dynamical generator govern temporal growth or decay of individual modes, while singular values of the frequency response can be used to quantify the amplification of disturbances for linearly stable flows. In this project, we revisit nonmodal analysis in inertialess 2D viscoelastic channel flows. Nonmodal analysis reveals enormous near-wall stress gradients in plane Poiseuille flow, and near-center stress gradients in plane Couette flow. The observed steep stress gradients can readily be resolved using recently developed well-conditioned spectral methods like the ultraspherical method and spectral integration method. Furthermore, even if the method of discretization is well-conditioned, frequency response calculations can be erroneous if singular values are computed as the eigenvalues of a composite system consisting of the regular operator and its adjoint. To address this, we use a feedback interconnected system to compute singular values for frequency responses. This feedback interconnected system avoids matrix inverses and allows calculation of frequency responses of viscoelastic channel flows at very high Weissenberg numbers (~ 500). This method can potentially be applied to related problems involving stiff computations such as compressible flows. Lastly, we find that for both Newtonian and viscoelastic fluids, the Chebyshev spectral integration method has an important advantage compared to conventional spectral methods since it does not need a staggered grid when the governing equations are considered in primitive variables.

1.2.3 Stress amplification in inertialess channel flows of viscoelastic fluids

Nonmodal analysis concerns the amplification of small-amplitude perturbations on a dynamical system. Large amplification of small-amplitude perturbations in fluid flows can drive the flow to a nonlinear state. In recent experiments on nearly inertialess channel flows of viscoelastic fluids, Qin et al. (Phys. Rev. Fluids. 2:083302, 2017) observed that the kinetic energy of the fluid first decreases along the channel length before increasing, eventually leading to a turbulent-like flow state. To rationalize this observation, we consider body forces that are nearly localized in space and sinusoidal functions of time. Using well-conditioned spectral methods, we show that large magnitudes of the stress can occur via the linearized governing equations even in the presence of weak kinetic energy growth. This may provide a mechanism for the initial stages of the transition observed by Qin et al.. We find that large magnitudes of the stress occur at localized regions in the channel, and this is overlooked by a square-integrated amplification measure (such as the kinetic energy) that is typically used in nonmodal analysis. Our analysis also provides insight into the location where localized amplification is prominent in the channel for a given temporal frequency of the body force.

1.2.4 An integral reformulation of the influence-matrix algorithm for direct numerical simulations of channel flows

Direct numerical simulations (DNS) of channel flows are useful to understand and devise strategies to control the initial and intermediate stages of transition to turbulence. Kleiser and Schumann’s influence-matrix algorithm is a computationally efficient method to perform DNS of channel flows using spectral methods [24, 37, 38]. This approach involves an influence-matrix correction step that has two defects: (a) The correction is specific to the type of spectral method used, so for a new spectral method (e.g., recent well-conditioned spectral integration or ultraspherical methods) the correction is not known, (b) the correction step ensures that the velocity satisfies mass conservation to machine precision, but compromises the accuracy of momentum conservation. We report an integral reformulation of Kleiser and Schumann’s influence matrix algorithm.

Our method needs no correction step, and the velocity satisfies both mass and momentum conservation to an accuracy equivalent to the numerical resolution of the velocity field.

Chapter 2

Amplification of localized body forces in channel flows of viscoelastic fluids

This chapter is adapted from publication [\[23\]](#).

2.1 Introduction

Seminal work by Groisman and Steinberg has demonstrated that dilute polymer solutions can produce a turbulent-like flow state at low Reynolds numbers [\[7\]](#). Such a flow state is called elastic turbulence and it has high potential for enhancing mixing [\[39\]](#) and heat transport [\[40\]](#) in microfluidic flows. It can also be used to produce nonlinear effects to build microscale control devices including nonlinear flow resistors and flow memory devices such as flip-flops analogous to those in electric circuits [\[11\]](#). However, elastic turbulence is not desired in certain industrial applications, e.g., those involving polymer processing and coating flows [\[13, 41\]](#).

Elastic turbulence observed in the experiments of Groisman and Steinberg [\[7\]](#) is thought to have originated from linear instability of curved streamlines to small-amplitude

perturbations. Even though analysis of the linearized governing equations predicts stability of inertialess channel flows with straight streamlines [13], recent experiments suggest that elastic turbulence can also occur in such flows [8, 9, 42]. This is a puzzling observation with both fundamental and technological ramifications. For example, polymer processing operations often involve flows through straight channels and instabilities at low Reynolds numbers are detrimental to the quality of the final products [13]. Furthermore, as indicated above, triggering elastic turbulence also finds positive applications in microfluidic devices.

The absence of linear modal instability does not preclude the possibility that the early stages of transition to elastic turbulence can be understood via analysis of the linearized equations. Nonmodal analysis considers the possibility that flow fluctuations that decay asymptotically can grow transiently and that exogenous disturbances can be significantly amplified by the underlying dynamics [16, 15, 43, 14]. Disturbances that experience linear nonmodal amplification can generate finite-amplitude perturbations that may trigger nonlinear flow states and induce transition to elastic turbulence.

In refs. [20] and [21], it was demonstrated that distributed body forces can experience significant nonmodal amplification in Couette and Poiseuille flows at low Reynolds numbers when viscoelastic effects are strong. This work showed that streamwise-constant flow structures in Oldroyd-B fluids become increasingly prominent with an increase in viscoelastic effects. This inspired Jovanović and Kumar to closely examine dynamics of streamwise-constant fluctuations in weakly inertial channel flows of viscoelastic fluids [22, 5]. Their work showed that nonmodal amplification arises from a coupling between the base-state stresses and flow fluctuations, demonstrated the existence of a viscoelastic analogue of the well-known inertial lift-up mechanism, and established conceptual and mathematical similarities between nonmodal amplification in viscoelastic channel flows at low Reynolds numbers and in Newtonian channel flows at high Reynolds numbers.

The joint influence of inertia and elasticity on the evolution of streamwise-elongated fluctuations in Couette flow of Oldroyd-B fluids was studied in ref. [44]. The response of the linearized equation for the wall-normal vorticity in the presence of a decaying streamwise vortex was computed and different regimes were identified based on the relation between the solvent diffusion and polymer relaxation times. The influence of

finite extensibility of polymer molecules on the worst-case amplification of deterministic distributed body forces has also been examined using the FENE-CR model [36]. This work demonstrated that even in flows with infinitely large Weissenberg numbers, the finite extensibility of polymer molecules limits the largest achievable amplification. In related work, the viscoelastic equivalent of the well-known Orr mechanism was studied for both the Oldroyd-B and FENE-P models [45].

The aforementioned work has provided important insights into the linearized dynamics of channel flows of viscoelastic fluids in the presence of distributed body forces. To achieve a direct correspondence between theory and experiment in the linearized setting, one would have to induce distributed body forces without significantly altering the mean flow, which is extremely challenging. Even if a distributed body force can be generated in an experiment and used as a starting point for a linearized analysis, it is still difficult to systematically segregate the different stages that lead to elastic turbulence by the introduction of such a force.

In contrast, localized body forces can be readily approximated in experiments and direct numerical simulations. Furthermore, flow transition arising from the introduction of a localized body force can be dissected to demonstrate the different stages of transition to nonlinear states. For this reason, localized body forces have been applied in many experimental studies of transition in Newtonian fluids at high Reynolds numbers [46, 47, 48]. Moreover, in theoretical and computational studies, a localized body force can be approximated by a spatio-temporal impulsive excitation. As demonstrated in refs. [49] and [50] and further expanded on in ref. [15], such an analysis exemplifies dominance of streamwise-elongated structures inside the resulting wave packet in the early stages of disturbance amplification. Recently, localized body forces were used in viscoelastic channel flows to study drag-reduction at high Reynolds numbers [51].

Any spatially varying and temporally distributed body force can be expressed as a summation of impulses of different magnitudes, spatial positions, and temporal occurrences [52]. The impulse response therefore contains useful information for characterizing responses of linear systems to exogenous excitation sources. As noted above, previous work on Newtonian fluids has shown that by examining the influence of spatio-temporal impulsive forcing on the linearized dynamics, several features of the early stages of transition to turbulence in high-Reynolds-number flows of Newtonian fluids

can be captured [49, 50, 15].

In this paper, we systematically analyze the response of the linearized dynamics of a viscoelastic fluid in Poiseuille flow to a localized body force. We first identify the wall-normal location at which the impulse has the largest impact on the flow. We then analyze the evolution of the energy of velocity fluctuations arising from the point force applied at the optimal location and demonstrate that the amplification increases with an increase in polymer concentration and with an increase in the polymer relaxation time. Finally, we analyze flow structures that result from the impulse and discuss their potential role in the early stages of transition to elastic turbulence.

The remainder of our presentation is organized as follows. In § 2.2, we describe the modeling and numerical methods employed in this work. In § 2.3, we present results pertaining to the identification of the optimal wall-normal location of the impulsive forcing. In § 2.4, we analyze the kinetic energy of flow fluctuations that arise from the application of a point force at the identified optimal wall-normal location. We discuss the resulting flow structures in § 2.5, summarize our findings in § 2.6, and relegate background technical material to the appendices.

2.2 Problem formulation

In this section, we present the governing equations in their evolution form, the numerical methods we use, and the way we characterize the kinetic energy of velocity fluctuations. We use the finitely extensible nonlinear elastic Chilcott-Rallison (FENE-CR) constitutive equation [53] as it accounts for the finite extensibility of polymer molecules and exhibits a constant shear viscosity. Results obtained using the FENE-CR model thus allows us to isolate the influence of fluid elasticity.

2.2.1 Evolution form of governing equations

We consider a dilute polymer solution of density ρ and relaxation time λ in a channel flow whose geometry is shown in Figure 2.1. Length is scaled with the half-channel width h , velocity with the maximum velocity in the channel U_0 , and time with h/U_0 . Pressure is scaled with $\eta_T U_0/h$, where $\eta_T = \eta_p + \eta_s$ is the total shear viscosity with η_p and η_s denoting the polymer and solvent contributions to η_T . Polymer stresses are scaled with $\eta_p U_0/h$.

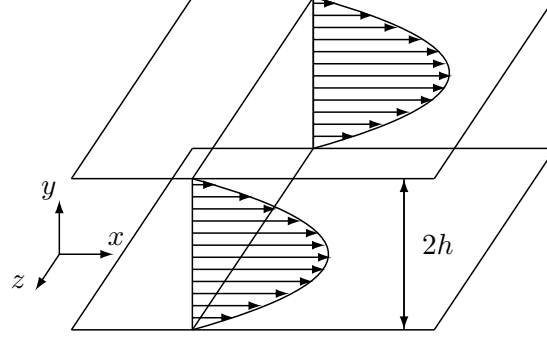


Figure 2.1: Flow geometry and the steady-state parabolic velocity profile for Poiseuille flow.

This scaling leads to three non-dimensional groups: the viscosity ratio, $\beta = \eta_s/(\eta_p + \eta_s)$, the Weissenberg number, $We = \lambda U_0/h$, and the Reynolds number, $Re = h\rho U_0/\eta_T$. The viscosity ratio provides a measure of the solvent contribution to the shear viscosity, the Weissenberg number gives the ratio of the relaxation time of the polymer to the characteristic flow time, h/U_0 , and the Reynolds number is the ratio of inertial forces to viscous forces. In addition, the elasticity number, $\mu = We/Re = \lambda/(h^2\rho/\eta_T)$, determines the ratio between the fluid relaxation time and characteristic vorticity diffusion time.

The dimensionless momentum and continuity equations are

$$Re(\partial_t \mathbf{V} + \mathbf{V} \cdot \nabla \mathbf{V}) = -\nabla P + \beta \Delta \mathbf{V} + (1 - \beta) \nabla \cdot \mathbf{T}, \quad (2.1a)$$

$$\nabla \cdot \mathbf{V} = 0, \quad (2.1b)$$

where ∂_t denotes a partial derivative with respect to time t , \mathbf{V} is the velocity vector, P is the pressure, and \mathbf{T} is the polymer contribution to the stress tensor.

The conformation tensor is the mean of the dyadic product of the end-to-end vector of the finitely extensible dumbbell that is the basis of the FENE-CR model. The polymer

stress tensor \mathbf{T} is related to the conformation tensor \mathbf{R} by

$$\partial_t \mathbf{R} + \mathbf{V} \cdot \nabla \mathbf{R} - \mathbf{R} \cdot \nabla \mathbf{V} - (\mathbf{R} \cdot \nabla \mathbf{V})^T = -\mathbf{T}, \quad (2.2a)$$

$$\frac{f}{We}(\mathbf{R} - \mathbf{I}) = \mathbf{T}, \quad (2.2b)$$

where \mathbf{I} is the identity tensor and f quantifies the nonlinear spring interaction,

$$f = \frac{L^2 - 3}{L^2 - \text{trace}(\mathbf{R})}. \quad (2.2c)$$

We note that \mathbf{R} and L^2 are scaled with kT/c , and k , T , and c are the Boltzmann constant, absolute temperature, and spring constant of the dumbbells, respectively. As $L \rightarrow \infty$, the FENE-CR model simplifies to the Oldroyd-B model. Furthermore, system (2.1) reduces to the Navier-Stokes equations as $\beta \rightarrow 1$.

The steady-state solution of system (2.1) for plane Poiseuille flow is

$$\bar{\mathbf{V}} = [\bar{U}(y) \quad 0 \quad 0]^T, \quad (2.3a)$$

$$\bar{\mathbf{R}} = \begin{bmatrix} 1 + 2 (We \bar{U}'(y)/\bar{f})^2 & We \bar{U}'(y)/\bar{f} & 0 \\ We \bar{U}'(y)/\bar{f} & 1 & 0 \\ 0 & 0 & 1 \end{bmatrix}, \quad (2.3b)$$

where

$$\bar{U}(y) = 1 - y^2, \quad \bar{f} = \frac{1}{2} \left(1 + \sqrt{1 + 8 \left(\frac{We \bar{U}'(y)}{\bar{L}} \right)^2} \right), \quad \bar{L}^2 = L^2 - 3. \quad (2.3c)$$

The steady-state velocity has the same parabolic profile as a Newtonian fluid because of the absence of shear-thinning effects in the FENE-CR constitutive equation. There is, however, a first normal stress difference in the FENE-CR fluid.

The linearized equations that govern the evolution of fluctuations about the steady-state (2.3) are given by

$$Re \partial_t \mathbf{v} = -\nabla p + (1 - \beta) \nabla \cdot \boldsymbol{\tau} + \beta \Delta \mathbf{v} - Re(\bar{\mathbf{V}} \cdot \nabla \mathbf{v} + \mathbf{v} \cdot \nabla \bar{\mathbf{V}}) + \mathbf{d}, \quad (2.4a)$$

$$\nabla \cdot \mathbf{v} = 0, \quad (2.4b)$$

$$\partial_t \mathbf{r} = \mathbf{r} \cdot \nabla \bar{\mathbf{V}} + \bar{\mathbf{R}} \cdot \nabla \mathbf{v} + (\mathbf{r} \cdot \nabla \bar{\mathbf{V}})^T + (\bar{\mathbf{R}} \cdot \nabla \mathbf{v})^T - \mathbf{v} \cdot \nabla \bar{\mathbf{R}} - \bar{\mathbf{V}} \cdot \nabla \mathbf{r} - \boldsymbol{\tau}, \quad (2.4c)$$

$$\boldsymbol{\tau} = \frac{\bar{f}}{We} \left(\mathbf{r} + \frac{\bar{f}(\bar{\mathbf{R}} - \mathbf{I})}{\bar{L}^2} \text{trace}(\mathbf{r}) \right). \quad (2.4d)$$

Here, \mathbf{v} , p , \mathbf{r} , and $\boldsymbol{\tau}$ denote velocity, pressure, conformation tensor, and stress tensor fluctuations about their respective base profiles, $\bar{\mathbf{V}}$, \bar{P} , $\bar{\mathbf{R}}$, and $\bar{\mathbf{T}}$. We denote the components of the velocity fluctuation vector by $\mathbf{v} = [u \ v \ w]^T$, where u , v , and w represent the streamwise (x), wall-normal (y), and spanwise (z) velocities, respectively. Although the total conformation tensor $\bar{\mathbf{R}} + \mathbf{r}$ has to be positive definite, this requirement does not hold for \mathbf{r} .

The body forcing \mathbf{d} is used to excite flow fluctuations. In this work, we use an impulsive body force,

$$\mathbf{d}(x, y, z, t) = \delta(x, y, z, t) \mathbf{e}_i = \delta(x) \delta(y) \delta(z) \delta(t) \mathbf{e}_i, \quad (2.5)$$

where \mathbf{e}_i is a unit vector in the i th coordinate direction and $\delta(\cdot)$ is the Dirac delta function.

System (2.4) can be simplified by eliminating pressure and expressing the velocity fluctuations in terms of wall-normal velocity v and vorticity $\eta := \partial_z u - \partial_x w$. This is done by taking the divergence of (2.4a) to get an explicit expression for p . Substituting this expression for p into (2.4a) yields the equation for the wall-normal velocity and the equation for η is determined by the y -component of the curl of (2.4a). Finally, the stress tensor can be eliminated in favor of the conformation tensor using relations (2.4c) and (2.4d).

After the above algebraic manipulations, and after taking a Fourier transform in the

x - and z -directions, we obtain the following evolution form for the linearized equations,

$$\begin{aligned}\partial_t \boldsymbol{\psi}(\boldsymbol{\kappa}, y, t) &= [\mathbf{A}(\boldsymbol{\kappa}) \boldsymbol{\psi}(\boldsymbol{\kappa}, \cdot, t)](y) + [\mathbf{B}(\boldsymbol{\kappa}) \mathbf{d}(\boldsymbol{\kappa}, \cdot, t)](y), \\ \boldsymbol{\phi}(\boldsymbol{\kappa}, y, t) &= [\mathbf{C}(\boldsymbol{\kappa}) \boldsymbol{\psi}(\boldsymbol{\kappa}, \cdot, t)](y),\end{aligned}\tag{2.6}$$

where $\boldsymbol{\psi} = [\mathbf{r}^T \ v \ \eta]^T$ is the state with \mathbf{r} denoting the vector of the six fluctuating components of the (symmetric) conformation tensor. The linear integro-differential operators in the wall-normal direction \mathbf{A} , \mathbf{B} , and \mathbf{C} are defined in the Appendix A and they map the input \mathbf{d} (i.e., the imposed forcing) to the output $\boldsymbol{\phi} = [u \ v \ w]^T$ (i.e., the vector of velocity fluctuations) through the evolution model. We define $\boldsymbol{\kappa} = (k_x, k_z)$, where k_x and k_z represent the wavenumbers in the x - and z -directions. The no-slip and no-penetration boundary conditions are applied to the wall-normal velocity and vorticity components in (2.6),

$$v(\boldsymbol{\kappa}, y = \pm 1, t) = \partial_y v(\boldsymbol{\kappa}, y = \pm 1, t) = \eta(\boldsymbol{\kappa}, y = \pm 1, t) = 0.\tag{2.7}$$

2.2.2 Numerical method

Evolution model (2.6) represents a system of integro-differential equations in y and t , parametrized by the wavevector $\boldsymbol{\kappa} = (k_x, k_z)$. The wall-normal direction is discretized using a Chebyshev pseudospectral technique with N collocation points to reduce (2.6) with boundary conditions (2.7) to a system of ordinary differential equations (ODEs) in time. All calculations are carried out using the Matlab Differentiation Matrix Suite of Weidmann and Reddy [32].

The Fourier transform in wall-parallel directions of the body force in (2.5) is given by

$$\mathbf{d}(\boldsymbol{\kappa}, y, t) = \delta(y)\delta(t) \mathbf{e}_i.\tag{2.8}$$

This is because the Fourier transform of $\delta(x)\delta(z)$ with respect to x and z is equal to one for all $\boldsymbol{\kappa} = (k_x, k_z)$ (cf. (A1) in Appendix A). Since the wall-normal direction is discretized on a finite grid of Chebyshev collocation points, we employ the following approximation for $\delta(y)$,

$$\delta_0(y) = \frac{1}{2\sqrt{\pi\epsilon}} e^{-\frac{(y-y_0)^2}{4\epsilon}}, \quad \epsilon > 0,\tag{2.9}$$

where y_0 denotes the location of the impulse in the wall-normal direction and ϵ is a small parameter. In this work, we set $\epsilon = 1/2000$. We found that this value is sufficiently small to represent an impulse as the results do not change significantly by further reducing ϵ . We discuss the choice of y_0 in § 2.3.

The forcing term in the evolution model (2.6) is then given by

$$[\mathbf{B}(\boldsymbol{\kappa}) \mathbf{d}(\boldsymbol{\kappa}, \cdot, t)](y) = \mathbf{F}_i(\boldsymbol{\kappa}, y) \delta(t), \quad (2.10)$$

where

$$\mathbf{F}_i(\boldsymbol{\kappa}, y) = [\mathbf{B}(\boldsymbol{\kappa}) \delta_0(\cdot) \mathbf{e}_i](y) \quad (2.11)$$

and \mathbf{e}_i is a unit vector in the i th coordinate direction with $i = x, y$, or z . The resulting finite-dimensional approximation to (2.6) is then given by

$$\begin{aligned} \dot{\psi}(\boldsymbol{\kappa}, t) &= A(\boldsymbol{\kappa}) \psi(\boldsymbol{\kappa}, t) + F_i(\boldsymbol{\kappa}) \delta(t), \\ \phi(\boldsymbol{\kappa}, t) &= C(\boldsymbol{\kappa}) \psi(\boldsymbol{\kappa}, t), \end{aligned} \quad (2.12)$$

where $\psi(\boldsymbol{\kappa}, t)$ and $\phi(\boldsymbol{\kappa}, t)$ are complex-valued vectors with $8N$ and $3N$ entries, respectively, $A(\boldsymbol{\kappa})$ and $C(\boldsymbol{\kappa})$ are the finite-dimensional approximations of the corresponding operators in (2.6), and $F_i(\boldsymbol{\kappa})$ is the discrete approximation to $\mathbf{F}_i(\boldsymbol{\kappa}, y)$ in (2.11).

The solution of (2.12) with zero initial conditions arising from the impulsive excitation in the i th coordinate direction is given by [17],

$$\phi_i(\boldsymbol{\kappa}, t) = C(\boldsymbol{\kappa}) \int_0^t e^{A(\boldsymbol{\kappa})(t-s)} F_i(\boldsymbol{\kappa}) \delta(s) ds = C(\boldsymbol{\kappa}) e^{A(\boldsymbol{\kappa})t} F_i(\boldsymbol{\kappa}). \quad (2.13)$$

Thus, the impulse response is directly obtained from the matrix exponential at a given time and the inverse Fourier transform in wall-parallel directions yields a solution in physical space.

2.2.3 Model parameters

The linearized equations (2.4) contain four parameters: the solvent contribution to the shear viscosity, β , the amount of extensibility of the polymer molecules, L , the Weissenberg number, We , and the Reynolds number, Re . A larger value of β implies a smaller polymer concentration. A larger value of We implies that the fluid has a

longer relaxation time. Due to the high computational expense of performing three-dimensional calculations on eight state variables (see § 2.2.1), we restrict our analysis to a limited range of parameters; our choice represents a compromise between values used in experimental studies and the need to avoid numerical instabilities.

We present results for $Re = 50$, which is well within the laminar flow limits for a Newtonian fluid. In straight channels, elastic turbulence has been reported at smaller Reynolds numbers [9, 8]; for example, recent experiments have shown turbulent features for Reynolds numbers between 2.5-150 (based on the half-channel width) [54]. We choose $Re = 50$ because resolving flow structures in physical space (§ 2.5) at lower values of Re requires larger values of k_x and k_z , which in turn requires a larger number of discrete Fourier modes for good resolution in physical space. Flow structures presented in § 2.5 use 512×512 linearly spaced grid points in the κ -plane with $\{k_{x,\min} = -50, k_{x,\max} = 49.80\}$ and $\{k_{z,\min} = -72, k_{z,\max} = 71.72\}$. Larger values of k_x and k_z also require more Chebyshev collocation points to discretize the wall-normal direction (see § 2.2.2) sufficiently to avoid numerical instabilities [55, 56], which further increases the computational cost. Typically 120 to 150 collocation points were used, and this was sufficient to obtain converged results.

In § 2.4 we present a parametric study for a range of Weissenberg numbers, but we choose a representative value of $We = 50$ for most results presented here. This is because we found that the amplification increases with We (see § 2.4), and $We = 50$ is the maximum value we could reach for grid-independent results without numerical instabilities. Confining ourselves to $We \leq 50$ fixes the upper limit of the elasticity number $\mu = We/Re$ in our simulations to $\mu = 1$. Using larger values of the Weissenberg number could bring out more distinctly features related to viscoelastic effects in flow structures, but at the cost of encountering and addressing numerical instabilities. In experiments concerning elastic turbulence, the Weissenberg number was varied between 20 and 1000 [54]. We note that all results presented in this work are free from any artificial diffusion, numerical filters, or diffusion-inducing numerical schemes commonly employed to address numerical instabilities when simulating viscoelastic channel flows [57, 58, 59].

Groisman and Steinberg [7] had $\beta = 0.765$ in curvilinear flows and refs. [8, 9] had a value between 0.25 and 0.5 for straight-channel flows. Unless otherwise noted, we choose $\beta = 0.5$. In modeling polymeric fluids, values of L have ranged widely, from

about 2.5 to infinity [53]. In the limit of infinite L , the FENE-CR model reduces to the Oldroyd-B model, which is successful in describing some features of dilute polymeric flows but becomes less accurate at higher shear rates [60, 61]. Since finite values of L have been shown to work better in modeling dilute polymeric flows [60, 61, 53], we set $L = 100$.

2.2.4 Energy of velocity fluctuations

The integral of the kinetic energy of the velocity fluctuations in the wall-normal direction can be evaluated using a weighted inner product of the output with itself

$$E_i(\boldsymbol{\kappa}, t) := \int_{-1}^1 \mathbf{v}_i^*(\boldsymbol{\kappa}, y, t) \mathbf{v}_i(\boldsymbol{\kappa}, y, t) dy = \phi_i^*(\boldsymbol{\kappa}, t) I_w \phi_i(\boldsymbol{\kappa}, t), \quad (2.14)$$

where $(\cdot)^*$ denotes the complex conjugate transpose and I_w is a diagonal matrix of the appropriate integration weights for the Chebyshev collocation points. We recall that the subscript i denotes the input direction of the impulsive excitation, cf. (2.13).

We further perform integration over time to obtain

$$\bar{E}_i(\boldsymbol{\kappa}) := \int_0^\infty E_i(\boldsymbol{\kappa}, t) dt, \quad (2.15a)$$

and note that for stable systems, the solution to the algebraic Lyapunov equation [16],

$$A(\boldsymbol{\kappa})X_i(\boldsymbol{\kappa}) + X_i(\boldsymbol{\kappa})A^\dagger(\boldsymbol{\kappa}) = -F_i(\boldsymbol{\kappa})F_i^\dagger(\boldsymbol{\kappa}), \quad (2.15b)$$

can be used to avoid explicit integration in (2.15a) and compute $\bar{E}_i(\boldsymbol{\kappa})$ as

$$\bar{E}_i(\boldsymbol{\kappa}) = \text{trace}(X_i(\boldsymbol{\kappa}) C^\dagger(\boldsymbol{\kappa}) C(\boldsymbol{\kappa})). \quad (2.15c)$$

For a derivation of this relationship, see [16]. Here, $(\cdot)^\dagger$ is the finite-dimensional approximation to the adjoints of the operators that appear in (2.6) and $\text{trace}(\cdot)$ is the matrix trace, i.e., the sum of its eigenvalues. Adjoint operators are defined with respect to a weighted inner product that determines the kinetic energy of velocity fluctuations [16]; see Appendix B for additional details.

In addition to the total kinetic energy, we also analyze the componentwise contribution of velocities $r = u, v$, or w to the total kinetic energy,

$$E_{ri}(\boldsymbol{\kappa}, t) := \int_{-1}^1 r_i^*(\boldsymbol{\kappa}, y, t) r_i(\boldsymbol{\kappa}, y, t) dy, \quad (2.16a)$$

$$\bar{E}_{ri}(\boldsymbol{\kappa}) := \int_0^\infty E_{ri}(\boldsymbol{\kappa}, t) dt, \quad (2.16b)$$

where E_{ri} and \bar{E}_{ri} represent the energy of the velocity component r arising from the impulsive forcing in the i th coordinate direction. We note that

$$E_i = E_{ui} + E_{vi} + E_{wi},$$

and that E_{ri} and \bar{E}_{ri} can be evaluated in a similar manner as the total kinetic energy in (2.14) and (2.15) by replacing $C(\boldsymbol{\kappa})$ in (2.15c) with $C_r(\boldsymbol{\kappa})$; see equation (A10) in Appendix A.

2.3 Flow sensitivity to the location of the impulse

The location of the impulse in the (x, z) -plane is immaterial because the x - and z -directions are translationally invariant. However, the sensitivity of the flow may vary with the choice of the location of the impulse in the wall-normal direction. We next examine how the sensitivity of a viscoelastic channel flow changes with the wall-normal location of impulsive forcing. We only introduce impulses in the lower half of the channel because the symmetry of plane Poiseuille flow implies that the same level of energy amplification would be obtained if the impulse was introduced at the corresponding location in the upper half of the channel.

We first calculate the kinetic energy averaged over the wall-normal direction and time (using (2.15)) as a function of $\boldsymbol{\kappa}$ for different values of y_0 . For example, Figure 2.2 shows the kinetic energy for an impulsive excitation in the streamwise direction (Figure 2.2a), wall-normal direction (Figure 2.2b), and spanwise direction (Figure 2.2c) for $y_0 = -0.75$ and $Re = 50$. The maximum value of the kinetic energy over all values of k_x and k_z is marked by the black dots in Figure 2.2. In Figure 2.3, we examine how these peak values depend on the location of the impulse, y_0 . We note that for $y_0 = -0.75$ the

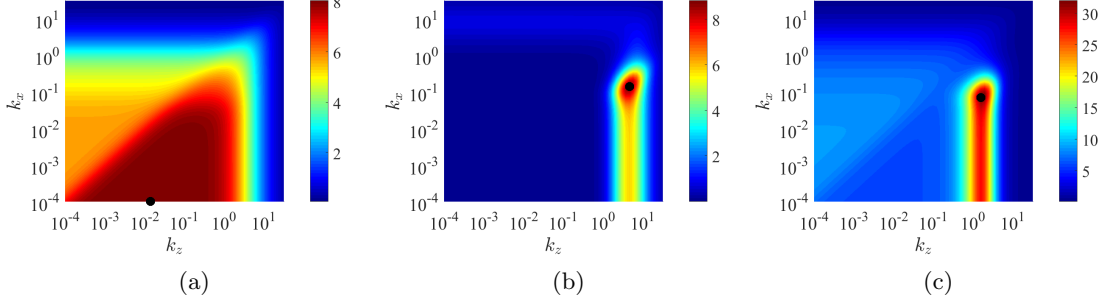


Figure 2.2: Kinetic energy integrated over the wall-normal direction and time, with an impulsive excitation located at $y_0 = -0.75$. Plots correspond to (a) \bar{E}_x , (b) \bar{E}_y , and (c) \bar{E}_z respectively, calculated from (2.15). Parameters used are $Re = 50$, $We = 50$, $L = 100$, and $\beta = 0.5$. The maximum value of the kinetic energy is marked by the black dots.

maximum value of the kinetic energy in Figure 2.2a occurs at $(k_x \approx 10^{-4}, k_z \approx 10^{-2})$, in Figure 2.2b at $(k_x \approx 10^{-1}, k_z \approx 1.5)$, and in Figure 2.2c at $(k_x \approx 10^{-1}, k_z \approx 10^0)$. These values change as we change y_0 .

Figure 2.3 shows how the largest value of kinetic energy depends on the wall-normal location y_0 of an impulsive excitation in the streamwise (Figure 2.3a), wall-normal (Figure 2.3b), and spanwise (Figure 2.3c) direction. The relative contribution of fluid elasticity compared to vorticity diffusion can be quantified in terms of the elasticity number $\mu = We/Re$. In Figure 2.3, the Newtonian fluid corresponds to $\mu = 0$ and the viscoelastic fluid to $\mu = 1$; as mentioned in § 2.2.3, since we set $Re = 50$ and confine our attention to $We \leq 50$, in our study we have $0 \leq \mu \leq 1$.

We see that the introduction of viscoelasticity increases the kinetic energy of velocity fluctuations for an impulsive excitation in any of the three directions. Larger amplification of disturbances in viscoelastic fluids indicates their greater sensitivity at relatively low values of the Reynolds number. As Figure 2.3a demonstrates, the influence of viscoelasticity is not as significant for an impulsive excitation in the streamwise direction. We observe more pronounced differences between Newtonian and viscoelastic responses for excitations in the wall-normal (Figure 2.3b) and spanwise (Figure 2.3c) directions. The largest discrepancy between corresponding kinetic energies occurs for the impulse in the spanwise direction (Figure 2.3c) at a location $y_0 = -0.75$.

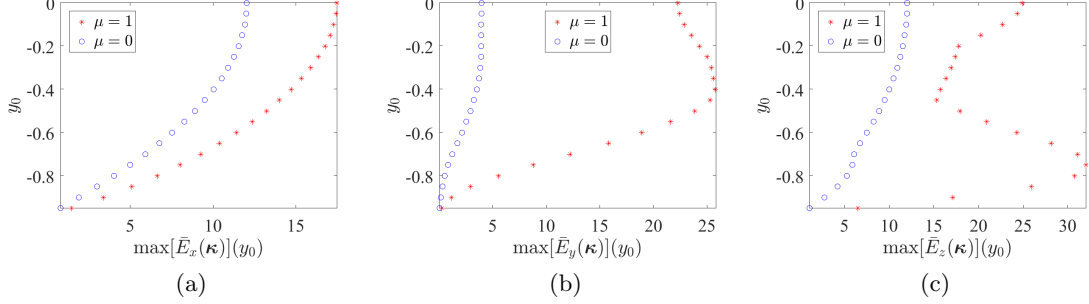


Figure 2.3: Maximum kinetic energy induced by an impulsive excitation in the (a) streamwise, (b) wall-normal, and (c) spanwise directions as a function of y_0 , calculated using (2.15). The Newtonian fluid corresponds to $\mu = 0$, and the viscoelastic fluid to $\mu = 1$ (the parameters are $Re = 50$, $We = 50$, $L = 100$, and $\beta = 0.5$).

Thus far we have studied the sensitivity of Newtonian and viscoelastic plane Poiseuille flow to the wall-normal location of point forces when $Re = 50$. Increasing Re to larger values shows interesting similarities between a Newtonian fluid at high Reynolds numbers and a viscoelastic fluid at low Reynolds numbers. Figure 2.4 shows similar plots of the maximum kinetic energy over all k_x and k_z when $Re = 1000$. We see that the plots for the largest kinetic energy for impulsive excitations in the wall-normal (Figure 2.4b) and spanwise (Figure 2.4c) directions are similar in shape for the Newtonian and viscoelastic fluids. This is because inertial forces dominate over elastic forces as reflected by the value of the elasticity numbers, $\mu = 0.05$ (viscoelastic) and $\mu = 0$ (Newtonian). The plots have very different shapes for a Newtonian and a viscoelastic fluid with an impulsive streamwise excitation (Figure 2.4a), in that the viscoelastic fluid is less energetic at high Reynolds numbers. However, the values of energy (as seen from the y -axis) are substantially lower when compared to impulsive excitations in the spanwise or wall-normal directions.

It is interesting to observe a similar maximum near the wall in Figure 2.4c in the Newtonian fluid at $Re = 1000$ that was seen in the viscoelastic fluid at $Re = 50$ (the peak located at $y_0 = -0.75$ in Figure 2.3c). We note that this maximum was absent in the Newtonian fluid at $Re = 50$ (Figure 2.3c). This indicates a striking similarity in the nonmodal amplification of a Newtonian fluid at high Reynolds numbers and a viscoelastic fluid at low Reynolds numbers and can be attributed to the viscoelastic

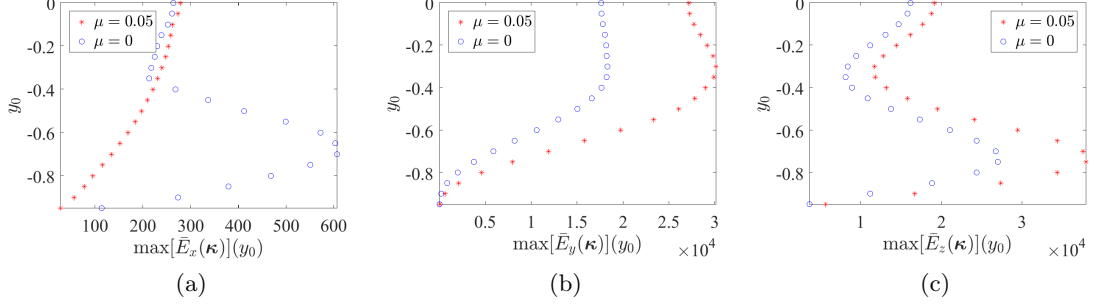


Figure 2.4: Maximum energy induced by an impulsive excitation in the (a) streamwise, (b) wall-normal, and (c) spanwise directions as a function of y_0 , calculated using (2.15). The Newtonian fluid corresponds to $\mu = 0$, and the viscoelastic fluid to $\mu = 0.05$ (the parameters are $Re = 1000$, $We = 50$, $L = 100$, and $\beta = 0.5$).

analogue of the well-known lift-up mechanism [22, 5].

The governing mechanism in Newtonian fluids that leads to nonmodal amplification comes from the vortex-tilting effect, and can be analyzed by examining the equation for the evolution of the wall-normal vorticity η ,

$$\partial_t \eta = -Re U' \partial_z v + \Delta \eta, \quad (2.17)$$

where the time is scaled with the diffusive time scale $h^2 \rho / \eta_T$. The second term in (2.17) is the Laplacian operator Δ that arises from viscous dissipation and it acts to decrease the wall-normal vorticity. The first term is solely responsible for non-modal amplification. The term $-U'$ is the spanwise vorticity in the base flow, and $\partial_z v$ can be interpreted as a stress which corresponds to a force in the wall-normal direction that varies in the spanwise direction. Thus the spanwise vorticity in the base flow is forced in the wall-normal direction so as to amplify the wall-normal vorticity [19].

For inertialess Oldroyd-B fluids, Jovanović and Kumar [5] derived the evolution equation for the wall-normal vorticity η ,

$$\partial_t \Delta \eta = -We \frac{1-\beta}{\beta} (U'(y) \Delta \partial_z + 2U''(y) \partial_{yz}) v - \frac{1}{\beta} \Delta \eta, \quad (2.18)$$

where time is scaled with the polymer relaxation time. Note that if time is rescaled with the convective time scale in (2.18) and the limit of a Newtonian fluid is considered,

we recover (2.17) with $Re = 0$; for additional information, see [5].

For Newtonian fluids, the vortex tilting term in (2.17) vanishes in the absence of inertia, i.e., at $Re = 0$. Viscoelastic fluids, however, have additional terms that can produce a vortex-tilting-like effect even at $Re = 0$; cf. (2.18). The terms U' and U'' in (2.18) come from the shear stress T_{12} in the base flow of the viscoelastic fluid [5].

Equations (2.17) and (2.18) suggest an underlying similarity between a Newtonian fluid at high Reynolds numbers and a viscoelastic fluid at low Reynolds numbers. A Newtonian fluid at high Reynolds numbers experiences amplification due to the spanwise vorticity in the base state. Similarly, a viscoelastic fluid at low Reynolds numbers experiences amplification due to a coupling between the polymeric stresses in the base state and velocity fluctuations. The amount of amplification scales with the Weissenberg number for the inertialess viscoelastic fluid and with the Reynolds number for the Newtonian fluid.

In this section, we have investigated the influence of the location of the impulse on the flow. We have demonstrated that the impulse in the spanwise direction has the maximum impact on the flow and that there is similarity in the nature of the most sensitive locations between a Newtonian fluid at high Reynolds numbers and a viscoelastic fluid at low Reynolds numbers. This similarity can be understood in terms of the well-known lift-up mechanism and its viscoelastic analogue, as discussed by Jovanović and Kumar [5]. In § 2.4, we examine energy of velocity fluctuations corresponding to an impulsive excitation at $y_0 = -0.75$ in a flow with $Re = 50$.

2.4 Energy evolution

In the previous section, we identified the location in the wall-normal direction where the localized point force has the maximum impact on the flow. In this section, we contrast the evolution of energy in viscoelastic and Newtonian fluids by introducing an impulse at the optimal location for viscoelastic fluids. We examine the impact on the streamwise, wall-normal, and spanwise velocity fluctuations separately and find that the streamwise velocity is most affected. We then study changes in the energy evolution with β (polymer concentration) and We (polymer relaxation time).

Figure 2.5 shows the kinetic energy averaged over the wall-normal direction and time at $Re = 50$, calculated from (2.15). Figures 2.5a-2.5c show the kinetic energy of

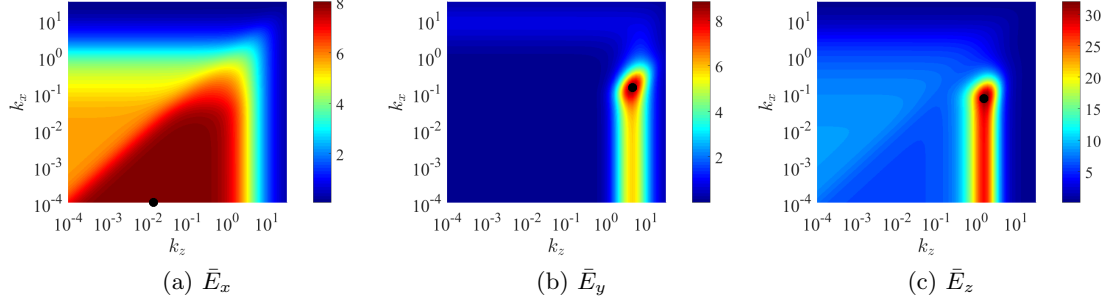
a viscoelastic fluid and Figures 2.5d-2.5f show the kinetic energy of a Newtonian fluid. Figures 2.5a and 2.5d correspond to an impulsive forcing in the streamwise direction, Figures 2.5b and 2.5e correspond to an impulsive excitation in the wall-normal direction, and Figures 2.5c and 2.5f correspond to an impulsive excitation in the spanwise direction. By observing the scales on the color bars we see that, in all cases, the kinetic energy of velocity fluctuations in the viscoelastic fluid is higher when compared to a Newtonian fluid. The additional energy in viscoelastic fluids comes from the elastic stresses in the base flow which are absent in Newtonian fluids [5, 36]; see the discussion toward the end of § 2.3 (and (2.18)).

It can be seen that there is not a significant difference in the kinetic energy for a streamwise impulsive excitation in the viscoelastic (Figure 2.5a) and Newtonian (Figure 2.5d) fluids. For impulsive excitations in the wall-normal and spanwise directions, however, differences are significant. Impulsive excitations in the wall-normal and spanwise directions for the viscoelastic fluid produce fluctuations that are nearly streamwise-constant with the maximum kinetic energy near $k_x \approx 10^{-1}, k_z \approx 10^0$ (Figures 2.5b and 2.5c). For the Newtonian fluid, the resulting fluctuations are less oblique ($k_x \approx 10^{-4}$; Figures 2.5e and 2.5f).

The spanwise impulsive excitation is amplified about six times more in viscoelastic fluid (Figure 2.5c) than in the Newtonian fluid (Figure 2.5f). Since the impulse in the spanwise direction induces the highest amount of energy, in what follows we only analyze the impact of the spanwise impulsive excitation on the evolution of velocity fluctuations.

The energy can be further analyzed based on the individual contributions from the streamwise, wall-normal, and spanwise velocities. Figure 2.6 shows the contribution of the total kinetic energy due to the streamwise velocity (Figure 2.6a), wall-normal velocity (Figure 2.6b), and spanwise velocity (Figure 2.6c). From the color bars, we notice that the streamwise velocity has the largest contribution to the overall energy. We thus conclude that the spanwise forcing has the maximum impact on the flow and that the streamwise velocity is most affected. This observation is again similar to what is seen for Newtonian fluids at high Reynolds numbers as investigated by Jovanović and Bamieh [16]. The difference is that the most amplified disturbances are more oblique ($k_x \approx 10^{-1}, k_z \approx 10^0$) in viscoelastic fluids when compared to Newtonian fluids at high Reynolds numbers, where the most prominent fluctuations are streamwise-constant

$\beta = 0.5$, $L = 100$, $\mu = 1$, and $Re = 50$ (Viscoelastic fluid):



$\mu = 0$ and $Re = 50$ (Newtonian fluid):

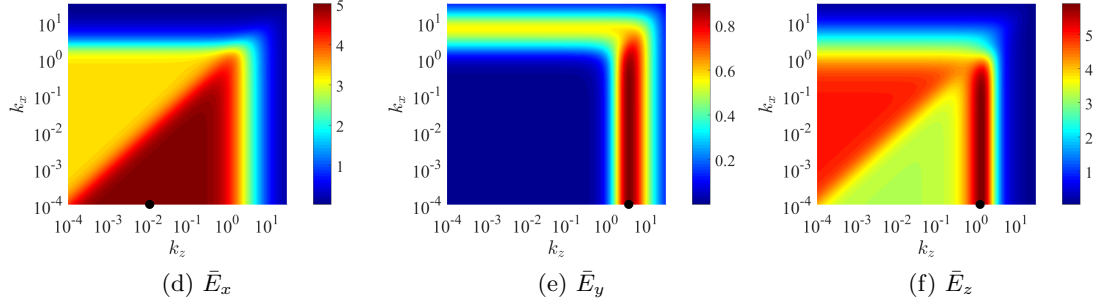


Figure 2.5: Kinetic energy integrated over the wall-normal direction and time, with an impulse in the direction i , calculated using (2.15). We consider a viscoelastic fluid with an impulsive excitation in the (a) streamwise, (b) wall-normal, and (c) spanwise directions, and a Newtonian fluid with an impulsive excitation in the (d) streamwise, (e) wall-normal, and (f) spanwise directions. The maximum value of the kinetic energy is marked by the black dots.

($k_x \approx 0$, $k_z \approx 10^0$). The analysis presented in this section provides deeper insight into the individual energies of each velocity component.

Figure 2.7 shows the transient evolution of the kinetic energy of the streamwise velocity fluctuation as a function of time; computations are done using (2.16a). Since Figure 2.6 demonstrates that the streamwise velocity is most amplified, we plot only the energy of the streamwise velocity fluctuations with $k_x = 10^{-1}$ and $k_z = 10^0$, a wavenumber pair which corresponds to the black dot in Figure 2.5c. In Figure 2.7a, we see that kinetic energy increases with increasing the Weissenberg number. We also see in Figure 2.7b an increase in energy upon increasing the polymer concentration.

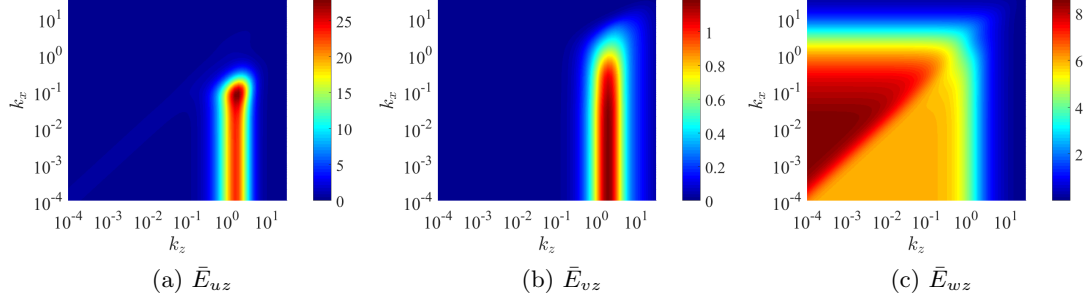


Figure 2.6: Componentwise contributions of (a) streamwise, (b) wall-normal, and (c) spanwise velocities to the total kinetic energy calculated from (2.16b) arising from an impulsive spanwise forcing in a flow with $Re = 50$, $We = 50$, $L = 100$, and $\beta = 0.5$.

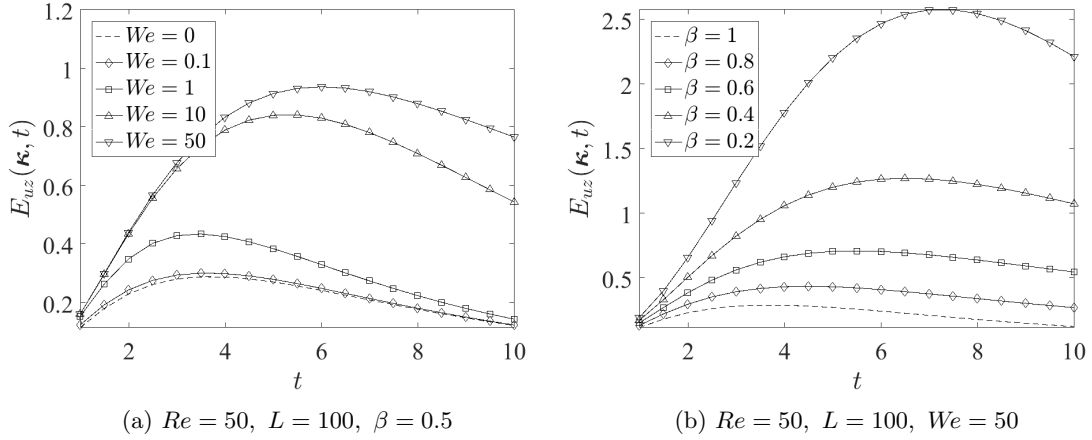


Figure 2.7: Transient evolution of kinetic energy of streamwise velocity fluctuations arising from an impulse in the spanwise direction, $E_{uuz}(\boldsymbol{\kappa}, t)$ calculated from (2.16a), in a flow with $k_x = 10^{-1}$ and $k_z = 10^0$. Panel (a) shows the effect of increasing the polymer relaxation time by increasing the Weissenberg number. $We = 0$ corresponds to the Newtonian fluid. Panel (b) shows the effect of increasing polymer concentration, $1 - \beta$. For a Newtonian fluid, $\beta = 1$.

Experiments on microchannel flows of viscoelastic solutions with an induced disturbance in the form of a cylindrical obstruction were recently reported in ref. [54]. The Reynolds numbers were between 2.5 and 150. Flow instabilities were observed at a localized region in the vicinity of the obstruction which became more prominent with an increase in polymer concentration. Although we confine our attention to the class of impulsive excitations (which are different from the excitations considered in ref. [54]), we observe qualitative agreement in the sense that the transient energy amplification increases as we increase the polymer concentration.

2.5 Spatio-temporal evolution of flow structures

We now examine flow structures that result from an impulsive excitation in the spanwise direction. Flow structures in physical space provide insight into patterns that result from a localized point force and can suggest potential mechanisms that govern the initial stages of transition to elastic turbulence at low Reynolds numbers. Flow structures presented here are obtained by the pseudospectral method described in § 2.2.2. Time series of flow structures can thus be interpreted as direct numerical simulations of the linearized FENE-CR fluid with an impulsive forcing. As described in § 2.2.2, time stepping procedures are avoided by exploiting linearity to directly obtain flow structures at a given time from the matrix exponential.

Figures 2.9 and 2.8 show three-dimensional isosurface plots of the streamwise velocity resulting from an impulsive excitation in the spanwise direction (u_z) at the optimal location $y_0 = -0.75$ for the viscoelastic fluid. Figures 2.8a, 2.8c, 2.9a and 2.9c show the time-evolution for a viscoelastic fluid, and Figures 2.8b, 2.8d, 2.9b and 2.9d show the time-evolution for a Newtonian fluid. As discussed in § 2.4, in Figure 2.5c we observe that viscoelastic fluids produce more oblique structures ($k_x \approx 10^{-1}$, $k_z \approx 10^0$) than Newtonian fluids (in Figure 2.5f the streamwise-constant structures with ($k_x \approx 10^{-4}$, $k_z \approx 10^0$) are most amplified). In Figures 2.8a and 2.8c, we see that at early times, the fluctuations in viscoelastic fluids are more oblique, showing a wavy nature in all three directions. At later times (Figures 2.9a and 2.9c) the wave packet stretches out in the streamwise direction and also spreads across the channel in the wall-normal direction. In contrast, the impulse-induced wave packet in the Newtonian fluid diffuses in space slowly (by observing the scales in the x -axis) with a slight amount of translation in the

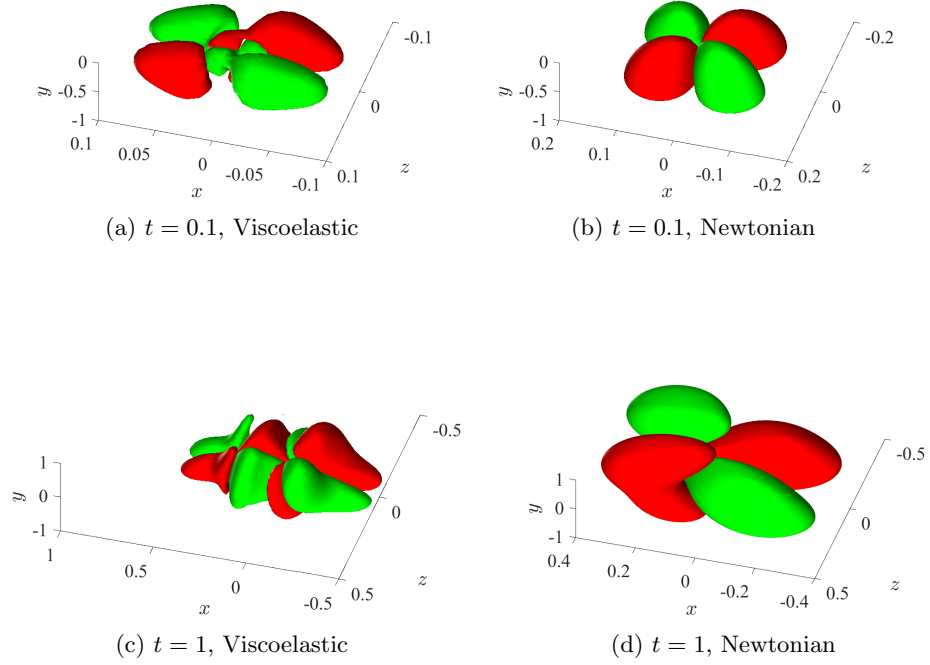


Figure 2.8: Isosurface plots of the streamwise velocity at $\pm u_{z,\max}/10$ at $Re = 50$. Red color denotes regions of high velocity and green color denotes regions of low velocity. Panels correspond to a viscoelastic fluid at (a) 0.1, and (c) 1 time units, and a Newtonian fluid at (b) 0.1, and (d) 1 time units, with parameters $L = 100$, $\beta = 0.5$ and $\mu = 1$ for the viscoelastic fluid.

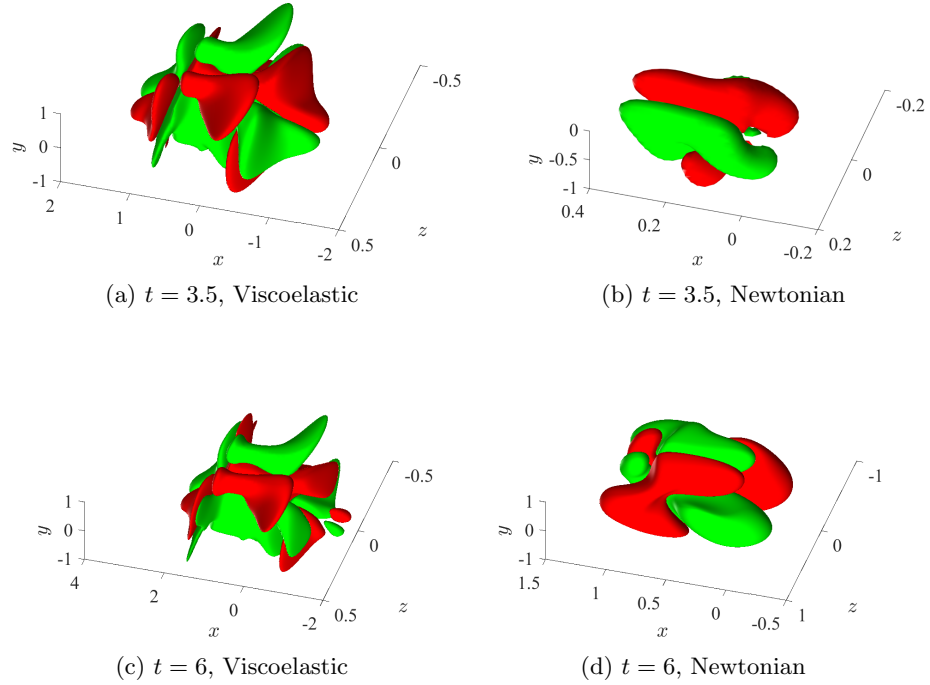


Figure 2.9: Isosurface plots of the streamwise velocity at $\pm u_{z,\max}/10$ at $Re = 50$. Red color denotes regions of high velocity and green color denotes regions of low velocity. Panels correspond to a viscoelastic fluid at (a) 3.5, and (c) 6 time units, and a Newtonian fluid at (b) 3.5, and (d) 6 time units, with parameters $L = 100$, $\beta = 0.5$ and $\mu = 1$ for the viscoelastic fluid.

streamwise direction. (Videos of the time-evolution can be found in the supplementary material.)

Flow structures can be further analyzed by examining three-dimensional streamtubes of the velocity fluctuation vector. Figures 2.10 and 2.11 show three-dimensional streamtubes that originate from the plane $y = 0.5$ for a viscoelastic fluid and a Newtonian fluid. The location $y = 0.5$ is far from the source of the impulse ($y_0 = -0.75$). At the location of the point force, the impulsive excitation is equivalent to an initial condition on the wall-normal velocity and vorticity. This can be seen by considering the general solution of a linear system of the form given in (2.12), for an initial condition $\psi_0(\boldsymbol{\kappa})$ with zero forcing ($F_i = 0$) [17],

$$\phi_i(\boldsymbol{\kappa}, t) = C e^{At} \psi_0(\boldsymbol{\kappa}). \quad (2.19)$$

The solution of the system with an initial condition in (2.19) and the solution with an impulse forcing given in (2.13) are equivalent if we choose an initial condition ψ_0 such that $\psi_0 = F_i(\boldsymbol{\kappa})$. We note that ψ is the discrete approximation to $\boldsymbol{\psi} = [\mathbf{r}^T \ v \ \eta]^T$, where \mathbf{r}^T represents the vector of the six components of the fluctuations of the (symmetric) conformation tensor, v is the wall-normal velocity, and η is the wall-normal vorticity. Thus, the impulsive forcing corresponds to an initial condition on the wall-normal velocity and vorticity. This initial condition produces vortical structures even in Newtonian fluids. The interesting feature here is the evolution of vortical structures away from the location of the point force for the viscoelastic fluid.

Figures 2.10b and 2.10d show the top and isometric views of streamtubes for a Newtonian fluid, and Figures 2.10a and 2.10c show the top and isometric views for a viscoelastic fluid at $t = 0.1$. The streamtubes for the Newtonian and viscoelastic fluids are very similar at $t = 0.1$ as both the Newtonian and viscoelastic fluids have the same initial condition, and at early times the impulse does not significantly contaminate regions away from its source. Figures 2.11b and 2.11d show the top and isometric views of streamtubes for a Newtonian fluid, and Figures 2.11a and 2.11c show the top and isometric views for a viscoelastic fluid at $t = 6$. We see in Figure 2.11a and 2.11c that the viscoelastic fluid generates two pairs of counter-rotating vortices at $x = \pm 1$ that spread out in the wall-normal direction with an oblique inclination.

In contrast, we do not find significant evolution of vortical structures in the Newtonian fluid (Figures 2.11b and 2.11d). In fact, streamtubes for the Newtonian fluid at $t = 6$ (Figures 2.11b and 2.11d) are almost the same as they were at $t = 0.1$ (Figure 2.10b and 2.10d) (videos of the time-evolution can be found in the supplementary material). The time-evolution of the vortical structures observed here is therefore a unique feature of viscoelastic fluids. Vortex breakdown is a well-known mechanism for transition to turbulence in Newtonian fluids at high Reynolds numbers [62]. Analyzing the existence of a breakdown and corresponding transition cannot be captured by the linearized dynamics and requires careful consideration of nonlinear effects. However, using the analysis of the linearized dynamics, we find the development of vortical structures that may be related to the initial stages of transition to elastic turbulence.

Curved streamlines are known to be unstable to small-amplitude perturbations in viscoelastic fluids and growth of these perturbations could eventually lead to elastic turbulence [63, 64, 65]. Here, we find that curved streamlines are generated by an impulsive excitation. If these grow to finite-amplitude, they may also become unstable. Recent work [8] suggests that finite-amplitude perturbations in straight-channel flows can induce elastic turbulence. A potential reason for this transition mechanism may be related to the generation of curved streamlines by nonmodal amplification of initially small-amplitude disturbances.

2.6 Concluding remarks

In this work, we have examined the response of a viscoelastic fluid to localized point forces. We analyzed the kinetic energies of the velocity fluctuations and identified an optimal location to trigger the impulse. The impulse in the optimal location has the maximum impact in the channel and was found to be located near the wall for the viscoelastic fluid. Our analysis has also demonstrated that viscoelastic fluids are more sensitive to small amplitude disturbances when compared to Newtonian fluids at low Reynolds numbers.

Our analysis of kinetic energy showed that the impulse in the spanwise direction has the maximum impact and that the streamwise velocity is most affected. We also found that the amount of amplification increases with increasing elasticity (We) and by increasing polymer concentration ($1 - \beta$). These observations agree with earlier studies

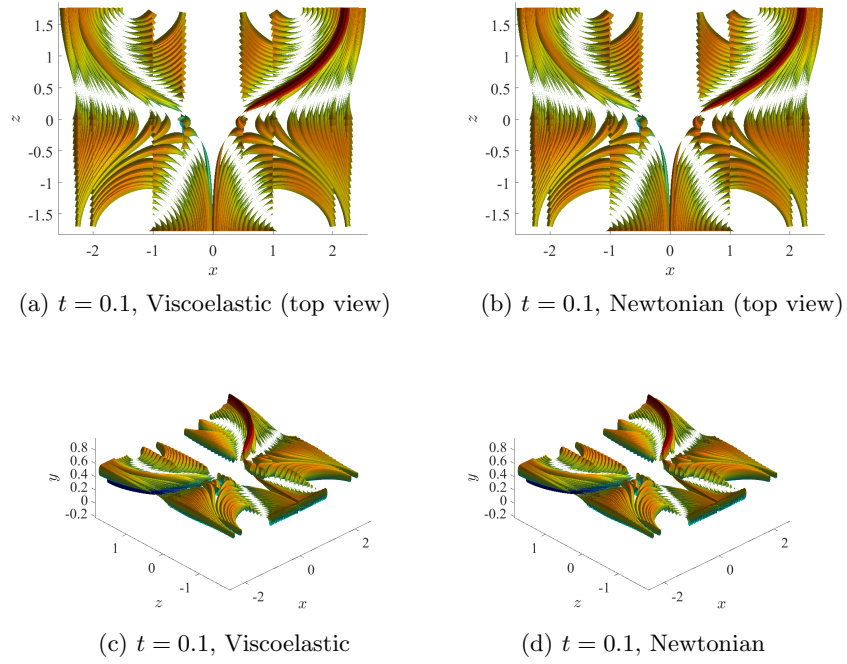


Figure 2.10: Three-dimensional streamtubes of the velocity fluctuation vector that originate from the plane $y = 0.5$ at $Re = 50$ with a spanwise impulsive excitation at $y_0 = -0.75$. Show are (a) top view and (c) isometric view for a viscoelastic fluid and (b) top view and (d) isometric view for a Newtonian fluid at $t = 0.1$. Parameters used for the viscoelastic fluid are $L = 100$, $\beta = 0.5$ and $\mu = 1$.

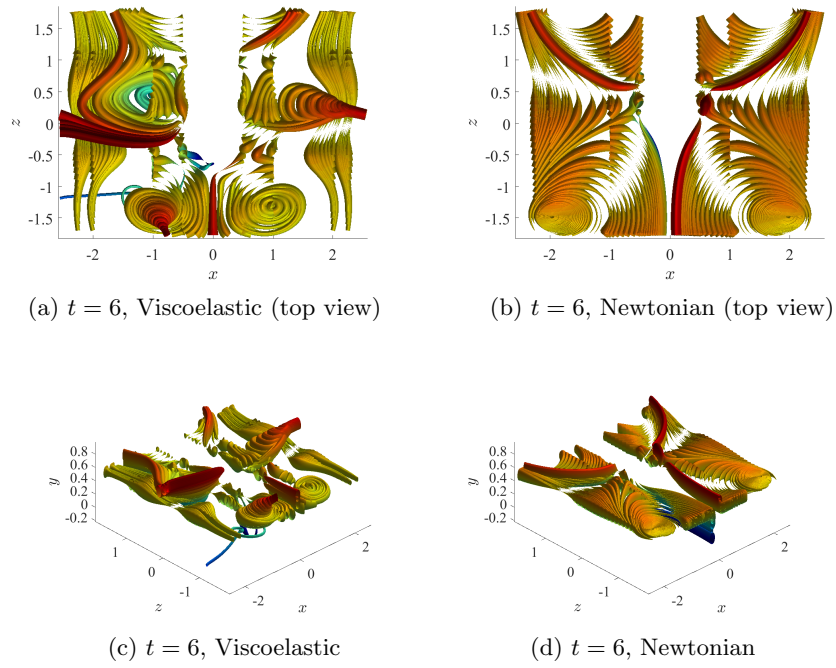


Figure 2.11: Three-dimensional streamtubes of the velocity fluctuation vector that originate from the plane $y = 0.5$ at $Re = 50$ with a spanwise impulsive excitation at $y_0 = -0.75$. Shown are (a) top view and (c) isometric view for a viscoelastic fluid and (b) top view and (d) isometric view for a Newtonian fluid at $t = 6$. Parameters used for the viscoelastic fluid are $L = 100$, $\beta = 0.5$ and $\mu = 1$.

on the amplification of unstructured channel-wide disturbances [22, 5, 36]; the latter observation is also qualitatively consistent with recent experiments [54]. The optimal location and direction of the impulse as well as the variation of kinetic energy with polymer concentration and relaxation time studied in this work may provide useful guidelines for inducing elastic turbulence in microfluidic devices and other experiments concerning elastic turbulence.

We have also shown the spatio-temporal evolution of the wave packet arising from the impulsive excitation. We have demonstrated that the wave packet in the viscoelastic fluid stretches in the streamwise direction. This is in contrast to its Newtonian counterpart which predominantly diffuses in space as a function of time. Three-dimensional streamtubes also revealed time-evolving vortical structures that were not as pronounced in Newtonian fluids. We note that this feature was not observed in previous studies with distributed channel-wide body forces [20, 21, 22, 5, 36]. These structures may provide a mechanism for triggering the initial stages of transition to elastic turbulence in dilute polymer solutions.

Our results may also be helpful in understanding viscoelastic channel flows that contain a finite-sized object, where the object exerts a drag force on the fluid. Since any spatially varying and temporally distributed force can be expressed as a summation of impulses, our results may be useful for interpreting the behavior of these more complex flows. An examination of the nonlinear evolution of fluctuations arising from localized point forces is the next natural step toward addressing the challenging problem of transition to elastic turbulence in viscoelastic channel flows.

Acknowledgments

This work is supported in part by the National Science Foundation under grant number CBET-1510654. The Minnesota Supercomputing Institute (MSI) at the University of Minnesota is gratefully acknowledged for providing computing resources.

Chapter 3

Well-conditioned ultraspherical and spectral integration methods for resolvent analysis of Newtonian and viscoelastic channel flows

3.1 Introduction

Linear analyses in hydrodynamic flow problems provide useful information concerning the early stages of transition to turbulence in Newtonian and viscoelastic fluids. Linear analysis broadly has two aspects to it: one being stability at long times (asymptotic stability), and the other being nonmodal amplification of disturbances in asymptotically stable systems [15, 14]. Linear nonmodal analysis involves examining the amplification of disturbances in systems governed by non-normal operators. Large nonmodal amplification in linearly stable systems can trigger transition to nonlinear states [15, 14]. Eigenvalues provide information about growth or decay of disturbances at long times, while singular values of frequency responses provide information about nonmodal amplification of disturbances.

Experimental observations of Newtonian and viscoelastic channel flows have shown that transition to nonlinear flow states can occur when the system is linearly stable, even when the system is well below the stability boundary. This kind of subcritical transition to turbulence in Newtonian fluids in simple geometries like wall-bounded channel flows was thought to have occurred solely due to nonlinear effects. However, it has become clear over time that the initial stages to transition are related to linear nonmodal amplification [15, 43].

Similarly, in dilute polymer solutions, transition to turbulence has been observed in experiments at very low Reynolds numbers ($Re \approx 0.01$) where the system is expected to be linearly stable [8, 7], and it is a debated issue as to whether the initial stages of the observed transition are related to linear nonmodal amplification [23, 8]. Understanding and controlling transition to turbulence at low Reynolds numbers has potential applications in enhancing transport in microfluidic devices [11, 10], and in controlling defects in polymer processing operations like extrusion [13, 41].

The linearized system governing the flow of a viscoelastic fluid in a channel generally has an associated continuous spectrum. This requires a large number of basis functions for good resolution [56, 66, 55] when using a spectral method. The conditioning of matrices generated as a result of discretization using conventional spectral methods deteriorates algebraically with an increase in the number of basis functions. For example, the condition numbers of matrices in spectral collocation for a second-order differential equation scale as N^4 , and those in the Chebyshev-Tau and Galerkin methods scale as N^2 , where N is the number of basis functions [29].

Effects due to an ill-conditioned matrix will surface as erroneous results that are sometimes grid-dependent [33, 29, 27]. Nonmodal analysis in a 2D viscoelastic channel flow in particular is strongly sensitive to ill-conditioned matrices [33]. Such effects due to discretization-induced ill-conditioning can be avoided by using a well-conditioned method, like the recently introduced ultraspherical method [26] and the Chebyshev spectral integration method [27]. Du showed that under similar conditions, the condition numbers of matrices involved in the Chebyshev spectral integration and the ultraspherical methods scale to a constant with arbitrary N in certain second-order differential equations, while condition numbers in conventional spectral collocation scale algebraically with N [27].

The ill-conditioning of a matrix is measured in terms of a condition number, and one commonly used condition number is the ratio of the largest to the smallest singular value, $\kappa = \sigma_{\max}/\sigma_{\min}$, where κ is the condition number [34]. Intuitively, we might expect an operator analogue to ill-conditioning, where an operator could have singular values that are vastly separated. We call this “ill-conditioning inherent to the operator”. If an operator is inherently ill-conditioned, merely using a well-conditioned method for discretization will not suffice to avoid erroneous results.

A robust method to compute frequency responses must avoid both sources of ill-conditioning, one originating from the discretization scheme, and the other inherent to an operator. As we already discussed, recent well-conditioned schemes can be used to address discretization-induced ill-conditioning. To address operator-inherent ill-conditioning, we introduce a feedback interconnected system to compute frequency responses.

Linear analyses of the incompressible Navier-Stokes (NS) equations are often conducted by converting the governing equations into an evolution form by eliminating pressure, as boundary conditions for pressure are unknown *a priori* [6]. In simple geometries, the linear stability problem is then solved by using a spectral method, like the Chebyshev collocation or the Chebyshev-Tau method [6]. Solving the same problem in primitive variables (i.e., without eliminating pressure) needs special care, as a staggered grid is required to avoid a spurious pressure mode [24]. We find that for Newtonian and viscoelastic fluids, such special treatment is not needed when using Chebyshev spectral integration, i.e., modal and nonmodal analysis can be conducted using a standard grid without running into spurious modes.

This paper is organized as follows. In Section 3.2 we present motivating examples that identify the need to consider well-conditioned methods in nonmodal analysis. In Section 3.3 we discuss the numerical methods used in this work, and in Section 3.4 we show several applications. We summarize our results in Section 3.5. Background technical details are relegated to the appendix.

3.2 Problem formulation and motivating examples

In this section, we formulate the problem and provide examples to motivate our developments. Our approach represents an outgrowth of the framework developed in [33], where a cascade connection of the frequency response operator and its adjoint was utilized in nonmodal analysis of stable linear dynamical systems in which the spatial variable belongs to a finite interval.

3.2.1 Problem formulation

We consider linear dynamical systems whose spatio-temporal frequency response $\mathcal{T}(\omega)$ can be cast as,

$$[\mathcal{A}(\omega) \phi(\cdot)](y) = [\mathcal{B}(\omega) \mathbf{d}(\cdot)](y), \quad (3.1a)$$

$$\xi(y) = [\mathcal{C}(\omega) \phi(\cdot)](y), \quad (3.1b)$$

$$[\mathcal{L}_a \phi(\cdot)](a) = [\mathcal{L}_b \phi(\cdot)](b) = 0, \quad (3.1c)$$

where $\omega \in \mathbb{R}$ is the temporal frequency and $y \in [a, b]$ is the spatial variable. The state, input, and output fields are respectively denoted by ϕ , \mathbf{d} , and ξ ; \mathcal{A} , \mathcal{B} , and \mathcal{C} are linear differential block matrix operators of appropriate dimensions with potentially non-constant coefficients in y ; and \mathcal{L}_a and \mathcal{L}_b are linear operators that specify the boundary conditions on ϕ . At any temporal frequency, we assume that the operator $\mathcal{A}(\omega)$ in (3.1) is invertible, thereby leading to,

$$\mathcal{T}(\omega) = \mathcal{C}(\omega) \mathcal{A}^{-1}(\omega) \mathcal{B}(\omega).$$

While we allow a nonlinear dependence of the operators \mathcal{A} , \mathcal{B} , and \mathcal{C} on ω , for systems that can be cast as,

$$\text{Dt}[\mathcal{E} \phi(\cdot, t)](y) = [\mathcal{F} \phi(\cdot, t)](y) + [\mathcal{B} \mathbf{d}(\cdot, t)](y), \quad (3.2a)$$

$$\xi(y, t) = [\mathcal{C} \phi(\cdot, t)](y), \quad (3.2b)$$

$$[\mathcal{L}_a \phi(\cdot, t)](a) = [\mathcal{L}_b \phi(\cdot, t)](b) = 0, \quad (3.2c)$$

the operator $\mathcal{A}(\omega)$ in (3.1) depends linearly on ω , where $t \in [0, \infty)$ is time. In this case, the application of the temporal Fourier transform yields the resolvent operator, $\mathcal{A}^{-1}(\omega) = (i\omega\mathcal{E} - \mathcal{F})^{-1}$, where i is the imaginary unit, and the operators \mathcal{B} and \mathcal{C} in (3.1) do not depend on ω .

The frequency response operator $\mathcal{T}(\omega)$ determines the steady-state response of a stable linear dynamical system to purely harmonic inputs. Namely, for $\mathbf{d}(y, t) = \hat{\mathbf{d}}(y, \omega)e^{i\omega t}$, the steady-state response is given by $\boldsymbol{\xi}(y, t) = \hat{\boldsymbol{\xi}}(y, \omega)e^{i\omega t}$ and $\mathcal{T}(\omega)$ maps a spatial input profile $\hat{\mathbf{d}}(y, \omega)$ into the corresponding output $\hat{\boldsymbol{\xi}}(y, \omega)$,

$$\hat{\boldsymbol{\xi}}(y, \omega) = \left[\mathcal{T}(\omega) \hat{\mathbf{d}}(\cdot, \omega) \right] (y).$$

The singular value decomposition (SVD) of $\mathcal{T}(\omega)$ can be used to determine the input shapes (i.e., the left singular functions $\hat{\mathbf{v}}_i(y, \omega)$), the resulting responses (i.e., the right singular functions $\hat{\mathbf{u}}_i(y, \omega)$), and the corresponding gains (i.e., the singular values $\sigma_i(\omega)$),

$$\hat{\boldsymbol{\xi}}(y, \omega) = \left[\mathcal{T}(\omega) \hat{\mathbf{d}}(\cdot, \omega) \right] (y) = \sum_{i=0}^{\infty} \sigma_i(\omega) \hat{\mathbf{u}}_i(y, \omega) \langle \hat{\mathbf{v}}_i(\cdot, \omega), \hat{\mathbf{d}}(\cdot, \omega) \rangle,$$

where $\langle \cdot, \cdot \rangle$ denotes the standard $L_2[a, b]$ inner product. SVD requires computation of the adjoint $\mathcal{T}^\dagger(\omega)$ of $\mathcal{T}(\omega)$,

$$\langle \mathcal{T}^\dagger(\omega) \hat{\boldsymbol{\xi}}, \hat{\mathbf{d}} \rangle = \langle \hat{\boldsymbol{\xi}}, \mathcal{T}(\omega) \hat{\mathbf{d}} \rangle,$$

and the eigenvalue decomposition of the composite operators $\mathcal{T}(\omega)\mathcal{T}^\dagger(\omega)$ and $\mathcal{T}^\dagger(\omega)\mathcal{T}(\omega)$ [33, 6],

$$\begin{aligned} \left[\mathcal{T}(\omega)\mathcal{T}^\dagger(\omega) \hat{\mathbf{u}}_i(\cdot, \omega) \right] (y) &= \sigma_i^2(\omega) \hat{\mathbf{u}}_i(y, \omega), \\ \left[\mathcal{T}^\dagger(\omega)\mathcal{T}(\omega) \hat{\mathbf{v}}_i(\cdot, \omega) \right] (y) &= \sigma_i^2(\omega) \hat{\mathbf{v}}_i(y, \omega). \end{aligned}$$

In general, $\mathcal{T}^\dagger(\omega)$ is not determined by the complex conjugate transpose of an operator-valued matrix $\mathcal{T}(\omega)$ and its computation typically involves integration by parts.

3.2.2 Reaction-diffusion equation: Ill-conditioning arising from operator

For the reaction-diffusion equation with $y \in [-1, 1]$ and homogeneous Neumann boundary conditions,

$$\begin{aligned}\partial_t \phi(y, t) &= \partial_{yy} \phi(y, t) - \epsilon^2 \phi(y, t) + d(y, t), \\ \partial_y \phi(\pm 1, t) &= 0,\end{aligned}\tag{3.3}$$

where ϵ is a real parameter, in representation (3.1) we have

$$\mathcal{A}(\omega) = i\omega I - D^2 + \epsilon^2 I, \quad \mathcal{B} = \mathcal{C} = I.$$

Here, I is the identity operator, $D = d/dy$, and the frequency response operator is determined by

$$\mathcal{T}(\omega) = (i\omega I - D^2 + \epsilon^2 I)^{-1}.\tag{3.4}$$

The dynamical generator $D^2 - \epsilon^2 I$ with homogeneous Neumann boundary conditions in (3.3) is self-adjoint and its eigen-pairs are given by [67, Example 5.4-1]

$$\begin{aligned}\lambda_n &= -(\epsilon^2 + n^2 \pi^2), & \phi_n(y) &= \cos(n\pi y), \\ \lambda_n &= -(\epsilon^2 + (n + \tfrac{1}{2})^2 \pi^2), & \phi_n(y) &= \sin((n + \tfrac{1}{2})\pi y),\end{aligned}\tag{3.5}$$

where $n \in \mathbb{Z}$. Furthermore, the singular values of the frequency response operator are determined by

$$\sigma_n^2(\omega) = \begin{cases} 1/(\omega^2 + (\epsilon^2 + n^2 \pi^2)^2), \\ 1/(\omega^2 + (\epsilon^2 + (n + \tfrac{1}{2})^2 \pi^2)^2), \end{cases}\tag{3.6}$$

and the largest value of $\sigma_n(\omega)$ occurs for $n = 0$ and $\omega = 0$, i.e., $\max_{n, \omega} \sigma_n(\omega) = \sigma_0(0) = 1/\epsilon^2$.

The separation between $\sigma_0(0)$ and $\sigma_1(0)$ increases with decrease in ϵ and this ill-conditioning negatively impacts performance of standard numerical schemes. Singular

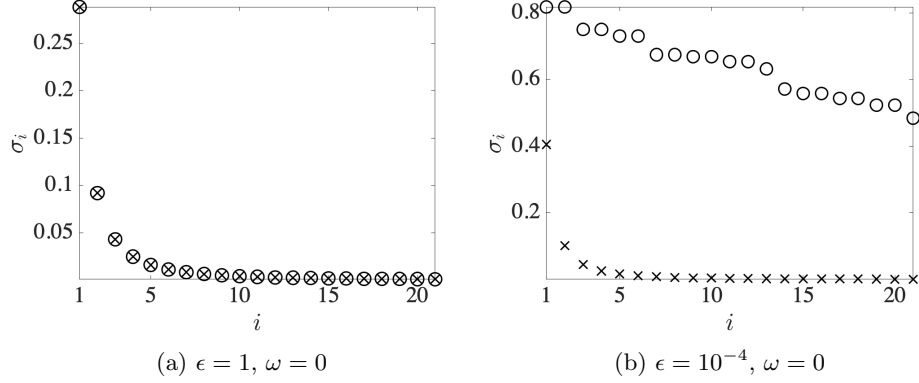


Figure 3.1: Singular values of the frequency response operator of the reaction-diffusion equation (3.3) obtained using Chebfun’s spectral scheme with $N = 64$ collocation points. Symbols represent exact values (\times) and the numerical solution resulting from the composite operator $\mathcal{T}(\omega)\mathcal{T}^\dagger(\omega)$ (\circ). The principal singular value is not shown as its value is very large compared to the remaining singular values.

value decomposition typically involves the resolvent operator and its numerical evaluation requires computation of the inverse of the discretized version of an operator-valued matrix. Figure 3.1 illustrates that computations based on the composite operator $\mathcal{T}(\omega)\mathcal{T}^\dagger(\omega)$ yield erroneous results for reaction-diffusion equation (3.3) with small values of ϵ . The collocation method with 64 Chebyshev basis functions is used and similar results are obtained even with a well-conditioned spectral integration scheme. For $\epsilon = 10^{-4}$, $\sigma_0(0) = 10^8$ is significantly larger than the other singular values and it is not shown in Figure 3.1. Even though the collocation method is well-conditioned for 64 basis functions [29], singular values resulting from spatial discretization of the composite operator $\mathcal{T}(\omega)\mathcal{T}^\dagger(\omega)$ have non-zero imaginary parts and their real parts significantly deviate from the true values; see Figure 3.1b. When the composite operator is used, increasing the number of basis functions does not fix this problem. In contrast, for $\epsilon = 1$ (Figure 3.1a), we observe a good match between analytical solutions (marked by crosses) and singular values calculated using the composite operator $\mathcal{T}(\omega)\mathcal{T}^\dagger(\omega)$ (marked by circles).

In this example, since $\mathcal{B} = \mathcal{C} = I$ and $\mathcal{T}^\dagger(\omega)\mathcal{T}(\omega) = \mathcal{A}^{-\dagger}(\omega)\mathcal{A}^{-1}(\omega) = (\mathcal{A}(\omega)\mathcal{A}^\dagger(\omega))^{-1}$, ill-conditioning can be circumvented by computing the eigenvalues of the operator

$\mathcal{A}(\omega)\mathcal{A}^\dagger(\omega)$. However, in general, \mathcal{B} and \mathcal{C} are nonsquare block-matrix operators and the computation of $\mathcal{A}^{-1}(\omega)$ and $\mathcal{A}^{-\dagger}(\omega)$ cannot be avoided when a cascade connection of $\mathcal{T}(\omega)$ and $\mathcal{T}^\dagger(\omega)$, shown in Figure 3.3, is used in the frequency response analysis. As described in § 3.4.2, similar operator-induced ill-conditioning arises in strongly elastic flows of viscoelastic fluids. In § 3.3.1 and § 3.4.1, we revisit the reaction-diffusion problem and show that the use of a feedback interconnection, shown in Figure 3.4, leads to a computational framework that is insensitive to ill-conditioning of the underlying operator.

3.2.3 Channel flow of viscoelastic fluids: Ill-conditioning arising from spatial discretization

We now examine the model that governs the dynamics of infinitesimal fluctuations around the laminar flow of a dilute polymer solution in a channel. This problem was used in [33] to demonstrate that spectral collocation and an integral reformulation of spectral collocation can produce significantly different results with accurate and grid-independent results only feasible with the latter. In § 3.4.2, we show that ultraspherical discretization offers a similar level of accuracy as spectral integration and that under similar conditions, spectral collocation performs poorly, which is in concert with the observations made in [33].

The linearized momentum, mass conservation, and constitutive equations for an incompressible flow of the Oldroyd-B fluid are given by [23, 5, 20],

$$Re(\partial_t \mathbf{v} + \mathbf{V} \cdot \nabla \mathbf{v} + \mathbf{v} \cdot \nabla \mathbf{V}) = -\nabla p + \beta \nabla^2 \mathbf{v} + (1 - \beta) \nabla \cdot \boldsymbol{\tau} + \mathbf{d}, \quad (3.7a)$$

$$\nabla \cdot \mathbf{v} = 0, \quad (3.7b)$$

$$\begin{aligned} \partial_t \boldsymbol{\tau} + \mathbf{V} \cdot \nabla \boldsymbol{\tau} + \mathbf{v} \cdot \nabla \boldsymbol{\tau} = & \boldsymbol{\tau} \cdot \nabla \mathbf{V} + (\boldsymbol{\tau} \cdot \nabla \mathbf{V})^T + \mathbf{T} \cdot \nabla \mathbf{v} + (\mathbf{T} \cdot \nabla \mathbf{v})^T + \\ & \frac{1}{We} (\nabla \mathbf{v} + \nabla \mathbf{v}^T - \boldsymbol{\tau}). \end{aligned} \quad (3.7c)$$

Here, \mathbf{v} , $\boldsymbol{\tau}$, and p are velocity, stress, and pressure fluctuations around the corresponding base-flow quantities \mathbf{V} , \mathbf{T} , and P , respectively. The length is normalized with the half-channel height h (see Figure 3.2 for geometry), velocity with the largest value of

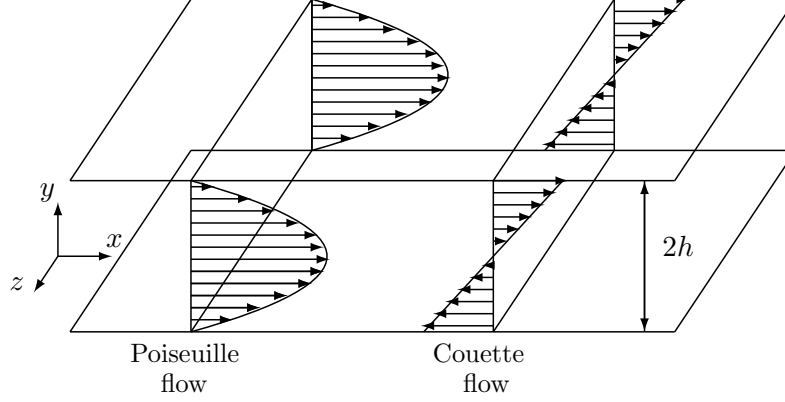


Figure 3.2: Geometry and steady-state velocity profiles in Poiseuille and Couette flows.

the steady-state velocity U_0 , time with h/U_0 , pressure with $\mu_T U_0/h$ where μ_T is the effective shear viscosity of the dilute viscoelastic solution, and the polymer stress \mathbf{T} with $\mu_p U_0/h$, where $\mu_p = \mu_T - \mu_s$ and μ_s is the pure-solvent viscosity. The Reynolds number, $Re = hU_0\rho/\mu_T$, quantifies the ratio between the inertial and viscous forces, where ρ is the fluid density; the Weissenberg number, $We = \lambda_p U_0/h$, provides a measure of the degree of elasticity in the fluid, where λ_p is the polymer relaxation time; and the viscosity ratio, $\beta = \mu_s/\mu_T$, determines the polymer concentration in the fluid. Setting $\beta = 0$ in (3.7) yields an upper convected Maxwell (UCM) model and for $\beta = 1$ a flow of Newtonian fluid is recovered.

In channel flow, the steady-state velocity profile only contains the streamwise component, i.e., $\mathbf{V} = (U(y), 0, 0)$, where $U(y) = 1 - y^2$ for pressure-driven Poiseuille flow and $U(y) = y$ for shear-driven Couette flow. The non-zero components of the base stress tensor are given by $T_{xx} = 2We(U'(y))^2$ and $T_{xy} = T_{yx} = U'(y)$, where the prime denotes a derivative with respect to y . For this base flow, the streamwise and spanwise directions are translationally invariant and the spatio-temporal Fourier transform brings (3.7) to a two-point boundary value problem in the wall-normal coordinate y .

In the absence of inertia, we can set $Re = 0$ in (3.7), rescale time with We , and examine the dynamics of 2D velocity fluctuations $\mathbf{v} = (u, v)$ in the streamwise/wall-normal plane (x, y) . Introducing the streamfunction ϕ so that the streamwise and wall-normal velocity components are given by $u = \partial_y \phi$ and $v = -ik_x \phi$ and eliminating

pressure and stress fluctuations from (3.7) brings the frequency response operator $\mathcal{T}(\omega)$ into the following form with $D = d/dy$,

$$\begin{aligned} \left(\sum_{n=0}^4 a_n(y, \omega) D^n \right) \phi(y, \omega) &= \begin{bmatrix} D & -ik_x \end{bmatrix} \begin{bmatrix} d_x(y, \omega) \\ d_y(y, \omega) \end{bmatrix}, \\ \begin{bmatrix} u(y, \omega) \\ v(y, \omega) \end{bmatrix} &= \begin{bmatrix} D \\ -ik_x \end{bmatrix} \phi(y, \omega), \\ \phi(\pm 1, \omega) &= [D\phi(\cdot, \omega)](\pm 1) = 0, \end{aligned} \quad (3.8a)$$

thereby implying that, in representation (3.1), we have,

$$\mathcal{A}(\omega) = \sum_{n=0}^4 a_n(y, \omega) D^n, \quad \mathcal{B} = \begin{bmatrix} D & -ik_x \end{bmatrix}, \quad \mathcal{C} = \begin{bmatrix} D \\ -ik_x \end{bmatrix}.$$

Alternatively, the components of the fluctuation stress tensor, which can play an active role in triggering instabilities in viscoelastic fluids [60], can be selected as the output in (3.8a),

$$\begin{bmatrix} \tau_{xx}(y, \omega) \\ \tau_{xy}(y, \omega) \\ \tau_{yy}(y, \omega) \end{bmatrix} = \begin{bmatrix} c_{11}(y, \omega) D^2 + c_{12}(y, \omega) D + c_{13}(y, \omega) \\ c_{21}(y, \omega) D^2 + c_{22}(y, \omega) D + c_{23}(y, \omega) \\ c_{31}(y, \omega) D + c_{32}(y, \omega) \end{bmatrix} \phi(y, \omega). \quad (3.8b)$$

The expressions for functions $a_n(y, \omega)$ and $c_{ij}(y, \omega)$ are provided in Appendix D.

3.2.4 The linearized Navier-Stokes equations: A model in the descriptor form

Setting $\beta = 1$ and rescaling pressure with Re in (3.7) yields the linearized NS equations,

$$\partial_t \mathbf{v} + \mathbf{V} \cdot \nabla \mathbf{v} + \mathbf{v} \cdot \nabla \mathbf{V} = -\nabla p + \frac{1}{Re} \nabla^2 \mathbf{v} + \mathbf{d}, \quad (3.9a)$$

$$\nabla \cdot \mathbf{v} = 0. \quad (3.9b)$$

At any time t , the velocity fluctuations in (3.9) have to satisfy the algebraic constraint given by the continuity equation (3.9b). In channel flow, the application of the Fourier transform in x , z , and t allows us to cast (3.9) in the form given by (3.1) which is parameterized by the wall-parallel wavenumbers (k_x, k_z) and the temporal frequency ω . Using a standard procedure [6, Chapter 3], pressure can be eliminated from (3.9) to obtain a model in the evolution form in which the state is captured by the wall-normal velocity and vorticity fluctuations, (v, η) . When the pressure is kept in the governing equations, we deal with a model in the *descriptor form* in which the state is captured by the primitive variables (u, v, w, p) .

Bringing (3.9) to the evolution form has advantages and disadvantages. This transformation eliminates the need to deal with pressure boundary conditions, which are unknown, and it yields a smaller number of state variables. However, there are considerable disadvantages both in Newtonian and viscoelastic fluids. As shown in [68, 69], for the same level of accuracy, the descriptor form in channel flows of Newtonian fluids requires a smaller number of basis functions compared to the evolution form. Furthermore, in flows of viscoelastic fluids, the transformation to the evolution form can result in a system that is algebraically cumbersome (e.g., see Appendices in [23, 70]) and eliminating pressure from (3.7) requires taking higher derivatives of the stress variables and necessitates specification of additional boundary conditions on stress fluctuations. Certain boundary conditions on stress fluctuations have been identified to produce reliable results [55], but the physical basis of these remains unclear.

Since the boundary conditions on pressure are not known, working with the model in the descriptor form requires use of a staggered grid for the velocity and pressure fields in the spectral collocation method. If velocity is evaluated at Chebyshev collocation points,

$$y_j = \cos(\pi j/N), \quad j = 0, 1, \dots, N, \quad (3.10a)$$

then the pressure is evaluated at the points

$$y_j = \cos(\pi(j + \frac{1}{2})/N), \quad j = 0, 1, \dots, N-1; \quad (3.10b)$$

when using a staggered grid. A similar procedure for the Chebyshev-Tau method is

described in [24]. By setting $j = 0$ and $j = N - 1$ in (3.10b), pressure is not evaluated at the boundaries, i.e., at $y = \pm 1$, and thus the need for specifying pressure boundary conditions is avoided. We refer the reader to [71] for implementation details of the staggered-grid formulation.

However, implementing a staggered grid can be challenging and there are well-developed open-source codes to solve two-point boundary value problems using spectral methods, e.g., A Matlab Differentiation Matrix Suite [32] and Chebfun [31]. Implementing staggered grids in such solvers requires special treatment and the standard solvers currently available in Chebfun do not cater to unconventional discretizations. In § 3.4.3, we demonstrate that the Chebyshev spectral integration method does not need a staggered grid when retaining the problem in the descriptor form and reinforcing algebraic constraint (3.9b) at the boundaries, $y = \pm 1$.

In channel flow of a viscoelastic fluid, the momentum equation in (3.7) contains the divergence of stress fluctuations and the presence of the y -derivative of $\boldsymbol{\tau}$ complicates determination of boundary conditions for the adjoint system. In § 3.3.4, we develop a method for resolvent analysis that retains the accuracy of the descriptor formulation and circumvents the challenge of dealing with stress boundary conditions. In our approach, we eliminate the stress fluctuations from (3.7), while retaining the pressure, and exploit the fact that the spectral integration method does not require a staggered grid when pressure is kept in the governing equations. In § 3.4.3, we demonstrate that our spectral integration implementation of the descriptor formulation provides a reliable tool for conducting the frequency response analysis in 3D channel flow of a viscoelastic fluid even in strongly elastic regimes.

3.3 SVD via feedback interconnection

In this section, we first summarize the standard procedure for computing the singular value decomposition of the frequency response operator $\mathcal{T}(\omega)$. This approach utilizes a cascade connection of $\mathcal{T}^\dagger(\omega)$ and $\mathcal{T}(\omega)$, shown in Figure 3.3, and it relies on computing inverses to determine the resolvent operator and its adjoint. Since it can suffer from ill-conditioning, we employ an alternative method that avoids inversion [4, Theorem 1]. This method extends the standard reflection technique [72, 73, 74] to our setup

and exploits feedback interconnection, shown in Figure 3.4, to avoid numerical errors and guard against ill-conditioning. We close the section with a discussion of numerical schemes that are utilized in this work.

The frequency response operator $\mathcal{T}(\omega) = \mathcal{C}(\omega)\mathcal{A}^{-1}(\omega)\mathcal{B}(\omega)$ in (3.1) is described by

$$\xi(y) = [\mathcal{T}d(\cdot)](y) \Leftrightarrow \begin{cases} [\mathcal{A}\phi(\cdot)](y) = [\mathcal{B}d(\cdot)](y), \\ \xi(y) = [\mathcal{C}\phi(\cdot)](y), \\ [\mathcal{L}_a\phi(\cdot)](a) = [\mathcal{L}_b\phi(\cdot)](b) = 0, \end{cases} \quad (3.11a)$$

and the adjoint operator $\mathcal{T}^\dagger(\omega) = \mathcal{B}^\dagger(\omega)\mathcal{A}^{-\dagger}(\omega)\mathcal{C}^\dagger(\omega)$ is determined by

$$\zeta(y) = [\mathcal{T}^\dagger g(\cdot)](y) \Leftrightarrow \begin{cases} [\mathcal{A}^\dagger\psi(\cdot)](y) = [\mathcal{C}^\dagger g(\cdot)](y), \\ \zeta(y) = [\mathcal{B}^\dagger\psi(\cdot)](y), \\ [\mathcal{L}_a^\dagger\psi(\cdot)](a) = [\mathcal{L}_b^\dagger\psi(\cdot)](b) = 0, \end{cases} \quad (3.11b)$$

where we suppress the dependence on ω for notational convenience. The adjoint operators are defined as [75],

$$\langle \psi, \mathcal{A}\phi \rangle = \langle \mathcal{A}^\dagger\psi, \phi \rangle, \quad (3.12a)$$

$$\langle \psi, \mathcal{B}d \rangle = \langle \mathcal{B}^\dagger\psi, d \rangle, \quad (3.12b)$$

$$\langle g, \mathcal{C}\phi \rangle = \langle \mathcal{C}^\dagger g, \phi \rangle, \quad (3.12c)$$

where the boundary conditions on \mathcal{L}_a^\dagger and \mathcal{L}_b^\dagger in (3.11b) are selected to ensure that (3.12a) holds. The analytical approach to computing the adjoint operators typically involves integration by parts whereas the numerical approach utilizes appropriate integration weights to make sure that the discrete approximation of the inner products in (3.12) holds true.

In [33], the adjoints and the corresponding boundary conditions were evaluated analytically for arbitrary block matrix operators using the procedure described in [75, Section 5]. We note that a similar procedure as in [33] is also used in the current Chebfun system to compute the formal adjoint of a linear differential operator [31]. While the method for determining formal adjoints described in [75, Section 5] and [33] can be

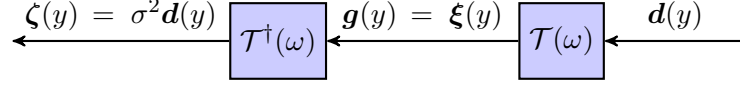


Figure 3.3: Block diagram of a cascade connection of the operators $\mathcal{T}^\dagger(\omega)$ and $\mathcal{T}(\omega)$. The composite operator, $\mathcal{T}^\dagger(\omega)\mathcal{T}(\omega)$, can be used to compute the singular values of the frequency response operator $\mathcal{T}(\omega)$.

also utilized for systems in the descriptor form, determination of the adjoint boundary conditions is subtle and requires additional attention. For the linearized NS equations described in § 3.2.4, the method developed in [75, Section 5] yields smaller number of boundary conditions than necessary to have a well-posed adjoint system. In § 3.3.3, we describe how this challenge can be overcome by utilizing the governing equations to impose additional boundary conditions in order to make the adjoint system well-posed.

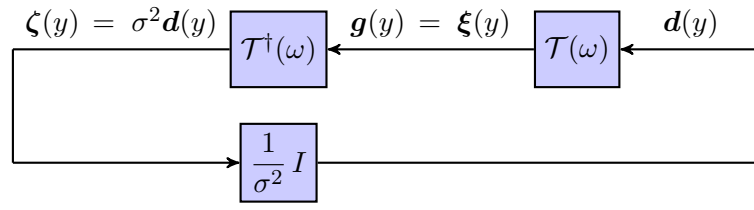
The eigenvalue decomposition of the composite operator $\mathcal{T}^\dagger(\omega)\mathcal{T}(\omega)$, whose block diagram is shown in Figure 3.3, can be used to obtain squares of the singular values. Detailed equations representing the composite operator can be found in [33]. Since the composite operator involves inverses of both \mathcal{A} and \mathcal{A}^\dagger , computations can be prone to ill-conditioning. In the next section, we show how to conduct the singular value decomposition of the frequency response operator $\mathcal{T}(\omega)$ without having to compute any inverses.

3.3.1 The feedback interconnection

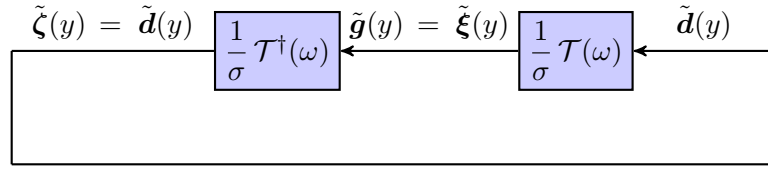
Singular values of the matrix $\mathbf{A} \in \mathbb{C}^{n \times n}$ are typically computed via the eigenvalue decomposition of the matrix $\mathbf{A}\mathbf{A}^\dagger$ (or $\mathbf{A}^\dagger\mathbf{A}$) [34]. Alternatively, they can be obtained from the eigenvalues of the matrix [72, 73, 74],

$$\begin{bmatrix} 0 & \mathbf{A} \\ \mathbf{A}^\dagger & 0 \end{bmatrix}.$$

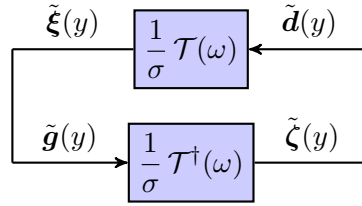
This so-called reflection technique avoids floating-point errors associated with computing the composite matrix $\mathbf{A}\mathbf{A}^\dagger$ [72, 73, 74]. In most cases this error is not significant and both methods should yield similar results. Since the frequency response operator and its adjoint involve inverses of the operators \mathcal{A} and \mathcal{A}^\dagger , for ill-conditioned problems errors



(a)



(b)



(c)

Figure 3.4: Through a sequence of equivalent transformations, the cascade connection of the operators $\mathcal{T}^\dagger(\omega)$ and $\mathcal{T}(\omega)$ shown in Figure 3.3 is cast as a feedback interconnection of the operators $(1/\sigma) \mathcal{T}^\dagger(\omega)$ and $(1/\sigma) \mathcal{T}(\omega)$ [4, Theorem 1].

associated with computing these inverses can become large [34]. In what follows, we employ a method that is inspired by the reflection technique and provide a reformulation that does not involve any inversions [4, Theorem 1].

Through a sequence of transformations, the composite system shown in Figure 3.3 can be brought into the feedback interconnection shown in the bottom block diagram of Figure 3.4. This representation requires realizations of the operators $(1/\sigma)\mathcal{T}(\omega)$ and $(1/\sigma)\mathcal{T}^\dagger(\omega)$ which are respectively determined by

$$\tilde{\xi}(y) = [\tfrac{1}{\sigma}\mathcal{T}\tilde{d}(\cdot)](y) \Leftrightarrow \begin{cases} [\mathcal{A}\tilde{\phi}(\cdot)](y) = [\mathcal{B}\tilde{d}(\cdot)](y), \\ \tilde{\xi}(y) = [\tfrac{1}{\sigma}\mathcal{C}\tilde{\phi}(\cdot)](y), \\ [\mathcal{L}_a\tilde{\phi}(\cdot)](a) = [\mathcal{L}_b\tilde{\phi}(\cdot)](b) = 0, \end{cases} \quad (3.13a)$$

and

$$\tilde{\zeta}(y) = [\tfrac{1}{\sigma}\mathcal{T}^\dagger\tilde{g}(\cdot)](y) \Leftrightarrow \begin{cases} [\mathcal{A}^\dagger\tilde{\psi}(\cdot)](y) = [\mathcal{C}^\dagger\tilde{g}(\cdot)](y), \\ \tilde{\zeta}(y) = [\tfrac{1}{\sigma}\mathcal{B}^\dagger\tilde{\psi}(\cdot)](y), \\ [\mathcal{L}_a^\dagger\tilde{\psi}(\cdot)](a) = [\mathcal{L}_b^\dagger\tilde{\psi}(\cdot)](b) = 0, \end{cases} \quad (3.13b)$$

The last block diagram in Figure 3.4 requires setting $\tilde{d}(y) = \tilde{\zeta}(y)$ and $\tilde{g}(y) = \tilde{\xi}(y)$ in (3.13), which yields

$$[\mathcal{A}^\dagger\tilde{\psi}(\cdot)](y) = [\tfrac{1}{\sigma}\mathcal{C}^\dagger\mathcal{C}\tilde{\phi}(\cdot)](y), \quad (3.14a)$$

$$[\mathcal{A}\tilde{\phi}(\cdot)](y) = [\tfrac{1}{\sigma}\mathcal{B}\mathcal{B}^\dagger\tilde{\psi}(\cdot)](y). \quad (3.14b)$$

This system can be equivalently expressed as the generalized eigenvalue problem,

$$\begin{bmatrix} 0 & \mathcal{B}\mathcal{B}^\dagger \\ \mathcal{C}^\dagger\mathcal{C} & 0 \end{bmatrix} \begin{bmatrix} \tilde{\phi} \\ \tilde{\psi} \end{bmatrix} = \gamma \begin{bmatrix} \mathcal{A} & 0 \\ 0 & \mathcal{A}^\dagger \end{bmatrix} \begin{bmatrix} \tilde{\phi} \\ \tilde{\psi} \end{bmatrix}, \quad (3.15)$$

where we suppress the dependence on the spatial variable y for brevity. Eigenvalues resulting from this approach determine the singular values in pairs of opposite signs, i.e., $\gamma = \pm\sigma$.

This approach offers two advantages relative to the computation of the eigenvalues using the composite operator $\mathcal{T}^\dagger(\omega)\mathcal{T}(\omega)$. First, it allows simultaneous computation

of both the right and the left singular functions, i.e., $\tilde{\phi}(y)$ and $\tilde{\psi}(y)$. The second and more important advantage is that it does not require computation of any inverses. This feature avoids a potential issue of ill-conditioning and allows application to systems in the descriptor form, thereby avoiding the need for determining the evolution form representation. Furthermore, compared to the composite operator $\mathcal{T}^\dagger(\omega)\mathcal{T}(\omega)$, implementing the feedback interconnected system is simpler as it avoids computing discretized operator inverses. We note that the QZ algorithm [76] can be used to solve the discretized version of generalized eigenvalue problem (3.15).

In most cases, it is of interest to compute only the few largest singular values. Since some eigenvalues corresponding to a generalized eigenvalue problem can be infinite, using a sparse eigenvalue solver to compute the eigenvalues with largest real part is not a viable option. In order to utilize sparse solvers, we search for the eigenvalues of the smallest magnitude for

$$\begin{bmatrix} \mathcal{A} & 0 \\ 0 & \mathcal{A}^\dagger \end{bmatrix} \begin{bmatrix} \tilde{\phi} \\ \tilde{\psi} \end{bmatrix} = \frac{1}{\gamma} \begin{bmatrix} 0 & \mathcal{B}\mathcal{B}^\dagger \\ \mathcal{C}^\dagger\mathcal{C} & 0 \end{bmatrix} \begin{bmatrix} \tilde{\phi} \\ \tilde{\psi} \end{bmatrix}. \quad (3.16)$$

When $\mathcal{A}(\omega) = i\omega\mathcal{E} - \mathcal{F}$, we next describe how the procedure of this section can be utilized to compute the \mathcal{H}_∞ norm, i.e., the smallest upper bound on the largest singular value of the frequency response operator across temporal frequencies. For stable linear dynamical systems, this quantity determines the L_2 -induced gain (i.e., the worst-case amplification of finite energy disturbances) and it has an appealing robustness interpretation [77, Section 4.10.2] that is closely related to the notion of pseudo-spectra of linear operators.

Computation of the \mathcal{H}_∞ norm

The peak of the largest singular value of the frequency response operator $\mathcal{T}(\omega)$ over all temporal frequencies $\omega \in \mathbb{R}$ determines the \mathcal{H}_∞ norm of a stable linear system,

$$\|\mathcal{T}\|_\infty := \sup_{\omega} \sigma_{\max}(\mathcal{T}(\omega)). \quad (3.17)$$

When $\mathcal{A}(\omega) = i\omega I - \mathcal{F}$, the \mathcal{H}_∞ norm can be computed to a desired accuracy using the purely imaginary eigenvalues of the Hamiltonian operator [4, 78],

$$\mathcal{M}_\gamma = \begin{bmatrix} \mathcal{F} & \frac{1}{\gamma} \mathcal{B}\mathcal{B}^\dagger \\ -\frac{1}{\gamma} \mathcal{C}^\dagger \mathcal{C} & -\mathcal{F}^\dagger \end{bmatrix}. \quad (3.18)$$

For a given $\omega = \omega_0$, the formulation based on a feedback interconnection (3.15) implies that γ is a singular value of $\mathcal{T}(\omega_0)$. The expression for \mathcal{M}_γ given by (3.18) can be obtained by rearranging (3.15), and a selected value of $\gamma = \gamma_1$ is a singular value of $\mathcal{T}(\omega)$ if and only if \mathcal{M}_{γ_1} has at least one purely imaginary eigenvalue [4, Theorem 2]. In this case, γ_1 provides a lower bound on $\|\mathcal{T}\|_\infty$ and the value of γ_1 can be updated using either the bi-section algorithm [4] or the method provided in [78] to compute the \mathcal{H}_∞ norm to a desired accuracy.

This procedure can be also extended to the problems with $\mathcal{A}(\omega) = i\omega\mathcal{E} - \mathcal{F}$; e.g., see [79]. The algorithm involves calculation that identifies the existence of purely imaginary eigenvalues for a generalized eigenvalue problem with operators $(\mathcal{M}_\gamma, \mathcal{N}_\gamma)$, where,

$$\mathcal{N}_\gamma = \begin{bmatrix} \mathcal{E} & 0 \\ 0 & \mathcal{E}^\dagger \end{bmatrix}. \quad (3.19)$$

3.3.2 Numerical approximation of spatial differential operators

Solving two-point boundary value problems via spectral methods requires expressing the variable of interest in a global basis of orthogonal functions, e.g., the Chebyshev polynomials. For example, in reaction-diffusion equation (3.3) the variable $\phi(y, t)$ can be expressed as

$$\phi(y, t) = \sum_{i=0}^{\infty}{}' a_i(t) T_i(y),$$

where $T_n(y)$ is the n th Chebyshev polynomial of the first kind, $a_n(t)$ is the n th spectral coefficient, and the prime denotes a summation with the first term halved.

Implementation using Chebfun

Chebfun is an open-source software for spectral methods that provides various standard discretizations [31]. We implement the feedback interconnection shown in Figure 3.4 using Chebfun in Matlab [31, 80] and explore the utility of different discretization schemes that Chebfun offers. As a representative of an ill-conditioned discretization scheme, we use Chebfun’s spectral collocation routine which utilizes Chebyshev polynomials of the second kind as basis functions and goes under the name `chebcolloc2`. Chebfun also provides a well-conditioned scheme based on the ultraspherical discretization. This method expresses the k th derivative of a function in terms of a series of ultraspherical polynomials and it goes under the name `ultraS` [26]. We develop a function that takes the operators \mathcal{A} , \mathcal{B} , and \mathcal{C} in (3.1) as inputs in the Chebfun syntax, and produces the singular values and the corresponding singular functions as outputs. For systems with $\mathcal{A}(\omega) = i\omega\mathcal{E} - \mathcal{F}$ and nonsingular \mathcal{E} , we also provide a function that computes the \mathcal{H}_∞ norm (3.17) and returns the frequency at which $\sigma_{\max}(\omega)$ peaks using the algorithm developed in [78]. All routines that utilize Chebfun are restricted to systems in the evolution form.

Implementation using spectral integration suite

We develop a spectral integration suite that implements the feedback interconnected system in Figure 3.4. The suite is based on the methods reported in [28, 27] with minor modifications that facilitates application to a broad class of infinite-dimensional problems and results in simple discretization matrices in Matlab and C++. As discussed in § 3.2.4, in contrast to conventional spectral methods, the spectral integration method is attractive because it does not require a staggered grid to deal with systems in the descriptor form. In the remainder of this section, we provide a brief summary of our implementation of the Chebyshev spectral integration method and relegate details to supplementary material § H.

In the spectral integration method, the highest derivative is expressed in the basis of Chebyshev polynomials (in our case, of the first kind) and expressions for lower derivatives are determined by integrating higher derivatives. For reaction-diffusion equation (3.3), the second derivative of $\phi(y)$ is expressed as

$$D^2\phi(y) = \sum_{i=0}^{\infty} \phi_i^{(2)} T_i(y) =: \mathbf{t}_y^T \mathbf{\Phi}, \quad (3.20a)$$

where $\mathbf{\Phi} = [\phi_0^{(2)} \ \phi_1^{(2)} \ \phi_2^{(2)} \ \dots]^T$ is the infinite vector of spectral coefficients and \mathbf{t}_y is the vector of Chebyshev polynomials of the first kind $T_i(y)$,

$$\mathbf{t}_y^T := [\tfrac{1}{2}T_0(y) \ T_1(y) \ T_2(y) \ \dots].$$

Subsequent indefinite integration of (3.20a) yields

$$D\phi(y) = \sum_{i=0}^N \phi_i^{(1)} T_i(y) + c_1^{(\phi)} =: \mathbf{t}_y^T \mathbf{\Phi}^{(1)} + c_1^{(\phi)}, \quad (3.20b)$$

$$\phi(y) = \sum_{i=0}^N \phi_i^{(0)} T_i(y) + c_1^{(\phi)} y + \tilde{c}_0^{(\phi)} =: \mathbf{t}_y^T \mathbf{\Phi}^{(0)} + c_1^{(\phi)} y + \tilde{c}_0^{(\phi)}, \quad (3.20c)$$

where $\tilde{c}_0^{(\phi)}$ and $c_1^{(\phi)}$ are constants of integration. The spectral coefficients of $\mathbf{\Phi}^{(1)}$ and $\mathbf{\Phi}^{(0)}$ are related to the spectral coefficients of $\mathbf{\Phi}$ as

$$\mathbf{\Phi}^{(1)} = \mathbf{J} \mathbf{\Phi}, \quad \mathbf{\Phi}^{(0)} = \mathbf{J}^2 \mathbf{\Phi}, \quad (3.21)$$

where \mathbf{J} is given by,

$$\mathbf{J} := \begin{bmatrix} 0 & \frac{1}{2} & 0 & \dots & & \\ \frac{1}{2} & 0 & -\frac{1}{2} & 0 & \dots & \\ 0 & \frac{1}{4} & 0 & -\frac{1}{4} & 0 & \dots \\ 0 & 0 & \frac{1}{6} & 0 & -\frac{1}{6} & 0 & \dots \\ \vdots & \vdots & & \ddots & \ddots & \ddots & \end{bmatrix}. \quad (3.22)$$

The first row of the integration operator \mathbf{J} we use in (3.22) is different from what is used in [27, Section 4] and [28, Eq. (12)], and its derivation is provided in supplementary material § H. In contrast to [28, 27] where the first row of \mathbf{J} is full, our representation for \mathbf{J} in (3.22) is given by a banded tri-diagonal matrix.

From the above, we can express $\phi(y)$, $D\phi(y)$, and $D^2\phi(y)$ and as

$$\phi(y) = \mathbf{t}_y^T (\mathbf{J}^2 \Phi + \mathbf{R}_2 \mathbf{c}^{(\phi)}), \quad (3.23a)$$

$$D\phi(y) = \mathbf{t}_y^T (\mathbf{J}^1 \Phi + \mathbf{R}_1 \mathbf{c}^{(\phi)}), \quad (3.23b)$$

$$D^2\phi(y) = \mathbf{t}_y^T (\mathbf{J}^0 \Phi + \mathbf{R}_0 \mathbf{c}^{(\phi)}), \quad (3.23c)$$

where \mathbf{R}_i are matrices that account for the constants of integration in a basis of Chebyshev polynomials, $\mathbf{c}^{(\phi)} := [c_0^{(\phi)} \ c_1^{(\phi)}]^T$, and $c_0^{(\phi)} = 2\tilde{c}_0^{(\phi)}$.

The feedback interconnection that is used to compute the frequency response of (3.3) is given by (see (3.15)),

$$\begin{bmatrix} 0 & I \\ I & 0 \end{bmatrix} \begin{bmatrix} \phi(y) \\ \psi(y) \end{bmatrix} = \gamma \begin{bmatrix} (i\omega + \epsilon^2)I - D^2 & 0 \\ 0 & (-i\omega + \epsilon^2)I - D^2 \end{bmatrix} \begin{bmatrix} \phi(y) \\ \psi(y) \end{bmatrix}, \quad (3.24a)$$

with boundary conditions

$$\begin{bmatrix} \mathcal{Q}(+1, D) & 0 \\ \mathcal{Q}(-1, D) & 0 \\ 0 & \mathcal{Q}(+1, D) \\ 0 & \mathcal{Q}(-1, D) \end{bmatrix} \begin{bmatrix} \phi(y) \\ \psi(y) \end{bmatrix} = 0, \quad (3.24b)$$

where $\mathcal{Q}(a, L)$ evaluates the action of the linear operator L on a variable at a point $y = a$. In particular, (3.24b) specifies homogeneous Neumann boundary conditions at $y = \pm 1$.

For the reaction-diffusion equation, the infinite-dimensional representation of the system shown in Figure 3.4 is obtained by combining (3.23) with (3.24a) and equating

terms that correspond to the same basis functions,

$$\begin{aligned}
 & \underbrace{\begin{bmatrix} \mathbf{0} & \mathbf{0} & \mathbf{J}^2 & \mathbf{R}_2 \\ \mathbf{J}^2 & \mathbf{R}_2 & \mathbf{0} & \mathbf{0} \end{bmatrix}}_{\mathbf{E}} \underbrace{\begin{bmatrix} \Phi \\ \mathbf{c}^{(\phi)} \\ \Psi \\ \mathbf{c}^{(\psi)} \end{bmatrix}}_{\mathbf{v}} = \\
 & \gamma \underbrace{\begin{bmatrix} (i\omega + \epsilon^2)\mathbf{J}^2 - \mathbf{I} & \mathbf{0} \\ (i\omega + \epsilon^2)\mathbf{R}_2 - \mathbf{R}_0 & \mathbf{0} \\ \mathbf{0} & (-i\omega + \epsilon^2)\mathbf{J}^2 - \mathbf{I} \\ \mathbf{0} & (-i\omega + \epsilon^2)\mathbf{R}_2 - \mathbf{R}_0 \end{bmatrix}^T}_{\mathbf{F}} \underbrace{\begin{bmatrix} \Phi \\ \mathbf{c}^{(\phi)} \\ \Psi \\ \mathbf{c}^{(\psi)} \end{bmatrix}}_{\mathbf{v}}, \\
 & \Rightarrow \mathbf{E} \mathbf{v} = \gamma \mathbf{F} \mathbf{v}. \tag{3.25a}
 \end{aligned}$$

Similarly, substitution of (3.23) to (3.24b) yields the representation of boundary conditions,

$$\underbrace{\begin{bmatrix} \mathbf{t}_{+1}^T \mathbf{J} & \mathbf{t}_{+1}^T \mathbf{R}_1 & \mathbf{0} & \mathbf{0} \\ \mathbf{t}_{-1}^T \mathbf{J} & \mathbf{t}_{-1}^T \mathbf{R}_1 & \mathbf{0} & \mathbf{0} \\ \mathbf{0} & \mathbf{0} & \mathbf{t}_{+1}^T \mathbf{J} & \mathbf{t}_{+1}^T \mathbf{R}_1 \\ \mathbf{0} & \mathbf{0} & \mathbf{t}_{-1}^T \mathbf{J} & \mathbf{t}_{-1}^T \mathbf{R}_1 \end{bmatrix}}_{\mathbf{M}} \begin{bmatrix} \Phi \\ \mathbf{c}^{(\phi)} \\ \Psi \\ \mathbf{c}^{(\psi)} \end{bmatrix} = \mathbf{0}. \tag{3.25b}$$

Thus, in the generalized eigenvalue problem (3.25a) only the eigenfunctions that belong to the null-space of the operator in (3.25b) are acceptable and the system of equations (S1-23) can be written as,

$$\begin{aligned}
 \mathbf{E} \mathbf{v} &= \gamma \mathbf{F} \mathbf{v}, \\
 \mathbf{M} \mathbf{v} &= \mathbf{0}.
 \end{aligned} \tag{3.26}$$

The finite-dimensional approximation of (3.26) is derived by utilizing a projection operator for the spectral coefficients

$$\mathbf{P} = [\mathbf{I}_{N+1} \ \mathbf{0}], \quad (3.27)$$

where \mathbf{P} has $N+1$ rows and an infinite number of columns. This yields a representation of (3.25) for the first $N+1$ spectral coefficients and the QR factorization or SVD of the matrix approximation of the operator in (3.25b) can be used to parameterize the null-space and obtain the eigenfunctions that satisfy the boundary conditions (see supplementary material § H for details) [81]. For example, the SVD of a full-row-rank fat-matrix \mathbf{M} of size $m \times n$ ($m < n$) in (3.25b) yields matrices \mathbf{U} , $\mathbf{\Sigma}$, and \mathbf{V} such that

$$\mathbf{M} \mathbf{v} = \mathbf{U} \mathbf{\Sigma} \mathbf{V}^\dagger \mathbf{v} = 0, \quad (3.28)$$

$$\Rightarrow \mathbf{M} \mathbf{v} = \mathbf{U} \begin{bmatrix} \mathbf{\Sigma}_1 & \mathbf{0} \end{bmatrix} \begin{bmatrix} \mathbf{V}_1^\dagger \\ \mathbf{V}_2^\dagger \end{bmatrix} \mathbf{v} = 0. \quad (3.29)$$

From (3.29), any \mathbf{v} such that

$$\mathbf{v} = \mathbf{V}_2 \mathbf{u}, \quad (3.30)$$

will satisfy (3.28), where \mathbf{u} is the vector that parametrizes the null-space (\mathbf{V}_2 in (3.30)) of \mathbf{M} [82]. Substituting (3.30) in (3.25a) yields the final generalized eigenvalue problem,

$$(\mathbf{E} \mathbf{V}_2) \mathbf{u} = \gamma (\mathbf{F} \mathbf{V}_2) \mathbf{u}, \quad (3.31)$$

which yields the singular values as $\gamma = \pm\sigma$, and \mathbf{u} .

Finite-dimensional approximations of more complex systems, e.g., the linearized NS equations (3.9) and the equations governing channel flow of a viscoelastic fluid (3.8a), are derived using a similar procedure to the one described in this section. Additional care is required to account for spatially varying coefficients and for the presence of a static-in-time constraint that arises from the continuity equation. An in-depth discussion of our implementation of spectral integration in both C++ and Matlab is provided in the supplementary material § H. Finally, we solve a generalized eigenvalue problem resulting from the finite-dimensional approximation to (3.15) using the sparse eigenvalue solver, `eigs` in Matlab, and LAPACK's `zggev` routine in C++.

As discussed in § 3.3.1, the feedback interconnection in Figure 3.4 can be used for systems in the descriptor form and the spectral integration method does not require a staggered grid when pressure is retained in the governing equations. We next describe how we handle pressure boundary conditions in the spectral integration method for channel flows of incompressible Newtonian and viscoelastic fluids.

3.3.3 Boundary conditions for linearized NS equations in the descriptor form

Boundary conditions for the frequency response operator

For the linearized NS in the descriptor form, the boundary conditions on pressure are unknown and it is necessary to impose additional constraints to guarantee well-posedness. These additional boundary conditions do not need to be imposed on pressure fluctuations [74]. In particular, the no-slip and no-penetration conditions at the walls, $\mathbf{v}(\pm 1) = 0$, can be used in conjunction with continuity equation (3.9b) (i.e., $ik_x u(y) + Dv(y) + ik_z w(y) = 0$ after the Fourier transform in the wall-parallel directions has been utilized) to obtain two additional constraints, $[Dv(\cdot)](\pm 1) = 0$. Thus, the velocity fluctuations in the descriptor formulation of the NS equations have to satisfy eight boundary conditions,

$$u(\pm 1) = v(\pm 1) = w(\pm 1) = [Dv(\cdot)](\pm 1) = 0. \quad (3.32)$$

As mentioned earlier, the number of integration constants has to be equal to the number of (linearly independent) constraints for the spectral integration method to ensure well-posed numerical implementation. Since $D^2 \mathbf{v}$ and Dp appear in (3.9), expressing them in terms of Chebyshev polynomials and integrating would give one integration constant less than the number of boundary conditions. A well-posed formulation can be obtained by expressing the second derivative of the pressure in a basis of Chebyshev polynomials,

$$D^2 p(y) = \sum_{i=0}^N p_i^{(2)} T_i(y). \quad (3.33)$$

Subsequent integration (as in (3.20b) and (3.20c)) yields two additional integration constants which can be used to account for $[Dv(\cdot)](\pm 1) = 0$. Such a treatment for pressure is not uncommon in numerical approximations of the linearized NS equations; for example, two homogeneous Neumann boundary conditions on pressure have been used for modal analysis of the formulation in primitive variables [83, 84, 69].

While conventional spectral methods (e.g., the Chebyshev-tau and collocation methods) require different numbers of basis functions for pressure and velocity fluctuations (i.e., a staggered grid) to avoid spurious modes [24, 29], we express velocity and pressure using an equal number of basis functions, i.e., $N+1$. Moreover, the additional Neumann boundary conditions on wall-normal velocity fluctuations simply result from imposing the no-slip and no-penetration conditions at the walls, $\mathbf{v}(\pm 1)$, on the continuity equation (3.9b). The same process of deriving linearly independent boundary conditions to make a spectral collocation method well-posed was previously used in pipe flow [68]. We note that, in contrast to the spectral integration method, the spectral collocation technique still requires a staggered grid [68].

In summary, we augment the linearized NS equations (3.9) with boundary conditions (3.32). In § 3.4.3, we demonstrate that these boundary conditions produce the correct eigenvalues for the formulation in primitive variables (i.e., the descriptor form characterization of the linearized NS equations) without a staggered grid.

Boundary conditions for the adjoint system

For the NS equations linearized around the base flow $(U(y), 0, 0)$, application of the Fourier transform in t , x , and z on (3.9) yields the operators \mathcal{A} , \mathcal{B} , and \mathcal{C} in (3.11a),

$$\begin{aligned}
\mathcal{A} &= \begin{bmatrix} i(\omega + k_x U) - \frac{\Delta}{Re} & U'(y) & 0 & ik_x \\ 0 & i(\omega + k_x U) - \frac{\Delta}{Re} & 0 & D \\ 0 & 0 & i(\omega + k_x U) - \frac{\Delta}{Re} & ik_z \\ ik_x & D & ik_z & 0 \end{bmatrix}, \\
\mathcal{B} &= \begin{bmatrix} I & 0 & 0 \\ 0 & I & 0 \\ 0 & 0 & I \\ 0 & 0 & 0 \end{bmatrix}, \quad \mathcal{C} = \begin{bmatrix} I & 0 & 0 & 0 \\ 0 & I & 0 & 0 \\ 0 & 0 & I & 0 \end{bmatrix},
\end{aligned} \tag{3.34}$$

where $\Delta := D^2 - (k_x^2 + k_z^2)I$. The operators \mathcal{A} and \mathcal{C} act on the vector of flow fluctuations in primitive variables, i.e., $\phi = [u \ v \ w \ p]^T$ in (3.11a); the operator \mathcal{B} acts on the vector of forcing fluctuations, $\mathbf{d} = [d_x \ d_y \ d_z]^T$; and the output is determined by the velocity fluctuation vector, $\xi = \mathbf{v} = [u \ v \ w]^T$. Following [75, Section 5], we can obtain the adjoint operators \mathcal{A}^\dagger , \mathcal{B}^\dagger , and \mathcal{C}^\dagger in (3.11b),

$$\begin{aligned}
\mathcal{A}^\dagger &= \begin{bmatrix} -i(\omega + k_x U) - \frac{\Delta}{Re} & 0 & 0 & -ik_x \\ U'(y) & -i(\omega + k_x U) - \frac{\Delta}{Re} & 0 & -D \\ 0 & 0 & -i(\omega + k_x U) - \frac{\Delta}{Re} & -ik_z \\ -ik_x & -D & -ik_z & 0 \end{bmatrix}, \\
\mathcal{B}^\dagger &= \begin{bmatrix} I & 0 & 0 & 0 \\ 0 & I & 0 & 0 \\ 0 & 0 & I & 0 \end{bmatrix}, \quad \mathcal{C} = \begin{bmatrix} I & 0 & 0 \\ 0 & I & 0 \\ 0 & 0 & I \\ 0 & 0 & 0 \end{bmatrix},
\end{aligned} \tag{3.35}$$

and show that the adjoint variables $\psi = [\hat{u} \ \hat{v} \ \hat{w} \ \hat{p}]^T$ in (3.11b) satisfy $\hat{u}(\pm 1) = \hat{v}(\pm 1) = \hat{w}(\pm 1) = 0$. Furthermore, evaluation of the last row in $[\mathcal{A}^\dagger \psi(\cdot)](y) = [\mathcal{C}^\dagger \mathbf{g}(\cdot)](y)$ at the walls yields two additional boundary conditions $D\hat{v}(\pm 1) = 0$. Thus, for the linearized NS equations in the descriptor form we impose the following boundary conditions on the adjoint of the frequency response operator,

$$\hat{u}(\pm 1) = \hat{v}(\pm 1) = \hat{w}(\pm 1) = [D\hat{v}(\cdot)](\pm 1) = 0, \tag{3.36}$$

on the components of the vector $\psi = [\hat{u} \ \hat{v} \ \hat{w} \ \hat{p}]^T$ in (3.11b). In § 3.4.3, we demonstrate that the spectral integration method with boundary conditions (3.32) on the frequency response operator along with the adjoint boundary conditions (3.36) can be used to correctly compute the resolvent norm for the linearized NS equations in the descriptor form. We next show how this formulation can be extended to viscoelastic fluids.

3.3.4 Frequency response analysis of 3D channel flow of a viscoelastic fluid

The flow of a viscoelastic fluid in a channel is governed by equations (3.7c) that account for the memory (time-dependent variation) of the stress in the fluid. As the stress has no boundary conditions specified, it is favorable to transform (3.7) in a manner that the stress is eliminated, and to retain as state variables quantities whose boundary conditions are known, i.e., the velocity and pressure (as discussed in § 3.3.3, velocity boundary conditions derived from the continuity equation account for pressure boundary conditions). After a spatio-temporal Fourier transform, the stress can be expressed in terms of the velocity as,

$$\tau(y) = [\mathcal{V} v(\cdot)](y), \quad (3.37)$$

The process to obtain \mathcal{V} is relegated to Appendix D. After eliminating the stress, there are two approaches to compute the frequency responses and these will be discussed in the following subsections.

The descriptor formulation with the stress eliminated

In this approach, we derive a system equivalent to (3.7) by using (3.37) to eliminate the stress variables. This results in a system of equations with state variables $\tilde{\phi} = [u \ v \ w \ p]^T$ in the representation in (3.11a). The operators \mathcal{A} , \mathcal{B} , and \mathcal{C} in (3.11a) for this system is given in Appendix D.2. The regular and adjoint boundary conditions for this system are the same as that for linearized NS equations, i.e., (3.32) and (3.36). In this paper the term “descriptor form” for the viscoelastic system always refers to the descriptor form with the stress eliminated.

The evolution form model

Once the stress is eliminated using the process discussed in § 3.3.4, the pressure can further be eliminated to bring the 3D viscoelastic system to a form where the state variables are $\tilde{\phi} = [v \ \eta]^T$, where $(\eta := i k_z u - i k_x w)$ [16, 6, 14]. As the pressure is eliminated, this system is now in the evolution form, and the standard process discussed in [75, Section 5] can be used to calculate the adjoint boundary conditions. The system representation (3.11a) of this form is given in Appendix D.1. In this paper the evolution form for a viscoelastic system always refers to the evolution form where the stress is eliminated.

3.4 Computational examples

In this section, we provide examples to demonstrate the merits and the effectiveness of the developed framework. For the reaction-diffusion equation, we show that the computations based on a feedback interconnection shown in Figure 3.4 are insensitive to the operator-induced ill-conditioning discussed in § 3.2.2. We next apply this feedback interconnection to the 2D viscoelastic system in the evolution form (3.8a) and show that our approach provides robust result over a much wider range of flow elasticities than the approach based on a cascade connection shown in Figure 3.3. Finally, we use the feedback interconnected system in conjunction with the spectral integration method to compute frequency responses of systems in the descriptor form.

3.4.1 Reaction-diffusion equation

As demonstrated in § 3.2.2, the singular value decomposition of the operator $\mathcal{T}(\omega)\mathcal{T}^\dagger(\omega)$ is ill-conditioned for small values of ϵ in (3.3). We revisit this example using the feedback interconnection shown in Figure 3.4. Figure 3.5 shows the first twenty singular values of the frequency response operator for reaction-diffusion equation (3.3) with $\epsilon = 10^{-4}$. While the values computed using the feedback connection (marked by circles) agree with the analytical solution (marked by crosses), the singular values resulting from the cascade connection (marked by diamonds) are erroneous. This mismatch arises from ill-conditioning of the operator $\mathcal{T}(\omega)\mathcal{T}^\dagger(\omega)$ and has nothing to do with the spatial discretization. It turns out that increasing N does not improve computations resulting

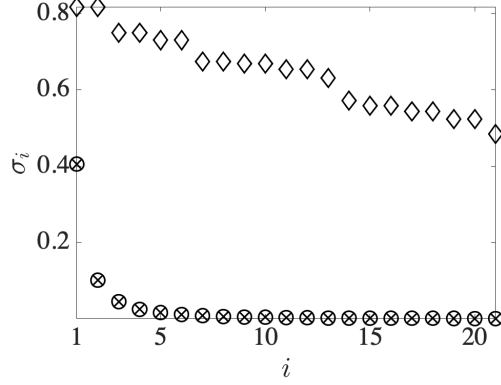


Figure 3.5: Singular values of the frequency response operator for reaction-diffusion equation (3.3) with $\epsilon = 10^{-4}$ and $\omega = 0$ resulting from the use of Chebfun’s spectral collocation scheme with $N = 64$. Symbols represent analytical solution (\times), and the computations based on the feedback interconnection shown in Figure 3.4 (\circ) and the cascade connection shown in Figure 3.3 (\diamond). The principal singular value (corresponding to $i = 0$) is not shown as its value is significantly larger than the remaining singular values.

from the cascade connection shown in Figure 3.3. Furthermore, the spectral integration method applied on the cascade connection also produces erroneous results (not shown). This observation was made using both our implementation of the spectral integration method and implementation developed in [33]. Since the error is induced by ill-conditioning of the operator $\mathcal{T}(\omega)\mathcal{T}^\dagger(\omega)$, we expect that the ultraspherical discretization of the cascade connection would also yield erroneous results.

3.4.2 2D viscoelastic channel flow

As a second application, we consider 2D channel flow of an Oldroyd-B fluid described in § 3.2.3. In contrast to operator-induced ill-conditioning, discretization-induced errors can be alleviated by employing a well-conditioned discretization scheme, e.g., the ultraspherical and spectral integration schemes discussed in § 3.3. In conventional spectral methods (e.g., Chebyshev collocation method), discretization matrices become increasingly ill-conditioned with an increase in the number of basis functions. Viscoelastic channel flow requires a large number of basis functions for good resolution and provides an excellent benchmark for studying effects that arise from both discretization- and

operator-induced ill-conditioning.

The frequency response operator $\mathcal{T}(\omega)$ for 2D channel flow of an Oldroyd-B fluid is described by (3.8a) and numerical implementation requires a large number of basis functions (about 4000) for good resolution in a flow with moderate Weissenberg numbers ($We \sim 50$). In strongly elastic flows (with $We \sim 500$), an operator-induced ill-conditioning, similar to the one discussed § 3.4.1, also arises. The discrete eigenvalues in a 2D flow scale as $1/We$ [56] and, at large We , the cascade connection shown in Figure 3.3 is prone to ill-conditioning because of the inversions in $\mathcal{T}(\omega)\mathcal{T}^\dagger(\omega)$. At high elasticities, only the feedback connection in Figure 3.4 produces reliable results and all calculations in this section are based on it.

Velocity output

We employ spectral collocation, ultraspherical discretization, and spectral integration methods to compute singular values of the frequency response operator (3.8a), with the velocity as the output, in 2D Couette flow of an Oldroyd-B fluid. In Figure 3.6, we show the largest singular value as a function of We for $Re = 0$, $\beta = 0.5$, $k_x = 1$, and $\omega = 0$. Calculations are performed using 479 (marked by circles) and 511 (marked by crosses) basis functions. Figures 3.6a and 3.6b demonstrate that the ultraspherical and spectral integration methods produce grid-independent results. In contrast, Figure 3.6c illustrates that the spectral collocation method produces grid-dependent results.

In [33], the performance of spectral integration and spectral collocation methods was compared using the same example. As in our study, it was observed that the collocation method produces unreliable, grid-dependent results, and that the spectral integration method yields reliable, grid-independent results. We find that the method based on ultraspherical discretization performs on par with the spectral integration method and that it produces grid-independent results for 2D Couette flow of an Oldroyd-B fluid with moderate We .

Stress output

When the stress fluctuations are selected as the output, we use the Chebfun's ultraspherical discretization in `Matlab` for the frequency response analysis. The computations are verified using our spectral integration method (not reported here). Among other

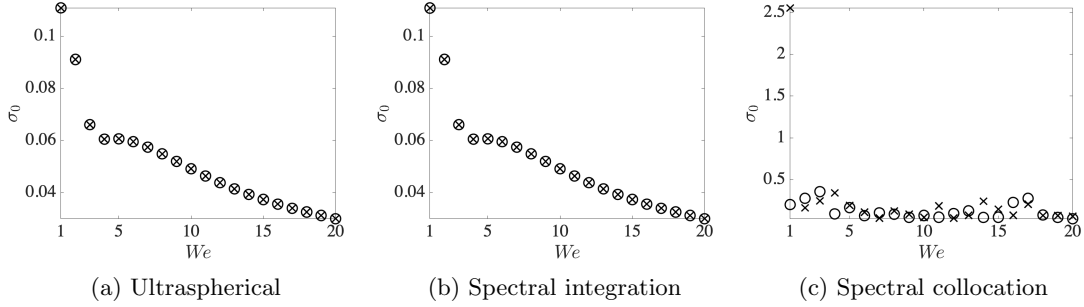


Figure 3.6: Principal singular values of the frequency response operator (3.8a) for inertialess 2D Couette flow of an Oldroyd-B fluid with $\beta = 0.5$, $k_x = 1$, and $\omega = 0$ as a function of fluid elasticity, We , resulting from the use of (a) ultraspherical; (b) spectral integration; and (c) spectral collocation methods. The velocity fluctuations are selected as the output and symbols represent $N = 479$ (\circ) and $N = 511$ (\times).

features, Chebfun offers the automatic collocation technique which increases the number of basis functions until the solution reaches machine precision [31].

The left singular functions associated with the largest singular value for the stress output reveal why these computations require a large number of basis functions. Figure 3.7 shows the principal left singular function of the first normal stress component, τ_{xx} , in inertialess 2D Couette flow with $We = 40$, $\beta = 0.5$, $\omega = 0$, and $k_x = 1$. Figure 3.7a illustrates τ_{xx} over the entire domain $y \in [-1, 1]$, and Figure 3.7b shows τ_{xx} in the region where the highest values are achieved (near the center of the channel). In spite of large peak magnitudes, the left singular function is smooth and well-resolved.

In contrast to the Couette flow computations, which require around 4000 basis functions, the computations for Poiseuille flow were resolved to machine precision with around 1000 basis functions. Figure 3.8 shows the principal left singular function for the stress output in Poiseuille flow that is obtained under the same conditions as Figure 3.7 for Couette flow ($Re = 0$, $We = 40$, $\beta = 0.5$, $k_x = 1$, and $\omega = 0$). While in Couette flow the stress shows a steep variation near the channel center (see Figure 3.7a), in Poiseuille flow the steep variation occurs near the walls (see Figure 3.8a). Since interpolations based on Chebyshev polynomials utilize points that are more densely populated near the ends of the domain, sharp variations in Poiseuille flows can be resolved with a smaller number of basis functions than sharp variations in Couette flow.

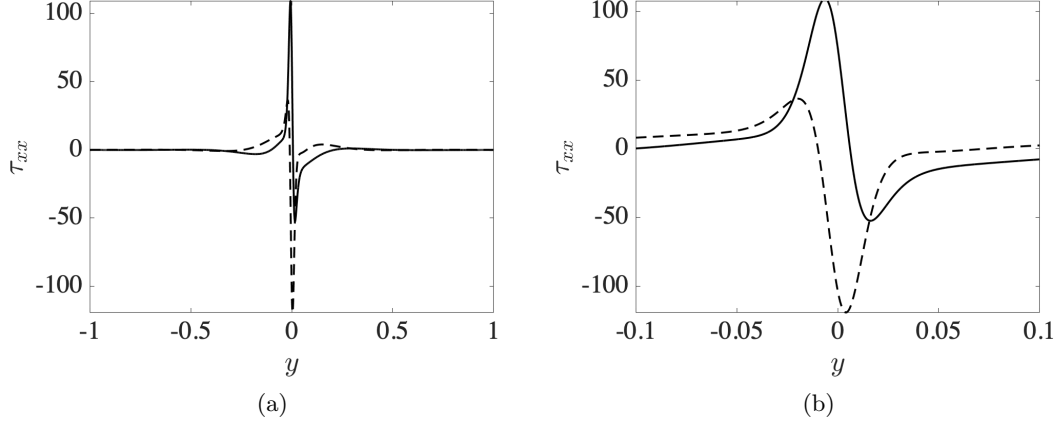


Figure 3.7: The left singular function associated with the principal singular value $\sigma_{\max} = 14.936$ of inertialess 2D Couette flow of an Oldroyd-B fluid with $We = 40$, $k_x = 1$, $\omega = 0$, and $\beta = 0.5$. The first normal stress component, τ_{xx} , (a) in the whole domain, $y \in [-1, 1]$; and (b) near $y = 0$ is shown. The stress fluctuations are selected as the output and the lines correspond to $\text{Re}(\tau_{xx})$ (-), and $\text{Im}(\tau_{xx})$ (- -).

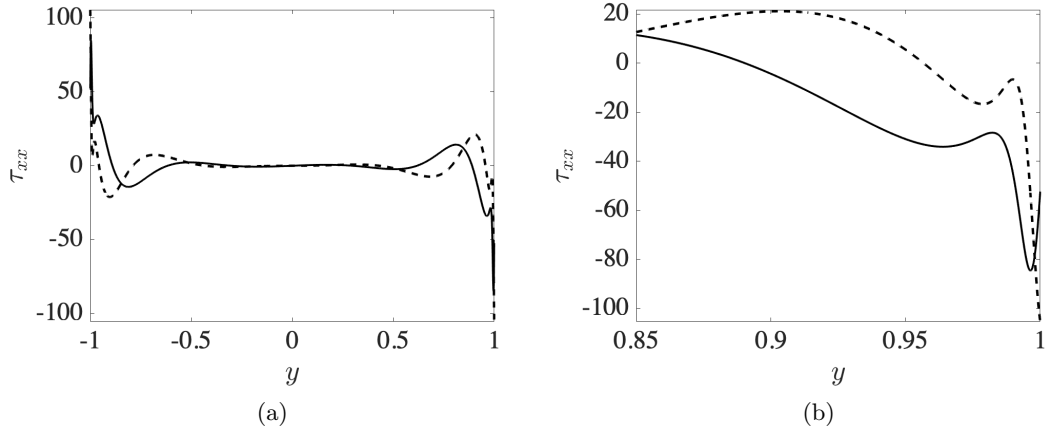


Figure 3.8: The left singular function associated with the principal singular value $\sigma_{\max} = 6.184$ of inertialess 2D Poiseuille flow of an Oldroyd-B fluid with $We = 40$, $k_x = 1$, $\omega = 0$ and $\beta = 0.5$. The first normal stress component, τ_{xx} , (a) in the whole domain, $y \in [-1, 1]$; and (b) near $y = 1$ is shown. The stress fluctuations are selected as the output and the lines correspond to $\text{Re}(\tau_{xx})$ (-), and $\text{Im}(\tau_{xx})$ (- -).

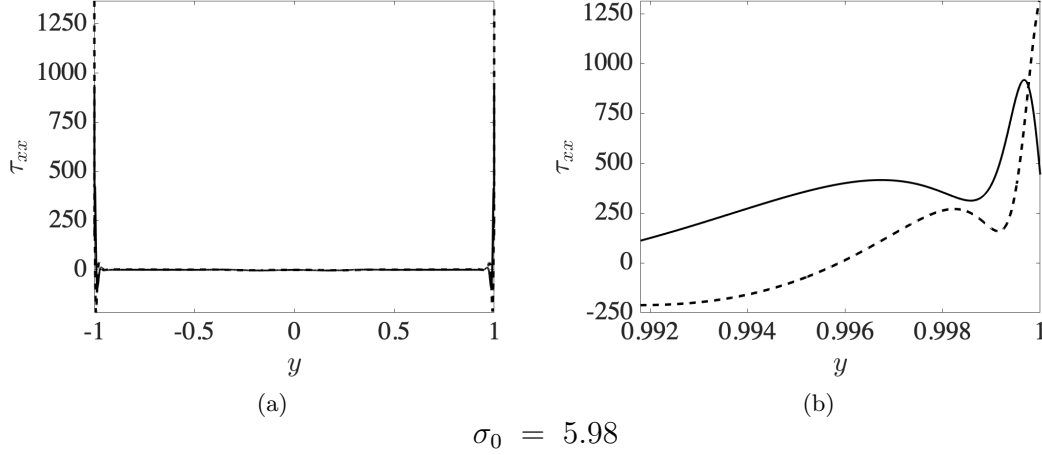


Figure 3.9: The left singular function associated with the principal singular value $\sigma_{\max} = 5.98$ of inertialess 2D Poiseuille flow of an Oldroyd-B fluid with $We = 500$, $k_x = 1$, $\omega = 0$, and $\beta = 0.5$. The first normal stress component, τ_{xx} , (a) in the whole domain, $y \in [-1, 1]$; and (b) near $y = 1$ is shown. The stress fluctuations are selected as the output and the lines correspond to $\text{Re}(\tau_{xx})$ (-), and $\text{Im}(\tau_{xx})$ (- -).

Finally, we consider inertialess 2D Poiseuille flow with high elasticity ($We = 500$), $\beta = 0.5$, $\omega = 0$, and $k_x = 1$. A well-resolved computation based on the feedback interconnection shown in Figure 3.4 requires around 15000 basis functions. We also used our implementation of the spectral integration method (described in § 3.3) as well as the spectral integration code developed in [33] to verify that the approach based on a cascade connection shown in Figure 3.3 fails to produce reliable results. The principal left singular function corresponding to τ_{xx} is shown in Figure 3.9. As expected, steep variations near $y = \pm 1$ are observed with the peak value of around 1000. Figure 3.9b shows a close-up of Figure 3.9a near $y = 1$ and demonstrates that the most amplified output direction is well-resolved even though the variation in τ_{xx} is spanning three orders in magnitude within the region of width 10^{-3} in $y \in [-1, 1]$.

3.4.3 Frequency response analysis of systems in the descriptor form

In the previous section we showed that the ultraspherical method and the spectral integration methods produce reliable results for resolvent norm calculations of 2D viscoelastic fluids in the evolution form. We next utilize the formulation based on the feedback interconnection shown in Figure 3.4 in conjunction with the spectral integration method for frequency response analysis of systems in the descriptor form. We examine the linearized NS equations presented in § 3.2.4 and the 3D flow of an Oldroyd-B fluid with the stress fluctuations eliminated (see § 3.3.4). As discussed in § 3.2.4, for incompressible flows in the descriptor form, conventional spectral methods require a staggered grid which may be difficult to implement in generic solvers like Chebfun [31]. Our spectral integration method overcomes this challenge by reinforcing the algebraic constraint (3.9b) at the walls; see § 3.3.3.

Channel flow of a Newtonian fluid

We first examine the linearized NS equations in Poiseuille flow; see (3.9) and Figure 3.2 for geometry. Modal analysis considers temporal growth or decay of infinitesimal fluctuations around the parabolic velocity profile $U(y) = 1 - y^2$. For $Re = 2000$, the linearized NS equations are stable [6] and Figure 3.10a shows the spectrum of the flow with $k_x = k_z = 1$. The results are obtained using the spectral integration method with 255 basis functions. Figure 3.10a shows that all eigenvalues are in the left-half of the complex plane and demonstrates the absence of spurious modes. We note that the computations based on the evolution form model (crosses) and the descriptor formulation (circles) agree with each other and with the results reported in the literature.

Figure 3.10b shows the dependence on the temporal frequency of the two largest singular values of the frequency response operator. For the principal singular value, the evolution form model results are marked by crosses and the descriptor formulation results are marked by circles. For the second largest singular value, the evolution form model results are marked by triangles and the descriptor formulation results are marked by inverted triangles. We observe excellent agreement in both cases.

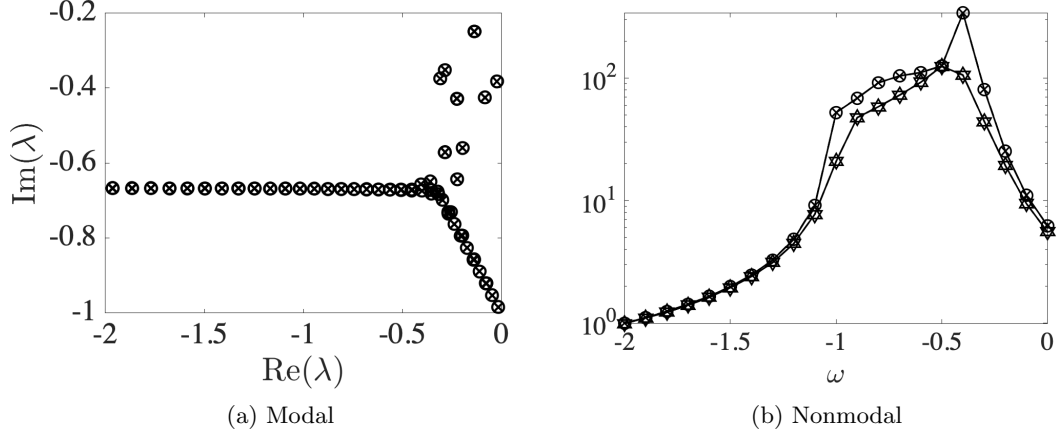


Figure 3.10: The linearized NS equations in Poiseuille flow with $Re = 2000$ and $k_x = k_z = 1$. The spectral integration method with $N = 255$ basis functions is used. (a) Spectrum resulting from the use of the evolution form model (\times) and the descriptor formulation (\circ); and (b) two largest singular values of the frequency response operator (evolution form (\times) and descriptor formulation (\circ) results for σ_{\max} ; evolution form (Δ) and descriptor formulation (∇) results for the second largest singular value).

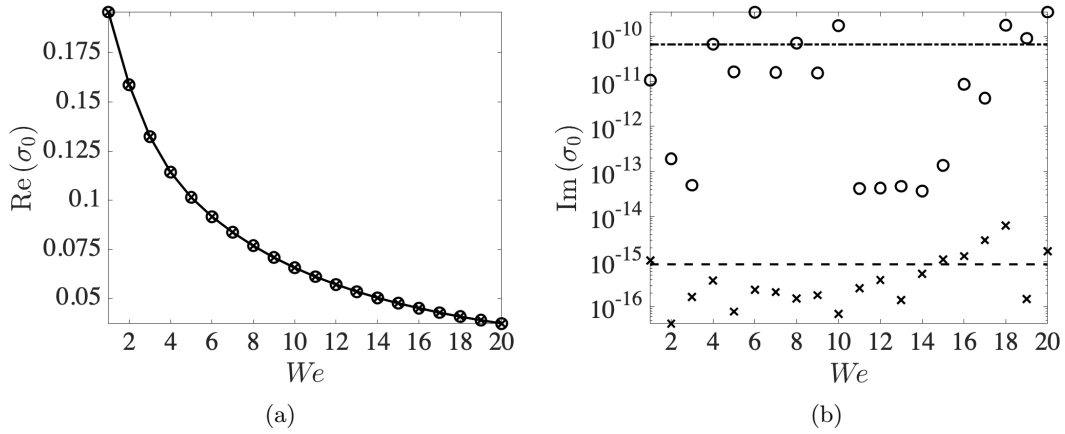


Figure 3.11: (a) Real; and (b) imaginary parts of the principal singular value in inertialess Couette flow of an Oldroyd-B fluid with $\beta = 0.5$, $k_x = k_z = 1$, and $\omega = 0$. The velocity fluctuations are selected as the output and the results are obtained using the descriptor formulation (\times) that eliminates stresses (see § 3.3.4) with $N = 383$ basis functions and the evolution form model (\circ) (see § 3.3.4) with $N = 1000$ basis functions.

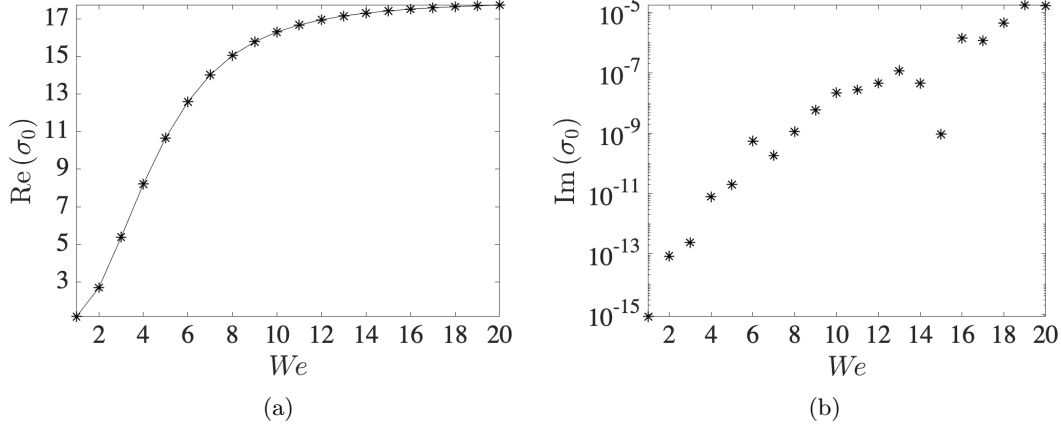


Figure 3.12: (a) Real; and (b) imaginary parts of the principal singular value in inertialess Couette flow of an Oldroyd-B fluid with $\beta = 0.5$, $k_x = k_z = 1$, and $\omega = 0$. The first normal stress component, τ_{xx} , is selected as the output and the results are obtained using the descriptor formulations that eliminates stresses (see § 3.3.4) with $N = 863$ basis functions.

Channel flow of an Oldroyd-B fluid

Figure 3.11a demonstrates the agreement between the singular values obtained using the descriptor formulation (\times) with $N = 383$ basis functions and the evolution model formulation (\circ) with $N = 1000$ basis functions. For inertialess Couette flow of an Oldroyd-B fluid with $\beta = 0.5$, $k_x = k_z = 1$, and $\omega = 0$, the velocity fluctuations are selected as the output and the influence of fluid elasticity We on the principal singular value is shown. Although the imaginary part of a computed singular value is zero in theory, the value of the imaginary part depends on the accuracy of the numerical method, and a smaller imaginary part indicates higher accuracy. Figure 3.11b displays the imaginary part of the principal singular value and we observe that the average imaginary part from the descriptor form with $N = 383$ is $\sim 10^{-15}$ (dashed line), and that from the evolution form with $N = 1000$ is $\sim 10^{-10}$ (dashed dotted line). This demonstrates the higher accuracy of the computations from the descriptor form.

Figure 3.12a shows the principal singular value of inertialess Couette flow of an Oldroyd-B fluid with $\beta = 0.5$, $k_x = k_z = 1$, and $\omega = 0$, as a function of We . The first normal stress component, τ_{xx} , is selected as the output and the computations are

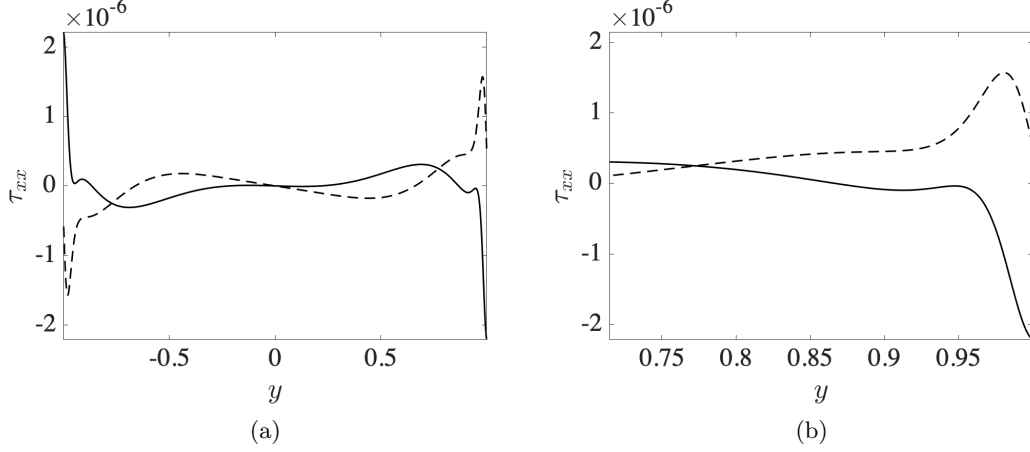


Figure 3.13: The left singular function corresponding to the principal singular value $\sigma_{\max} = 7.434$ in inertialess Poiseuille flow of an Oldroyd-B fluid with $We = 10$, $\beta = 0.5$, $k_x = k_z = 1$, and $\omega = 0$. The first normal stress component, τ_{xx} , is selected as the output and the results are obtained using the descriptor formulations that eliminates stresses with $N = 863$ basis functions. The lines correspond to $\text{Re}(\tau_{xx})$ (-) and $\text{Im}(\tau_{xx})$ (- -) and the results (a) in the entire domain, $y \in [-1, 1]$; and (b) near $y = 1$, are shown.

obtained using the descriptor formulation with $N = 863$ basis functions. The principal singular value increases with fluid elasticity but it appears to saturate at large values of We . For fixed N , Figure 3.12b demonstrates that the imaginary part of the principal singular value becomes larger with an increase in We . We further observe that for $We > 20$, the accuracy of the computed singular values does not improve with a further increase in N beyond certain value (≈ 863) and that the frequency response analysis of plane Poiseuille flow with stress as the output shows similar trends (not shown).

Figure 3.13 illustrates the principal left singular function for inertialess Poiseuille flow with $We = 10$, $\beta = 0.5$, $k_x = k_z = 1$, and $\omega = 0$. The first normal stress component, τ_{xx} , is selected as the output and the descriptor formulation is used in our computations. As in 2D flow, we observe sharp stress gradients near the walls.

3.5 Concluding remarks

In this paper, we explore the merits of recently developed well-conditioned ultraspherical and spectral integration methods for nonmodal analysis of channel flows of Newtonian and viscoelastic. We develop a framework for resolvent analysis that is based on a feedback interconnection of the frequency response operator with its adjoint and demonstrate its advantages over the standard formulation that utilizes a cascade connection. For ill-conditioned problems, we show that a combination of the formulation based on this feedback interconnection with well-conditioned ultraspherical and spectral integration methods can be used to overcome limitations of standard spectral collocation techniques. In particular, we demonstrate that our approach provides robust results in channels flows of Oldroyd-B fluids with high elasticity and show that the spectral integration method does not require a staggered grid for modal or nonmodal analysis of channel flows of incompressible fluids in descriptor form. This facilitates analysis of relevant flow physics in strongly elastic regimes and enables computations using the formulation with primitive variables. For a given number of basis functions, we show that the computations resulting from the descriptor formulation are more accurate than the computations based on the evolution form model. Even though we focus on nonmodal analysis of channel flows of Newtonian and viscoelastic fluids, the developed framework is general enough to find use for a variety of problems in fluid mechanics and beyond.

Acknowledgments

This work is supported in part by the National Science Foundation under grant number CBET-1510654. The Minnesota Supercomputing Institute (MSI) at the University of Minnesota is acknowledged for providing computing resources.

Chapter 4

Stress amplification in inertialess channel flows of viscoelastic fluids

4.1 Introduction

A Newtonian fluid transitions from a laminar to a turbulent flow state when its inertia is sufficiently large, whereas certain viscoelastic fluids move to a turbulent-like flow state even with negligible inertia [7, 3, 8, 9]. This turbulent-like flow state [8, 9] (elastic turbulence) occurs due to the predominance of elastic forces compared to viscous forces in the fluid. Elastic turbulence has potential applications in enhancing transport [39] in systems with weak inertia, e.g., in drug delivery systems, medical diagnostic devices, and high heat-flux integrated circuits [85]. In contrast, elasticity-driven instabilities in polymer processing operations like extrusion are detrimental to the quality of final products [13, 41]. Therefore, it is important to understand and control the initial stages of elastic turbulence.

4.1.1 Experimental observations on elastic turbulence

This paper is motivated by recent experimental observations on elastic turbulence in straight channels by Pan et al. [8] and Qin et al. [9]. They examined the flow of a viscoelastic fluid in a channel of length 3 cm and cross-section $90\text{ }\mu\text{m} \times 100\text{ }\mu\text{m}$ with a Reynolds number of ~ 0.01 . They [8, 9] used an array of cylinders (diameter $\sim 50\text{ }\mu\text{m}$)

in the entry region of the channel to perturb the flow, and the flow was visualized using dye-advection experiments and tracked using velocimetry. Qin et al. (Figure 3, inset, in [9]) observe that the steady-state kinetic energy of the fluid first decreases along the channel length before increasing, leading to elastic turbulence. In this paper we try to understand potential linear mechanisms that may explain this phenomenon.

We consider the 2D linearized model for flow of an Oldroyd-B fluid in a channel, and analyze effects of a body force which is a sinusoidal function of time and is nearly localized in space. We show that conditions exist where the steady-state stress is significantly amplified while the kinetic energy is relatively weak. Elastic turbulence [8, 9] was triggered using a different body force in channels, i.e., the drag force of cylindrical obstructions. The cylindrical obstructions exert a drag force on the fluid, and in turn the fluid experiences a persistent body force that is localized in space.

The velocity field generated downstream of a single cylinder is a periodic function of time (Figure 19c in [86]) that is generated by an instability associated with the flow around a cylinder. At sufficiently low Reynolds numbers in Newtonian fluids, this instability decays along the channel length due to strong viscous forces [86]. Pan et al. [8] observe similar behavior for viscoelastic channel flow. However, the instability evolves to a nonlinear flow state when more than one cylinder is used [8].

Assuming that the instability generated by the cylinders acts as a persistent small-amplitude perturbation, and that the resultant quasi-steady velocity is approximately a sinusoidal function of time (Figure 19c, [86]), then an equivalent body force that can generate this sinusoidal velocity will be a sinusoidal function of time as well. This is because for a linear flow system, a sinusoidal body force of a particular frequency results in a sinusoidal quasi-steady velocity (or stress) field of the same frequency [87, 6].

We will see in § 4.4 that the body forces we impose are similarly persistent and periodic functions of time, and are nearly localized in space, although they are not the same as that generated by finite-sized objects such as cylinders. We use this simplified model to explore possible mechanisms that may explain the observations by Qin et al. (Figure 3, inset, in [9]) of decreasing kinetic energy along the channel length, followed by an increase further downstream.

4.1.2 Linear analysis

Linear analysis concerns the evolution of small-amplitude perturbations on a dynamical system about a stationary (i.e., time-invariant) steady-state. Modal analysis considers the long-time growth (linearly unstable) or decay (asymptotically stable) of a small-amplitude perturbation on a dynamical system [17, 88]. A growing perturbation can trigger a nonlinear flow state that may result in a transition to elastic turbulence. Prior works on modal stability suggest that channel flow of a viscoelastic fluid is linearly stable under conditions of elastic turbulence [13]. Hence, the initial stages of elastic turbulence [8, 9] are unlikely to be related to modal instability.

However, even if a system governing the flow of a fluid in a channel is linearly stable, a persistent small-amplitude body force that is localized in space (e.g., the drag force exerted by the cylindrical obstructions in the experiments by Qin et al. [9]) may result in a velocity or stress that is significantly amplified. Finite-amplitude perturbations are known to be unstable [41, 89] in viscoelastic channel flows, and a velocity or stress perturbation that is significantly amplified may act as a finite-amplitude initial condition to trigger a nonlinear flow-state (observed as elastic turbulence).

Nonmodal analysis examines the amount of amplification of small-amplitude perturbations on a dynamical system [6, 43, 16, 14]. The amplification in nonmodal analysis is typically measured with quantities that are square-integrated along the channel width [14, 16, 90, 6], e.g., the square-integration of the velocity gives the kinetic energy in the channel [14, 16, 90]. Previous studies reveal that viscoelastic channel flows have large nonmodal amplification under conditions of elastic turbulence, and the amount of nonmodal amplification increases with an increase in the amount of polymer elasticity or concentration [20, 21, 22, 5, 36, 23].

Hence, one possible mechanism for the initial stages of transition to elastic turbulence [8, 9] in the absence of linear instability [13] is that small-amplitude perturbations undergo significant nonmodal amplification, and they act as finite-amplitude perturbations. As finite-amplitude perturbations are unstable [89, 41], they may trigger a nonlinear flow state, i.e., elastic turbulence.

However, in their experiments on elastic turbulence, Pan et al. [8] observe that the disturbance induced by a single cylinder in the entry region merely decays without any sign of amplification. Furthermore, they observe that a transition to elastic turbulence

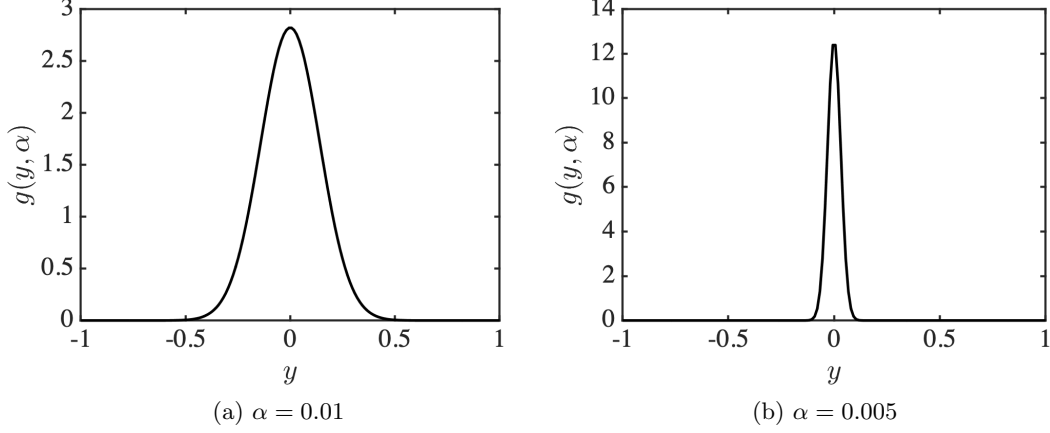


Figure 4.1: The Gaussian function (4.1) with (a) $\alpha = 0.01$, and (b) $\alpha = 0.005$.

needs more than one cylinder in the entry region, suggesting that the perturbation needs to be relatively strong to induce a transition.

From the perspective of nonmodal theory [6, 43], one might expect an initial condition of the velocity induced by the cylinders to grow along the channel length, and then trigger a nonlinear flow state [43, 6] at large channel lengths. As noted previously, Qin et al. (Figure 3, inset in [9]) report that the kinetic energy of the flow initially decreases along the channel length, and then increases later on.

The authors of Refs. [8, 9] therefore conclude that the initial stages of elastic turbulence are unlikely to be related to a linear (modal or nonmodal growth) mechanism, and are likely to be related to finite-amplitude effects. As mentioned before, nonmodal analysis measures amplification in terms of quantities that are square-integrated along the width of the channel [16, 90, 6]. However, this measure may be misleading in viscoelastic fluids, where the stress can be significantly amplified at a localized region in the channel. We note that other studies on flows viscoelastic fluids have shown that the stress can be highly localized [91, 66].

4.1.3 Localized amplification

As noted above, nonmodal analysis quantifies amplification in terms of a square-integrated measure [90, 16, 6] such as the kinetic energy. To understand why a square-integrated

measure is not apt for functions that are locally amplified in a small region, let us consider a function [23, 52] whose square yields the Gaussian function with a small standard deviation, α ,

$$g^2(y) = \frac{1}{2\sqrt{\pi\alpha}} e^{-\frac{y^2}{4\alpha}}. \quad (4.1)$$

The Gaussian function (4.1) has a property that its peak value increases with a decrease in α (Figure 4.1). In Figure 4.1a, when $\alpha = 0.01$, the peak value of the Gaussian function (4.1) is about ~ 3 , whereas in Figure 4.1b, when $\alpha = 0.005$, the peak value is about ~ 12 .

However, no matter how large the peak value of the Gaussian function is (i.e., no matter how small α is) in (4.1), its integration always yields a unit magnitude, i.e.,

$$\int_{-\infty}^{\infty} g^2(y) dy = 1. \quad (4.2)$$

The square-integrated measure in (4.2) does not weight the large magnitude of the Gaussian function in Figure 4.1b over a small region that distinguishes it from Figure 4.1a. Similarly, if the stress in the channel has a large magnitude over a small region in the channel, the square-integrated measure used in nonmodal analysis is likely to overlook its sheer magnitude in that region.

In this paper, we consider a linear mechanism motivated by this argument. We examine the stress that results from a persistent small-amplitude body force that is localized in space (which is similar to the drag force exerted by finite-sized objects such as cylinders used in experiments [8, 9]). The idea is that the stress can be significantly amplified in a small (localized) region in the channel, while the velocity (or kinetic energy) amplification is much weaker for such forces. The large and localized stress may act as a finite-amplitude perturbation that can trigger a nonlinear flow-state [41, 89] such as elastic turbulence.

This paper is organized as follows. In § 4.2 we present the problem formulation, and in § 4.3 we discuss the numerical methods used. In § 4.4 we compare localized and square-integrated amplification of the stress in inertialess channel flows of viscoelastic fluids. In § 4.5 we discuss mechanisms that contribute to localized amplification of the stress. We summarize our findings in § 4.6, and relegate technical details to the appendix.

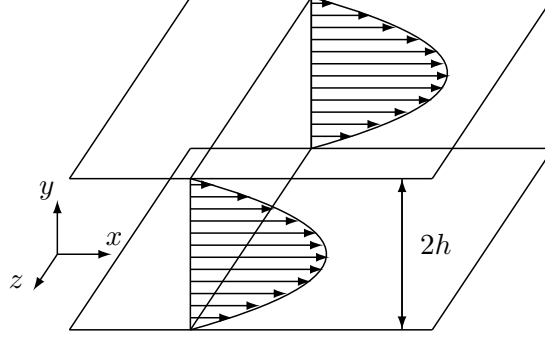


Figure 4.2: Flow geometry and the steady-state velocity profile for plane Poiseuille flow.

4.2 Problem formulation

4.2.1 Governing equations

We consider inertialess pressure-driven flow of an Oldroyd-B fluid between two parallel planes separated by a distance $2h$ (Figure 4.2) as related experiments use a pressure-driven flow [8, 9]. We present the governing equations by scaling length with h , velocity with the maximum velocity under steady laminar conditions, U_0 , and time with h/U_0 . Pressure is scaled with $\mu_T U_0/h$, where μ_T is the effective shear viscosity of the fluid, and the polymer stress with $\mu_p U_0/h$, where $\mu_p = \mu_T - \mu_s$ and μ_s is the solvent viscosity.

Two non-dimensional groups result from this scaling that characterize the material properties of the fluid: the viscosity ratio, $\beta = \mu_s/\mu_T$, which gives the ratio between the solvent to the total viscosity, and the Weissenberg number $We = \lambda_p U_0/h$, which gives the ratio between the relaxation time λ_p of the polymer to the characteristic flow time h/U_0 .

Equations governing the flow of a viscoelastic fluid come from momentum and mass conservation for an incompressible fluid [60, 61]

$$-\nabla P + \beta \nabla^2 \mathbf{V} + (1 - \beta) \nabla \cdot \mathbf{T} + \mathbf{D} = 0, \quad (4.3a)$$

$$\nabla \cdot \mathbf{V} = 0, \quad (4.3b)$$

where $\mathbf{V} = [U \ V \ W]^T$ is the velocity vector, \mathbf{T} is the polymer stress tensor, P is the pressure, and \mathbf{D} is the body force. We use the Oldroyd-B constitutive equation for the polymer stress tensor,

$$\partial_t \mathbf{T} + \mathbf{V} \cdot \nabla \mathbf{T} - \mathbf{T} \cdot \nabla \mathbf{V} - (\mathbf{T} \cdot \nabla \mathbf{V})^T = -\frac{1}{We} \mathbf{T} + \frac{1}{We} (\nabla \mathbf{V} + \nabla \mathbf{V}^T). \quad (4.3c)$$

The steady-state velocity and nonzero components of the stress are given by,

$$\bar{\mathbf{V}} = [\bar{U}(y) \ 0 \ 0]^T, \quad \bar{T}_{xx} = 2We \bar{U}'(y)^2, \quad \bar{T}_{xy} = \bar{T}_{yx} = \bar{U}'(y), \quad (4.4)$$

where $\bar{U}(y) = 1 - y^2$ for plane Poiseuille flow (see Figure 4.2), and the prime refers to a derivative with respect to y . We consider the dynamics of fluctuations about the steady-state (4.4) using a base-fluctuation decomposition in (4.3), $\mathbf{V} = \bar{\mathbf{V}} + \mathbf{v}$, $\mathbf{T} = \bar{\mathbf{T}} + \boldsymbol{\tau}$, $P = \bar{P} + p$, and $\mathbf{D} = \bar{\mathbf{D}} + \mathbf{d}$, where \mathbf{v} , $\boldsymbol{\tau}$, p and \mathbf{d} are fluctuations of the velocity, stress, pressure and body force respectively.

Retaining terms that are linear in the fluctuations leads to the linearized governing equations,

$$-\nabla p + \beta \nabla^2 \mathbf{v} + (1 - \beta) \nabla \cdot \boldsymbol{\tau} + \mathbf{d} = 0, \quad (4.5a)$$

$$\nabla \cdot \mathbf{v} = 0, \quad (4.5b)$$

$$\begin{aligned} & -\frac{1}{We} \boldsymbol{\tau} + \frac{1}{We} (\nabla \mathbf{v} + \nabla \mathbf{v}^T) = \\ & \partial_t \boldsymbol{\tau} + \bar{\mathbf{V}} \cdot \nabla \boldsymbol{\tau} + \mathbf{v} \cdot \nabla \bar{\mathbf{T}} - \bar{\mathbf{T}} \cdot \nabla \mathbf{v} - \boldsymbol{\tau} \cdot \nabla \bar{\mathbf{V}} - (\bar{\mathbf{T}} \cdot \nabla \mathbf{v})^T - (\boldsymbol{\tau} \cdot \nabla \bar{\mathbf{V}})^T. \end{aligned} \quad (4.5c)$$

The boundary conditions come from no-slip and no-penetration of the velocity at the channel walls,

$$\mathbf{v}(\pm 1) = 0. \quad (4.5d)$$

We consider the effects of a persistent body force \mathbf{d} of the form

$$\mathbf{d}(x, y, z, t) = \mathbf{d}(y) \delta(x) \delta(z) e^{i\omega t} \quad (4.5e)$$

where $\delta(\cdot)$ is the Dirac delta function, i is the imaginary unit, and ω is the temporal

frequency. Notice from (4.5e) that the body force is localized in the x - and z -directions and is harmonic in time. As we will see in § 4.4 (Figures 4.6c and 4.6d), the body force we consider is nearly localized at specific points in the y -direction as well.

As discussed in § 4.1, we use this body force as a simple model to understand the potential effects of finite-sized objects such as cylinders that perturb the flow. A finite-sized object may exert a persistent body force which is localized in space, and may generate velocity fluctuations that are periodic functions of time (Figure 19c in [86]). If these velocity fluctuations are approximately represented by small-amplitude sinusoidal functions of time, then an equivalent body force that generates this velocity field is a sinusoidal function of time as well. This is a consequence of small-amplitude fluctuations being governed by the linearized equations [6, 87].

4.2.2 Recasting the governing equations

We apply a Fourier transform on (4.5) in the x - and z -directions, and as the resultant stress and velocity fields must have the same temporal frequency ω [6] as the body force in (4.5e), we substitute $\mathbf{v}(\boldsymbol{\kappa}, y, t) = \mathbf{v}(\boldsymbol{\kappa}, y) e^{i\omega t}$, $\boldsymbol{\tau}(\boldsymbol{\kappa}, y, t) = \boldsymbol{\tau}(\boldsymbol{\kappa}, y) e^{i\omega t}$ and $p(\boldsymbol{\kappa}, y, t) = p(\boldsymbol{\kappa}, y) e^{i\omega t}$ in (4.5). Here $\boldsymbol{\kappa} = (k_x, k_z)$ is the vector of Fourier modes corresponding to the x - and z -directions. We then use this transformed version of (4.5c) to express the stress in terms of the velocity. Next, we use this expression to eliminate the stress in the momentum equations (4.5a) to arrive at a representation of (4.5) given by

$$[\mathcal{A}(\boldsymbol{\kappa}, \omega, \beta, We) \boldsymbol{\phi}(\cdot)](y) = [\mathcal{B}(\boldsymbol{\kappa}) \mathbf{d}(\cdot)](y), \quad (4.6a)$$

$$\mathbf{v}(y) = [\mathcal{C}_v(\boldsymbol{\kappa}) \boldsymbol{\phi}(\cdot)](y), \quad (4.6b)$$

$$\tau_{xx}(y) = [\mathcal{C}_{xx}(\boldsymbol{\kappa}, \omega, We) \boldsymbol{\phi}(\cdot)](y). \quad (4.6c)$$

The input \mathbf{d} is the body force in (4.5a), and $\boldsymbol{\phi} = [u \ v \ w \ p]^T$. The output is either the velocity vector (4.6b), or the component τ_{xx} (4.6c) of the stress tensor.

\mathcal{A} , \mathcal{B} , \mathcal{C}_v and \mathcal{C}_{xx} in (4.6) are block-matrices of differential operators in $y \in [-1 \ 1]$ (relegated to Appendix E). We consider the velocity vector as the output in (4.6b) instead of individual components as this enables us to measure the maximum value of the kinetic energy of velocity fluctuations as we explain later in this section (see (4.12)). We consider the xx -component of the stress in (4.6c) as we found that it shows the

largest stress amplification compared to other components.

System (4.6) can be further simplified (Chapter 3 of [6]) by eliminating pressure and recasting \mathcal{A} , \mathcal{B} , \mathcal{C}_v , and \mathcal{C}_{xx} to a form where $\phi = [v \ \eta]^T$ with $\eta = ik_z u - ik_x w$ being the wall-normal vorticity. We refer to the form in which $\phi = [u \ v \ w \ p]^T$ as the descriptor form, and the form in which $\phi = [v \ \eta]^T$ as the evolution form. The descriptor form is a larger system that involves four variables (u , v , w , and p), whereas the evolution form involves two variables (v and η). However, a numerical solution (see § 4.3) using the descriptor form needs fewer basis functions compared to the evolution form [69].

We perform calculations using both forms to confirm our expressions and results. Expressions for \mathcal{A} , \mathcal{B} , \mathcal{C}_v , and \mathcal{C}_{xx} in (4.6) in both forms are relegated to Appendix E. We make a note that the same set of equations in (4.6) results by using a body force that is a sinusoidal function of x and z in all space,

$$\mathbf{d}(x, y, z, t) = \mathbf{d}(y) e^{i\omega t + i k_x x + i k_z z} \quad (4.7a)$$

Substituting for the velocity, stress and pressure of the same spatial and temporal frequencies as the body force (4.7a) in (4.5), i.e., $\mathbf{v}(x, y, z, t) = \mathbf{v}(y) e^{i\omega t + i k_x x + i k_z z}$, $\boldsymbol{\tau}(x, y, z, t) = \boldsymbol{\tau}(y) e^{i\omega t + i k_x x + i k_z z}$ and $p(x, y, z, t) = p(y) e^{i\omega t + i k_x x + i k_z z}$ we obtain the same system (4.6).

Therefore solutions to (4.6) can be interpreted as being results of (a) a force that is a sinusoidal function of x and z in all space (4.7a), or (b) a force that is localized at one point in the x - and z -directions, i.e., at $x = 0$, $z = 0$ (4.5e). We use the localized interpretation in (4.5e) as finite-sized objects used in related experiments in refs. [9, 8] exert a body force on the fluid that is persistent in time and localized in space.

Modal analysis

The eigensystem of (4.6) that characterizes modal stability of (4.5) is given by pairs of (nonzero) eigenvectors $\phi(y)$ and eigenvalues λ , where $\omega = -i\lambda$, $\lambda \in \mathbb{C}$ (where \mathbb{C} is the set of complex numbers) for which

$$[\mathcal{A}(\boldsymbol{\kappa}, \lambda, \beta, We) \phi(\cdot)](y) = 0. \quad (4.7b)$$

System (4.6) is linearly unstable for any $\{\kappa, \beta, We\}$ where $\text{Re}(\lambda) > 0$, where $\text{Re}(\cdot)$ is the real part. Prior works have shown that inertialess Couette flow of a viscoelastic fluid is linearly stable for all $\{\kappa, We\}$ when $\beta = 0$ [56, 92]. For all other parameters of plane Couette and Poiseuille flows, several numerical solutions show that system (4.6) is linearly stable, although, to the best of our knowledge, there are no rigorous proofs for linear stability in the full parameter space of $\{\kappa, \beta, We\}$ [66, 13].

One known solution to (4.7b) is the continuous spectrum [56, 93, 66],

$$\lambda(y) = -\frac{1}{We} - i k_x \bar{U}(y), \quad (4.7c)$$

which has a negative real part $-1/We$ and is hence linearly stable (here \bar{U} is the steady-state velocity under laminar conditions, see (4.4)). The λ in (4.7c) is called the continuous spectrum as it varies in y according to the continuous function, $\bar{U}(y)$. The continuous spectrum reverts to a discrete eigenvalue $\lambda = -1/We$ when $k_x = 0$ in (4.7c). We find that (4.7c) plays an important role in inducing large stress amplification from small-amplitude body forces as we will discuss in § 4.5.1.

Nonmodal analysis

While modal analysis is centered around finding solutions to (4.7b), nonmodal analysis considers the resolvent operator [6] $\mathcal{A}^{-1}(\kappa, \omega, \beta, We)$ (see (4.6a)) in conjunction with the input body force (\mathbf{d} in (4.5a)) and a selected velocity or stress output (see (4.6b) and (4.6c) respectively). In particular, the resolvent operators that map the body force to the velocity and stress are given by,

$$\mathbf{v}(y) = [\mathcal{T}_v(\omega) \mathbf{d}(\cdot)](y), \quad (4.8a)$$

$$\tau_{xx}(y) = [\mathcal{T}_{xx}(\omega) \mathbf{d}(\cdot)](y), \quad (4.8b)$$

where \mathcal{T}_v is the resolvent operator that maps the body force (\mathbf{d} in (4.5a)) to the velocity, and \mathcal{T}_{xx} to the stress,

$$\mathcal{T}_v(\omega) = \mathcal{C}_v \mathcal{A}^{-1}(\omega) \mathcal{B}, \quad \mathcal{T}_{xx}(\omega) = \mathcal{C}_{xx}(\omega) \mathcal{A}^{-1}(\omega) \mathcal{B}. \quad (4.8c)$$

Note that operators \mathcal{C}_v , \mathcal{A} , \mathcal{B} , and \mathcal{C}_{xx} in (4.8c) are introduced in (4.6). We suppress the dependence of the operators on $\{\kappa, \beta, We\}$ in (4.8) for notational convenience.

One measure of the amount of nonmodal amplification in a system is the resolvent norm [6]. We now discuss the resolvent norm of a generic resolvent operator \mathcal{T} corresponding to an output operator \mathcal{C} in (4.6) that holds for both the velocity (\mathcal{C}_v in (4.6b)) and the stress (\mathcal{C}_{xx} in (4.6c)) outputs in (4.8),

$$\mathcal{T}(\omega) = \mathcal{C}(\omega) \mathcal{A}^{-1}(\omega) \mathcal{B}. \quad (4.9)$$

4.2.3 The resolvent norm

The resolvent norm of \mathcal{T} (in (4.9)) is defined as the maximum value of the square-integrated velocity (4.6b) (for \mathcal{T}_v) or the stress (4.6c) (for \mathcal{T}_{xx}) in the y -direction,

$$\int_{-1}^1 \mathbf{v}^\dagger(y) \mathbf{v}(y) \, dy, \quad \int_{-1}^1 \tau_{xx}^\dagger(y) \tau_{xx}(y) \, dy, \quad (4.10)$$

for any square-integrable body force (\mathbf{d} in (4.5a)) of a unit $L^2[-1, 1]$ norm,

$$\|\mathbf{d}\|_2^2 := \int_{-1}^1 \mathbf{d}^\dagger(y) \mathbf{d}(y) \, dy. \quad (4.11)$$

where $\|\cdot\|_2$ is the $L^2[-1, 1]$ norm, and $(\cdot)^\dagger$ is the adjoint [6, 16]. Observe that the square-integrated velocity in (4.10) yields the kinetic energy of velocity perturbations integrated over $y \in [-1, 1]$,

$$\int_{-1}^1 \mathbf{v}^\dagger(y) \mathbf{v}(y) \, dy = \int_{-1}^1 |u(y)|^2 + |v(y)|^2 + |w(y)|^2 \, dy. \quad (4.12)$$

Linear nonmodal analysis generally studies a perturbation integrated in the y -direction as a measure (as in (4.10)) of amplification [90, 6, 16].

The resolvent norm is given by the principal singular value of \mathcal{T} [6, 33], and is formally defined as

$$\max_{\mathbf{d} \in \mathbb{H}^{3 \times 1}, \mathbf{d} \neq 0} \frac{\|\mathcal{T}(\omega) \mathbf{d}\|_2}{\|\mathbf{d}\|_2} = \sigma_0[\mathcal{T}], \quad (4.13)$$

where \mathbb{H} is the set of square-integrable functions. The principal singular value is computed using a singular value decomposition (SVD) of \mathcal{T} . Details of how we compute an SVD of \mathcal{T} are deferred to § 4.3. We will now discuss quantities obtained from an SVD of \mathcal{T} , and their physical interpretations.

The SVD of $\mathcal{T}_{\mathbf{v}}$ in (4.8a) yields the singular values σ , body forces, and velocities such that [33]

$$\sigma \hat{\mathbf{v}}(y) = [\mathcal{T}_{\mathbf{v}}(\omega) \hat{\mathbf{d}}(\cdot)](y). \quad (4.14)$$

where $\hat{\mathbf{v}}$ and $\hat{\mathbf{d}}$ are quantities with a unit $L^2[-1, 1]$ norm (4.11). Expression (4.14) implies that a body force $\hat{\mathbf{d}}$ acting on $\mathcal{T}_{\mathbf{v}}$ results in a $\hat{\mathbf{v}}$ with an amplification of magnitude σ . Comparing (4.8a) and (4.14), the velocity that results from the body force $\hat{\mathbf{d}}$ in (4.14) is given by,

$$\mathbf{v}(y) = \sigma \hat{\mathbf{v}}(y). \quad (4.15)$$

Taking an $L^2[-1, 1]$ norm (4.11) on both sides of (4.15) we have

$$\|\mathbf{v}\|_2^2 = \sigma^2 \|\hat{\mathbf{v}}\|_2^2 = \sigma^2, \quad (4.16)$$

where the last equality in (4.16) holds as $\hat{\mathbf{v}}$ has a unit $L^2[-1, 1]$ norm (4.11). Thus from (4.16) and (4.14), the square of the largest (principal) singular value gives the maximum possible value of the kinetic energy of velocity fluctuations integrated in the y -direction ($\|\mathbf{v}\|_2^2$ in (4.12), also see (4.11)) for any square-integrable body force of a unit $L^2[-1, 1]$ norm (4.11) (for a rigorous proof that the largest singular value is the resolvent norm (4.13), see [34]).

Similar to (4.14)-(4.16), the SVD of \mathcal{T}_{xx} in (4.8b) yields the singular values σ , body forces, and stress functions such that [33],

$$\sigma \hat{\tau}_{xx}(y) = [\mathcal{T}_{xx}(\omega) \hat{\mathbf{d}}(\cdot)](y), \quad (4.17)$$

where $\hat{\tau}_{xx}$ is a quantity with a unit $L^2[-1, 1]$ norm. Similar to (4.15), we have by using (4.8b) and (4.17)

$$\tau_{xx}(y) = \sigma \hat{\tau}_{xx}(y), \quad (4.18)$$

and taking an $L^2[-1, 1]$ norm (4.11) on both sides of (4.18) we arrive at

$$\|\tau_{xx}\|_2^2 = \sigma^2 \quad (4.19)$$

From (4.17) and (4.19), the largest singular value from the SVD of \mathcal{T}_{xx} gives the maximum possible value of the square-integrated stress (4.10), for any square-integrable body force of a unit $L^2[-1, 1]$ norm [33].

4.2.4 Localized amplification

As we discussed, nonmodal analysis quantifies amplification using the velocity or the stress that is square-integrated in the y -direction (see (4.10)). However, this measure may be misleading in viscoelastic fluids where the stress may have localized amplification over a small region in the channel (as we discussed in Figure 4.1). We observe that localized amplification occurs in $\hat{\tau}_{xx}$ computed from the SVD (4.17) with the stress as the output.

A quantity that is square-integrated in y is not a good measure for quantities that are locally amplified in y . We illustrated an example of this using the Gaussian function (4.1) in Figure 4.1. The Gaussian function (4.1) attains larger magnitudes with a smaller standard deviation, α , and no matter how large its magnitude, its integration in y is of always of a unit magnitude (see (4.2)).

According to nonmodal theory, perturbation amplification (square-integrated in y) acts as finite-amplitude perturbation to trigger a nonlinear flow state [16, 90, 6]. Similarly, we hypothesize that localized amplification over a small region in y may act as a finite-amplitude perturbation as well. In this paper we quantify localized amplification as,

$$\mathbf{v}(y^*) := |\mathbf{v}(y)|_{\max}, \quad \tau_{xx}(y^*) := |\tau_{xx}(y)|_{\max}, \quad (4.20)$$

where y^* is the location at which the maximum occurs for a given body force. In this paper we refer to “localized amplification” when we quantify amplification in terms of (4.20) and to “nonmodal amplification” or “square-integrated amplification” when we refer to amplification in terms of quantities square-integrated in the y -direction (as in (4.10)).

Prior works on nonmodal analysis [20, 21, 22, 5, 36] show that the maximum (square-integrated-in- y) nonmodal amplification (as in (4.10)) results from a system where $k_x = 0$ in (4.6). System (4.6) when $k_x = 0$ is frequently referred as the two-dimensional three-component (2D3C) model in the literature [94, 21, 22, 5, 36]. However, we find that localized amplification (as defined in (4.20)) is more prominent in the 2D system, which is derived by setting $k_z = 0$ in (4.6), and restricting the stress tensor, velocity, and body force vectors to the (x, y) -plane.

We compare results from standard nonmodal analysis and our analysis based on localized amplification (see (4.20)) by comparing results from the 2D3C model (which exhibits the largest nonmodal amplification [20, 21, 22, 5, 36]) with the 2D model (which has large localized amplification (4.20)) in § 4.4. In this paper we only consider these two systems and do not consider the full 3D system owing to numerical limitations (see Chapter 3).

4.3 Numerical methods

The SVD of \mathcal{T} in (4.9) is determined by using an eigenvalue decomposition [72, 4]

$$\begin{bmatrix} 0 & \mathcal{B}\mathcal{B}^\dagger \\ \mathcal{C}^\dagger\mathcal{C} & 0 \end{bmatrix} \begin{bmatrix} \phi \\ \psi \end{bmatrix} = \gamma \begin{bmatrix} \mathcal{A} & 0 \\ 0 & \mathcal{A}^\dagger \end{bmatrix} \begin{bmatrix} \phi \\ \psi \end{bmatrix}, \quad (4.21)$$

where we suppress the dependence on $\{\kappa, \omega, We, \beta, y\}$ for brevity, and the eigenvalues $\gamma = \pm \sigma$ yield the singular values, and ψ is the vector of adjoint variables corresponding to ϕ in (4.6).

The eigenvalue problem (4.21) consists of differential (infinite-dimensional) operators that act on continuous functions, ϕ and ψ . The operators in (4.21) are discretized using two well-conditioned spectral methods: the spectral integration method [27, 28], and the ultraspherical method [26]. We now briefly discuss spectral methods and their well-conditioned variants.

Spectral methods express a variable in a differential equation in a basis of orthogonal

polynomials like the Chebyshev polynomials, e.g.,

$$u(y) = \sum_{i=0}^{\infty}{}' u_i T_i(y), \quad (4.22)$$

where u_i are the unknown spectral coefficients to be solved for, $T_i(y)$ are the i th Chebyshev polynomials of the first kind, and \sum' denotes a summation whose first term is halved (this convention is commonly used in a Chebyshev basis [29, 28]).

Expressions for higher derivatives of the variable $u(y)$ are derived by using a Chebyshev differentiation operator [28]. The differentiation operator produces ill-conditioned matrix approximations to differential operators in (4.21) [29] that produce erroneous results for calculations of the resolvent norm (4.13) at moderate to large We [33] (also see Chapter 3).

The recent well-conditioned ultraspherical [26] and spectral integration [27] methods avoid using the differentiation operator. For example, the spectral integration method avoids the differentiation operator by expressing the highest derivative in a differential equation in a Chebyshev basis, and expressing lower derivatives by using an integration operator. The highest derivative of u in (4.5) is of second order, hence the second-derivative of u is expressed as

$$\frac{d^2 u}{dy^2} = \sum_{i=0}^N{}' u_i^{(2)} T_i(y). \quad (4.23)$$

Expressions for lower derivatives of u in (4.23) are derived using the recurrence relation for the integration of Chebyshev polynomials [28],

$$\frac{du}{dy} = \sum_{i=0}^N{}' u_i^{(1)} T_i(y) + c_0, \quad (4.24)$$

where c_0 is a constant of integration and

$$u_i^{(1)} = \begin{cases} \frac{1}{2i} (u_{i-1}^{(2)} - u_{i+1}^{(2)}), & 0 < i < N, \\ \frac{1}{2} u_1^{(2)}, & i = 0, \\ \frac{1}{2N} u_{i-1}^{(2)}, & i = N. \end{cases} \quad (4.25)$$

The constants of integration can be computed using the boundary conditions in (4.5d).

Similarly, the ultraspherical method expresses a variable and its derivatives in a basis of ultraspherical polynomials [26],

$$\frac{d^n u}{dy^n} = \sum_{k=1}^N k u_k^{(n)} \frac{d^{n-1} C_{k-1}^{(1)}(y)}{dy^{n-1}}, \quad (4.26)$$

where $C_k^{(\alpha)}$ is the k th ultraspherical polynomial of the α kind. The derivatives of ultraspherical polynomials in (4.26) are related through the recurrence relation [26],

$$\frac{dC_k^{(\alpha)}}{dy} = \begin{cases} 2\alpha C_{k-1}^{(\alpha+1)}, & k \geq 1, \\ 0, & k = 0, \end{cases} \quad (4.27)$$

which forms a well-conditioned mapping between the variable and its derivatives, unlike the differentiation operator used in conventional spectral methods [26].

The spectral integration method is implemented in **Matlab** (see Chapter 3 and supplementary material, § H) to derive finite-dimensional approximations to (4.21) in both the evolution and descriptor forms (see (4.6) and Appendix E). The ultraspherical discretization in Chebfun [31, 26] is used to derive a finite-dimensional approximation in the evolution form (see Appendix E.1). As these well-conditioned methods are relatively new, we are currently not aware of how to use the ultraspherical method with the descriptor form. For all calculations reported in this paper, the corresponding velocity and stress from the SVD (see (4.14) and (4.17)) are resolved to machine precision by using up to 15,000 basis functions with these well-conditioned spectral methods.

These two approaches (evolution form with the ultraspherical method, descriptor and evolution forms with the spectral integration method, see (4.6) and Appendix E) produce the same singular values (a few representative validations are relegated to

Appendix F), confirming the accuracy of our results. Furthermore, at large We for 2D3C Couette flow, our results agree with the We and We^2 scaling of the velocity \mathbf{v} and stress τ_{xx} singular values (relegated to Appendix F) reported in Figures 3 and 4 of [5].

4.4 Localized and square-integrated amplification of the stress

In this section, we establish that although the square-integrated amplification (see (4.10)) is the largest in the 2D3C system [20, 22, 5, 36], localized amplification (as defined in (4.20)) in the channel is larger in the 2D system. We will consider square-integrated amplification in inertialess plane Poiseuille flow in § 4.4.1, and localized amplification in § 4.4.2.

4.4.1 Square-integrated amplification

Figure 4.3 shows the principal singular value as a function of We for 2D3C Poiseuille flow ($k_x = 0$, $k_z = 1$) of an Oldroyd-B fluid with $\beta = 0.5$, and $\omega = 0$. Figure 4.3a shows the velocity singular values obtained from the SVD of \mathcal{T}_v in (4.14), and we notice a linear growth with We when $We > \sim 20$ (the dashed line shows the slope of the scaling with We). Note that the singular value is a square-integrated-in- y measure of the velocity or the stress, as we discussed in § 4.2.3 (see (4.10), (4.16) and (4.19)).

Figure 4.3b shows the stress singular values obtained from the SVD of \mathcal{T}_{xx} , see (4.17). We observe in Figure 4.3b that the stress singular values grow quadratically with We (on a log-log plot, the dashed line shows the slope of the scaling with We) for $We > \sim 4$. The We and We^2 scaling of the velocity and stress singular values in Figures 4.3a and 4.3b respectively are in agreement with the scaling arguments of Jovanović and Kumar in Figures 3 and 4 of [5].

Figure 4.4 shows the principal singular values as a function of We for 2D Poiseuille flow ($k_x = 1$, $k_z = 0$) with the same parameters as in Figure 4.3, i.e., $\beta = 0.5$, and $\omega = 0$. Figure 4.4a shows the velocity singular values computed from the SVD of \mathcal{T}_v in (4.14). We observe in Figure 4.4a that the singular values grow at small We ($< \sim 5$) and decay at large We . As discussed in § 4.2.3 (see (4.12)), the principal singular value

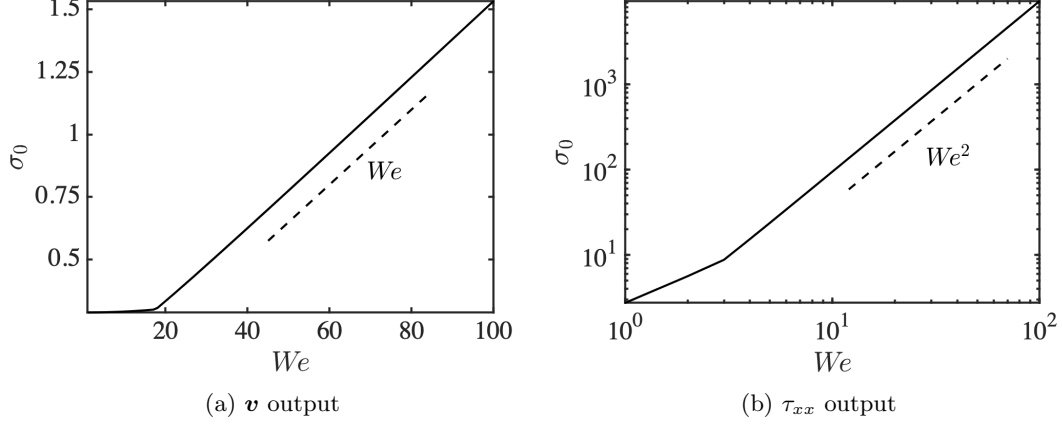


Figure 4.3: Principal singular values of (a) \mathcal{T}_v in (4.14) and (b) \mathcal{T}_{xx} in (4.17) of 2D3C Poiseuille flow of an Oldroyd-B fluid with $\beta = 0.5$, $k_z = 1$, and $\omega = 0$. The solid lines mark singular values, and the dashed lines show the slope of their scaling with We .

gives the maximum possible kinetic energy of the velocity perturbations for any square-integrable body force, and we see in Figure 4.4a that this maximum possible kinetic energy decreases with an increase in the elasticity of the fluid, We .

However, the stress singular values in Figure 4.4b (the maximum possible square-integrated stress (4.10)) computed from the SVD of \mathcal{T}_{xx} in (4.17) show a different trend. The singular values grow with an increase in We until $We \sim 20$ and then plateau at large We . The dashed line in Figure 4.4b shows the value of σ_0 when $We = 500$, implying that there is no significant variation of the principal singular values of \mathcal{T}_{xx} in (4.17) at large We .

When we compare Figures 4.4a and 4.4b, we observe that the maximum possible (square-integrated) velocity decreases with an increase in the elasticity of the fluid, whereas the maximum possible (square-integrated) stress increases and plateaus with an increase in the elasticity of the fluid. Thus with an increase in the elasticity, the disparity between the square-integrated velocity and stress increases. This observation is tied to the theme of this paper, that the stress can have large amplification even with a relatively weak magnitude of the velocity for a small-amplitude body force. We defer the relevance of this observation to experiments by Qin et al. [9] until later in § 4.4.3. For now, we focus on the relative importance of the 2D3C singular values in Figure 4.3

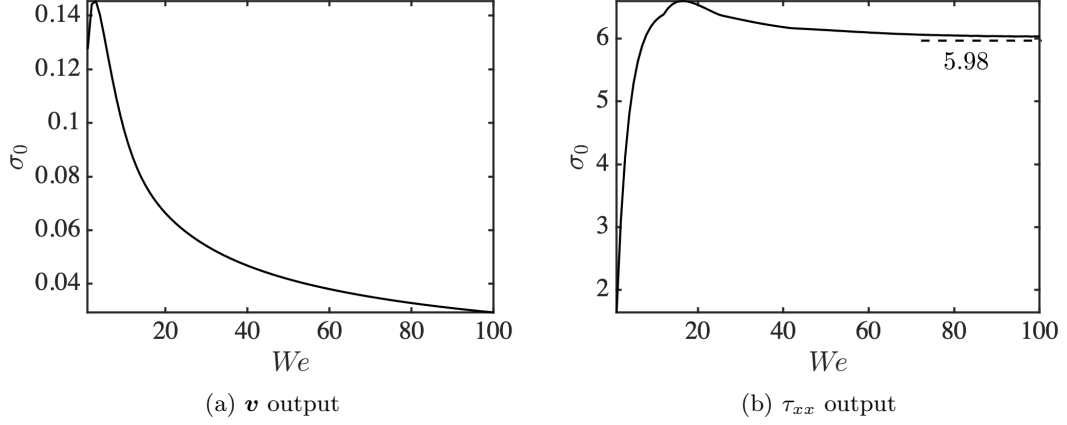


Figure 4.4: Principal singular values of (a) $\mathcal{T}_{\mathbf{v}}$ in (4.14) and (b) \mathcal{T}_{xx} in (4.17) of 2D Poiseuille flow of an Oldroyd-B fluid with $\beta = 0.5$, $k_x = 1$, and $\omega = 0$. The solid lines mark singular values, and the dashed line in (b) shows the magnitude of the singular value when $We = 500$.

and the 2D singular values in Figure 4.4.

From the perspective of nonmodal analysis, the 2D3C case in Figure 4.3 has a square-integrated-in- y velocity and stress (i.e., singular values, see (4.10), (4.16) and (4.19)) that scale as We and We^2 respectively. However, in the 2D case in Figure 4.4 the square-integrated-in- y velocity and stress have no scaling with We . Therefore the 2D3C system has larger “nonmodal amplification” at large We , where the measure is in terms of the singular value, a quantity that refers to a square-integrated velocity or stress (see (4.10), (4.16) and (4.19)). However, the analysis reverses if we observe from the perspective of localized amplification (see (4.20) and Figure 4.1) over a small region in $y \in [-1, 1]$ (i.e., without square-integrating in y) as we will see in the section that follows.

4.4.2 Localized amplification

Figure 4.5a shows $\hat{\tau}_{xx}$ (see (4.18) and (4.19)) corresponding to the principal singular value with $We = 100$ from Figure 4.3b (2D3C with $\beta = 0.5$, $k_z = 1$, and $\omega = 0$), Figure 4.5b shows $\hat{\tau}_{xx}$ corresponding to the principal singular value with $We = 100$ from Figure 4.4b (2D with $\beta = 0.5$, $k_x = 1$, and $\omega = 0$). Figure 4.5c enlarges the region

near $y = 1$ in Figure 4.5b for clarity.

In Figure 4.5a, the principal singular value for the 2D3C case ($\sigma_0 = 9422.386$) is about a thousand times greater than the 2D case ($\sigma_0 = 6.033$) in Figures 4.5b and 4.5c. However, the peak magnitude of the stress for the 2D3C case in Figure 4.5a (see (4.17) and (4.20)) is $\sigma_0 |\hat{\tau}_{xx}|_{\max} \approx 9422.386 \times 0.01 = 94.22$. In contrast, for the 2D case in Figures 4.5b and 4.5c (see (4.17) and (4.20)) $\sigma_0 |\hat{\tau}_{xx}|_{\max} \approx 6.033 \times 300 = 1809.00$; this is about twenty times more significant compared to the 2D3C case.

In Figure 4.5, both, the 2D3C and the 2D cases have their optimal body forces of unit $L^2[-1, 1]$ norms (4.11), but the 2D system generates larger localized amplification compared to the 2D3C system under the same conditions. Therefore, we conclude from Figure 4.5 that if we measure amplification in terms of localized amplification (4.20) in the place of quantities that are square-integrated in y (as in (4.10)), the 2D system in this case produces larger stress amplification with small-amplitude body forces compared to the 2D3C system.

Nonmodal analysis considers that small-amplitude body forces result in large velocity or stress amplification that may act as a finite-amplitude initial condition to trigger a nonlinear flow state [41, 89]. If this were the case, then the stress that results from small-amplitude body forces on the 2D system is more likely to trigger a transition to elastic turbulence compared to the 2D3C system as localized amplification is larger in the 2D system. Moreover, note that this large localized stress amplification in Figures 4.5b and 4.5c occurs simultaneously with a relatively weak magnitude of velocity amplification as seen in Figure 4.4a.

Figures 4.6a and 4.6b show the components of the velocity $\mathbf{v} = [u \ v]^T$ corresponding to the SVD of \mathcal{T}_{xx} (4.17) in Figures 4.5b and 4.5c (2D with $We = 100$, $\beta = 0.5$, $k_x = 1$, and $\omega = 0$). Observe from the y -axis of Figures 4.6a and 4.6b that the magnitude of the velocity is of $\mathcal{O}(0.1)$ which is weaker by about 5 orders of magnitude compared to the stress in Figure 4.5b ($\sigma_0 |\hat{\tau}_{xx}|_{\max} \approx 6.023 \times 300 = 1809$ in Figure 4.5b, compared to $\mathcal{O}(0.1)$ magnitude of $\mathbf{v} = [u \ v]^T$ in Figures 4.6a and 4.6b). Note that the velocity shown in Figures 4.6a and 4.6b is not normalized to have a unit $L^2[-1, 1]$ norm (4.11).

Figures 4.6c and 4.6d show the x - and y -components of the body force that induce the velocity fields in Figures 4.6a and 4.6b, and the stress in Figures 4.5b and 4.5c. The magnitude of the x -component of the body force in Figure 4.6c is significantly larger

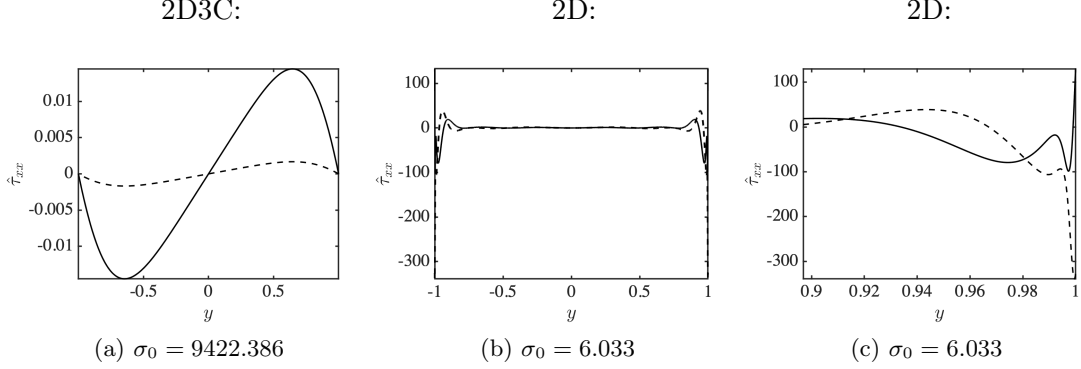


Figure 4.5: The quantity $\hat{\tau}_{xx}$ (see (4.18)) corresponding to the principal singular value from the SVD of \mathcal{T}_{xx} in (4.17) of inertialess (a) 2D3C ($k_z = 1$), and (b,c) 2D ($k_x = 1$) Poiseuille flow of an Oldroyd-B fluid with $We = 100$, $\beta = 0.5$, and $\omega = 0$. Solid lines mark the real parts and the dashed lines mark the imaginary parts of $\hat{\tau}_{xx}$. Figure (c) enlarges (b) near $y = 1$.

compared to the y -component in Figure 4.6d. However, we observe a similarity between the two components of the body force in Figures 4.6c and 4.6d in that they are locally amplified near $y = \pm 1$, which are the same locations where localized amplification occurs in the stress in Figures 4.5b and 4.5c.

Lastly, in Figure 4.7 we plot contours of the steady-state kinetic energy $u^2 + v^2$ and the square of the stress τ_{xx}^2 in physical space that result from the body force shown in Figures 4.6c and 4.6d. Note that the persistent body force we use is of form (4.5e), which is localized in x and z . Plots in physical space are obtained by applying an inverse Fourier transform to the velocity and stress by linearly sampling 24 wavenumbers from $k_{x,\min} = -2.5$ to $k_{x,\max} = 2.29$. Red represents regions of high magnitude, and blue represents regions of low magnitude (as indicated in the color bars).

We observe in Figure 4.7a that the kinetic energy, $u^2 + v^2$, has a peak value near the channel center at $y = 0$ (of $\mathcal{O}(10^{-3})$ from the color bar). This agrees with observations in Figures 4.6a and 4.6b where the magnitude of the velocity in Fourier space is the largest near the channel center ($y = 0$) and smaller near the channel walls ($y = \pm 1$). Figures 4.7b, 4.7c and 4.7d consider the steady-state square of the stress, τ_{xx}^2 . Figure 4.7b is almost entirely blue which corresponds to near zero squared stress (as indicated in the color bar). This is because large magnitudes of the stress are localized in regions near the walls (i.e., near $y = \pm 1$). This can be observed in Figures 4.7c and 4.7d,

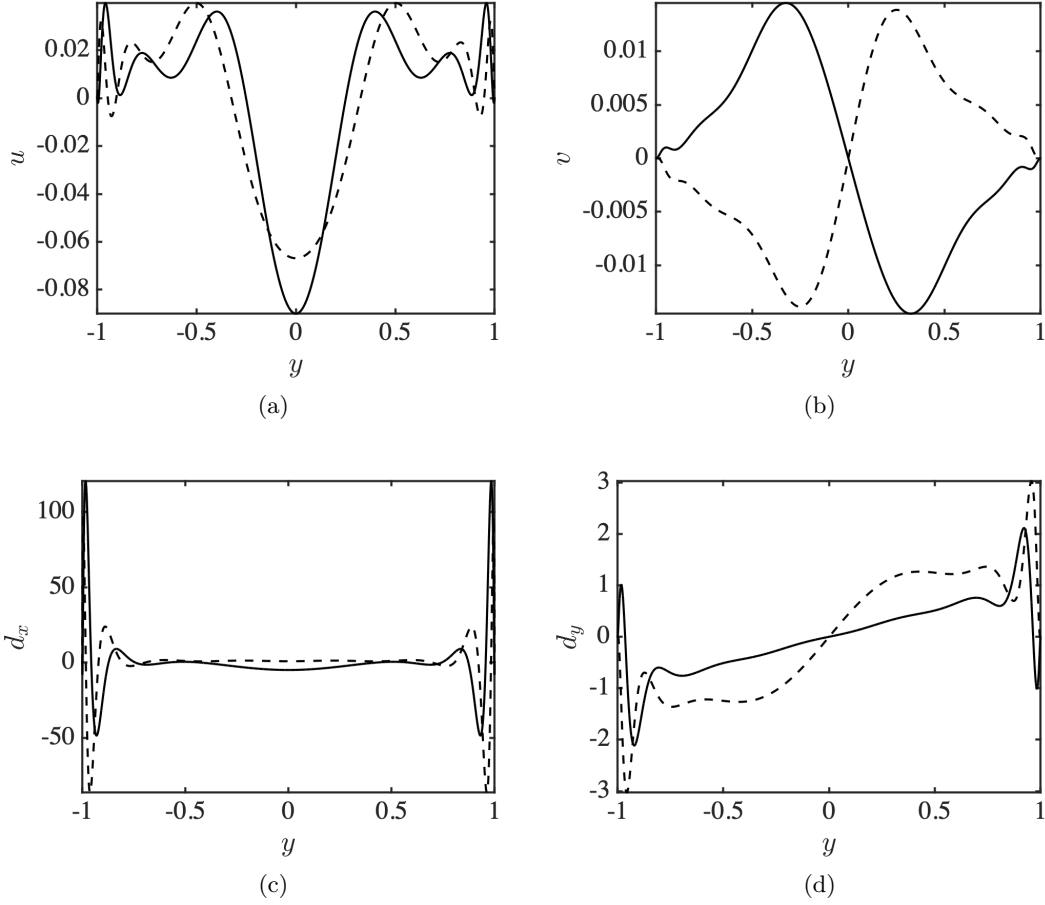


Figure 4.6: The (a,b) velocity components $\mathbf{v} = [u \ v]^T$ respectively, and (c,d) x - and y -components of the body force \mathbf{d} corresponding to the principal singular value from the SVD of \mathcal{T}_{xx} in (4.17) of 2D Poiseuille flow of an Oldroyd-B fluid with $We = 100$, $\beta = 0.5$, $k_x = 1$, and $\omega = 0$. The solid lines mark the real parts and the dashed lines mark the imaginary parts of the velocity and body force vectors.

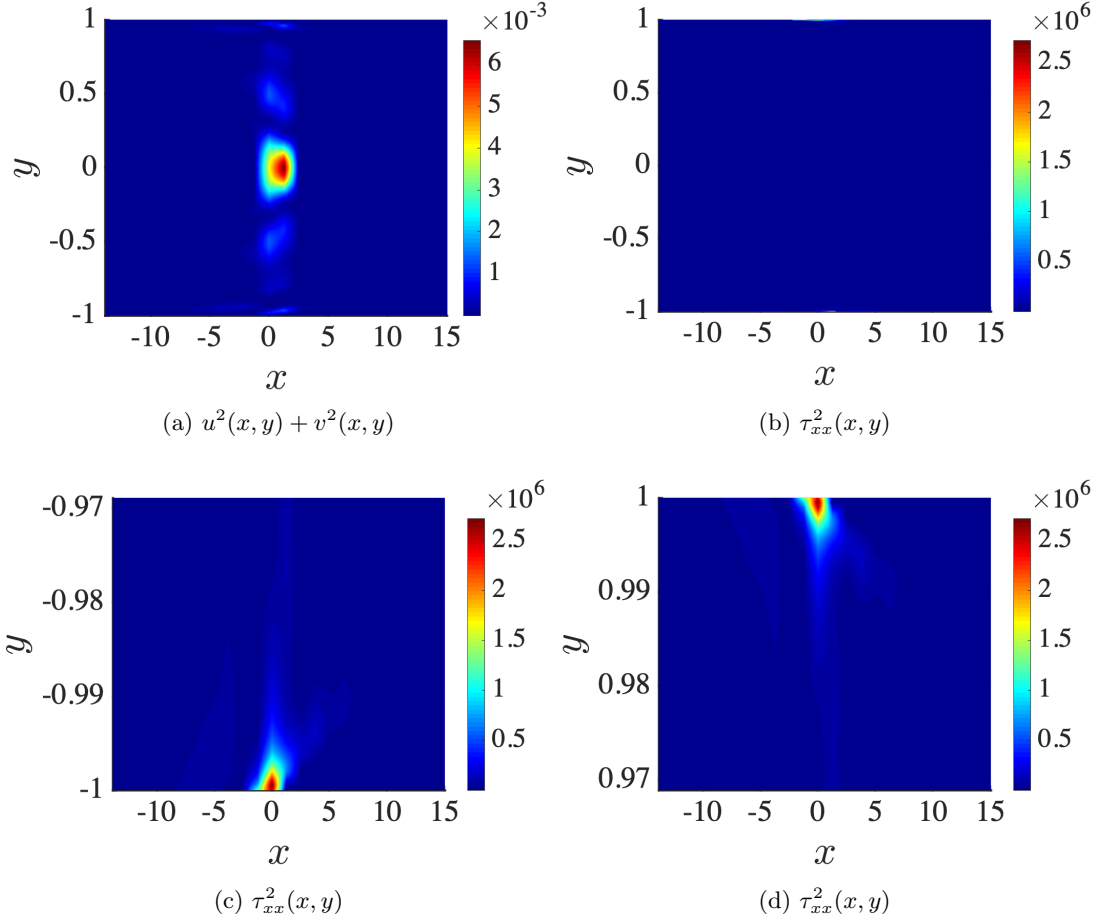


Figure 4.7: The steady-state (a) kinetic energy $u^2 + v^2$, and (b,c,d) squared stress τ_{xx}^2 that result from a persistent body force of the form in (4.5e) with a frequency $\omega = 0$, and a variation in y shown in Figures 4.6c and 4.6d in the 2D system of (4.5), with $We = 100$ and $\beta = 0.5$. Figure (c) enlarges (b) near $y = -1$, and Figure (d) enlarges (b) near $y = 1$. Plots in physical space are obtained by applying an inverse Fourier transform to the velocity and stress by linearly sampling 24 wavenumbers from $k_{x,\min} = -2.5$ to $k_{x,\max} = 2.29$, and using 6000 Chebyshev basis functions in the y -direction.

where Figure 4.7b is enlarged in the regions near $y = -1$ and $y = +1$ respectively.

We observe from the color bars in Figures 4.7b, 4.7c and 4.7d that the steady-state squared stress reaches a value of $\mathcal{O}(10^6)$. This large value is prominent near the channel wall at $y = \pm 1$ as seen in Figures 4.7c and 4.7d. Furthermore, the steady-state kinetic energy ($\mathcal{O}(10^{-3})$ in Figure 4.7a) and the square of the stress ($\mathcal{O}(10^6)$ in Figures 4.7b, 4.7c and 4.7d) have a disparity of about nine orders of magnitude. This observation may provide an alternative linear mechanism for the transition to elastic turbulence reported by Qin et al. [9].

4.4.3 A potential mechanism: Flow transition via localized amplification

Qin et al. [9] observed a transition to elastic turbulence in a microfluidic channel at a Reynolds number ~ 0.01 . They induced perturbations into the channel using instabilities that arise from cylindrical obstructions. We know from previous experimental and theoretical studies [86] that the velocity field downstream of a single cylinder is a periodic function of time, and we argued in § 4.1.1 and § 4.2.1 that if the instability induced by the cylinders is considered a small-amplitude perturbation on the rest of the channel downstream [8], and if the velocity is assumed to be a sinusoidal function of time, then an equivalent body force is a sinusoidal function of time as well [87, 6].

The body force we consider is not induced by a finite-sized object like a cylinder. However, the body force is nearly localized (see (4.5e), and Figures 4.6c and 4.6d), and is a periodic function of time. The key observation we make for such forces is that there is a large disparity between the magnitudes of the velocity (Figure 4.7a) and the stress (Figures 4.7b, 4.7c and 4.7d). Qin et al. [9] observe that the kinetic energy first decreases along the channel length (see Figure 3, inset, in reference [9]), and then undergoes an increase at large channel lengths.

A potential mechanism for this puzzling observation (as in general, a transition to a nonlinear state occurs with a strong growth of velocity perturbations [6, 15]) is that *the stress could have significant localized amplification and act as a finite-amplitude perturbation (see (4.20)) even when there is relatively weak kinetic energy growth* (like the kinetic energy in Figure 4.7a relative to the stress in Figures 4.7b, 4.7c and 4.7d).

Therefore although the kinetic energy decreases along the channel length in the observations of Qin et al. (Figure 3, inset, in reference [9]), the magnitude of the stress may have been significantly larger and act as a finite-amplitude perturbation to trigger a nonlinear flow state [41, 89].

In related numerical simulations, Grilli et al. [95] considered the fully nonlinear, nearly inertialess ($Re = 2.4 \times 10^{-2}$, $\beta = 0.5$, and $We = 1.3$) 2D flow of an Oldroyd-B fluid around a linear array of cylinders. The cylinders were separated by a distance 2.5 times their radius. They observe similar steep stress gradients as in Figures 4.7b, 4.7c and 4.7d generated by cylindrical obstructions in viscoelastic channel flow (see Figure 4 in [95]). Furthermore, the flow was observed to transition to a nonlinear flow state [95].

We observe these steep stress gradients generated from the simplified linearized inertialess 2D model of the Oldroyd-B equations subject to a body force which is nearly localized in space and a harmonic function of time (§ 4.2.1 (4.5e), and Figures 4.6c and 4.6d). We further note that similar arguments were made on the importance of localized stress amplification in ref. [96] for low-inertia ($Re \sim 100$) transition to turbulence in viscoelastic channel flows.

In this section we compared the velocity and stress amplification generated from the 2D and 2D3C systems and showed that although the square-integrated amplification is the largest in the 2D3C system, localized amplification is larger in the 2D system (Figure 4.5). We point out that this localized amplification (see (4.20)) may act as a finite-amplitude perturbation to trigger a nonlinear flow state. In the next section, we show that this localized amplification originates from the continuous spectrum (4.7c), and we identify the location where this localized amplification of the stress (see (4.20)) occurs in the channel for a given frequency of the body force, ω (4.5e), and spatial wavenumber $k_x = 1$.

4.5 Mechanisms for localized amplification

4.5.1 The role of the continuous spectrum

In this section we demonstrate that localized amplification of the stress in Figures 4.5b and 4.5c is related to the continuous spectrum $\lambda(y) = -i k_x \bar{U}(y) - 1/We$ (see § 4.2.1, (4.7c)).

Note that the continuous spectrum reverts to a discrete eigenvalue $\lambda = -1/We$ by setting $k_x = 0$ in (4.7c). We start by looking at the expression for τ_{xx} .

The expression for τ_{xx} from (4.6c) (see Appendix E, (E7)) for the full 3D system is given by

$$\tau_{xx} = c_{1,11}Du + c_{0,11}u + c_{1,12}Dv + c_{0,12}v, \quad (4.28)$$

where $D := d/dy$. Note that the expression of τ_{xx} in (4.28) is the same for the 2D system (this is true as (4.28) is k_z - and w -independent, where w is the z -component of \mathbf{v}), and the expression of τ_{xx} for the 2D3C system in (4.28) can be derived by setting $k_x = 0$. Let us consider the first term, $c_{1,11}$ in (4.28),

$$c_{1,11}Du = \frac{2(We c(y)\bar{T}_{xy}(y) + \bar{U}'(y))}{We c(y)^2}Du. \quad (4.29)$$

So far no assumption is made about 2D or 2D3C in (4.29), and

$$c(y) = i\omega + 1/We + i k_x \bar{U}(y). \quad (4.30)$$

Note that $c(y) = i\omega - \lambda(y)$ where $\lambda(y)$ is the continuous spectrum (see (4.7c)). Also, the expression for τ_{xx} in (4.28), and hence (4.29), is k_z - and β -independent to begin with.

Equation (4.29) can be rearranged as

$$c_{1,11}Du = \underbrace{\frac{2\bar{T}_{xy}(y)}{i\omega + \frac{1}{We} + i k_x \bar{U}(y)}}_{g_1(y,\omega,k_x,We)} Du + \underbrace{\frac{2\bar{U}'(y)}{We(i\omega + \frac{1}{We} + i k_x \bar{U}(y))^2}}_{g_2(y,\omega,k_x,We)} Du. \quad (4.31)$$

In (4.31), \bar{T}_{xy} and $\bar{U}'(y)$ are the same, i.e., $\bar{T}_{xy} = \bar{U}'(y)$ (see (4.4)), but we retain them separately to isolate their influence on τ_{xx} . The contribution from \bar{T}_{xy} in (4.31) comes from $\bar{\mathbf{T}} \cdot \nabla \mathbf{v}$ in (4.5c), and that from $\bar{U}'(y)$ in (4.31) comes from $\boldsymbol{\tau} \cdot \nabla \bar{\mathbf{V}}$ in (4.5c).

We next plot g_1 in (4.31) to understand its role in generating localized amplification in τ_{xx} (in (4.28), see Figures 4.5b and 4.5c). Figure 4.8 shows g_1 under the same conditions as Figure 4.5 for τ_{xx} , i.e., with $We = 100$, $k_x = 1$, and $\omega = 0$. Note that g_1 in (4.31) is k_z - and β -independent.

We observe in the 2D case ($k_x = 1$) in Figures 4.8a and 4.8b that g_1 shows localized

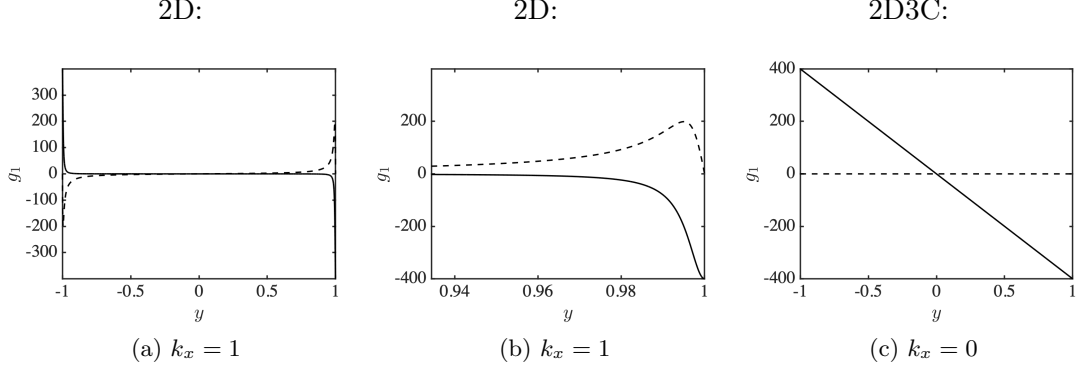


Figure 4.8: The function g_1 in (4.31) with $We = 100$, and $\omega = 0$ (a,b) $k_x = 1$, and (c) $k_x = 0$. The solid lines mark the real parts and the dashed lines mark the imaginary parts of g_1 in (4.31). Figure (b) enlarges (a) near $y = 1$.

amplification near $y = \pm 1$. Figure 4.8b enlarges Figure 4.8a near $y = 1$ for clarity, and we observe that g_1 has a maximum magnitude of about ~ 400 . Furthermore, the locations of localized amplification $y = \pm 1$ (see (4.20)) of $\hat{\tau}_{xx}$ in Figures 4.5b and 4.5c is the same as that for g_1 in Figures 4.8a and 4.8b.

In Figure 4.8c we plot g_1 for the 2D3C case ($k_x = 0$, in which case, $g_1(y) = -2We\bar{U}'(y)$), and we observe a smooth function without prominent localized amplification. This is again similar to the 2D3C case in Figure 4.5a, where τ_{xx} is a smooth function without prominent localized amplification.

To recapitulate, we are interested in answering why localized amplification occurs in the stress in Figures 4.5b and 4.5c, and we found that the function g_1 in the expression for τ_{xx} in (4.31) has similar localized amplification as τ_{xx} itself (in Figures 4.8a and 4.8b). We can extract information about the locations of localized amplification from g_1 in (4.31). This is easier to do with g_1 as it is a simpler function compared to the full expression for the stress in (4.28).

Two questions arise by observing g_1 as a function of y in Figure 4.8: (a) What causes localized amplification of g_1 in (4.31)? (b) For any ω , does localized amplification occur at the same locations for g_1 in (4.31) and τ_{xx} in (4.28)?

We attempt to answer these questions next. Answers to the above questions allow us to identify where localized stress amplification happens in the channel, for a given frequency of the body force (4.5e), ω . As we discussed in § 4.1.1 and § 4.2.1, the body

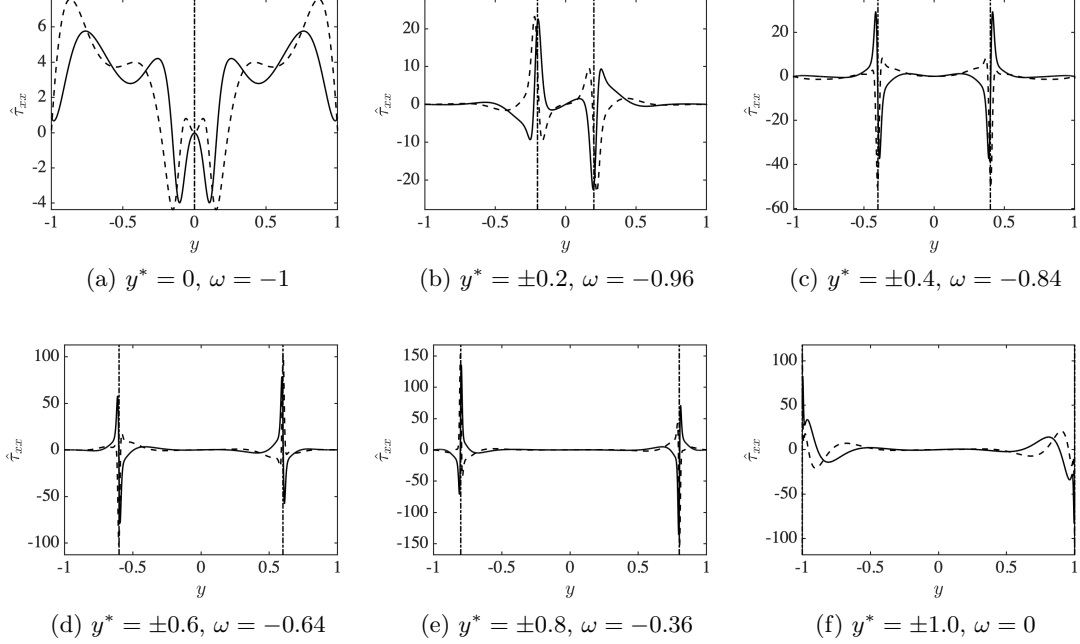


Figure 4.9: Stress τ_{xx} corresponding to the principal singular value from the SVD of \mathcal{T}_{xx} in (4.17) with $We = 40$, $\beta = 0.5$, and $k_x = 1$, and (a) $y^* = 0$, (b) $y^* = \pm 0.2$, (c) $y^* = \pm 0.4$, (d) $y^* = \pm 0.6$, (e) $y^* = \pm 0.8$, and (f) $y^* = \pm 1$. For a given value of k_x and y^* , ω is calculated from (4.33). The solid lines mark the real parts and the dashed lines mark the imaginary parts of $\hat{\tau}_{xx}$. The dashed-dotted lines mark $y = \pm y^*$. Figure G4 (relegated to Appendix G) shows the region enlarged near $y = y^*$.

forces we consider are nearly localized in space, and are sinusoidal functions of time, which are similar to small-amplitude perturbations induced by finite-sized objects such as cylinders.

We first answer what causes localized amplification in g_1 in Figure 4.8. Separating the real and imaginary parts of g_1 in (4.31) we have

$$g_1(y) = \frac{2\bar{T}_{xy}(y)(1/We - i(\omega + k_x\bar{U}(y)))}{1/We^2 + (\omega + k_x\bar{U}(y))^2}. \quad (4.32)$$

The function g_1 in (4.32) reaches its largest magnitude when its denominator is at its minimum (for a finite numerator). As the denominator is a sum of two squares in (4.32),

it is minimized when

$$\omega + k_x \bar{U}(y^*) = 0, \quad (4.33)$$

where y^* is the location where the magnitude of g_1 in (4.32) is maximized.

This increase in the magnitude of g_1 with an increase in We happens at particular points $y = y^*$ in the channel that satisfy (4.33). This is consistent with the localized amplification observed in Figures 4.8a and 4.8b in the 2D case. However, observe that in the 2D3C case, when $k_x = 0$ in (4.33), we no longer have specific points y^* where the magnitude of g_1 in (4.31) is maximized. This is consistent with localized amplification is not being prominent in Figure 4.8c.

Furthermore we note that as $We \rightarrow \infty$, the minimum value of the denominator of (4.32) is 0, in which case $|\tau_{xx}|_{\max} \rightarrow \infty$ at specific points $y = y^*$ in the channel (from (4.33)). This corresponds to the infinite-extensibility of the polymer molecules [60]. Although the singular values were observed to plateau with large We in Figure 4.4b, the peak magnitude of the singular function, $|\hat{\tau}_{xx}|_{\max} \rightarrow \infty$ as $We \rightarrow \infty$. In contrast, for the 2D3C case when $k_x = 0$, there are no specific locations y^* for localized amplification (from (4.33)). However, the singular values (the square-integrated amplification, see (4.17)) themselves tend to infinity, $\sigma \rightarrow \infty$ as $We \rightarrow \infty$ as seen in Figure 4.3b.

Equation (4.33) identifies where localized amplification occurs (y^*) for a given value of ω and k_x in g_1 in (4.31). Note that this expression is valid for Couette flow as well. For example, for the case in Figure 4.8, substituting $\omega = 0$, $k_x = 1$, in (4.33), yields $y^* = \pm 1$ for plane Poiseuille flow, where y^* are the locations of localized amplification (see (4.20)), and this agrees with observations in Figures 4.8a and 4.8b (in fact, also for the stress in Figures 4.5b and 4.5c).

The feature in g_1 in (4.31) that induces localized amplification is the function $c(y)$ (see (4.30)) in its denominator, and localized amplification occurs at locations in the channel *where the imaginary part of $c(y)$, $\omega + k_x \bar{U}(y)$, is zero*. We did this analysis by considering one term, $c_{1,11}$ in (4.29) and on one function within this term, g_1 in (4.31). However, all functions, $c_{1,11}$, $c_{0,11}$, $c_{1,12}$, and $c_{0,12}$ in (4.28) contain $c(y)$ or its powers in the denominator (see (E8) in Appendix E) in a similar manner as g_1 in (4.31), and all of them have similar local amplification (as g_1 in Figures 4.8a and 4.8b) at locations y^*

where the imaginary part of $c(y)$ in (4.30) is zero for $k_x = 1$.

Thus far we answered the first question in relation to observations on Figure 4.8 as to why localized amplification occurs in g_1 in (4.31). As both g_1 in Figures 4.8a and 4.8b and the stress $\hat{\tau}_{xx}$ in Figures 4.5b and 4.5c have localized amplification at the same locations, $y^* = \pm 1$, we next examine if this trend is general for any ω by choosing different values of ω .

4.5.2 Locations of localized amplification

We pick several values of $y^* \in [-1, 1]$ in the channel, fix $k_x = 1$ (with $We = 40$ and $\beta = 0.5$) in Figure 4.9, and calculate ω from the relation in (4.33). We then use this value of ω and compute an SVD of \mathcal{T}_{xx} in (4.17). The solid and dashed lines mark the real and imaginary parts of $\hat{\tau}_{xx}$ corresponding to the principal singular value from the SVD of \mathcal{T}_{xx} in (4.17), and the dashed-dotted lines mark $y = y^*$. If the dashed-dotted lines, i.e., $y = y^*$ match with the locations where localized amplification occurs for $\hat{\tau}_{xx}$, we can conclude that relation (4.33) is valid for $\hat{\tau}_{xx}$.

We first consider the case when $y^* = 0$ and $k_x = 1$ and fix ω based on (4.33) in Figure 4.9a, and we observe that the dashed-dotted line, $y = y^*$ does not coincide with the location of localized amplification of $\hat{\tau}_{xx}$. Thus, when $y^* = 0$, (4.33) is not a valid expression for the location of localized amplification of $\hat{\tau}_{xx}$ (Figure 4.9a). In Figure 4.9b we consider $y^* = \pm 0.2$ and $k_x = 1$ and fix ω based on (4.33), and we observe that the dashed-dotted lines ($y = y^*$) and the locations of localized amplification (see (4.20)) of $\hat{\tau}_{xx}$ coincide. This implies that (4.33) is valid for the locations of localized amplification of $\hat{\tau}_{xx}$ in this case.

Similarly, in Figure 4.9c we choose $y^* = 0.4$ and $k_x = 1$ and fix ω based on (4.33); the locations of localized amplification (see (4.20)) in $\hat{\tau}_{xx}$ coincide with $y = y^*$ (the dashed-dotted lines), implying that (4.33) is valid for this case as well. Figures 4.9d-4.9f consider cases with $y^* = 0.6$, $y^* = 0.8$ and $y^* = 1.0$ respectively with $k_x = 1$. In every case, ω is computed from (4.33), and in every case, we observe that the locations of localized amplification (see (4.20)) of $\hat{\tau}_{xx}$ and $y = y^*$ (the dashed-dotted lines) coincide according to (4.33). For the purpose of clarity, the region near $y = y^*$ for all panels in Figure 4.9 is enlarged in Figure G4, Appendix G.

In summary, although the relationship in (4.33) identifies the locations of localized

amplification of the functions $c_{1,11}$, $c_{0,11}$, $c_{1,12}$, and $c_{0,12}$ in (4.28), it seems to be valid for the stress that result from an SVD of \mathcal{T}_{xx} in (4.17) for all ω , except when the resultant location is such that $y^* = 0$ (as the dashed-dotted line and the location of localized amplification do not match for this case in Figure 4.9a). We now discuss the reason $y^* = 0$ is an exception where the dashed-dotted lines and the locations of localized amplification of $\hat{\tau}_{xx}$ do not match in Figure 4.9a, unlike all other cases in Figure 4.9.

The exception when $y^* = 0$ in Figure 4.9a (where the dashed-dotted lines, $y = y^*$ do not coincide with the locations of local amplification (4.20) of $\hat{\tau}_{xx}$, unlike all other cases in Figure 4.9) can be understood by going back to the functions $c_{1,11}$, $c_{0,11}$, $c_{1,12}$, and $c_{0,12}$ in (4.28). For example, the function g_1 which is a function in $c_{1,11}$ in (4.31) is locally amplified according to (4.33), only when (4.32) has a finite numerator. However, when $y^* = 0$, its numerator becomes zero as $\bar{U}'(y^*) = -2y^*$.

Therefore g_1 (and hence $c_{1,11}$ in (4.28)) is not locally amplified when the numerator is zero, i.e., when $y^* = 0$. The term $\bar{U}'(y)$ appears in all functions $c_{1,11}$, $c_{0,11}$, $c_{1,12}$, and $c_{0,12}$ in (4.28) (see (E8) in Appendix E), and when $y^* = 0$ the only nonzero term that survives is

$$c_{0,11} = \frac{2i k_x}{We c(y)}, \quad (4.34)$$

and using (4.33) and (4.30), we have $c(y^*) = 1/We$, so (4.34) reduces to a constant

$$c_{0,11} = 2i k_x, \quad (4.35)$$

and this constant does not produce prominent localized amplification compared to g_1 in (4.31) when $y^* \neq 0$.

The absence of localized amplification at $y = 0$ can also be understood from a physical perspective by considering that the normal and shear components of the stress in the base-state (\bar{T}_{xx} and \bar{T}_{xy} in (4.4)) vanish at $y = 0$, thus there is no driving force to locally amplify the stress at $y = y^* = 0$. This explains why the dashed-dotted lines (corresponding to $y = y^*$) do not coincide with the locations where $\hat{\tau}_{xx}$ is locally amplified when $y^* = 0$ in Figure 4.9a, unlike all other cases in Figure 4.9.

As the localized amplification of τ_{xx} seems to occur at same locations where the functions $c_{1,11}$, $c_{0,11}$, $c_{1,12}$, and $c_{0,12}$ in (4.28) are locally amplified, physical mechanisms for the local amplification of τ_{xx} are likely to be embedded in these functions. These

functions are listed in (E8) in Appendix E, and the prominent feature of these functions apart from the continuous spectrum (discussed in § 4.5.1) is the coupling of the base-state stress, \bar{T}_{xx} and \bar{T}_{xy} , and the base-state velocity gradient, \bar{U}' (see (4.4)) with the velocity fluctuations and their derivatives (see (4.28)). The influence of the base-state stress and velocity gradient in (4.4) on the localized amplification of the stress is further evidenced from the observation that the localized amplification becomes less prominent at locations where they are zero, i.e., at $y = 0$ (Figure 4.9a).

Lastly, we find that the expression (4.33) for the locations of localized amplification of $\hat{\tau}_{xx}$ that result from the SVD of \mathcal{T}_{xx} in (4.17) is valid for other k_x as well (an example of $k_x = 3$ is relegated to Appendix G, Figure G3). However, we do not know if (4.33) is valid for all $k_x \in \mathbb{R}$ where \mathbb{R} is the set of real numbers, as computational limitations preclude a comprehensive verification. Stress singular functions (see (4.18)) become increasingly steep with an increase in $k_x > 3$ and need a large number of basis functions for good resolution; this makes an SVD (4.17) prohibitively expensive.

We found in § 4.4 that localized amplification of the stress is more prominent in the 2D case (Figures 4.5b and 4.5c) compared to the 2D3C case (Figure 4.5a). In this section we sought to understand why and where does the stress τ_{xx} have localized amplification for a body force (4.5e) of frequency ω as observed in Figures 4.5b and 4.5c. We find that the localized amplification of $\hat{\tau}_{xx}$ computed from the SVD of \mathcal{T}_{xx} in (4.17), is essentially related to the continuous spectrum (4.7c). The expression $\omega + k_x \bar{U}(y^*) = 0$ (as discussed in Figure 4.9) estimates the locations where the stress has localized amplification when $k_x = 1$, except when the normal and shear components of the stress in the base-state (4.4) become zero, i.e., $\bar{U}'(y) = 0$.

4.6 Summary and conclusions

This paper explores a linear mechanism that may explain recent experimental observations by Qin et al. [9]. They found that the kinetic energy of perturbations induced in the channel decrease along the length of the channel, followed by an increase at larger channel lengths (Figure 3, inset, in [9]). This phenomenon is unlikely to be related to a standard modal or nonmodal growth mechanism, as in both cases, the kinetic energy of the velocity perturbations should increase, and then trigger a nonlinear flow state.

We demonstrated in this paper that the stress can be significantly amplified locally even when there is much weaker growth of the kinetic energy. The locally amplified stress may act as a finite-amplitude perturbation to drive a viscoelastic fluid to a nonlinear flow state [89, 41]. Nonmodal analysis typically focuses on a square-integrated measure of perturbation amplification (see Figure 4.1), which we argue may be misleading for the stress, which may amplify very significantly in a localized region in the channel.

We found that the localized amplification of the stress is dominant in the 2D system (Figure 4.5), and that it occurs in regions in the channel where the imaginary part of the function $c(y) = i\omega - \lambda(y)$ (4.30) is zero, where $\lambda(y)$ is the continuous spectrum (see (4.7c)). The continuous spectrum, in conjunction with the base-state stress and the velocity gradient, plays an important role in locally amplifying the stress in channel flows of viscoelastic fluids.

Acknowledgments

This work is supported in part by the National Science Foundation under grant number CBET-1510654. The Minnesota Supercomputing Institute (MSI) at the University of Minnesota is acknowledged for providing computing resources.

Chapter 5

An integral reformulation of the influence-matrix algorithm for direct numerical simulations of channel flows

5.1 Introduction

Spectral methods are used to solve differential equations owing to their superior accuracy [29, 24, 35] and they naturally fit into direct numerical simulations (DNS) to study fluid flow [24, 25]. In DNS of channel flows using spectral methods, the temporal variation is approximated using a time-stepping scheme, and the spatial variation using sets of orthogonal basis functions [24, 25] for each spatial dimension. The wall-parallel directions are assumed to be periodic, and hence Fourier series are used in these directions, and a basis of Chebyshev polynomials is used for the non-periodic wall-normal direction [24, 25].

DNS of channel flow of incompressible fluids have a complication as the pressure is coupled with the velocity field, but the boundary conditions on pressure are unknown *a priori* [24, 25]. All that is known is that the boundary conditions are such that mass and momentum conservation is preserved. The Navier-Stokes (NS) equations describe the

spatio-temporal evolution of the flow field of a Newtonian fluid. Once the NS equations are discretized in time, two approaches have been used to address pressure coupling: One approach eliminates pressure by using higher derivatives (e.g., see [97, 1]), and the second approach estimates the proper boundary conditions on pressure [98].

The NS equations are a set of partial differential equations (PDE) with second-order spatial derivatives, and eliminating pressure leads to a set of fourth-order PDEs [97, 1]. When marching in time using a time-stepping scheme, spurious (non-physical) solutions result from this fourth-order PDE when using the Chebyshev basis for the wall-normal direction [99, 29]. While procedures to alleviate these non-physical solutions are known for conventional spectral methods [29], to the best of our knowledge, there are no direct extensions to these procedures to relatively new well-conditioned spectral methods, like the ultraspherical [26] and spectral integration [27] methods.

The second approach to address pressure coupling involves estimating the proper boundary conditions on pressure using an influence-matrix [37, 38] (see § 5.3.1, (5.13)). This approach has a correction step which depends on the type of spectral method used. This correction step is essential to ensure that the velocity satisfies mass conservation (i.e., the velocity is divergence-free (5.3b)) [24]. However, the correction procedure is not obvious for recent well-conditioned spectral methods [27, 26].

Moreover, the correction is such that errors associated with mass conservation are removed by carrying them over to the momentum conservation equations [100, 38]. This ensures that the velocity is divergence-free to machine precision, albeit with a mild compromise (about $\sim 10^{-1}$ - 10^{-3} units relative to machine precision, $\sim 10^{-15}$ [100, 38]) in the accuracy of momentum conservation [38].

In this chapter we provide an alternative procedure that involves an integral reformulation of Kleiser and Schumann's influence-matrix method [37]. The advantage of this method is two-fold: (a) It does not need a correction step and is therefore more easily adaptable to the new spectral methods mentioned above, and (b) it simultaneously satisfies both mass and momentum conservation to the precision of our calculations.

By precision of our calculations, we mean the extent to which the velocity field is resolved. For example, consider a function $u(y)$ expressed in a sufficiently large, but

finite number of Chebyshev basis functions,

$$u(y) = u_0 \frac{1}{2} T_0(y) + u_1 T_1(y) + u_2 T_2(y) \cdots + u_N T_N(y), \quad (5.1)$$

where u_i are the spectral coefficients, and $T_i(y)$ are the i th Chebyshev polynomials of the first kind. As (5.1) is a spectral expansion on an orthogonal set of basis functions [67], the precision to which $u(y)$ is resolved is approximately equal to the average of the last two spectral coefficients, $(|u_N| + |u_{N-1}|)/2$ (if the function is resolved to machine precision, this average would result in a value of $\sim 10^{-15}$). Note that an average of the last two spectral coefficients is needed as some functions are composed of either purely odd or even Chebyshev polynomials [101].

In the approach we present in this paper, the velocity is divergence-free to the precision to which the velocity field is resolved, and there are no compromises to either mass or momentum conservation. In our approach, if the velocity is resolved to machine precision, then the velocity is also divergence-free to machine precision. We end this section by briefly reviewing related work concerning the influence-matrix method.

Werne proposed a correction to Kleiser and Schumann's influence matrix method [100], however Kleiser clarified that there was no mistake in the original approach [38], and that Werne's procedure [100] is a valid alternative to the correction step. Phillips and Soliman [102] show a method to extend the influence-matrix approach to viscoelastic fluids. More recently, Liu [103] extended the original influence-matrix method [37] to general mixed boundary conditions on the velocity. The common point of these approaches is that a correction step is needed, whereas our approach needs no correction step.

This paper is organized as follows. In Section 5.2, we formally present the problem and governing equations. In Section 5.3 we present our method. In Section 5.4 we show several examples using our method, and in Section 5.5 we summarize this work.

5.2 Governing equations

We consider flow of a Newtonian fluid of density ρ and viscosity μ between two parallel planes as shown in Figure 5.1. We use the following scaling to present the governing

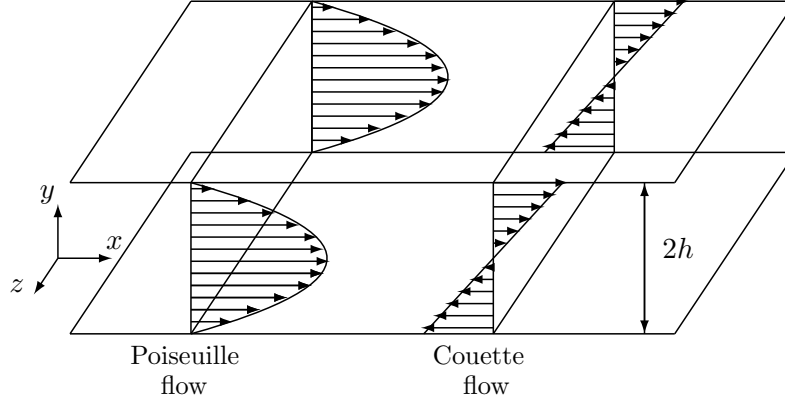


Figure 5.1: Flow geometry showing the steady-state laminar velocity profile for plane Poiseuille and Couette flows.

equations: Velocity is scaled with the maximum velocity under steady, laminar conditions, U_0 , length with the half-channel width, h , time with h/U_0 , and pressure with ρU_0^2 .

The governing equations are given by

$$\partial_t \mathbf{V} + \mathbf{V} \cdot \nabla \mathbf{V} = -\nabla P + \frac{1}{Re} \nabla^2 \mathbf{V}, \quad (5.2a)$$

$$\nabla \cdot \mathbf{V} = 0, \quad (5.2b)$$

where, $\mathbf{V} = [U \ V \ W]^T$ is the velocity vector, P is the pressure, $Re = hU_0\rho/\mu$ is the Reynolds number, ∇ is the gradient and ∇^2 is the Laplacian. The boundary conditions for system (5.2) come from no-slip and no-penetration of the velocity at the channel walls. System (5.2) can alternatively be expressed as a superposition of a base flow under steady laminar conditions and fluctuating components, $\mathbf{V} = \bar{\mathbf{V}} + \mathbf{v}$, and $P = \bar{P} + p$, where quantities with an overbar represent the steady-state laminar profiles, and \mathbf{v} and p are the velocity and pressure fluctuations. In this representation, system (5.2) takes

the form

$$\partial_t \mathbf{v} + \bar{\mathbf{V}} \cdot \nabla \mathbf{v} + \mathbf{v} \cdot \nabla \bar{\mathbf{V}} + \mathbf{v} \cdot \nabla \mathbf{v} = -\nabla p - \Pi_x \mathbf{e}_x + \frac{1}{Re} \nabla^2 \mathbf{v}, \quad (5.3a)$$

$$\nabla \cdot \mathbf{v} = 0, \quad (5.3b)$$

$$\mathbf{v}(\pm 1) = 0, \quad (5.3c)$$

where $\mathbf{v} = [u \ v \ w]^T$, is the vector of velocity fluctuations, p is the pressure fluctuation, and $\Pi_x = \partial_x \bar{P}$ is a constant external pressure gradient, and \mathbf{e}_x is a unit vector in the x -direction. For plane Couette flow, Π_x is zero, and for plane Poiseuille flow it is equal to a constant. The steady-state laminar velocity is given by $\bar{\mathbf{V}} = [U(y) \ 0 \ 0]^T$, where $U(y) = 1 - y^2$ for plane Poiseuille flow, and $U(y) = y$ for plane Couette flow.

We use representation (5.3) to illustrate our method as boundary conditions are homogeneous unlike the representation in (5.2). However, the algorithm can be easily extended to nonhomogeneous boundary conditions as well in a similar manner as Klieser and Schumann's influence-matrix method [37, 24].

5.3 Numerical method

When performing DNS of channel flows using spectral methods, Fourier transforms are applied to the wall-parallel directions, and a basis of Chebyshev polynomials is used to approximate the wall-normal direction (see Figure 5.1). There are different approaches to use Chebyshev polynomials as basis functions: The Chebyshev-tau, the Chebyshev collocation, and the spectral integration methods [24, 1, 28]. Algorithms to use the Chebyshev-tau and collocation methods are well-known and documented in Refs. [24, 25].

Henningson et al. [1] used an algorithm for DNS of channel flows using the spectral integration method. The implementation of the spectral integration method for DNS by Henningson et al. [1] uses an integration correction, although the details of this correction are different from the influence-matrix correction [37], this approach also ensures that the velocity field is divergence-free while mildly compromising on the accuracy of momentum conservation to ensure numerical stability [1].

The alternative we propose herein needs no correction step. The velocity is divergence-free up to the precision of our calculations, and there are no compromises made to either mass or momentum conservation. In this section, we first discuss the discretized representation of (5.3), and revisit Kleiser and Schumann’s influence-matrix method [37]. We then present our variant of this method that avoids a correction step.

Equation (5.3a) has both advection ($\bar{\mathbf{V}} \cdot \nabla \mathbf{v}$, $\mathbf{v} \cdot \nabla \bar{\mathbf{V}}$, and $\mathbf{v} \cdot \nabla \mathbf{v}$) and diffusion ($\nabla^2 \mathbf{v}$) terms. A time-stepping scheme can either be explicit (where the value of the velocity at a given time is calculated using values of the advective and diffusive terms from a previous time-step) or implicit (where the value of the velocity is solved simultaneously with the advective and diffusive terms at any given time). Note that pressure must be treated implicitly [24, Section 7.3] as it adjusts instantaneously in a manner so that velocity is divergence-free (i.e., satisfies (5.3b)).

In DNS, terms related to diffusion are typically treated implicitly in time to ensure numerical stability. An explicit treatment of diffusion terms requires a time step of size $\sim 1/(N+1)^4$, where $N+1$ is the number of Chebyshev basis functions, and an implicit treatment requires a time step of size $\sim 1/(N+1)^2$ [24, Section 7.3], i.e., an implicit treatment ensures numerical stability with a larger time step. The advective terms are treated explicitly as they need a time step of size $\sim 1/(N+1)^2$.

After simplifying (5.3a), the advective terms that are treated explicitly in time can be grouped into \mathbf{f} where

$$\mathbf{f} = -(U\partial_x \mathbf{v} + vU'\mathbf{e}_x + \mathbf{v} \cdot \nabla \mathbf{v}). \quad (5.4)$$

Using (5.4), (5.3a) can be expressed as

$$\partial_t \mathbf{v} = \mathbf{f} + -\nabla p + \frac{1}{Re} \nabla^2 \mathbf{v} - \Pi_x \mathbf{e}_x. \quad (5.5)$$

Applying a Fourier transform in the x - and z -directions on (5.5) and (5.3b), and discretizing in time by using an implicit-explicit scheme [2] (the schemes we use in this

work are relegated to Appendix H), system (5.3) takes the form,

$$a D^2 \mathbf{v}^{n+1} - b \mathbf{v}^{n+1} - \hat{\nabla} p^{n+1} = \mathbf{r}^n, \quad (5.6a)$$

$$\hat{\nabla} \cdot \mathbf{v}^{n+1} = 0, \quad (5.6b)$$

where the superscript $n + 1$ refers to (unknown) quantities to be computed in a future time step, and the quantities superscripted with n refer to (known) terms from a previous time step. The unknown quantities (\mathbf{v}^{n+1} and p^{n+1}) are on the left-hand side of (5.6), and the known quantities (\mathbf{r}^n) are on the right-hand side. Also, $D = d/dy$, $\hat{\nabla} = [ik_x \ D \ ik_z]^T$ is the gradient operator in Fourier space, k_x and k_z are the Fourier modes corresponding to the x - and z -directions, and $\mathbf{r} = [r_u \ r_v \ r_w]^T$. The values for constants a and b and the function \mathbf{r}^n depend on the choice of the implicit-explicit time discretization used (relegated to Appendix H).

5.3.1 Kleiser and Schumann's influence-matrix method

Kleiser and Schumann used an efficient method to solve (5.6) [98, 24, 25, 37]. An implementation of their algorithm is found in the open source `Channelflow` solver [104, 105]. In this section we review Kleiser and Schumann's influence-matrix method. Toward the end of this section we will see that this method needs an influence-matrix correction that makes a mild compromise on the accuracy of the momentum conservation equations to obtain a divergence-free velocity [38]. We then show an approach that does not need such a correction, and simultaneously satisfies both mass and momentum conservation.

Taking the divergence of (5.6a) and using (5.6b), we obtain an equation for pressure without velocities. System (5.6) is thus recast to

$$D^2 p^{n+1} - k^2 p^{n+1} = -\hat{\nabla} \cdot \mathbf{r}^n, \quad D v^{n+1}(\pm 1) = 0, \quad (5.7a)$$

$$a D^2 v^{n+1} - b v^{n+1} - D p^{n+1} = r_v^n, \quad v^{n+1}(\pm 1) = 0, \quad (5.7b)$$

where $k^2 = k_x^2 + k_z^2$. In the developments to follow we omit the superscripts n and $n + 1$ with the understanding that \mathbf{r} is a forcing, and \mathbf{v} and p in (5.6) need to be solved for. The boundary conditions $\partial_y v(\pm 1) = 0$ in (5.7a) come from using (5.3c) and (5.3b).

Observe that (5.7) has two second-order differential equations, one for pressure (5.7a)

and the other for the wall-normal velocity (5.7b). There are four boundary conditions on velocity, and no boundary conditions on pressure. Each differential equation in (5.7) is a Helmholtz equation and can be efficiently solved in $\mathcal{O}(N)$ operations [24, Section 5.1.2] where N is the number of Chebyshev polynomials used, provided appropriate boundary conditions on pressure (corresponding to velocity boundary conditions in (5.7a)) are known. Kleiser and Schumann used the principle of linear superposition to estimate the boundary conditions on pressure [37, 98] corresponding to the velocity boundary conditions in (5.7a).

The solution to system (5.7), is obtained by solving three sets of equations as listed below. Variables p and v are expressed as

$$\begin{bmatrix} p \\ v \end{bmatrix} = \begin{bmatrix} p_* \\ v_* \end{bmatrix} + \delta_- \begin{bmatrix} p_- \\ v_- \end{bmatrix} + \delta_+ \begin{bmatrix} p_+ \\ v_+ \end{bmatrix}, \quad (5.8)$$

where $Dp(\pm 1) = \delta_{\pm}$ are the boundary conditions on pressure that satisfy the velocity boundary conditions in (5.7a), p_* and v_* solve for the forcing in (5.7a) with homogeneous boundary conditions on both p_* and v_* ,

$$D^2 p_* - k^2 p_* = -\hat{\nabla} \mathbf{r}^n, \quad D p_*(\pm 1) = 0, \quad (5.9a)$$

$$D^2 v_* - \lambda v_* - D p_* = r_v, \quad v_*(\pm 1) = 0, \quad (5.9b)$$

and p_- and v_- are solutions to

$$D^2 p_- - k^2 p_- = 0, \quad D p_-(1) = 0, D p_-(-1) = 1, \quad (5.10a)$$

$$D^2 v_- - \lambda v_- - D p_- = 0, \quad v_-(\pm 1) = 0, \quad (5.10b)$$

and p_+ and v_+ are solutions to

$$D^2 p_+ - k^2 p_+ = 0, \quad D p_+(1) = 1, D p_+(-1) = 0, \quad (5.11a)$$

$$D^2 v_+ - \lambda v_+ - D p_+ = 0, \quad v_+(\pm 1) = 0. \quad (5.11b)$$

After obtaining solutions for p_* and v_* using (5.9), p_- and v_- using (5.10), and p_+ and v_+ using (5.11), the constants $\delta_{\pm 1}$ in (5.8) are estimated using linear superposition

to satisfy the velocity boundary conditions in (5.7a),

$$D v(1) = 0 \Rightarrow D v_*(1) + \delta_- D v_-(1) + \delta_+ D v_+(1) = 0, \quad (5.12a)$$

$$D v(-1) = 0 \Rightarrow D v_*(-1) + \delta_- D v_-(-1) + \delta_+ D v_+(-1) = 0. \quad (5.12b)$$

Rearranging (5.12), we have

$$\begin{bmatrix} D v_+(1) & D v_-(1) \\ D v_+(-1) & D v_-(-1) \end{bmatrix} \begin{bmatrix} \delta_+ \\ \delta_- \end{bmatrix} = - \begin{bmatrix} D v_*(1) \\ D v_*(-1) \end{bmatrix}. \quad (5.13)$$

The matrix in (5.13) is the influence-matrix that determines $\delta_{\pm 1}$ in (5.8), and results in Neumann boundary conditions $D p(\pm 1) = \delta_{\pm 1}$ that satisfy $D v(\pm 1) = 0$ in (5.7a). The choice of Neumann boundary conditions on pressure is arbitrary, we could have chosen Dirichlet boundary conditions on pressure in (5.9), (5.10) and (5.11) and estimated Dirichlet boundary conditions on p for (5.7a).

Once v and p have been estimated using (5.8)-(5.13), u and w can be found using (5.6a). Contrary to intuition, the velocity computed in this manner is not necessarily divergence-free, i.e., $\hat{\nabla} \cdot \mathbf{v} \neq 0$ (see (5.3b)). This method finds solutions v and p so that (5.7) is satisfied, while it does not imply anything about the original equation from where (5.7) was derived, i.e., (5.6), being valid for the computed \mathbf{v} . Kleiser and Schumann noticed this in their original work and used an influence-matrix correction [98, 37].

Details of the influence-matrix correction can be found in Refs. [37, 24]. The essential feature of this correction is to solve a modified Helmholtz equation for pressure given by,

$$D^2 p - k^2 p + D \sigma = -\hat{\nabla} \mathbf{r}, \quad D v(\pm 1) = 0, \quad (5.14a)$$

$$a D^2 v - b v - D p + \sigma = r_v, \quad v(\pm 1) = 0, \quad (5.14b)$$

where σ is a term used adjust the momentum conservation equations to make the velocity divergence-free. Canuto et al. [24, Chapter 7] discuss that the velocity is not divergence-free without this correction step owing to discrete defects that are introduced when using the divergence operator on the momentum equations (5.6a) to arrive at (5.7a). In the

following section, we present an integral reformulation of this method where we side-step the use of the divergence operator, and compute a divergence-free velocity without a correction step.

5.3.2 An integral reformulation of the influence-matrix method

We now present our method to solve system (5.6). We apply a dot product of the indefinite integral of the gradient operator, $\hat{\Delta} := \int \hat{\nabla} dy$ with (5.6a) to obtain

$$a \underbrace{D \hat{\nabla} \cdot \mathbf{v}}_{\text{Term 1}} - b \underbrace{\hat{\Delta} \cdot \mathbf{v}}_{\text{Term 2}} - (p' - k^2 \int p dy) = \hat{\Delta} \cdot \mathbf{r} + c, \quad (5.15)$$

where c is the constant of integration. Term 1 in (5.15) is the y -derivative of the continuity equation (i.e., (5.3b)) and is equal to zero. Term 2 is the indefinite integral of (5.3b) with respect to y , and hence this is a constant. We define the integral of pressure as

$$q := \int p dy. \quad (5.16)$$

Thus (5.15) can be rewritten using (5.16) as

$$D^2 q - k^2 q = -\hat{\Delta} \cdot \mathbf{r} + c_1, \quad (5.17)$$

where $c_1 = -c - b \hat{\Delta} \cdot \mathbf{v}$. Notice that in this formulation (5.17) the boundary conditions on q , and the constant c_1 are unknowns. To summarize, we need to solve the following pair of equations

$$D^2 q - k^2 q = -\hat{\Delta} \cdot \mathbf{r} + c_1, \quad Dv(\pm 1) = 0, \quad (5.18a)$$

$$a D^2 v - b v - D^2 q = r_v, \quad v(\pm 1) = 0, \quad (5.18b)$$

where the boundary conditions $\partial_y v(\pm 1) = 0$ in (5.18a) come from using (5.3c) and (5.3b).

System (5.18) is analogous to system (5.7) in the original method by Kleiser and Schumann [37]. But unlike (5.7), we now have an additional unknown, i.e., c_1 in (5.18a). Assuming that we know the value of c_1 in (5.18a), the linear superposition discussed in (5.8)-(5.13) can be used to solve for appropriate boundary conditions for $Dq(\pm 1) =$

$\delta_{\pm 1}$ in the place of p , and u and w can be estimated using (5.6a) and (5.16). We now show that the constant c_1 in (5.18a) is inconsequential and can be set to zero.

Theorem 1. *The constant of integration c_1 in (5.18a) can be arbitrarily chosen to satisfy (5.6) when using appropriate Neumann boundary conditions on q that satisfy the velocity boundary conditions $D v(\pm 1) = 0$.*

Proof. Let the appropriate Neumann boundary conditions on q that satisfy the velocity boundary conditions in (5.18a) ($D v(\pm 1) = 0$) be given by $D q(\pm 1) = c_{\pm 1}$. We now have a problem that is equivalent to (5.18),

$$D^2 q - k^2 q = -\hat{\Delta} \cdot \mathbf{r} + c_1, \quad D q(\pm 1) = c_{\pm 1}, \quad (5.19a)$$

$$a D^2 v - b v - D^2 q = r_v, \quad v(\pm 1) = 0, \quad (5.19b)$$

As (5.19a) is a linear equation, we decompose the problem into $q = q_1 + q_2$ where

$$D^2 q_1 - k^2 q_1 = -\hat{\Delta} \cdot \mathbf{r}, \quad D q_1(\pm 1) = c_{\pm} \quad (5.20a)$$

$$D^2 q_2 - k^2 q_2 = c_1, \quad D q_2(\pm 1) = 0. \quad (5.20b)$$

The solution to (5.20b) is given by $q_2 = -c_1/k^2$, another constant (see [106] for the solution procedure). The total solution is hence given by $q = q_1 + q_2$. As $p = D q = D(q_1 + q_2) = D q_1$ (see (5.16)), there is no need to consider the second part of the solution involving q_2 . Notice in (5.18b) that only $D^2 q$ is needed to compute v , similarly, to estimate u and w using (5.6a), we need $p = D q = D q_1$. Therefore c_1 in (5.18) can be arbitrarily chosen to satisfy (5.6). \square

In summary, to solve (5.6), we solve system (5.18) by setting $c_1 = 0$. System (5.18) is solved in the same manner as (5.7) (see (5.8)-(5.13)). Once v and q are determined in this way, u and w can be computed from (5.6a) and (5.16). Unlike Kleiser and Schumann's influence-matrix method [37, 24], this approach needs no correction as we do not use the divergence operator (which necessitates differentiating the velocity) and hence avoid associated discrete defects [24]. Instead, we derive a Helmholtz equation for the integral of pressure (5.18a) by applying an indefinite integral of the divergence operator on (5.6a).

5.4 Computational experiments

We present two test cases to demonstrate that our approach can simulate channel flows without a correction step. We use spectral integration discussed in § 3.3.2 to numerically approximate spatial derivatives in the y -direction and two time-stepping schemes, the modified Crank-Nicholson for implicit terms, and Adams-Bashforth for explicit terms (MCNAB) [2], and Crank-Nicholson for implicit and three-stage Runge-Kutta (RK) for explicit terms [1] (see Appendix H for details on these time-stepping schemes).

The MCNAB scheme is more accurate [2], but has a low energy damping rate which is undesirable to simulate sustained turbulence (as discussed in [24, Chapter 4]). In contrast, the RK scheme is a self-starting scheme that needs one initial condition, and is well-suited to simulate sustained turbulence [97, 1, 24]. Therefore to simulate sustained turbulence we use the RK scheme, and for all other calculations we use the MCNAB scheme.

We start by comparing solutions of the linearized NS equations to an impulsive excitation whose solutions are available from Chapter 2 using the matrix exponential, (2.13). We then consider nonlinear solutions of the NS equations and compare our results with previous works.

5.4.1 The impulse response of the linearized NS equations

In this section we consider the impulse response of the linearized NS equations using the algorithm for DNS presented in § 5.3.2 (by switching off the nonlinear term $\mathbf{v} \cdot \nabla \mathbf{v}$ in (5.3)) and compare results from the matrix exponential (2.13). We consider streamwise-constant flow ($k_x = 0$) in plane Poiseuille flow of a Newtonian fluid with $Re = 2000$, with $N_z = 256$ linearly spaced Fourier modes in the z -direction. We use $N = 127$ where $N + 1$ is the number of Chebyshev basis functions in the wall-normal direction, and the largest (Nyquist) frequency of $k_{z,\max} = 5$ (corresponds to a periodic channel of length $L_z = N_z \pi / k_{z,\max} = 160.85$) and a time step of 0.01 units. We consider an impulsive excitation (2.9) as a body force to the linearized NS equations.

We denote the kinetic energy averaged in dimensions $\{i, j\}$ by \mathcal{G}_{ij} , e.g., the kinetic

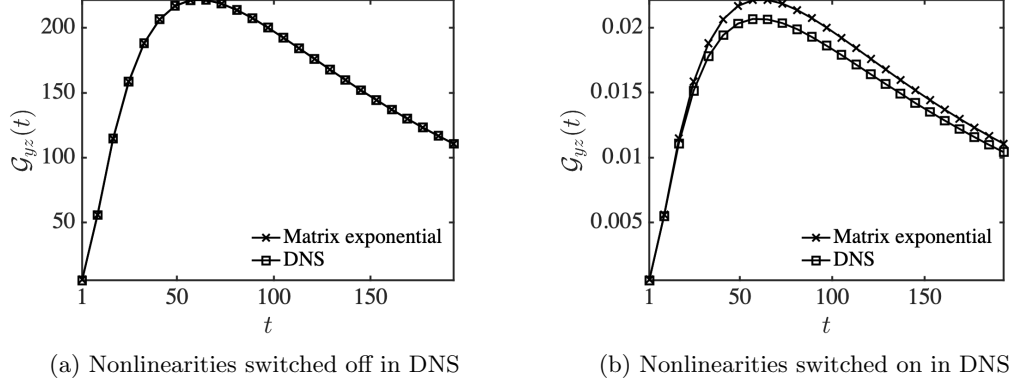


Figure 5.2: The impulse response (2.9) of a Newtonian fluid with $Re = 2000$, $k_x = 0$, $N_z = 256$, $k_{z,\max} = 5$, $N = 127$, using the matrix-exponential solution from (2.9) (\times) and the DNS algorithm in § 5.3.2 (\square) with the nonlinear term $\mathbf{v} \cdot \nabla \mathbf{v}$ in (5.3) (a) switched off, and (b) switched on. Note that in (b) the impulsive body force is attenuated by a factor of 100 to restrict the nonlinear terms to a maximum frequency $k_{z,\max} = 5$.

energy averaged in y and z is represented as

$$\mathcal{G}_{yz}(t) := \frac{1}{2L_z} \left[\int_{y=-1}^1 \int_{z=0}^{L_z} \mathbf{v} \cdot \mathbf{v} \, dz \, dy \right] (t). \quad (5.21)$$

Figure 5.2a shows the kinetic energy averaged in space as a function of time computed using the matrix-exponential (2.13), and the DNS algorithm by switching off nonlinearities in the flow. We see in Figure 5.2a that the results from the two approaches are in excellent agreement. This demonstrates that our approach works well without any correction step as discussed in § 5.3.2.

In Figure 5.2b we plot the kinetic energy obtained when nonlinear terms are switched on in the governing equations in DNS. Note that the matrix exponential solution produces solutions to the linearized governing equations (with nonlinear terms switched off). We attenuate the strength of the impulse by a factor of 100 to contain the response within the maximum frequency selected for this run, i.e., $k_{z,\max} = 5$. We see in Figure 5.2b that the results from the two approaches overlap at early times, and at later times, the approach using the matrix exponential results in larger kinetic energy compared to DNS. The active nonlinear terms are responsible for this decreased kinetic

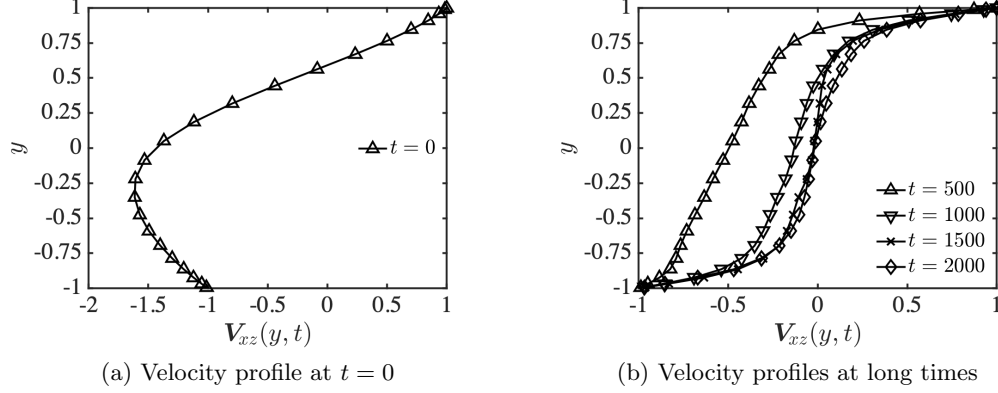


Figure 5.3: The velocity profile of plane Couette flow averaged in the x - and z -directions, with $Re = 1250$ ($Re_\tau = 73$), (a) the initial condition at $t = 0$, and (b) the profiles at times 500, 1000, 1500, and 2000 units.

energy compared to the linearized dynamics at later times.

In this section we simulated the impulse response using the algorithm proposed in § 5.3.2 and compared with solutions from the matrix exponential in (2.13). We found a good agreement between the two approaches without a correction step in implementing our version of the influence-matrix algorithm (§ 5.3.2).

5.4.2 Simulating a sustained turbulent flow state of plane Couette flow

We consider plane Couette flow in a box of dimensions $1.75\pi \times 2 \times 1.2\pi$ in (x, y, z) , with $N_x = 32$, $N = 91$, and $N_z = 32$. The Reynolds number based on the maximum velocity (i.e., the velocity of the channel wall) is set to 1250, this corresponds to a wall-friction Reynolds number (Re_τ) of 73. We use a fixed time step of 0.01, and a random, divergence-free velocity as an initial condition (Figure 5.3a) and simulate its evolution as a function of time.

The random initial velocity field is such that the velocity in Fourier-space is set to zero for all $k_x, k_z \neq 0$, so that the velocity naturally satisfies the divergence-free constraint, $i k_x U + \partial_y V + i k_z W = 0$ (see (5.2b)). At $k_x = k_z = 0$, we further set

$V = W = 0$, and the second-derivative of the streamwise velocity is expressed as

$$D^2U(k_x = 0, y, k_z = 0, t = 0) = a_0^{(2)}/2 T_0(y) + a_1^{(2)} T_1(y) + a_2^{(2)} T_2(y) \cdots + a_N^{(2)} T_N(y), \quad (5.22)$$

where the coefficients $a_i^{(2)}$ in (5.22) are random numbers multiplied with a decay-rate factor so that the last spectral coefficient, a_N is zero to machine precision, 10^{-15} . Equation (5.22) is then integrated twice to derive an expression for the streamwise velocity,

$$U(k_x = 0, y, k_z = 0, t = 0) = a_0/2 T_0(y) + a_1 T_1(y) + a_2 T_2(y) \cdots + a_N T_N(y) + c_1 + c_2 y, \quad (5.23)$$

where c_1 and c_2 are integration constants, which are fixed using the no-slip boundary conditions at the channel walls.

We define the velocity averaged in the x - and z -directions as

$$\mathbf{V}_{xz}(y, t) := \frac{1}{L_x L_z} \int_0^{L_x} \int_0^{L_z} \mathbf{V}(x, y, z, t) \, dx \, dz. \quad (5.24)$$

With an increase in time, we see in Figure 5.3b that the velocity averaged in the x - and z -directions (5.24) acquires a profile that is steep near the wall ($y = \pm 1$) and flat near the center ($y = 0$), as expected in a turbulent flow state for plane Couette flow [107]. The profile is steep near the wall as the momentum from the moving wall is imparted to the fluid, and the fluid satisfies the no-slip boundary conditions at the channel walls. In contrast, far away from the wall, the flow acquires a turbulent flow state that is nearly independent of the no-slip boundary conditions at the channel walls.

Wall-bounded turbulent flow shows nearly universal characteristics near the wall [67, Section 13.4], exemplified by the wall-law. We now verify that our simulations conform with well-known statistical measures near the wall. The wall-friction velocity is defined as [67, Section 13.4],

$$u_\tau := \sqrt{\frac{1}{Re} \frac{d \langle U_{xz} \rangle}{dy}} \bigg|_{y=-1}, \quad (5.25)$$

where $\langle \cdot \rangle$ denotes a time average taken over an interval after the simulation is run for sufficiently long times (from 1200 to 1300 time units), and U_{xz} is the streamwise velocity averaged in the x - and z -directions.

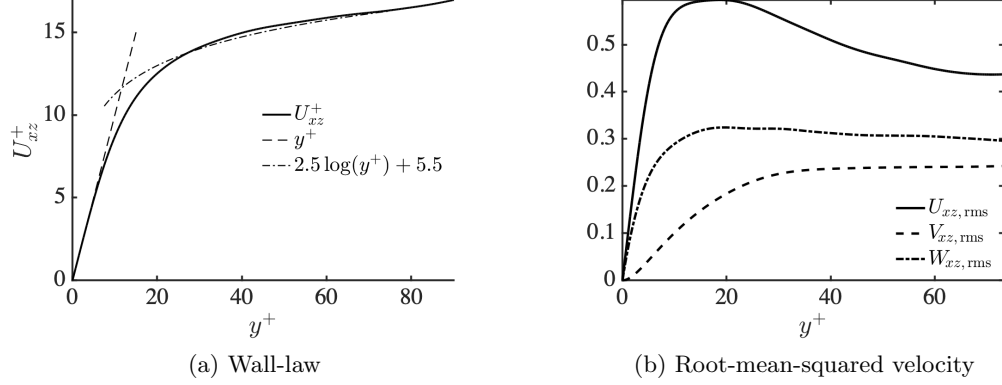


Figure 5.4: Couette flow with $Re = 1250$ ($Re_\tau = 73$) using the DNS algorithm in § 5.3.2, (a) the streamwise velocity (rescaled with wall-friction velocity, see (5.26)) averaged in the x - and z -directions, conforming with the wall-law (5.27), (b) RMS of the velocity averaged in the x - and z -directions (see (5.28)).

The velocity and length rescaled with u_τ (see (5.25)) are defined as [67, Section 13.4]

$$\mathbf{V}^+ = \mathbf{V}/u_\tau, \quad (5.26a)$$

$$y^+ = Re u_\tau y. \quad (5.26b)$$

The asymptotic limits of the streamwise velocity near the wall are given by [67, Equations 13.4-21 and 13.4-24],

$$U^+(y) = \begin{cases} y^+, & y^+ \rightarrow 0, \\ 2.5 \ln(y^+) + 5.5, & y^+ \rightarrow \infty. \end{cases} \quad (5.27)$$

In Figure 5.4a we plot U_{xz}^+ (i.e., U^+ averaged in the x - and z -directions) computed from DNS of Couette flow using the influence matrix algorithm in § 5.3.2, and compare with the wall-law in (5.27). The solid line marks U_{xz}^+ from our calculations, the dashed lined marks y^+ , and the dashed-dotted line marks the logarithmic equation in (5.27). We observe a good agreement with the asymptotic limits in (5.27) in Figure 5.4a.

Lastly, we plot the root-mean-squared (RMS) velocity given by,

$$\mathbf{V}_{xz, \text{rms}}(y) := \sqrt{\left\langle \left(\mathbf{V}_{xz}(y) - \langle \mathbf{V}_{xz}(y) \rangle \right)^2 \right\rangle}, \quad (5.28)$$

in Figure 5.4b. The solid line marks the RMS streamwise velocity, the dashed line marks the wall-normal velocity and the dashed-dotted line marks the spanwise velocity. We observe in Figure 5.4b that the RMS streamwise velocity has the largest magnitude, followed by the spanwise velocity, and then the wall-normal velocity. This trend of the RMS values near the wall in Figure 5.4b is in agreement with previous experimental [108] and theoretical observations [97] of near-wall turbulence.

5.5 Summary and conclusions

In this work we provide an integral reformulation of the Kleiser and Schumann’s influence matrix algorithm. Our approach does not need a correction step and makes no compromise in satisfying mass and momentum conservation accurately to the precision of our calculations.

The integral reformulation of the influence-matrix method proposed in this work makes use of a Helmholtz equation that governs the indefinite integral of pressure. We used the fact that appropriate Neumann boundary conditions can be used to derive a divergence-free velocity field without a correction step. As the method reported here needs no correction step, adopting it in recently developed, well-conditioned spectral methods [26, 27] will be straightforward in principle.

Acknowledgments

This work is supported in part by the National Science Foundation under grant number CBET-1510654. The Minnesota Supercomputing Institute (MSI) at the University of Minnesota is gratefully acknowledged for providing computing resources.

Chapter 6

Summary

Elastic turbulence has many potential applications to enhance transport in systems with weak inertia like medical diagnostic devices and environmental sensor applications. Low-inertia elastic instabilities are sometimes undesirable e.g., in materials processing and coating operations. A good understanding of the initial stages of transition to turbulence in channel flows of viscoelastic fluids will form a firm foundation for devising strategies to control elastic turbulence.

Linear analysis provides information regarding the evolution of the velocity and stress perturbations that arise from small-amplitude disturbances [6, 16] and can uncover potential mechanisms governing the initial stages of a transition to elastic turbulence. This thesis uses linear systems theory, together with recent well-conditioned spectral methods, to explore potential mechanisms that may govern the initial stages of a transition to elastic turbulence.

Localized body forces considered in Chapter 2 confirm observations from previous work on distributed body forces [20, 21, 22, 5, 36] that the amount of nonmodal amplification increases with the polymer concentration and relaxation time. Localized body forces also provide information that is not obtainable from distributed body forces, e.g., identifying the location in the channel where a disturbance can induce the largest kinetic energy growth, and the vortical structures in Figures 2.10 and 2.11 that arise in the flow. Examining the nonlinear evolution of a localized body force is a natural step forward to analyzing a transition to elastic turbulence.

Recent experimental observations by Qin et al. [9] motivated us to revisit linear

analysis in 2D channel flows of viscoelastic fluids. Experiments by Qin et al. [9] showed that a transition occurs while the kinetic energy in the fluid decreases along the length of the channel. This is hard to understand from the point of view of the standard nonmodal theory, as we would expect a growth of the kinetic energy followed by a transition to elastic turbulence [9, 8, 15].

Linear analysis of the 2D system is a numerically stiff problem that needs recent well-conditioned spectral methods for good resolution. In Chapter 3, we employed a reflection technique of Lanczos [72] in conjunction with recent well-conditioned spectral methods [26, 27] that enables linear analysis with fluids of large elasticity.

Motivated by the experiments of Qin et al. [9] and Pan et al. [8], we considered the effects of a persistent body force which is localized in space, and harmonic in time. We found that such forces can induce large stresses in localized regions in the channel simultaneously with a weak growth of the kinetic energy. This provides a potential linear mechanism for the initial stages of transition to elastic turbulence observed by Qin et al. [9].

Qin et al. [9] observe that the kinetic energy of the fluid decreases along the channel length, followed by a transition to elastic turbulence. The initial stages of this transition are unlikely related to a conventional linear growth mechanism as the kinetic energy decreases along the channel length. However, although the kinetic energy decreases, a large stress may have been simultaneously generated through a linear mechanism as discussed in Chapter 4. The large stress in a localized region (Figure 4.7) may have acted as a finite-amplitude perturbation to trigger a nonlinear flow state [41, 89].

We learnt from Chapters 3 and 4 that well-conditioned spectral methods are useful in linear analysis of viscoelastic channel flows. We further saw in Chapter 3 that the conventional spectral collocation method can produce erroneous results (Figure 3.6). A natural next step is to extend these well-conditioned spectral methods for use in direct numerical simulations of channel flows of viscoelastic fluids. However, it is essential to have an algorithm for DNS of channel flows of a Newtonian fluid using these well-conditioned spectral methods before we consider a viscoelastic fluid.

Kleiser and Schumann's influence-matrix method [37] is a computationally efficient method to perform DNS of channel flows using conventional spectral methods. This method has a correction step that varies with the type of spectral discretization. An

extension of the correction procedure is not obvious for a new spectral method like the recent ultraspherical and spectral integration methods [26, 27]. Furthermore, this correction step ensures that mass conservation is satisfied to machine precision, but with a mild compromise on the accuracy of momentum conservation [38, 100]. In Chapter 4 we developed an integral reformulation of this method which is (a) devoid of a correction step and (b) satisfies mass and momentum conservation to the extent that the velocity field is resolved.

This thesis aims to understand the initial stages of transition to elastic turbulence using linear systems analysis in conjunction with recent well-conditioned spectral methods. Our work provides many useful guidelines to enhance nonmodal growth and to generate finite-amplitude stresses in a channel. This may aid understanding of the role of small-amplitude perturbations in triggering a transition to elastic turbulence in experiments. For example, we identified that a disturbance induced near the channel wall generates the large kinetic energy growth in the channel in Chapter 2, and in Chapter 4 we identified that body forces which are localized in space and persistent in time (which are similar to forces exerted by finite-sized objects in the flow) produce stress amplification at a location in the channel as governed by a fairly simple equation in (4.33).

Chapter 7

Future directions

7.1 Complementary experiments on effects of localized body forces in channel flows of viscoelastic fluids

We studied the effects of localized body forces in channel flows of viscoelastic fluids in Chapter 2. Localized body forces in Newtonian channel flows at high Reynolds numbers provide insights into mechanisms that govern the initial stages of a transition to turbulence [46, 49]. Experiments reveal streamwise streaks during the initial stages of a transition [46] and these were thought to be related to nonlinear effects. However, Jovanović [49] showed that such flow structures [46] can be recovered by merely simulating the response of localized body forces on the linearized governing equations.

In Chapter 2 we performed numerical simulations of responses of channel flows of viscoelastic fluids to localized body forces. However, to the best of our knowledge, complementary experiments have not been reported using such forces. Most experiments that we are aware of have focused on flows in microfluidic channels [54, 8, 9] and it is relatively hard to induce localized body forces in such systems. Experiments similar to those used to study transition to turbulence in channel flows of Newtonian fluids at high Reynolds numbers [46] may be used with channel flows of viscoelastic solutions. When numerical results presented in Chapter 2 are compared to such experiments, the significance of linearized dynamics on transition to elastic turbulence will become more clear.

7.2 Well-conditioned spectral methods to study effects of impulsive body forces in channel flows

We discussed in Chapter 2 the advantage of using a spatio-temporal impulsive body force to study flow transition, that they can be approximated in experiments [46, 48] and in numerical simulations [23, 49, 50] relatively easily. The responses of the linearized equations governing the flow of a viscoelastic fluid to impulsive body forces considered in Chapter 2 were limited to a minimum Reynolds number of 50. In contrast, elastic turbulence has been observed in experiments with a Reynolds number as low as 0.01 [8, 9]. Calculations in Chapter 2 were limited to a Reynolds number of 50 as reducing it further lead to significant numerical errors (see § 2.2.3).

Although inertial effects are expected to be relatively small at a Reynolds number of 50 (considered in Chapter 2), lowering the Reynolds number further will enable us to isolate effects associated with elasticity from effects associated with inertia in the flow. However, note that we were able to simulate responses of flows with $Re = 0$ in Chapters 3 and 4 by using *well-conditioned spectral methods* (that are less prone to numerical errors) for body forces that are persistent in time (see Figure 3.6). These well-conditioned spectral methods (see Chapter 3) may allow simulating responses of instantaneous body forces (like the spatio-temporal impulse in Chapter 2) well below a Reynolds number of 50 as well.

However, the procedure to use these well-conditioned spectral methods with body forces that are instantaneous in time (such as the spatio-temporal impulse in Chapter 2) are yet to be uncovered. The DNS algorithm in Chapter 5 provides the first step, e.g., we simulate the impulse response of the linearized Navier-Stokes equations using a well-conditioned spectral method in § 5.4.1.

However, a DNS procedure is intended for use with nonlinear simulations; it does not take advantage of the linearity of the linearized governing equations. The DNS procedure needs to step in time to reach the evolution of a localized body force at a particular time. In contrast, the matrix exponential (that takes advantage of linearity) used in (2.13) in Chapter 2 can directly compute the flow structure at any given time.

In addition, the operator-Lyapunov equations (2.15) can be used to directly compute the total kinetic energy of velocity fluctuations (over all time) that is generated by an

impulsive body force (a result from linear systems theory, see § 2.2.4). In contrast, a DNS code can only provide a reasonable approximation by running an arduous time-stepping simulation over a long time interval.

In order to use the operator-Lyapunov equations (2.15) on or the matrix exponential (2.13) of a linear dynamical system, the system must be inherently stable [17]. Also, the numerical discretization scheme used to approximate differential operators should not introduce artificial instabilities. We typically obtain two spurious (non-physical and sometimes unstable) eigenvalues whose magnitudes are close to $\pm\infty$ [29] when using a Chebyshev basis to approximate differential operators in (2.12). Even one spurious mode is sufficient to ruin numerical evaluations of the operator-Lyapunov equations or a matrix exponential.

While methods to avoid these spurious modes associated with a Chebyshev basis are known for conventional spectral methods [109, Section 6.2.1][32, Section 4.2], such procedures are not known (to the best of our knowledge) for the recent well-conditioned spectral methods [26, 27]. Once we alleviate these spurious modes in the context of these new well-conditioned spectral methods, we can obtain reliable calculations of the matrix exponential (2.13) and solutions of the operator-Lyapunov equations (2.15).

Reliable solutions of the operator-Lyapunov equations and evaluations of the matrix exponential may facilitate studying the effects of impulsive body forces in the nearly inertialess regime. In this way, we may be able to isolate the elastic effects from inertial effects while using the impulsive body force to study the initial stages of transition to elastic turbulence.

7.3 DNS of elastic turbulence using well-conditioned spectral methods

In Chapter 3 we saw that recent well-conditioned spectral methods can resolve steep stress gradients without being hindered by effects arising from ill-conditioned matrices. The superiority of these well-conditioned spectral methods compared to conventional spectral methods in the context of viscoelastic channel flows is clear. To the best of our knowledge, there are no reports of DNS on elastic turbulence (low-inertia, $Re < 0.1$ and high elasticity regime), and most simulations focus on elasto-inertial turbulence

($Re > 20$) and moderate elasticity due to numerical difficulties associated with resolving steep stress gradients.

The well-conditioned spectral methods considered in Chapter 3 have good potential to resolve such steep stress gradients in the high-elasticity, low-inertia regime. An efficient algorithm needs to be developed and validated using these well-conditioned spectral methods. The key challenge is to devise an efficient method to solve the non-linear velocity-stress coupled equations that govern the dynamics of the stress tensor.

7.4 Control of elastic turbulence

Much of this thesis was devoted to understanding the initial stages of a transition to elastic turbulence. As discussed in Chapter 1, elastic turbulence has potential utility to improve transport in microfluidic channel flows. However, in certain applications like polymer processing operations, a transition to elastic turbulence needs to be prevented to avoid defective end products. Thus, it is necessary to devise strategies to control a transition to elastic turbulence.

Flow control has been extensively studied in high-inertia channel flows of Newtonian fluids [110, 111, 112, 113, 114]. For example, high-inertia turbulence in Newtonian fluids can be suppressed by small-amplitude transverse wall oscillations [110, 113]. Similarly, turbulence can be enhanced and suppressed using streamwise traveling waves generated by subjecting the channel walls to vibrations of certain spatial and temporal frequencies [111, 112]. Similar studies on low-inertia channel flows of viscoelastic fluids may provide means to suppress (or enhance) elastic turbulence when necessary.

7.5 Concluding remarks

Analyzing transition to turbulence in viscoelastic channel flows is a challenging problem that needs a multi-faceted approach involving linear and nonlinear systems theory, robust numerical methods, and complementary experiments. We believe that this dissertation provides new insights into possible mechanisms that may govern the initial stages of a transition to elastic turbulence using linear systems theory and recent numerical methods. We further hope that the numerical methods studied in this dissertation will

open new avenues to simulate and analyze flow transition in complex fluids.

References

- [1] D. S. Henningson, A. Lundbladh, and A. V. Johansson. A mechanism for bypass transition from localized disturbances in wall-bounded shear flows. *J. Fluid Mech.*, 250:169–207, 1993.
- [2] U. M. Ascher, S. J. Ruuth, and B. T. R. Wetton. Implicit-explicit methods for time-dependent partial differential equations. *SIAM J. Numer. Anal.*, 32:797–823, 1995.
- [3] A. Groisman and V. Steinberg. Elastic turbulence in curvilinear flows of polymer solutions. *New J. Phys.*, 6:29, 2004.
- [4] S. Boyd, V. Balakrishnan, and P. Kabamba. A bisection method for computing the \mathcal{H}_∞ norm of a transfer matrix and related problems. *Math. Control Signals Syst.*, 2:207–219, 1989.
- [5] M. R. Jovanović and S. Kumar. Nonmodal amplification of stochastic disturbances in strongly elastic channel flows. *J. Non-Newtonian Fluid Mech.*, 166:755–778, 2011.
- [6] P. J. Schmid and D. S. Henningson. *Stability and transition in shear flows*. Springer Science and Business Media, 2012.
- [7] A. Groisman and V. Steinberg. Elastic turbulence in a polymer solution flow. *Nature*, 405:53–55, 2000.
- [8] L. Pan, A. N. Morozov, C. Wagner, and P. E. Arratia. Nonlinear elastic instability in channel flows at low Reynolds numbers. *Phys. Rev. Lett.*, 110:174502, 2013.

- [9] B. Qin and P. E. Arratia. Characterizing elastic turbulence in channel flows at low Reynolds number. *Phys. Rev. Fluids*, 2:083302, 2017.
- [10] A. Groisman and S. R. Quake. A microfluidic rectifier: Anisotropic flow resistance at low Reynolds numbers. *Phys. Rev. Lett.*, 92:094501, 2004.
- [11] A. Groisman, M. Enzelberger, and S. R. Quake. Microfluidic memory and control devices. *Science*, 300:955–958, 2003.
- [12] B. Meulenbroek, C. Storm, A. N. Morozov, and W. van Saarloos. Weakly nonlinear subcritical instability of visco-elastic Poiseuille flow. *J. Non-Newtonian Fluid Mech.*, 116:235–268, 2004.
- [13] R. G. Larson. Instabilities in viscoelastic flows. *Rheol. Acta*, 31:213–263, 1992.
- [14] M. R. Jovanović. From bypass transition to flow control and data-driven turbulence modeling: An input-output viewpoint. *Annu. Rev. Fluid Mech.*, 2020. submitted; also arXiv:2003.10104.
- [15] P. J. Schmid. Nonmodal stability theory. *Annu. Rev. Fluid Mech.*, pages 129–162, 2007.
- [16] M. R. Jovanović and B. Bamieh. Componentwise energy amplification in channel flows. *J. Fluid Mech.*, 534:145–183, 2005.
- [17] J. P. Hespanha. *Linear systems theory*. Princeton University Press, 2009.
- [18] S. Grossmann. The onset of shear flow turbulence. *Rev. Mod. Phys.*, 72:603–618, 2000.
- [19] K. M. Butler and B. F. Farrell. Three-dimensional optimal perturbations in viscous shear flow. *Phys. Fluids A*, 4:1637–1650, 1992.
- [20] N. Hoda, M. R. Jovanović, and S. Kumar. Energy amplification in channel flows of viscoelastic fluids. *J. Fluid Mech.*, 601:407–424, 2008.
- [21] N. Hoda, M. R. Jovanović, and S. Kumar. Frequency responses of streamwise-constant perturbations in channel flows of Oldroyd-B fluids. *J. Fluid Mech.*, 625:411–434, 2009.

- [22] M. R. Jovanović and S. Kumar. Transient growth without inertia. *Phys. Fluids*, 22:023101, 2010.
- [23] G. Hariharan, M. R. Jovanović, and S. Kumar. Amplification of localized body forces in channel flows of viscoelastic fluids. *J. Non-Newtonian Fluid Mech.*, 260:40–53, 2018.
- [24] C. Canuto, M. Y. Hussaini, A. Quarteroni, and T. A. Zang. *Spectral methods in fluid dynamics*. Springer Science and Business Media, 2012.
- [25] R. Peyret. *Spectral methods for incompressible viscous flow*. Springer Science and Business Media, 2013.
- [26] S. Olver and A. Townsend. A fast and well-conditioned spectral method. *SIAM Rev.*, 55:462–489, 2013.
- [27] K. Du. On well-conditioned spectral collocation and spectral methods by the integral reformulation. *SIAM J. Sci. Comp.*, 38:A3247–A3263, 2016.
- [28] L. Greengard. Spectral integration and two-point boundary value problems. *SIAM J. Numer. Anal.*, 28:1071–1080, 1991.
- [29] J. P. Boyd. *Chebyshev and Fourier spectral methods*. Courier Corporation, 2001.
- [30] A. Gil, J. Segura, and N. M. Temme. *Numerical methods for special functions*. Society for Industrial and Applied Mathematics, 2007.
- [31] T. A. Driscoll, N. Hale, and L. N. Trefethen. *Chebfun guide*. Pafnuty Publications, 2014.
- [32] J. A. Weideman and S. C. Reddy. A MATLAB differentiation matrix suite. *ACM TOMS*, 26:465–519, 2000.
- [33] B. K. Lieu and M. R. Jovanović. Computation of frequency responses for linear time-invariant PDEs on a compact interval. *J. Comput. Phys.*, 250:246–269, 2013.
- [34] G. H. Golub and C. F. Van Loan. *Matrix computations*. JHU Press, 2012.

- [35] L. N. Trefethen. *Spectral methods in MATLAB*. Society for Industrial and Applied Mathematics, 2000.
- [36] B. K. Lieu, M. R. Jovanović, and S. Kumar. Worst-case amplification of disturbances in inertialess Couette flow of viscoelastic fluids. *J. Fluid Mech.*, 723:232–263, 2013.
- [37] L. Kleiser. Spectral simulations of laminar-turbulent transition in plane Poiseuille flow and comparison with experiments. In *Eighth International Conference on Numerical Methods in Fluid Dynamics*, pages 280–285. Springer, 1982.
- [38] L. Kleiser, C. Hartel, and T. Wintergerste. LETTER TO THE EDITOR: There is no error in the Kleiser and Schumann influence matrix method. *J. Comput. Phys.*, 141:85–87, 1998.
- [39] T. Burghlea, E. Segre, I. Bar-Joseph, A. Groisman, and V. Steinberg. Chaotic flow and efficient mixing in a microchannel with a polymer solution. *Phys. Rev. E*, 69:066305, 2004.
- [40] D. Copeland, C. Ren, M. Su, and P. Ligrani. Elastic turbulence influences and convective heat transfer within a miniature viscous disk pump. *Int. J. Heat Mass Transfer*, 108:1764–1774, 2017.
- [41] A. N. Morozov and W. van Saarloos. Subcritical finite-amplitude solutions for plane Couette flow of viscoelastic fluids. *Phys. Rev. Lett.*, 95:024501, 2005.
- [42] D. Bonn, F. Ingremeau, Y. Amarouchene, and H. Kellay. Large velocity fluctuations in small-Reynolds-number pipe flow of polymer solutions. *Phys. Rev. E*, 84:045301, 2011.
- [43] L. N. Trefethen, A. E. Trefethen, S. C. Reddy, and T. A. Driscoll. Hydrodynamic stability without eigenvalues. *Science*, 261:578–584, 1993.
- [44] J. Page and T. A. Zaki. Streak evolution in viscoelastic Couette flow. *J. Fluid Mech.*, 742:520–551, 2014.
- [45] J. Page and T. A. Zaki. The dynamics of spanwise vorticity perturbations in homogeneous viscoelastic shear flow. *J. Fluid Mech.*, 777:327–363, 2015.

- [46] D. R. Carlson, S. E. Widnall, and M. F. Peeters. A flow-visualization study of transition in plane Poiseuille flow. *J. Fluid Mech.*, 121:487–505, 1982.
- [47] B. G. B. Klingmann. On transition due to three-dimensional disturbances in plane Poiseuille flow. *J. Fluid Mech.*, 240:167–195, 1992.
- [48] G. Lemoult, K. Gumowski, J.-L. Aider, and J. E. Wesfreid. Turbulent spots in channel flow: An experimental study. *Eur. Phys. J. E*, 37:25, 2014.
- [49] M. R. Jovanović. *Modeling, analysis, and control of spatially distributed systems*. PhD thesis, University of California, Santa Barbara, 2004.
- [50] M. R. Jovanović and B. Bamieh. The spatio-temporal impulse response of the linearized Navier-Stokes equations. In *Proceedings of the 2001 American Control Conference*, pages 1948–1953, Arlington, VA, 2001.
- [51] A. Agarwal, L. Brandt, and T. A. Zaki. Linear and nonlinear evolution of a localized disturbance in polymeric channel flow. *J. Fluid Mech.*, 760:278–303, 2014.
- [52] P. Huerre. Open shear flow instabilities. In G. K. Batchelor, H. K. Moffatt, and M. G. Worster, editors, *Perspectives in fluid dynamics*, chapter 4, pages 159–229. Cambridge University Press, 2000.
- [53] M. D. Chilcott and J. M. Rallison. Creeping flow of dilute polymer solutions past cylinders and spheres. *J. Non-Newtonian Fluid Mech.*, 29:381–432, 1988.
- [54] K. P. Nolan, A. Agarwal, S. Lei, and R. Shields. Viscoelastic flow in an obstructed microchannel at high Weissenberg number. *Microfluid. Nanofluidics*, 20:1–12, 2016.
- [55] M. D. Graham. Effect of axial flow on viscoelastic Taylor–Couette instability. *J. Fluid Mech.*, 360:341–374, 1998.
- [56] M. Renardy and Y. Renardy. Linear stability of plane Couette flow of an upper convected Maxwell fluid. *J. Non-Newtonian Fluid Mech.*, 22:23–33, 1986.

- [57] S. J. Lee and T. A. Zaki. Simulations of natural transition in viscoelastic channel flow. *J. Fluid Mech.*, 820:232–262, 2017.
- [58] A. Gupta, P. Perlekar, and R. Pandit. Two-dimensional homogeneous isotropic fluid turbulence with polymer additives. *Phys. Rev. E*, 91:033013, 2015.
- [59] K. D. Housiadas and A. N. Beris. An efficient fully implicit spectral scheme for DNS of turbulent viscoelastic channel flow. *J. Non-Newtonian Fluid Mech.*, 122:243–262, 2004.
- [60] R. G. Larson. *The structure and rheology of complex fluids*. Oxford University Press, 1998.
- [61] R. B. Bird, C. F. Curtiss, R. C. Armstrong, and O. Hassager. *Dynamics of polymeric liquids, Vol. 2, kinetic theory*. John Wiley and Sons, 1987.
- [62] M. G. Hall. Vortex breakdown. *Annu. Rev. Fluid Mech.*, 4:195–218, 1972.
- [63] R. G. Larson, E. S. G. Shaqfeh, and S. J. Muller. A purely elastic instability in Taylor–Couette flow. *J. Fluid Mech.*, 218:573–600, 1990.
- [64] P. Pakdel and G. H. McKinley. Elastic instability and curved streamlines. *Phys. Rev. Lett.*, 77:2459–2462, 1996.
- [65] A. N. Morozov and W. van Saarloos. An introductory essay on subcritical instabilities and the transition to turbulence in visco-elastic parallel shear flows. *Phys. Rep.*, 447:112–143, 2007.
- [66] R. Sureshkumar and A. N. Beris. Linear stability analysis of viscoelastic Poiseuille flow using an Arnoldi-based orthogonalization algorithm. *J. Non-Newtonian Fluid Mech.*, 56:151–182, 1995.
- [67] W. M. Deen. *Analysis of transport phenomena*. Oxford University Press, 1998.
- [68] M. R. Khorrami. A Chebyshev spectral collocation method using a staggered grid for the stability of cylindrical flows. *Int. J. Num. Meth. Fluids*, 12:825–833, 1991.
- [69] M. R. Khorrami, M. R. Malik, and R. L. Ash. Application of spectral collocation techniques to the stability of swirling flows. *J. Comput. Phys.*, 81:206–229, 1989.

- [70] M. Zhang, I. Lashgari, T. A. Zaki, and L. Brandt. Linear stability analysis of channel flow of viscoelastic Oldroyd-B and FENE-P fluids. *J. Fluid Mech.*, 737:249–279, 2013.
- [71] D. Gottlieb and S. A. Orszag. *Numerical analysis of spectral methods: Theory and applications*. Society for Industrial and Applied Mathematics, 1977.
- [72] C. Lanczos. *Linear differential operators*. Society for Industrial and Applied Mathematics, 1996.
- [73] G. Golub and W. Kahan. Calculating the singular values and pseudo-inverse of a matrix. *J. Soc. Ind. App. Math. B Numer. Anal.*, 2:205–224, 1965.
- [74] J. L. Aurentz and L. N. Trefethen. Block operators and spectral discretizations. *SIAM Rev.*, 59:423–446, 2017.
- [75] M. Renardy and R. C. Rogers. *An introduction to partial differential equations*. Springer Science and Business Media, 2006.
- [76] C. B. Moler and G. W. Stewart. An algorithm for generalized matrix eigenvalue problems. *SIAM J. Numer. Anal.*, 10:241–256, 1973.
- [77] S. Skogestad and I. Postlethwaite. *Multivariable feedback control: Analysis and design*. Wiley, 2007.
- [78] N. A. Bruinsma and M. Steinbuch. A fast algorithm to compute the \mathcal{H}_∞ -norm of a transfer function matrix. *Syst. Control Lett.*, 14:287–293, 1990.
- [79] P. Benner, V. Sima, and M. Voigt. \mathcal{L}_∞ -norm computation for continuous-time descriptor systems using structured matrix pencils. *IEEE Trans. Autom. Control*, 57:233–238, 2012.
- [80] T. A. Driscoll. Automatic spectral collocation for integral, integro-differential, and integrally reformulated differential equations. *J. Comput. Phys.*, 229:5980–5998, 2010.
- [81] M. R. Jovanović and B. Bamieh. A formula for frequency responses of distributed systems with one spatial variable. *Syst. Control Lett.*, 55:27–37, 2006.

- [82] G. Strang. The fundamental theorem of linear algebra. *Amer. Math. Monthly*, 100:848–855, 1993.
- [83] P. M. Gresho and R. L. Sani. On pressure boundary conditions for the incompressible Navier-Stokes equations. *Int. J. Numer. Meth. Fluids*, 7:1111–1145, 1987.
- [84] D. Gottlieb and S. A. Orszag. Models of incompressible fluid dynamics. In *Numerical analysis of spectral methods*, chapter 13, pages 143–148. Society for Industrial and Applied Mathematics, 1977.
- [85] S. G. Kandlikar. High flux heat removal with microchannels - A roadmap of challenges and opportunities. *Heat Trans. Eng.*, 26:5–14, 2005.
- [86] G. H. McKinley, R. C. Armstrong, and R. A. Brown. The wake instability in viscoelastic flow past confined circular cylinders. *Philos. Trans. R. Soc. A*, 344:265–304, 1993.
- [87] M. D. Graham and J. B. Rawlings. *Modeling and analysis principles for chemical and biological engineers*. Nob Hill Publishing, 2013.
- [88] C.-T. Chen. *Linear system theory and design*. Oxford University Press, 1998.
- [89] A. N. Morozov and W. van Saarloos. Subcritical instabilities in plane Poiseuille flow of an Oldroyd-B fluid. *J. Stat. Phys.*, 175:554–577, 2019.
- [90] B. F. Farrell and P. J. Ioannou. Stochastic forcing of the linearized Navier-Stokes equations. *Phys. Fluids A*, 5:2600–2609, 1993.
- [91] B. Thomases and M. Shelley. Emergence of singular structures in Oldroyd-B fluids. *Phys. Fluids*, 19:103103, 2007.
- [92] V. A. Gorodtsov and A. I. Leonov. On a linear instability of a plane parallel Couette flow of viscoelastic fluid. *J. Appl. Math. Mech.*, 31:310–319, 1967.
- [93] M. Renardy. Location of the continuous spectrum in complex flows of the UCM fluid. *J. Non-Newtonian Fluid Mech.*, 94:75–85, 2000.

- [94] W. C. Reynolds and S. C. Kassinos. One-point modelling of rapidly deformed homogeneous turbulence. *Proc. R. Soc. Lond. A Math. Phys. Sci.*, 451:87–104, 1995.
- [95] M. Grilli, A. Vázquez-Quesada, and M. Ellero. Transition to turbulence and mixing in a viscoelastic fluid flowing inside a channel with a periodic array of cylindrical obstacles. *Phys. Rev. Lett.*, 110:174501, 2013.
- [96] A. Shekar, R. M. McMullen, S.-N. Wang, B. J. McKeon, and M. D. Graham. Critical-layer structures and mechanisms in elastoinertial turbulence. *Phys. Rev. Lett.*, 122:124503, 2019.
- [97] J. Kim, P. Moin, and R. Moser. Turbulence statistics in fully developed channel flow at low Reynolds number. *J. Fluid Mech.*, 177:133–166, 1987.
- [98] L. Kleiser and U. Schumann. Treatment of incompressibility and boundary conditions in 3D numerical spectral simulations of plane channel flows. In *Proceedings of the Third GAMM Conference on Numerical Methods in Fluid Mechanics*, pages 165–173. Springer, 1980.
- [99] D. Bourne. Hydrodynamic stability, the Chebyshev tau method and spurious eigenvalues. *Cont. Mech. Therm.*, 15:571–579, 2003.
- [100] J. Werne. Incompressibility and no-slip boundaries in the Chebyshev-tau approximation: Correction to Kleiser and Schumann’s influence-matrix solution. *J. Comput. Phys.*, pages 260–265, 1995.
- [101] A. Gil, J. Segura, and N. M. Temme. Chebyshev expansions. In *Numerical methods for special functions*, chapter 3, pages 51–86. Society for Industrial and Applied Mathematics, 2007.
- [102] T. N. Phillips and I. M. Soliman. Influence matrix technique for the numerical spectral simulation of viscous incompressible flows. *Numer. Meth. Partial Diff. Equations*, 7:9–24, 1991.
- [103] X. Liu. Extension of Kleiser and Schumann’s influence-matrix method for generalized velocity boundary conditions. *J. Comput. Phys.*, 230:7911–7916, 2011.

- [104] J. F. Gibson. Channelflow: A spectral Navier-Stokes simulator in C++. Technical report, University of New Hampshire, 2014. Channelflow.org.
- [105] J. F. Gibson, J. Halcrow, and P. Cvitanović. Visualizing the geometry of state space in plane Couette flow. *J. Fluid Mech.*, 611:107–130, 2008.
- [106] Y. Pinchover and J. Rubinstein. *An introduction to partial differential equations*. Cambridge University Press, 2005.
- [107] J. Komminaho, A. Lundbladh, and A. V. Johansson. Very large structures in plane turbulent Couette flow. *J. Fluid Mech.*, 320:259–285, 1996.
- [108] H.-P. Kreplin and H. Eckelmann. Behavior of the three fluctuating velocity components in the wall region of a turbulent channel flow. *Phys. Fluids*, 22:1233–1239, 1979.
- [109] J. Shen, T. Tang, and L.-L. Wang. *Spectral methods: Algorithms, analysis and applications*. Springer Science and Business Media, 2011.
- [110] R. Moarref and M. R. Jovanović. Model-based design of transverse wall oscillations for turbulent drag reduction. *J. Fluid Mech.*, 707:205–240, 2012.
- [111] R. Moarref and M. R. Jovanović. Controlling the onset of turbulence by streamwise traveling waves. Part 1: Receptivity analysis. *J. Fluid Mech.*, 663:70–99, 2010.
- [112] B. K. Lieu, R. Moarref, and M. R. Jovanović. Controlling the onset of turbulence by streamwise traveling waves. Part 2: Direct numerical simulations. *J. Fluid Mech.*, 663:100–119, 2010.
- [113] M. R. Jovanović. Turbulence suppression in channel flows by small amplitude transverse wall oscillations. *Phys. Fluids*, 20:014101 (11 pages), 2008.
- [114] W. Ran, A. Zare, and M. R. Jovanović. Model-based design of riblets for turbulent drag reduction. *J. Fluid Mech.*, 2020. submitted; also arXiv:2002.01671.
- [115] W. H. Press, S. A. Teukolsky, W. T. Vetterling, and B. P. Flannery. *Numerical recipes 3rd Edition: The art of scientific computing*. Cambridge University Press, 2007.

Appendix

A Operators in Poiseuille flow of FENE-CR fluids

In this section, we define the underlying operators that appear in (2.6) in § 2.2.1. We use a Fourier transform defined by

$$X(\boldsymbol{\kappa}, y, t) = \int_{-\infty}^{\infty} \int_{-\infty}^{\infty} X(x, y, z, t) e^{-j(xk_x + zk_z)} dx dz. \quad (\text{A1})$$

The operator \mathbf{A} in (2.6) is given by

$$\mathbf{A} = \begin{bmatrix} \mathcal{R} & \mathcal{V} & \mathcal{N} \\ \mathcal{P}^T & \mathcal{L}_{OS} & 0 \\ \mathcal{Q}^T & \mathcal{C}_p & \mathcal{S} \end{bmatrix}. \quad (\text{A2})$$

Each of the operators that make up \mathbf{A} are given below in Fourier space. The operator \mathcal{R} is defined as

$$\mathcal{R} = \begin{bmatrix} \mathcal{R}_{11} & \mathcal{R}_{12} \\ 0_{3 \times 3} & \mathcal{R}_{22} \end{bmatrix}, \quad (\text{A3})$$

where

$$\mathcal{R}_{11} = \begin{pmatrix} -\bar{f}/We - 2We(\bar{U}')^2/\bar{L}^2 - j\bar{U}k_x & 2\bar{U}' & 0 \\ -\bar{f}\bar{U}'/\bar{L}^2 & -\bar{f}/We - j\bar{U}k_x & 0 \\ 0 & 0 & -\bar{f}/We - j\bar{U}k_x \end{pmatrix},$$

$$\mathcal{R}_{12} = \begin{pmatrix} -2We (\bar{U}')^2 / \bar{L}^2 & 0 & -2We (\bar{U}')^2 / \bar{L}^2 \\ \bar{U}' - \bar{f} \bar{U}' / \bar{L}^2 & 0 & -\bar{f} \bar{U}' / \bar{L}^2 \\ 0 & \bar{U}' & 0 \end{pmatrix},$$

$$\mathcal{R}_{22} = \begin{pmatrix} -\bar{f}/We - j\bar{U}k_x & 0 & 0 \\ 0 & -\bar{f}/We - j\bar{U}k_x & 0 \\ 0 & 0 & -\bar{f}/We - j\bar{U}k_x \end{pmatrix}.$$

The operator \mathcal{V} is defined as

$$\mathcal{V} = \mathcal{V}_1 + \mathcal{V}_2 \partial_y + \mathcal{V}_3 \partial_{yy}, \quad (\text{A4})$$

where \mathcal{V}_1 , \mathcal{V}_2 , and \mathcal{V}_3 are given by

$$\mathcal{V}_1 = \begin{pmatrix} (4We^2 \bar{U}' (\bar{U}' \bar{f}' - \bar{f} \bar{U}'')) / \bar{f}^3 \\ (We \bar{U}' (\bar{f}' + 2jWe k_x \bar{U}') + j\bar{f}^2 k_x - We \bar{f} \bar{U}'') / \bar{f}^2 \\ 0 \\ (2jWe k_x \bar{U}') / \bar{f} \\ jk_z \\ 0 \end{pmatrix},$$

$$\mathcal{V}_2 = \begin{pmatrix} -\left(2k_x^2 (\bar{f}^2 + 2We^2 (\bar{U}')^2)\right) / (k^2 \bar{f}^2) \\ (We \bar{U}' (-k_x^2 + k^2)) / (k^2 \bar{f}) \\ -\left(2k_x k_z (\bar{f}^2 + We^2 (\bar{U}')^2)\right) / (k^2 \bar{f}^2) \\ 2 \\ -(We k_x k_z \bar{U}') / (k^2 \bar{f}) \\ -(2k_z^2) / (k^2) \end{pmatrix},$$

$$\mathcal{V}_3 = \begin{pmatrix} (2jWek_x \bar{U}') / (k^2 \bar{f}) \\ (jk_x) / (k^2) \\ (jWek_z \bar{U}') / (k^2 \bar{f}) \\ 0 \\ (jk_z) / (k^2) \\ 0 \end{pmatrix},$$

where $k^2 = k_x^2 + k_z^2$. The operator \mathcal{N} is defined as

$$\mathcal{N} = \mathcal{N}_1 + \mathcal{N}_2 \partial_y, \quad (\text{A5})$$

where

$$\mathcal{N}_1 = \begin{pmatrix} \left(2k_x k_z \left(\bar{f}^2 + 2We^2 (U')^2 \right) \right) / (k^2 \bar{f}^2) \\ (Wek_x k_z \bar{U}') / (k^2 \bar{f}) \\ - \left(\bar{f}^2 (k_x^2 - k_z^2) + 2We^2 k_x^2 (U')^2 \right) / (k^2 \bar{f}^2) \\ 0 \\ - (Wek_x^2 \bar{U}') / (k^2 \bar{f}) \\ - (2k_x k_z) (k^2) \end{pmatrix},$$

$$\mathcal{N}_2 = \begin{pmatrix} - (2jWek_z \bar{U}') / (k^2 \bar{f}) \\ - (jk_z) / (k^2) \\ (jWek_x \bar{U}') / (k^2 \bar{f}) \\ 0 \\ (jk_x) / (k^2) \\ 0 \end{pmatrix}.$$

The operator \mathcal{P} is defined as

$$\mathcal{P}^T = \frac{(1 - \beta)}{Re} \Delta^{-1} (\mathcal{P}_1^T + \mathcal{P}_2^T \partial_y + \mathcal{P}_3^T \partial_{yy}), \quad (\text{A6})$$

where $\Delta = \partial_{yy} - k^2$ is the Laplacian in Fourier space, and

$$\mathcal{P}_1 = \begin{pmatrix} (k_x (\bar{f}' (\bar{L}^2 k_x - 2jWe\bar{U}'') + We\bar{U}' (4Wek_x\bar{U}'' - j(k^2\bar{f} + \bar{f}'')))) / (We\bar{L}^2) \\ - (jk_x (k^2\bar{f} + \bar{f}'')) / We \\ (2k_x k_z \bar{f}') / We \\ (-\bar{f}' (k^2\bar{L}^2 + 2jWek_x\bar{U}'') - Wek_x\bar{U}' (jk^2\bar{f} + j\bar{f}'' - 4Wek_x\bar{U}'')) / (We\bar{L}^2) \\ - (jk_z (k^2\bar{f} + \bar{f}'')) / (We) \\ (\bar{f}' (\bar{L}^2 k_z^2 - 2jWek_x\bar{U}'') - Wek_x\bar{U}' (jk^2\bar{f} + j\bar{f}'' - 4Wek_x\bar{U}'')) / (We\bar{L}^2) \end{pmatrix},$$

$$\mathcal{P}_2 = \begin{pmatrix} (k_x (\bar{f} (\bar{L}^2 k_x - 2jWe\bar{U}'') + 2We\bar{U}' (Wek_x\bar{U}' - j\bar{f}')))) / (We\bar{L}^2) \\ - (2jk_x \bar{f}') / We \\ (2\bar{f} k_x k_z) / We \\ (2Wek_x\bar{U}' (Wek_x\bar{U}' - j\bar{f}') - \bar{f} (k^2\bar{L}^2 + 2jWek_x\bar{U}'')) / (We\bar{L}^2) \\ - (2jk_z \bar{f}') / We \\ (\bar{f} (\bar{L}^2 k_z^2 - 2jWek_x\bar{U}'') + 2Wek_x\bar{U}' (Wek_x\bar{U}' - j\bar{f}')) / (We\bar{L}^2) \end{pmatrix},$$

$$\mathcal{P}_3 = \begin{pmatrix} - (j\bar{f} k_x \bar{U}') / (\bar{L}^2) \\ - (j\bar{f} k_x) / We \\ 0 \\ - (j\bar{f} k_x \bar{U}') / \bar{L}^2 \\ - (j\bar{f} k_z) / We \\ - (j\bar{f} k_x \bar{U}') / \bar{L}^2 \end{pmatrix}.$$

The operator \mathcal{Q} is defined as

$$\mathcal{Q} = \frac{(1 - \beta)}{Re} (\mathcal{Q}_1 + \mathcal{Q}_2 \partial_y), \quad (\text{A7})$$

where

$$\mathcal{Q}_1 = \begin{pmatrix} (k_z (\bar{f} (jWe\bar{U}'' - \bar{L}^2 k_x) + We\bar{U}' (j\bar{f}' - 2We k_x \bar{U}')) / (We\bar{L}^2) \\ (jk_z \bar{f}') / We \\ (\bar{f} (k_x - k_z) (k_x + k_z)) / We \\ (k_z (j\bar{f}\bar{U}'' + j\bar{U}'\bar{f}' - 2We k_x (\bar{U}')^2)) / \bar{L}^2 \\ - (jk_x \bar{f}') / We \\ (k_z (\bar{f} (\bar{L}^2 k_x + jWe\bar{U}'') + We\bar{U}' (j\bar{f}' - 2We k_x \bar{U}')) / (We\bar{L}^2) \end{pmatrix},$$

$$\mathcal{Q}_2 = \begin{pmatrix} (j\bar{f}k_z \bar{U}') / \bar{L}^2 \\ (j\bar{f}k_z) / We \\ 0 \\ (j\bar{f}k_z \bar{U}') / \bar{L}^2 \\ -(j\bar{f}k_x) / We \\ (j\bar{f}k_z \bar{U}') / \bar{L}^2 \end{pmatrix}.$$

The operators \mathcal{L}_{OS} , \mathcal{C}_p and \mathcal{S} are the Orr-Sommerfeld, coupling, and Squire operators respectively,

$$\begin{aligned} \mathcal{L}_{OS} &= \Delta^{-1} \left(-jk_x \bar{U} \Delta + jk_x \bar{U}'' + \frac{\beta}{Re} \Delta^2 \right), \\ \mathcal{C}_p &= -jk_z \bar{U}', \\ \mathcal{S} &= -jk_x \bar{U} + \frac{\beta}{Re} \Delta. \end{aligned} \tag{A8}$$

The operator \mathbf{B} in (2.6) is given by

$$\mathbf{B} = \begin{bmatrix} 0_{6 \times 3} \\ \mathbf{B}_1 \\ \mathbf{B}_2 \end{bmatrix}, \tag{A9}$$

where $0_{6 \times 3}$ represents a 6×3 matrix of zeros, and

$$\mathbf{B}_1 = \Delta^{-1} \begin{bmatrix} -jk_x \partial_y \\ -k^2 I \\ -jk_z \partial_y \end{bmatrix}^T, \quad \mathbf{B}_2 = \begin{bmatrix} jk_z I \\ 0 \\ -jk_x I \end{bmatrix}^T.$$

The operator \mathbf{C} in (2.6) is given by

$$\mathbf{C} = \begin{bmatrix} \mathbf{C}_u \\ \mathbf{C}_v \\ \mathbf{C}_w \end{bmatrix} = \begin{bmatrix} \mathbf{C}_u \\ \mathbf{C}_v \\ \mathbf{C}_w \end{bmatrix} = \frac{1}{k^2} \begin{bmatrix} 0_{1 \times 6} & jk_x \partial_y & -jk_z I \\ 0_{1 \times 6} & k^2 I & 0 \\ 0_{1 \times 6} & jk_z \partial_y & jk_x I \end{bmatrix}. \quad (\text{A10})$$

where $0_{1 \times 6}$ represents a 1×6 submatrix of zeros.

B Inner product that determines the kinetic energy

In this section, we define the inner product that determines the kinetic energy of fluctuations discussed in § 2.2.4.

The Hilbert space for the operator \mathbf{A} (see (2.6) in § 2.2.1) can be defined on the basis of its domain and boundary conditions [16, 19]. We define the space of functions \mathbb{H}_{OS}

$$\mathbb{H}_{OS} := \{g \in L^2[-1, 1]; g'' \in L^2[-1, 1]; g(\pm 1) = 0\}. \quad (\text{B1})$$

The domain of the operators \mathcal{P} , \mathcal{Q} , \mathcal{V} , and \mathcal{N} is $\mathbb{H}_{OS}^{6 \times 1}$, and the domain of \mathcal{S} is \mathbb{H}_{OS} . The domain of the \mathcal{L}_{OS} can be defined as

$$\mathcal{D}(\mathcal{L}_{OS}) := \{g \in \mathbb{H}_{OS}; g'''' \in L^2[-1, 1]; g'(\pm 1) = 0\}. \quad (\text{B2})$$

We define the following weighted inner product for functions $\boldsymbol{\xi}_1, \boldsymbol{\xi}_2 \in \mathbb{H}_{OS}^{8 \times 1}$,

$$\langle \boldsymbol{\xi}_1, Q\boldsymbol{\xi}_2 \rangle := \langle \boldsymbol{\xi}_1, \boldsymbol{\xi}_2 \rangle_e, \quad (\text{B3})$$

where $\langle \cdot, \cdot \rangle$ is the standard $L^2[-1, -1]$ inner product and Q is a linear operator given

by,

$$Q = \lim_{\iota \rightarrow 0^+} \frac{1}{k^2} \begin{bmatrix} \iota I_{6 \times 6} & 0 & 0 \\ 0 & -\Delta & 0 \\ 0 & 0 & I \end{bmatrix},$$

where, $I_{m \times n}$ is a block matrix identity operator of dimensions m by n . The inner product defined in (B3) determines the energy of velocity fluctuations. It can be verified that (see [19]) that the kinetic energy can be evaluated as

$$\langle \boldsymbol{\psi}(\boldsymbol{\kappa}, t), \boldsymbol{\psi}(\boldsymbol{\kappa}, t) \rangle_e = \langle \boldsymbol{\phi}_i(\boldsymbol{\kappa}, t), \boldsymbol{\phi}_i(\boldsymbol{\kappa}, t) \rangle = \int_{-1}^1 \mathbf{v}_i^*(\boldsymbol{\kappa}, y, t) \mathbf{v}_i(\boldsymbol{\kappa}, y, t) dy, \quad (\text{B4})$$

where $\boldsymbol{\phi}$ is the vector of outputs (i.e., the velocity fluctuations $\boldsymbol{\phi} = [u \ v \ w]^T$) and $\boldsymbol{\psi} = [\mathbf{r}^T \ v \ \eta]^T$ is the vector of state variables that appear in state-space representation (2.6) of the FENE-CR model presented in § 2.2.1. The adjoints of \mathbf{A} , \mathbf{F}_i , and \mathbf{C} are defined with respect to the inner-product defined in (B3) as

$$\begin{aligned} \langle \boldsymbol{\psi}, \mathbf{A}\boldsymbol{\psi} \rangle_e &= \left\langle \mathbf{A}^\dagger \boldsymbol{\psi}, \boldsymbol{\psi} \right\rangle_e \\ \langle \boldsymbol{\psi}, \mathbf{F}_i g(t) \rangle_e &= \left\langle \mathbf{F}_i^\dagger \boldsymbol{\psi}, g(t) \right\rangle_{\mathbb{C}} \\ \langle \boldsymbol{\phi}, \mathbf{C}\boldsymbol{\psi} \rangle &= \left\langle \mathbf{C}^\dagger \boldsymbol{\phi}, \boldsymbol{\psi} \right\rangle_e \end{aligned} \quad (\text{B5})$$

Here, $\langle \cdot, \cdot \rangle_e$ is the weighted inner product defined in (B3), $\langle \cdot, \cdot \rangle$ is the standard $L^2[-1, -1]$ inner product, and $\langle \cdot, \cdot \rangle_{\mathbb{C}}$ is the standard vector inner product that induces a Euclidean norm.

C Operators governing 2D channel flow of an Oldroyd-B fluid

The variable coefficients for the operator in (3.8a) are given by (we have suppressed the dependence on ω for the sake of brevity, e.g., $a_0(y, \omega)$ is denoted as $a_0(y)$)

$$\begin{aligned}
a_4(y) &= \frac{\beta - 1}{c(y)} - \beta, \\
a_3(y) &= -\frac{2(\beta - 1)(c'(y) - i k_x We c(y) U'(y))}{c(y)^2}, \\
a_2(y) &= \frac{(1 - \beta) c''(y)}{c(y)^2} + \frac{2i(1 - \beta) k_x We c'(y) U'(y)}{c(y)^2} \\
&\quad - \frac{2(1 - \beta) k_x^2 We^2 U'(y)^2}{c(y)^2} + \frac{2i(1 - \beta) k_x We U''(y)}{c(y)^2} \\
&\quad - \frac{4i(1 - \beta) k_x We c'(y) U'(y)}{c(y)^3} - \frac{2(1 - \beta) c'(y)^2}{c(y)^3} - \frac{4(1 - \beta) k_x^2 We^2 U'(y)^2}{c(y)^3} \\
&\quad + \frac{2(1 - \beta) k_x^2 We^2 U'(y)^2}{c(y)} + \frac{2(1 - \beta) k_x^2}{c(y)} - \frac{3i(1 - \beta) k_x We U''(y)}{c(y)} + 2\beta k_x^2, \\
a_1(y) &= \frac{12(1 - \beta) k_x^2 We^2 c'(y) U'(y)^2}{c(y)^4} + \frac{12i(1 - \beta) k_x We c'(y)^2 U'(y)}{c(y)^4} \\
&\quad - \frac{4i(1 - \beta) k_x We c''(y) U'(y)}{c(y)^3} + \frac{8(1 - \beta) k_x^2 We^2 c'(y) U'(y)^2}{c(y)^3} \\
&\quad - \frac{8i(1 - \beta) k_x We c'(y) U''(y)}{c(y)^3} - \frac{4i(1 - \beta) k_x^3 We^3 U'(y)^3}{c(y)^3} \\
&\quad - \frac{8(1 - \beta) k_x^2 We^2 U'(y) U''(y)}{c(y)^3} \\
&\quad - \frac{2(1 - \beta) k_x^2 c'(y)}{c(y)^2} + \frac{2i(1 - \beta) k_x We c'(y) U''(y)}{c(y)^2} \\
&\quad - \frac{4i(1 - \beta) k_x^3 We^3 U'(y)^3}{c(y)^2} - \frac{6(1 - \beta) k_x^2 We^2 U'(y) U''(y)}{c(y)^2} \\
&\quad + \frac{2i(1 - \beta) k_x^3 We U'(y)}{c(y)} + \frac{4(1 - \beta) k_x^2 We^2 U'(y) U''(y)}{c(y)},
\end{aligned}$$

where $c(y) = i\omega + 1 + i k_x We U(y)$,

$$\begin{aligned}
c_{11}(y) &= \frac{2 We U'(y)}{c(y)} + \frac{2 We U'(y)}{c(y)^2}, \\
c_{12}(y) &= \frac{4i k_x We^2 U'(y)^2}{c(y)} - \frac{4i k_x We^2 U'(y)^2}{c(y)^3} + \frac{2i k_x}{c(y)}, \\
c_{13}(y) &= + \frac{4 k_x^2 We^3 U'(y)^3}{c(y)^3} \\
&\quad + \frac{4 k_x^2 We^3 U'(y)^3}{c(y)^2} + \frac{2 k_x^2 We U'(y)}{c(y)^2} + \frac{2i k_x We^2 U'(y) U''(y)}{c(y)^2} \\
&\quad + \frac{4i k_x We^2 U'(y) U''(y)}{c(y)}, \\
c_{21}(y) &= \frac{1}{c(y)}, \\
c_{22}(y) &= - \frac{2i k_x We U'(y)}{c(y)^2}, \\
c_{23}(y) &= \frac{2 k_x^2 We^2 U'(y)^2}{c(y)} + \frac{2 k_x^2 We^2 U'(y)^2}{c(y)^2} + \frac{k_x^2}{c(y)} + \frac{i k_x We U''(y)}{c(y)}, \\
c_{31}(y) &= - \frac{2i k_x}{c(y)}, \\
c_{32}(y) &= \frac{2 k_x^2 We U'(y)}{c(y)}.
\end{aligned}$$

D Operators governing 3D channel flow of an Oldroyd-B fluid

The nonzero components in the operator \mathcal{V} in (3.37) are derived from the following relations that come from (3.7c). Note that $c(y) = i\omega + 1/We + i k_x U(y)$ in this section.

$$\tau_{zz}(y) = \frac{2 i k_z}{We c(y)} w(y) \quad (D1a)$$

$$\tau_{yz}(y) = \frac{1}{c(y)} \left(\frac{i k_z}{We} v(y) + i k_x T_{xy}(y) w(y) + \frac{w'(y)}{We} \right) \quad (D1b)$$

$$\tau_{yy}(y) = \frac{2 i k_x T_{xy}(y)}{c(y)} v(y) + \frac{2}{We c(y)} v'(y) \quad (D1c)$$

$$\tau_{xz}(y) = \frac{1}{c(y)} \left(U'(y) \tau_{yz}(y) + i k_x T_{xx}(y) w(y) + \frac{i k_z}{We} u(y) + \frac{i k_x}{We} w(y) + T_{xy}(y) w'(y) \right) \quad (D1d)$$

$$\begin{aligned} \tau_{xy}(y) = & \frac{1}{c(y)} \left(i k_x T_{xy}(y) u(y) + i k_x T_{xx}(y) v(y) - T'_{xy}(y) v(y) \right) + \\ & + \frac{1}{c(y)} \left(\frac{i k_x}{We} v(y) + \frac{1}{We} u'(y) + U'(y) \tau_{yy} + T_{xy}(y) v'(y) \right) \end{aligned} \quad (D1e)$$

$$\begin{aligned} \tau_{xx}(y) = & \quad (D1f) \\ & \frac{1}{c(y)} \left(\frac{2 i k_x}{We} u(y) + 2 k_x T_{xx}(y) u(y) - T'_{xx}(y) v(y) + 2 T_{xy}(y) u'(y) + 2 U'(y) \tau_{xy}(y) \right) \end{aligned} \quad (D1g)$$

D.1 Evolution form

The state variables for this system are the wall-normal velocity and vorticity, $\phi = [v \ \eta]^T$ in (4.6). The boundary conditions are

$$v(\pm 1) = [Dv(\cdot)](\pm 1) = \eta(\pm 1) = 0. \quad (D2)$$

The operator-valued matrices \mathcal{A} , \mathcal{B} , \mathcal{C}_v , and \mathcal{C}_{xx} in are detailed in this section. \mathcal{A} is of size 2×2 with non-zero elements

$$\begin{aligned}\mathcal{A}(1,1) &= \left(\sum_{n=0}^4 a_{n,11}(y, \omega) D^n \right), \\ \mathcal{A}(2,1) &= \left(\sum_{n=0}^2 a_{n,21}(y, \omega) D^n \right), \\ \mathcal{A}(2,2) &= \left(\sum_{n=0}^2 a_{n,22}(y, \omega) D^n \right),\end{aligned}$$

where

$$\begin{aligned}a_{4,11} &= -\frac{(1-\beta)}{We c(y)} - \beta, \\ a_{3,11} &= \frac{2(1-\beta) c'(y)}{We c(y)^2} - \frac{2i(1-\beta) k_x T_{xy}(y)}{c(y)}, \\ a_{2,11} &= \frac{(1-\beta) c''(y)}{We c(y)^2} + \frac{2i(1-\beta) k_x T_{xy}(y) c'(y)}{c(y)^2} - \frac{4i(1-\beta) k_x c'(y) U'(y)}{We c(y)^3} \\ &\quad - \frac{2(1-\beta) c'(y)^2}{We c(y)^3} + \frac{2(1-\beta) k^2}{We c(y)} + \frac{(1-\beta) k_x^2 T_{xx}(y)}{c(y)} \\ &\quad - \frac{2(1-\beta) k_x^2 T_{xy}(y) U'(y)}{c(y)^2} - \frac{4(1-\beta) k_x^2 U'(y)^2}{We c(y)^3} \\ &\quad - \frac{3i(1-\beta) k_x T'_{xy}(y)}{c(y)} + \frac{2i(1-\beta) k_x U''(y)}{We c(y)^2} + 2\beta k^2, \\ a_{1,11} &= -\frac{4i(1-\beta) k_x c''(y) U'(y)}{We c(y)^3} + \frac{8(1-\beta) k_x^2 T_{xy}(y) c'(y) U'(y)}{c(y)^3} \\ &\quad + \frac{12(1-\beta) k_x^2 c'(y) U'(y)^2}{We c(y)^4} - \frac{2(1-\beta) k_x^2 c'(y)}{We c(y)^2} + \frac{2i(1-\beta) k_x c'(y) T'_{xy}(y)}{c(y)^2} \\ &\quad - \frac{8i(1-\beta) k_x c'(y) U''(y)}{We c(y)^3} + \frac{12i(1-\beta) k_x c'(y)^2 U'(y)}{We c(y)^4} - \frac{2(1-\beta) k_x^2 c'(y)}{We c(y)^2} \\ &\quad + \frac{2i(1-\beta) k^2 k_x T_{xy}(y)}{c(y)} - \frac{2i(1-\beta) k_x^3 T_{xx}(y) U'(y)}{c(y)^2} \\ &\quad - \frac{4i(1-\beta) k_x^3 T_{xy}(y) U'(y)^2}{c(y)^3} + \frac{(1-\beta) k_x^2 T'_{xx}(y)}{c(y)} - \frac{2(1-\beta) k_x^2 T'_{xy}(y) U'(y)}{c(y)^2} \\ &\quad - \frac{4(1-\beta) k_x^2 T_{xy}(y) U''(y)}{c(y)^2} - \frac{8(1-\beta) k_x^2 U'(y) U''(y)}{We c(y)^3},\end{aligned}$$

$$\begin{aligned}
a_{0,11} = & \frac{(1-\beta)k^2c''(y)}{We c(y)^2} + \frac{(1-\beta)k_x^2 T_{xx}(y)c''(y)}{c(y)^2} + \frac{4(1-\beta)k_x^2 T_{xy}(y)c''(y)U'(y)}{c(y)^3} \\
& + \frac{i(1-\beta)k_x c''(y)T'_{xy}(y)}{c(y)^2} - \frac{2i(1-\beta)k^2 k_x T_{xy}(y)c'(y)}{c(y)^2} \\
& + \frac{4i(1-\beta)k^2 k_x c'(y)U'(y)}{We c(y)^3} - \frac{2(1-\beta)k^2 c'(y)^2}{We c(y)^3} \\
& + \frac{4i(1-\beta)k_x^3 T_{xx}(y)c'(y)U'(y)}{c(y)^3} \\
& + \frac{12i(1-\beta)k_x^3 T_{xy}(y)c'(y)U'(y)^2}{c(y)^4} + \frac{(1-\beta)k_x^2 c'(y)T'_{xx}(y)}{c(y)^2} \\
& - \frac{2(1-\beta)k_x^2 T_{xx}(y)c'(y)^2}{c(y)^3} + \frac{4(1-\beta)k_x^2 c'(y)T'_{xy}(y)U'(y)}{c(y)^3} \\
& + \frac{8(1-\beta)k_x^2 T_{xy}(y)c'(y)U''(y)}{c(y)^3} - \frac{12(1-\beta)k_x^2 T_{xy}(y)c'(y)^2 U'(y)}{c(y)^4} \\
& - \frac{2i(1-\beta)k_x c'(y)^2 T'_{xy}(y)}{c(y)^3} - \frac{(1-\beta)k^4}{We c(y)} - \frac{(1-\beta)k^2 k_x^2 T_{xx}(y)}{c(y)} \\
& - \frac{2(1-\beta)k^2 k_x^2 T_{xy}(y)U'(y)}{c(y)^2} + \frac{i(1-\beta)k^2 k_x T'_{xy}(y)}{c(y)} - \frac{2i(1-\beta)k^2 k_x U''(y)}{We c(y)^2} \\
& - \frac{2i(1-\beta)k_x^3 T'_{xx}(y)U'(y)}{c(y)^2} - \frac{2i(1-\beta)k_x^3 T_{xx}(y)U''(y)}{c(y)^2} \\
& - \frac{4i(1-\beta)k_x^3 T'_{xy}(y)U'(y)^2}{c(y)^3} - \frac{8i(1-\beta)k_x^3 T_{xy}(y)U'(y)U''(y)}{c(y)^3} \\
& - \frac{2(1-\beta)k_x^2 T'_{xy}(y)U''(y)}{c(y)^2} - \beta k^4, \\
a_{2,21} = & -\frac{i(1-\beta)k_z U'(y)}{We c(y)^2}, \\
a_{1,21} = & \frac{i(1-\beta)k_z T_{xy}(y)c'(y)}{c(y)^2} + \frac{4i(1-\beta)k_z c'(y)U'(y)}{We c(y)^3} + \frac{3(1-\beta)k_x k_z T_{xy}(y)U'(y)}{c(y)^2} \\
& + \frac{4(1-\beta)k_x k_z U'(y)^2}{We c(y)^3} - \frac{2i(1-\beta)k_z U''(y)}{We c(y)^2}, \\
a_{0,21} = & -\frac{(1-\beta)k_x k_z T_{xx}(y)c'(y)}{c(y)^2} - \frac{4(1-\beta)k_x k_z T_{xy}(y)c'(y)U'(y)}{c(y)^3} \\
& - \frac{i(1-\beta)k_z c'(y)T'_{xy}(y)}{c(y)^2} + \frac{2i(1-\beta)k_x^2 k_z T_{xx}(y)U'(y)}{c(y)^2} \\
& + \frac{4i(1-\beta)k_x^2 k_z T_{xy}(y)U'(y)^2}{c(y)^3} + \frac{i(1-\beta)k_x^2 k_z U'(y)}{We c(y)^2} \\
& + \frac{2(1-\beta)k_x k_z T_{xy}(y)U''(y)}{c(y)^2} + \frac{i(1-\beta)k_z^3 U'(y)}{We c(y)^2},
\end{aligned}$$

$$\begin{aligned}
a_{2,22} &= -\frac{(1-\beta)}{We c(y)} - \beta, \\
a_{1,22} &= \frac{(1-\beta) c'(y)}{We c(y)^2} - \frac{2i(1-\beta) k_x T_{xy}(y)}{c(y)} - \frac{i(1-\beta) k_x U'(y)}{We c(y)^2}, \\
a_{0,22} &= \frac{i(1-\beta) k_x T_{xy}(y) c'(y)}{c(y)^2} + \frac{(1-\beta) k^2}{We c(y)} + \frac{(1-\beta) k_x^2 T_{xx}(y)}{c(y)} \\
&\quad + \frac{(1-\beta) k_x^2 T_{xy}(y) U'(y)}{c(y)^2} - \frac{i(1-\beta) k_x T'_{xy}(y)}{c(y)} + \beta k^2.
\end{aligned}$$

The operators \mathcal{C} (for the velocity output) and \mathcal{B} are given by [16]

$$\mathcal{C} = \frac{1}{k^2} \begin{bmatrix} i k_x D & -i k_z \\ k^2 & 0 \\ i k_z D & i k_x \end{bmatrix}, \quad \mathcal{B} = \begin{bmatrix} -i k_x D & -k^2 & -i k_z D \\ i k_z & 0 & -i k_x \end{bmatrix}. \quad (\text{D3a})$$

For the stress output τ_{xx} , \mathcal{C}_{xx} is 1×2 block-matrix operator with

$$\begin{aligned}
\mathcal{C}_{xx}(1, 1) &= \left(\sum_{n=0}^2 c_{n,11}(y, \omega) D^n \right), \\
\mathcal{C}_{xx}(1, 2) &= \left(\sum_{n=0}^1 c_{n,12}(y, \omega) D^n \right),
\end{aligned} \quad (\text{D3b})$$

where,

$$\begin{aligned}
c_{2,11} &= \frac{2ik_x T_{xy}(y)}{k^2 c(y)} + \frac{2ik_x U'(y)}{k^2 We c(y)^2}, \\
c_{1,11} &= -\frac{2k_x^2 T_{xx}(y)}{k^2 c(y)} - \frac{2k_x^2}{k^2 We c(y)} + \frac{2k_z^2 T_{xy}(y) U'(y)}{k^2 c(y)^2} + \frac{4U'(y)^2}{We c(y)^3}, \\
c_{0,11} &= \frac{2ik_x T_{xx}(y) U'(y)}{c(y)^2} + \frac{4ik_x T_{xy}(y) U'(y)^2}{c(y)^3} \\
&\quad + \frac{2ik_x U'(y)}{We c(y)^2} - \frac{T'_{xx}(y)}{c(y)} - \frac{2T'_{xy}(y) U'(y)}{c(y)^2}, \\
c_{1,12} &= -\frac{2ik_z T_{xy}(y)}{k^2 c(y)} - \frac{2ik_z U'(y)}{k^2 We c(y)^2}, \\
c_{0,12} &= \frac{2k_x k_z T_{xx}(y)}{k^2 c(y)} + \frac{2k_x k_z T_{xy}(y) U'(y)}{k^2 c(y)^2} + \frac{2k_x k_z}{k^2 We c(y)}.
\end{aligned}$$

D.2 Descriptor form with the stress eliminated

The state variables are the velocity and pressure, $\phi = [u \ v \ w \ p]^T$ in (4.6), and the boundary conditions are

$$u(\pm 1) = v(\pm 1) = w(\pm 1) = [Dv(\cdot)](\pm 1) = 0.$$

In this representation the operator-valued matrix \mathcal{A} is of size 4×4 with components

$$\mathcal{A}(i, j) = \left(\sum_{n=0}^2 a_{n,ij}(y, \omega) D^n \right),$$

where the non-zero coefficients $a_{n,ij}$ are given by

$$\begin{aligned} a_{2,11} &= -\frac{(1-\beta)}{We \ c(y)} - \beta, \\ a_{1,11} &= \frac{(1-\beta) \ (c'(y) - ik_x \ (3We \ c(y)T_{xy}(y) + 2U'(y)))}{We \ c(y)^2}, \\ a_{0,11} &= \frac{(1-\beta) \ k_x \ T_{xy}(y) \ (2k_x \ U'(y) + ic'(y))}{c(y)^2} \\ &\quad + \frac{(1-\beta) \ (2k_x^2 + k_x \ We \ (2k_x \ T_{xx}(y) - iT'_{xy}(y)) + k_z^2)}{We \ c(y)} + \beta k^2, \\ a_{2,12} &= -\frac{(1-\beta) \ (We \ c(y)T_{xy}(y) + 2U'(y))}{We \ c(y)^2}, \\ a_{1,12} &= \frac{(1-\beta) \ T_{xy}(y)c'(y)}{c(y)^2} + \frac{4(1-\beta) \ c'(y)U'(y)}{We \ c(y)^3} - \frac{i(1-\beta) \ k_x \ T_{xx}(y)}{c(y)} \\ &\quad - \frac{4i(1-\beta) \ k_x \ T_{xy}(y)U'(y)}{c(y)^2} - \frac{4i(1-\beta) \ k_x \ U'(y)^2}{We \ c(y)^3} \\ &\quad - \frac{i(1-\beta) \ k_x}{We \ c(y)} - \frac{2(1-\beta) \ U''(y)}{We \ c(y)^2}, \end{aligned}$$

$$\begin{aligned}
a_{0,12} &= \frac{i(1-\beta)k_x T_{xx}(y)c'(y)}{c(y)^2} + \frac{4i(1-\beta)k_x T_{xy}(y)c'(y)U'(y)}{c(y)^3} \\
&\quad + \frac{i(1-\beta)k_x c'(y)}{We c(y)^2} - \frac{(1-\beta)c'(y)T'_{xy}(y)}{c(y)^2} \\
&\quad + \frac{2(1-\beta)k_x^2 T_{xx}(y)U'(y)}{c(y)^2} + \frac{4(1-\beta)k_x^2 T_{xy}(y)U'(y)^2}{c(y)^3} + \frac{2(1-\beta)k_x^2 U'(y)}{We c(y)^2} \\
&\quad - \frac{2i(1-\beta)k_x T_{xy}(y)U''(y)}{c(y)^2} + \frac{(1-\beta)k_z^2 U'(y)}{We c(y)^2}, \\
a_{1,13} &= -\frac{i(1-\beta)k_z (We c(y)T_{xy}(y) + U'(y))}{We c(y)^2}, \\
a_{0,13} &= \frac{(1-\beta)k_x k_z (We c(y)T_{xx}(y) + c(y) + We T_{xy}(y)U'(y))}{We c(y)^2}, \\
a_{0,14} &= ik_x, \\
a_{1,21} &= -\frac{i(1-\beta)k_x}{We c(y)}, \\
a_{0,21} &= \frac{(1-\beta)k_x^2 T_{xy}(y)}{c(y)}, \\
a_{2,22} &= -\frac{2(1-\beta)}{We c(y)} - \beta, \\
a_{1,22} &= \frac{2(1-\beta)c'(y)}{We c(y)^2} - \frac{3i(1-\beta)k_x T_{xy}(y)}{c(y)} - \frac{2i(1-\beta)k_x U'(y)}{We c(y)^2},
\end{aligned}$$

$$\begin{aligned}
a_{0,22} &= \frac{2i(1-\beta)k_x T_{xy}(y)c'(y)}{c(y)^2} + \frac{(1-\beta)k_x^2 T_{xx}(y)}{c(y)} + \frac{2(1-\beta)k_x^2 T_{xy}(y)U'(y)}{c(y)^2} \\
&\quad + \frac{(1-\beta)k_x^2}{We c(y)} - \frac{i(1-\beta)k_x T'_{xy}(y)}{c(y)} + \frac{(1-\beta)k_z^2}{We c(y)} + \beta k^2, \\
a_{1,23} &= -\frac{i(1-\beta)k_z}{We c(y)}, \\
a_{0,23} &= \frac{(1-\beta)k_x k_z T_{xy}(y)}{c(y)}, \\
a_{1,24} &= 1, \\
a_{0,31} &= \frac{(1-\beta)k_x k_z}{We c(y)}, \\
a_{1,32} &= -\frac{i(1-\beta)k_z}{We c(y)}, \\
a_{0,32} &= \frac{(1-\beta)k_z(k_x U'(y) + i c'(y))}{We c(y)^2}, \\
a_{2,33} &= -\frac{(1-\beta)}{We c(y)} - \beta, \\
a_{1,33} &= \frac{(1-\beta)c'(y)}{We c(y)^2} - \frac{2i(1-\beta)k_x T_{xy}(y)}{c(y)} - \frac{i(1-\beta)k_x U'(y)}{We c(y)^2}, \\
a_{0,33} &= \frac{i(1-\beta)k_x T_{xy}(y)c'(y)}{c(y)^2} + \frac{(1-\beta)k_x^2 T_{xx}(y)}{c(y)} + \frac{(1-\beta)k_x^2 T_{xy}(y)U'(y)}{c(y)^2} \\
&\quad + \frac{(1-\beta)k_x^2}{We c(y)} - \frac{i(1-\beta)k_x T'_{xy}(y)}{c(y)} + \frac{2(1-\beta)k_z^2}{We c(y)} + \beta k^2, \\
a_{0,34} &= i k_z.
\end{aligned}$$

The expressions for \mathcal{B} and \mathcal{C}_v are given by

$$\mathcal{B} = \begin{bmatrix} 1 & 0 & 0 \\ 0 & 1 & 0 \\ 0 & 0 & 1 \\ 0 & 0 & 0 \end{bmatrix}, \quad \mathcal{C} = \begin{bmatrix} 1 & 0 & 0 & 0 \\ 0 & 1 & 0 & 0 \\ 0 & 0 & 1 & 0 \end{bmatrix},$$

and for the stress output τ_{xx} , \mathcal{C}_{xx} is a 1×4 block-matrix operator given by

$$\mathcal{C}_{xx}(i, j) = \left(\sum_{n=0}^1 c_{n,ij}(y, \omega) D^n \right), \quad (\text{D4})$$

where the non-zero coefficients $c_{n,ij}$ are given by

$$\begin{aligned}
c_{1,11} &= \frac{2 (We c(y) T_{xy}(y) + U'(y))}{We c(y)^2}, \\
c_{0,11} &= \frac{2ik_x (We c(y) T_{xx}(y) + c(y) + We T_{xy}(y) U'(y))}{We c(y)^2}, \\
c_{1,12} &= \frac{2U'(y) (We c(y) T_{xy}(y) + 2U'(y))}{We c(y)^3}, \\
c_{0,12} &= \frac{2ic(y)U'(y) (k_x We T_{xx}(y) + k_x + iWe T'_{xy}(y))}{We c(y)^3} \\
&\quad + \frac{-We c(y)^2 T'_{xx}(y) + 4ik_x We T_{xy}(y) U'(y)^2}{We c(y)^3}.
\end{aligned}$$

E Operators governing channel flow of an Oldroyd-B fluid

The equations governing channel flow of an Oldroyd-B fluid (4.5) can be recast to the representation in (4.6) as discussed in § 4.2.1. System (4.6) can be expressed in two forms, the evolution form (where the pressure is eliminated), and the descriptor form (where the pressure is not eliminated). In this section we present the operators \mathcal{A} , \mathcal{B} , \mathcal{C}_v , and \mathcal{C}_{xx} in (4.6) in both forms.

E.1 Evolution form

The state variables for the evolution form [6] are the wall-normal velocity and vorticity, $\phi = [v \ \eta]^T$ in (4.6). The boundary conditions are

$$v(\pm 1) = [Dv(\cdot)](\pm 1) = \eta(\pm 1) = 0. \quad (\text{E5})$$

The operator-valued matrices \mathcal{A} , \mathcal{B} , \mathcal{C}_v , and \mathcal{C}_{xx} are detailed in this section. \mathcal{A} is of size 2×2 with elements

$$\begin{aligned} \mathcal{A}(1, 1) &= \left(\sum_{n=0}^4 a_{n,11}(y, \omega) D^n \right), \\ \mathcal{A}(1, 2) &= 0, \\ \mathcal{A}(2, 1) &= \left(\sum_{n=0}^2 a_{n,21}(y, \omega) D^n \right), \\ \mathcal{A}(2, 2) &= \left(\sum_{n=0}^2 a_{n,22}(y, \omega) D^n \right), \end{aligned}$$

where the dependence on ω enters through the $c(y)$ in (4.30), and the nonzero coefficients $a_{n,ij}$ are given by

$$\begin{aligned}
a_{4,11} &= -\frac{(1-\beta)}{We c(y)} - \beta, \\
a_{3,11} &= \frac{2(1-\beta) c'(y)}{We c(y)^2} - \frac{2i(1-\beta) k_x \bar{T}_{xy}(y)}{c(y)}, \\
a_{2,11} &= \frac{(1-\beta) c''(y)}{We c(y)^2} + \frac{2i(1-\beta) k_x \bar{T}_{xy}(y) c'(y)}{c(y)^2} - \frac{4i(1-\beta) k_x c'(y) \bar{U}'(y)}{We c(y)^3} \\
&\quad - \frac{2(1-\beta) c'(y)^2}{We c(y)^3} + \frac{2(1-\beta) k^2}{We c(y)} + \frac{(1-\beta) k_x^2 \bar{T}_{xx}(y)}{c(y)} \\
&\quad - \frac{2(1-\beta) k_x^2 \bar{T}_{xy}(y) \bar{U}'(y)}{c(y)^2} - \frac{4(1-\beta) k_x^2 \bar{U}'(y)^2}{We c(y)^3} \\
&\quad - \frac{3i(1-\beta) k_x \bar{T}'_{xy}(y)}{c(y)} + \frac{2i(1-\beta) k_x \bar{U}''(y)}{We c(y)^2} + 2\beta k^2, \\
a_{1,11} &= -\frac{4i(1-\beta) k_x c''(y) \bar{U}'(y)}{We c(y)^3} + \frac{8(1-\beta) k_x^2 \bar{T}_{xy}(y) c'(y) \bar{U}'(y)}{c(y)^3} \\
&\quad + \frac{12(1-\beta) k_x^2 c'(y) \bar{U}'(y)^2}{We c(y)^4} - \frac{2(1-\beta) k_x^2 c'(y)}{We c(y)^2} + \frac{2i(1-\beta) k_x c'(y) \bar{T}'_{xy}(y)}{c(y)^2} \\
&\quad - \frac{8i(1-\beta) k_x c'(y) \bar{U}''(y)}{We c(y)^3} + \frac{12i(1-\beta) k_x c'(y)^2 \bar{U}'(y)}{We c(y)^4} - \frac{2(1-\beta) k_x^2 c'(y)}{We c(y)^2} \\
&\quad + \frac{2i(1-\beta) k^2 k_x \bar{T}_{xy}(y)}{c(y)} - \frac{2i(1-\beta) k_x^3 \bar{T}_{xx}(y) \bar{U}'(y)}{c(y)^2} \\
&\quad - \frac{4i(1-\beta) k_x^3 \bar{T}_{xy}(y) \bar{U}'(y)^2}{c(y)^3} + \frac{(1-\beta) k_x^2 \bar{T}'_{xx}(y)}{c(y)} \\
&\quad - \frac{2(1-\beta) k_x^2 \bar{T}'_{xy}(y) \bar{U}'(y)}{c(y)^2} - \frac{4(1-\beta) k_x^2 \bar{T}_{xy}(y) \bar{U}''(y)}{c(y)^2} \\
&\quad - \frac{8(1-\beta) k_x^2 \bar{U}'(y) \bar{U}''(y)}{We c(y)^3},
\end{aligned}$$

$$\begin{aligned}
a_{0,11} = & \frac{(1-\beta)k^2c''(y)}{We c(y)^2} + \frac{(1-\beta)k_x^2\bar{T}_{xx}(y)c''(y)}{c(y)^2} + \frac{4(1-\beta)k_x^2\bar{T}_{xy}(y)c''(y)\bar{U}'(y)}{c(y)^3} \\
& + \frac{i(1-\beta)k_xc''(y)\bar{T}'_{xy}(y)}{c(y)^2} - \frac{2i(1-\beta)k^2k_x\bar{T}_{xy}(y)c'(y)}{c(y)^2} \\
& + \frac{4i(1-\beta)k^2k_xc'(y)\bar{U}'(y)}{We c(y)^3} - \frac{2(1-\beta)k^2c'(y)^2}{We c(y)^3} \\
& + \frac{4i(1-\beta)k_x^3\bar{T}_{xx}(y)c'(y)\bar{U}'(y)}{c(y)^3} \\
& + \frac{12i(1-\beta)k_x^3\bar{T}_{xy}(y)c'(y)\bar{U}'(y)^2}{c(y)^4} + \frac{(1-\beta)k_x^2c'(y)\bar{T}'_{xx}(y)}{c(y)^2} \\
& - \frac{2(1-\beta)k_x^2\bar{T}_{xx}(y)c'(y)^2}{c(y)^3} + \frac{4(1-\beta)k_x^2c'(y)\bar{T}'_{xy}(y)\bar{U}'(y)}{c(y)^3} \\
& + \frac{8(1-\beta)k_x^2\bar{T}_{xy}(y)c'(y)\bar{U}''(y)}{c(y)^3} - \frac{12(1-\beta)k_x^2\bar{T}_{xy}(y)c'(y)^2\bar{U}'(y)}{c(y)^4} \\
& - \frac{2i(1-\beta)k_xc'(y)^2\bar{T}'_{xy}(y)}{c(y)^3} - \frac{(1-\beta)k^4}{We c(y)} - \frac{(1-\beta)k^2k_x^2\bar{T}_{xx}(y)}{c(y)} \\
& - \frac{2(1-\beta)k^2k_x^2\bar{T}_{xy}(y)\bar{U}'(y)}{c(y)^2} + \frac{i(1-\beta)k^2k_x\bar{T}'_{xy}(y)}{c(y)} - \frac{2i(1-\beta)k^2k_x\bar{U}''(y)}{We c(y)^2} \\
& - \frac{2i(1-\beta)k_x^3\bar{T}'_{xx}(y)\bar{U}'(y)}{c(y)^2} - \frac{2i(1-\beta)k_x^3\bar{T}_{xx}(y)\bar{U}''(y)}{c(y)^2} \\
& - \frac{4i(1-\beta)k_x^3\bar{T}_{xy}(y)\bar{U}'(y)^2}{c(y)^3} - \frac{8i(1-\beta)k_x^3\bar{T}_{xy}(y)\bar{U}'(y)\bar{U}''(y)}{c(y)^3} \\
& - \frac{2(1-\beta)k_x^2\bar{T}'_{xy}(y)\bar{U}''(y)}{c(y)^2} - \beta k^4, \\
a_{2,21} = & -\frac{i(1-\beta)k_z\bar{U}'(y)}{We c(y)^2}, \\
a_{1,21} = & \frac{i(1-\beta)k_z\bar{T}_{xy}(y)c'(y)}{c(y)^2} + \frac{4i(1-\beta)k_zc'(y)\bar{U}'(y)}{We c(y)^3} + \frac{3(1-\beta)k_xk_z\bar{T}_{xy}(y)\bar{U}'(y)}{c(y)^2} \\
& + \frac{4(1-\beta)k_xk_z\bar{U}'(y)^2}{We c(y)^3} - \frac{2i(1-\beta)k_z\bar{U}''(y)}{We c(y)^2}, \\
a_{0,21} = & -\frac{(1-\beta)k_xk_z\bar{T}_{xx}(y)c'(y)}{c(y)^2} - \frac{4(1-\beta)k_xk_z\bar{T}_{xy}(y)c'(y)\bar{U}'(y)}{c(y)^3} \\
& - \frac{i(1-\beta)k_zc'(y)\bar{T}'_{xy}(y)}{c(y)^2} + \frac{2i(1-\beta)k_x^2k_z\bar{T}_{xx}(y)\bar{U}'(y)}{c(y)^2} \\
& + \frac{4i(1-\beta)k_x^2k_z\bar{T}_{xy}(y)\bar{U}'(y)^2}{c(y)^3} + \frac{i(1-\beta)k_x^2k_z\bar{U}'(y)}{We c(y)^2} \\
& + \frac{2(1-\beta)k_xk_z\bar{T}_{xy}(y)\bar{U}''(y)}{c(y)^2} + \frac{i(1-\beta)k_z^3\bar{U}'(y)}{We c(y)^2},
\end{aligned}$$

$$\begin{aligned}
a_{2,22} &= -\frac{(1-\beta)}{We c(y)} - \beta, \\
a_{1,22} &= \frac{(1-\beta) c'(y)}{We c(y)^2} - \frac{2i(1-\beta) k_x \bar{T}_{xy}(y)}{c(y)} - \frac{i(1-\beta) k_x \bar{U}'(y)}{We c(y)^2}, \\
a_{0,22} &= \frac{i(1-\beta) k_x \bar{T}_{xy}(y) c'(y)}{c(y)^2} + \frac{(1-\beta) k^2}{We c(y)} + \frac{(1-\beta) k_x^2 \bar{T}_{xx}(y)}{c(y)} + \frac{(1-\beta) k_x^2 \bar{T}_{xy}(y) \bar{U}'(y)}{c(y)^2} \\
&\quad - \frac{i(1-\beta) k_x \bar{T}'_{xy}(y)}{c(y)} + \beta k^2,
\end{aligned}$$

where $c(y) = i\omega + 1/We + i k_x \bar{U}(y)$ (see (4.30)).

The operators \mathcal{C}_v (for the velocity output) and \mathcal{B} are given by [16]

$$\mathcal{C}_v = \frac{1}{k^2} \begin{bmatrix} i k_x D & -i k_z \\ k^2 & 0 \\ i k_z D & i k_x \end{bmatrix}, \quad \mathcal{B} = \begin{bmatrix} -i k_x D & -k^2 & -i k_z D \\ i k_z & 0 & -i k_x \end{bmatrix}. \quad (\text{E6a})$$

For the stress output τ_{xx} , \mathcal{C}_{xx} is 1×2 block-matrix operator with

$$\begin{aligned}
\mathcal{C}_{xx}(1,1) &= \left(\sum_{n=0}^2 c_{n,11}(y, \omega) D^n \right), \\
\mathcal{C}_{xx}(1,2) &= \left(\sum_{n=0}^1 c_{n,12}(y, \omega) D^n \right),
\end{aligned} \quad (\text{E6b})$$

where the nonzero coefficients $c_{n,ij}$ are given by

$$\begin{aligned}
c_{2,11} &= \frac{2i k_x \bar{T}_{xy}(y)}{k^2 c(y)} + \frac{2i k_x \bar{U}'(y)}{k^2 We c(y)^2}, \\
c_{1,11} &= -\frac{2k_x^2 \bar{T}_{xx}(y)}{k^2 c(y)} - \frac{2k_x^2}{k^2 We c(y)} + \frac{2k_z^2 \bar{T}_{xy}(y) \bar{U}'(y)}{k^2 c(y)^2} + \frac{4\bar{U}'(y)^2}{We c(y)^3}, \\
c_{0,11} &= \frac{2i k_x \bar{T}_{xx}(y) \bar{U}'(y)}{c(y)^2} + \frac{4i k_x \bar{T}_{xy}(y) \bar{U}'(y)^2}{c(y)^3} + \frac{2i k_x \bar{U}'(y)}{We c(y)^2} - \frac{\bar{T}'_{xx}(y)}{c(y)} - \frac{2\bar{T}'_{xy}(y) \bar{U}'(y)}{c(y)^2}, \\
c_{1,12} &= -\frac{2i k_z \bar{T}_{xy}(y)}{k^2 c(y)} - \frac{2i k_z \bar{U}'(y)}{k^2 We c(y)^2}, \\
c_{0,12} &= \frac{2k_x k_z \bar{T}_{xx}(y)}{k^2 c(y)} + \frac{2k_x k_z \bar{T}_{xy}(y) \bar{U}'(y)}{k^2 c(y)^2} + \frac{2k_x k_z}{k^2 We c(y)}.
\end{aligned}$$

E.2 Descriptor form

The state variables of the descriptor form are the velocity and pressure, i.e., $\phi = [u \ v \ w \ p]^T$ in (4.6). The boundary conditions are

$$u(\pm 1) = v(\pm 1) = w(\pm 1) = [Dv(\cdot)](\pm 1) = 0.$$

In this representation the operator-valued matrix \mathcal{A} is of size 4×4 with components

$$\mathcal{A}(i, j) = \left(\sum_{n=0}^2 a_{n,ij}(y, \omega) D^n \right),$$

where the nonzero coefficients $a_{n,ij}$ are given by

$$\begin{aligned} a_{2,11} &= -\frac{(1-\beta)}{We\,c(y)} - \beta, \\ a_{1,11} &= \frac{(1-\beta) \left(c'(y) - ik_x (3We\,c(y)\bar{T}_{xy}(y) + 2\bar{U}'(y)) \right)}{We\,c(y)^2}, \\ a_{0,11} &= \frac{(1-\beta) k_x \bar{T}_{xy}(y) (2k_x \bar{U}'(y) + ic'(y))}{c(y)^2} \\ &\quad + \frac{(1-\beta) (2k_x^2 + k_x We (2k_x \bar{T}_{xx}(y) - i\bar{T}'_{xy}(y)) + k_z^2)}{We\,c(y)} + \beta k^2, \\ a_{2,12} &= -\frac{(1-\beta) (We\,c(y)\bar{T}_{xy}(y) + 2\bar{U}'(y))}{We\,c(y)^2}, \\ a_{1,12} &= \frac{(1-\beta) \bar{T}_{xy}(y)c'(y)}{c(y)^2} + \frac{4(1-\beta) c'(y)\bar{U}'(y)}{We\,c(y)^3} - \frac{i(1-\beta) k_x \bar{T}_{xx}(y)}{c(y)} \\ &\quad - \frac{4i(1-\beta) k_x \bar{T}_{xy}(y)\bar{U}'(y)}{c(y)^2} - \frac{4i(1-\beta) k_x \bar{U}'(y)^2}{We\,c(y)^3} - \frac{i(1-\beta) k_x}{We\,c(y)} \\ &\quad - \frac{2(1-\beta) \bar{U}''(y)}{We\,c(y)^2}, \end{aligned}$$

$$\begin{aligned}
a_{0,12} &= \frac{i(1-\beta)k_x\bar{T}_{xx}(y)c'(y)}{c(y)^2} + \frac{4i(1-\beta)k_x\bar{T}_{xy}(y)c'(y)\bar{U}'(y)}{c(y)^3} \\
&\quad + \frac{i(1-\beta)k_xc'(y)}{We c(y)^2} - \frac{(1-\beta)c'(y)\bar{T}'_{xy}(y)}{c(y)^2} \\
&\quad + \frac{2(1-\beta)k_x^2\bar{T}_{xx}(y)\bar{U}'(y)}{c(y)^2} + \frac{4(1-\beta)k_x^2\bar{T}_{xy}(y)\bar{U}'(y)^2}{c(y)^3} + \frac{2(1-\beta)k_x^2\bar{U}'(y)}{We c(y)^2} \\
&\quad - \frac{2i(1-\beta)k_x\bar{T}_{xy}(y)\bar{U}''(y)}{c(y)^2} + \frac{(1-\beta)k_z^2\bar{U}'(y)}{We c(y)^2}, \\
a_{1,13} &= -\frac{i(1-\beta)k_z(We c(y)\bar{T}_{xy}(y) + \bar{U}'(y))}{We c(y)^2}, \\
a_{0,13} &= \frac{(1-\beta)k_xk_z(We c(y)\bar{T}_{xx}(y) + c(y) + We\bar{T}_{xy}(y)\bar{U}'(y))}{We c(y)^2}, \\
a_{0,14} &= ik_x, \\
a_{1,21} &= -\frac{i(1-\beta)k_x}{We c(y)}, \\
a_{0,21} &= \frac{(1-\beta)k_x^2\bar{T}_{xy}(y)}{c(y)}, \\
a_{2,22} &= -\frac{2(1-\beta)}{We c(y)} - \beta, \\
a_{1,22} &= \frac{2(1-\beta)c'(y)}{We c(y)^2} - \frac{3i(1-\beta)k_x\bar{T}_{xy}(y)}{c(y)} - \frac{2i(1-\beta)k_x\bar{U}'(y)}{We c(y)^2}, \\
a_{0,22} &= \frac{2i(1-\beta)k_x\bar{T}_{xy}(y)c'(y)}{c(y)^2} + \frac{(1-\beta)k_x^2\bar{T}_{xx}(y)}{c(y)} + \frac{2(1-\beta)k_x^2\bar{T}_{xy}(y)\bar{U}'(y)}{c(y)^2} \\
&\quad + \frac{(1-\beta)k_x^2}{We c(y)} - \frac{i(1-\beta)k_x\bar{T}'_{xy}(y)}{c(y)} + \frac{(1-\beta)k_z^2}{We c(y)} + \beta k^2, \\
a_{1,23} &= -\frac{i(1-\beta)k_z}{We c(y)}, \\
a_{0,23} &= \frac{(1-\beta)k_xk_z\bar{T}_{xy}(y)}{c(y)}, \\
a_{1,24} &= 1, \\
a_{0,31} &= \frac{(1-\beta)k_xk_z}{We c(y)}, \\
a_{1,32} &= -\frac{i(1-\beta)k_z}{We c(y)}, \\
a_{0,32} &= \frac{(1-\beta)k_z(k_x\bar{U}'(y) + ic'(y))}{We c(y)^2},
\end{aligned}$$

$$\begin{aligned}
a_{2,33} &= -\frac{(1-\beta)}{We c(y)} - \beta, \\
a_{1,33} &= \frac{(1-\beta) c'(y)}{We c(y)^2} - \frac{2i(1-\beta) k_x \bar{T}_{xy}(y)}{c(y)} - \frac{i(1-\beta) k_x \bar{U}'(y)}{We c(y)^2}, \\
a_{0,33} &= \frac{i(1-\beta) k_x \bar{T}_{xy}(y) c'(y)}{c(y)^2} + \frac{(1-\beta) k_x^2 \bar{T}_{xx}(y)}{c(y)} + \frac{(1-\beta) k_x^2 \bar{T}_{xy}(y) \bar{U}'(y)}{c(y)^2} \\
&\quad + \frac{(1-\beta) k_x^2}{We c(y)} - \frac{i(1-\beta) k_x \bar{T}'_{xy}(y)}{c(y)} + \frac{2(1-\beta) k_z^2}{We c(y)} + \beta k^2, \\
a_{0,34} &= i k_z.
\end{aligned}$$

The expressions for \mathcal{B} and \mathcal{C}_v are given by

$$\mathcal{B} = \begin{bmatrix} 1 & 0 & 0 \\ 0 & 1 & 0 \\ 0 & 0 & 1 \\ 0 & 0 & 0 \end{bmatrix}, \quad \mathcal{C}_v = \begin{bmatrix} 1 & 0 & 0 & 0 \\ 0 & 1 & 0 & 0 \\ 0 & 0 & 1 & 0 \end{bmatrix},$$

and for the stress output τ_{xx} , \mathcal{C}_{xx} is a 1×4 block-matrix operator given by

$$\mathcal{C}_{xx}(i, j) = \left(\sum_{n=0}^1 c_{n,ij}(y, \omega) D^n \right), \quad (\text{E7})$$

where the nonzero coefficients $c_{n,ij}$ are given by

$$\begin{aligned}
c_{1,11} &= \frac{2(We c(y) \bar{T}_{xy}(y) + \bar{U}'(y))}{We c(y)^2}, \\
c_{0,11} &= \frac{2i k_x (We c(y) \bar{T}_{xx}(y) + c(y) + We \bar{T}_{xy}(y) \bar{U}'(y))}{We c(y)^2}, \\
c_{1,12} &= \frac{2\bar{U}'(y) (We c(y) \bar{T}_{xy}(y) + 2\bar{U}'(y))}{We c(y)^3}, \\
c_{0,12} &= \frac{2i\bar{U}'(y) (k_x We \bar{T}_{xx}(y) + k_x + iWe \bar{T}'_{xy}(y))}{We c(y)^2} \\
&\quad + \frac{-c(y)^2 \bar{T}'_{xx}(y) + 4i k_x \bar{T}_{xy}(y) \bar{U}'(y)^2}{c(y)^3}.
\end{aligned} \quad (\text{E8})$$

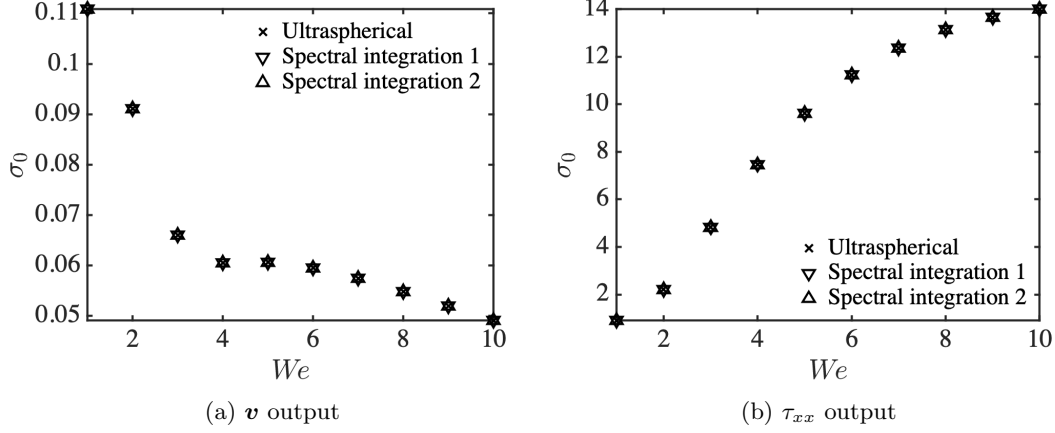


Figure F1: Principal singular values of (a) \mathcal{T}_v in (4.14) and (b) \mathcal{T}_{xx} in (4.17) of 2D Couette flow of an Oldroyd-B fluid with $\beta = 0.5$, $k_x = 1$, and $\omega = 0$. Spectral integration 1 uses the descriptor form in § E.2, and Spectral integration 2 uses the evolution form in § E.1. The ultraspherical method uses the evolution form.

F Validation

In this section we present a few representative calculations that validate our numerical discretization presented in § 4.3. Figure F1 shows calculations with 2D Couette flow with $\beta = 0.5$, $\omega = 0$, and $k_x = 1$ using three approaches: the ultraspherical method with the evolution form (see § E.1), the spectral integration method with the descriptor form (see § E.2), and the spectral integration method with the evolution form (see § E.1) using 150 basis functions in each case. Figure F1a shows singular values of \mathcal{T}_v in (4.14), and Figure F1b shows singular values of \mathcal{T}_{xx} in (4.17). We find good agreement in the results obtained from the three approaches. Furthermore the singular values of \mathcal{T}_v in Figure F1a agree quantitatively with the results of Lieu and Jovanović, Figure 8a in [33].

Next we plot the principal singular values from the SVD of \mathcal{T}_v (4.14) and \mathcal{T}_{xx} (4.17) for 2D3C Couette flow with $\beta = 0.5$, $k_z = 1$, and $\omega = 0$ in Figure F2. We present results that use the ultraspherical method, although we have confirmed that the spectral integration method (using both the descriptor and evolution forms) produces identical results. Figure F2a shows singular values of \mathcal{T}_v in (4.14) as a function of We , and we

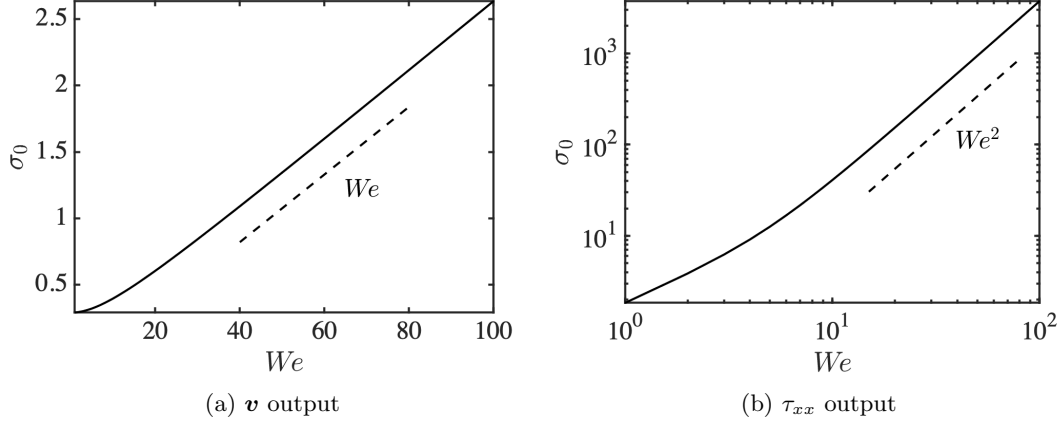


Figure F2: Principal singular values of (a) \mathcal{T}_v in (4.14) and (b) \mathcal{T}_{xx} in (4.17) of 2D3C Couette flow of an Oldroyd-B fluid with $\beta = 0.5$, $k_z = 1$, and $\omega = 0$. The solid lines mark singular values, and the dashed lines show the slope of their scaling with We [5].

observe that the singular values scale linearly with We (as indicated by the dashed line). Figure F2b shows singular values of \mathcal{T}_{xx} in (4.17) scaling as We^2 on a log-log plot, as indicated by the dashed line. These scaling of the velocity and the stress singular values with We are in agreement with Figures 3 and 4 in [5].

G Additional figures for § 4.5

In § 4.5.2 we showed that the localized amplification of the stress occurs at locations $y = y^*$ in the channel where $k_x = 1$ and $\omega + k_x \bar{U}(y^*) = 0$ (see (4.33) and Figure 4.9). In this section we show that the relation (4.33) is also valid for $k_x = 3$. Figure G3 considers $\hat{\tau}_{xx}$ from the SVD of \mathcal{T}_{xx} in (4.17) with the same values of We and β as in Figure 4.9, $We = 40$ and $\beta = 0.5$, but uses $k_x = 3$ in the place of $k_x = 1$. In the same way as we did in Figure 4.9, we vary y^* , compute ω according to (4.33), and use this ω to compute the SVD of \mathcal{T}_{xx} in (4.17). If the dashed-dotted line $y = y^*$ coincides with the location where $\hat{\tau}_{xx}$ (see (4.17)) has the maximum magnitude, then (4.33) is valid for $k_x = 3$ as well.

When $y^* = 0$ in Figure G3a ($k_x = 3$), we observe that the stress has a similar structure as when $k_x = 1$ (Figure 4.9a), however we observe that the stress is of a

larger magnitude compared to Figure 4.9a. Similar to Figure 4.9a, in Figure G3a the dashed-dotted line corresponding to $y = y^*$ does not coincide with the location of the maximum magnitude of $\hat{\tau}_{xx}$, implying that the relation in (4.33) is not valid in this case.

In Figure G3b ($k_x = 3$), we fix $y^* = 0.2$ and calculate ω from (4.33) and compute an SVD of \mathcal{T}_{xx} in (4.17). We observe that the locations of the maximum magnitude of $\hat{\tau}_{xx}$ coincide with $y = y^*$ (dashed-dotted lines). When compared to Figure 4.9b ($k_x = 1$), $\hat{\tau}_{xx}$ in Figure G3b ($k_x = 3$) has a larger magnitude.

Similarly, Figures G3c-G3f plot $\hat{\tau}_{xx}$ computed from the SVD of \mathcal{T}_{xx} in (4.17), with $y^* = 0.4, 0.6, 0.8$, and 1 respectively and $k_x = 3$. In each case ω is computed to satisfy (4.33). We observe that the magnitudes of $\hat{\tau}_{xx}$ in Figures G3c-G3f ($k_x = 3$) is larger compared to their counterparts in Figures 4.9c-4.9f ($k_x = 1$), and that the locations of localized amplification of $\hat{\tau}_{xx}$ coincide with the dashed-dotted lines ($y = y^*$). This suggests that the relation (4.33) is valid for $k_x = 3$ as well. Lastly, Figures G4 and G5 enlarge the region near $y = y^*$ in Figures 4.9 and G3 respectively.

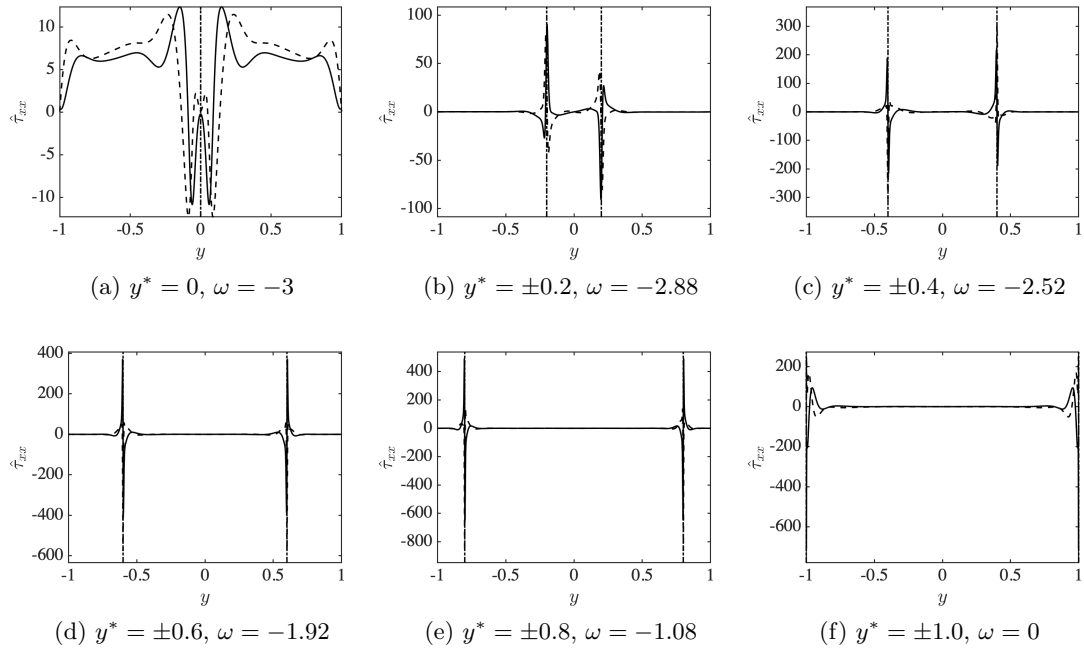


Figure G3: Stress τ_{xx} corresponding to the principal singular value from the SVD of \mathcal{T}_{xx} in (4.17) with $We = 40$, $\beta = 0.5$ and $k_x = 3$, and (a) $y^* = 0$, (b) $y^* = \pm 0.2$, (c) $y^* = \pm 0.4$, (d) $y^* = \pm 0.6$, (e) $y^* = \pm 0.8$, and (f) $y^* = \pm 1$. For a given value of k_x and y^* , ω is calculated from (4.33). The solid lines mark the real parts and the dashed lines mark the imaginary parts of $\hat{\tau}_{xx}$. The dashed-dotted lines mark $y = \pm y^*$. Figure G5 shows the region enlarged near $y = y^*$.

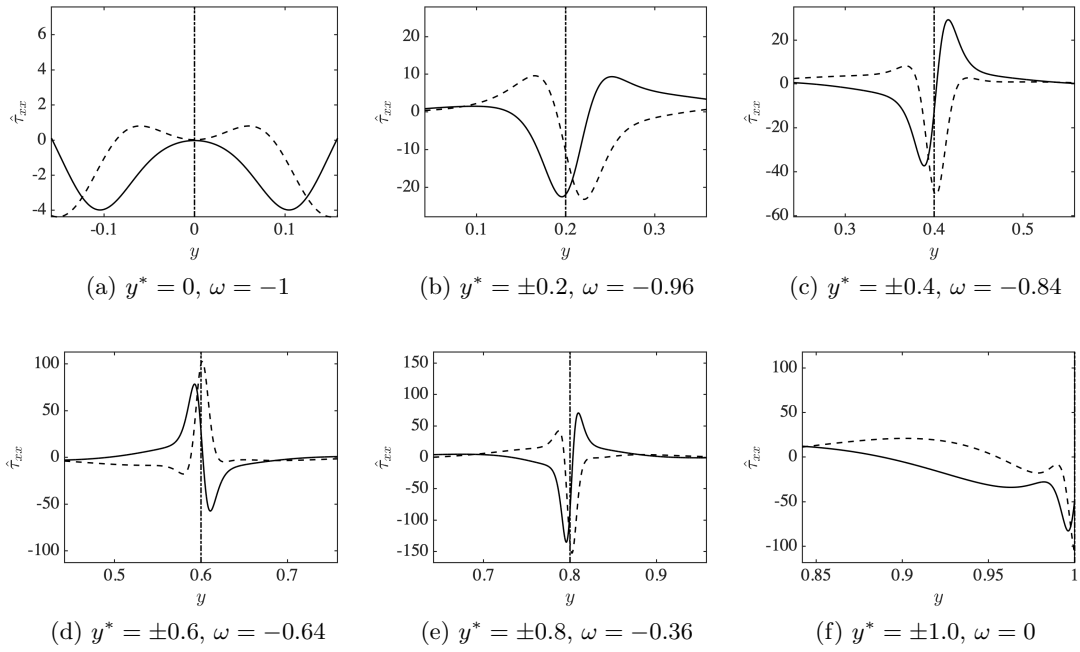


Figure G4: Stress τ_{xx} corresponding to the principal singular value from the SVD of \mathcal{T}_{xx} in (4.17) with $We = 40$, $\beta = 0.5$, and $k_x = 1$, and (a) $y^* = 0$, (b) $y^* = \pm 0.2$, (c) $y^* = \pm 0.4$, (d) $y^* = \pm 0.6$, (e) $y^* = \pm 0.8$, and (f) $y^* = \pm 1$. For a given value of k_x and y^* , ω is calculated from (4.33). The solid lines mark the real parts and the dashed lines mark the imaginary parts of $\hat{\tau}_{xx}$. The dashed-dotted lines mark $y = y^*$. Figure 4.9 shows corresponding plots in the full domain, i.e., $y \in [-1, 1]$.

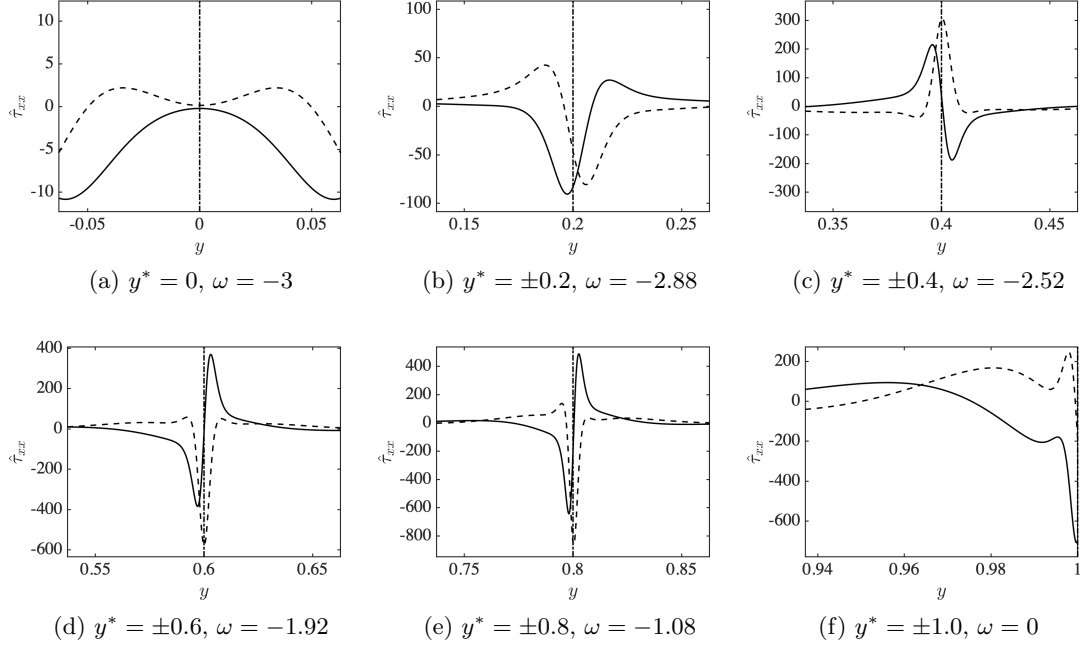


Figure G5: Stress τ_{xx} corresponding to the principal singular value from the SVD of \mathcal{T}_{xx} in (4.17) with $We = 40$, $\beta = 0.5$, and $k_x = 3$, and (a) $y^* = 0$, (b) $y^* = \pm 0.2$, (c) $y^* = \pm 0.4$, (d) $y^* = \pm 0.6$, (e) $y^* = \pm 0.8$, and (f) $y^* = \pm 1$. For a given value of k_x and y^* , ω is calculated from (4.33). The solid lines mark the real parts and the dashed lines mark the imaginary parts of $\hat{\tau}_{xx}$. The dashed-dotted lines mark $y = y^*$. Figure G3 shows corresponding plots in the full domain, i.e., $y \in [-1, 1]$.

H Time-stepping schemes for DNS

Time-stepping schemes are organized in the following manner. Equation (5.5) is discretized in time as

$$\lambda_v \mathbf{v}^{n+1} = -\nabla p^{n+1} + \frac{1}{Re} \nabla^2 \mathbf{v}^{n+1} - \mathbf{r}^n, \quad (\text{H1})$$

where $n + 1$ refers to future-time values, and n to past-time values, and

$$\mathbf{r}^n = -\sum_{i=0}^m (a_i \mathbf{g}^i + b_i \mathbf{f}^i + c_i \mathbf{v}^i) + \Pi_x \mathbf{e}_x, \quad (\text{H2})$$

where a_i , b_i , and c_i are defined based on the time discretization (Table H1). The index i is for memory such that $i = 0$ is the most recent. For example, for a third-order scheme that needs to remember quantities of present time, past time, and time past of past time, a_0 stores present, a_1 the past, and a_2 the past of past. Note that a time-stepping scheme can have several stages for n , e.g., the three-stage RK scheme (Table H1). The \mathbf{g}^i in (H2) is given by

$$\mathbf{g}^i = -\nabla p^i + \frac{1}{Re} \nabla^2 \mathbf{v}^i. \quad (\text{H3})$$

Notice that (H2) is general and can accommodate a new implicit-explicit time stepping scheme by assigning values of a_i , b_i , and c_i .

Finally, rearranging (H1) we have in (5.6)

$$a = \frac{1}{Re}, \quad (\text{H4})$$

$$b = \frac{k^2}{Re} + \lambda_v. \quad (\text{H5})$$

Stage	Memory, i	λ_v	a_i	b_i	c_i
Family of second-order schemes					
0	0	$\frac{\gamma+0.5}{h(\gamma+0.5c)}$	$\frac{1-\gamma-c}{\gamma+0.5c}$	$\frac{\gamma+1}{\gamma+0.5c}$	$\frac{2\gamma}{h(\gamma+0.5c)}$
	1		$\frac{0.5c}{\gamma+0.5c}$	$\frac{-\gamma}{\gamma+0.5c}$	$-\frac{\gamma-0.5}{h(\gamma+0.5c)}$
Crank-Nicholson, three-stage RK					
0	0	$\frac{15}{4h}$	1	2	$\frac{15}{4h}$
1	0	$\frac{15}{h}$	1	$\frac{25}{4}$	$\frac{15}{h}$
	1	-	0	$-\frac{17}{4}$	0
2	0	$\frac{6}{h}$	1	$\frac{9}{2}$	$\frac{6}{h}$
	1	-	0	$-\frac{5}{2}$	0
Crank-Nicholson, four-stage RK					
0	0	$\frac{17}{4h}$	1	2	$\frac{17}{4h}$
1	0	$\frac{255}{h8}$	1	$\frac{289}{32}$	$\frac{255}{h8}$
	1	-	0	$-\frac{225}{32}$	0
2	0	$\frac{15}{h}$	1	$\frac{25}{4}$	$\frac{15}{h}$
	1	-	0	$-\frac{17}{4}$	0
3	0	$\frac{6}{h}$	1	$\frac{9}{2}$	$\frac{6}{h}$
	1	-	0	$-\frac{5}{2}$	0

Table H1: Implicit-explicit time-stepping schemes used in DNS, where h is the time step [1, 2]; see Table H2 for values of γ and c . The first name refers the implicit part, e.g., in “Crank-Nicholson, three-stage RK”, quantities treated implicitly use Crank-Nicholson, and quantities treated explicitly use three-stage RK time discretization.

Implicit-explicit scheme	Abbreviation	γ	c
Crank-Nicholson Adams-Bashforth	CNAB	0.5	0
Modified Crank-Nicholson Adams-Bashforth	MCNAB	0.5	0.125
Crank-Nicholson Leap-frog	CNLF	0	1
Semi-implicit backward differentiation formula	SBDF	1	0

Table H2: Family of second-order time-stepping schemes implemented in DNS (Chapter 5), taken from [2]. The first name refers the implicit part, e.g., in “Crank-Nicholson, Adams-Bashforth”, quantities treated implicitly use Crank-Nicholson, and quantities treated explicitly use Adams-Bashforth time discretization.

Supplementary material

S1 A Matlab spectral integration suite

S1.1 Introduction

We develop a customized Matlab spectral integration suite that is based on the method described by Greengard [28] and Du [27]. In order to facilitate application to n th order differential equations, our implementation introduces minor modifications that we describe next.

An example: A reaction-diffusion equation

Let us consider a second-order linear differential equation,

$$D^2 u(y) - k^2 u(y) = f(y), \tag{S1-1a}$$

with either homogeneous Dirichlet,

$$u(\pm 1) = 0, \tag{S1-1b}$$

or Neumann boundary conditions,

$$D u(\pm 1) = 0. \tag{S1-1c}$$

Here, u is the field of interest, f is an input, $k \in \mathbb{R}$ is a given constant, $y \in [-1, 1]$, and $D := d/dy$.

In the spectral integration method, the highest derivative in a differential equation

is expressed in a basis of Chebyshev polynomials. In particular, for equation (S1-1a),

$$D^2 u(y) = \sum_{i=0}^{\infty}{}' u_i^{(2)} T_i(y) =: \mathbf{t}_y^T \mathbf{u}, \quad (\text{S1-2})$$

where \sum' denotes a summation with the first term halved, $\mathbf{u} := [u_0^{(2)} \ u_1^{(2)} \ u_2^{(2)} \ \dots]^T$ is the infinite vector of spectral coefficients $u_i^{(2)}$, and \mathbf{t}_y is the vector of Chebyshev polynomials of the first kind $T_i(y)$,

$$\mathbf{t}_y^T := [\tfrac{1}{2}T_0(y) \ T_1(y) \ T_2(y) \ \dots]. \quad (\text{S1-3})$$

Integration of (S1-2) in conjunction with the recurrence relations for integration of Chebyshev polynomials is used to determine spectral coefficients corresponding to lower derivatives of u . For example, indefinite integration of (S1-2) yields

$$D u(y) = \sum_{i=0}^{\infty}{}' u_i^{(1)} T_i(y) + c_1 =: \mathbf{t}_y^T \mathbf{u}^{(1)} + c_1, \quad (\text{S1-4})$$

where c_1 is a constant of integration and

$$u_i^{(1)} = \begin{cases} \frac{1}{2} u_1^{(2)}, & i = 0, \\ \frac{1}{2i} (u_{i-1}^{(2)} - u_{i+1}^{(2)}), & i \geq 1. \end{cases} \quad (\text{S1-5})$$

These expressions for $u_i^{(1)}$ are derived in § S1.4.

Similarly, indefinite integration of $D u$ in (S1-4) allows us to express u as

$$u(y) = \sum_{i=0}^{\infty}{}' u_i^{(0)} T_i(y) + \tilde{c}_0 + c_1 y =: \mathbf{t}_y^T \mathbf{u}^{(0)} + \tilde{c}_0 + c_1 y,$$

where \tilde{c}_0 and c_1 are integration constants and

$$u_i^{(0)} = \begin{cases} \frac{1}{2} u_1^{(1)}, & i = 0, \\ \frac{1}{2i} (u_{i-1}^{(1)} - u_{i+1}^{(1)}), & i \geq 1. \end{cases}$$

Equation (S1-5) provides a recursive relation that is used to determine spectral coefficients of lower derivatives from the spectral coefficients of the highest derivative of the variable u ,

$$\mathbf{u}^{(1)} = \mathbf{J}\mathbf{u}, \quad \mathbf{u}^{(0)} = \mathbf{J}^2\mathbf{u},$$

where $\mathbf{J}^2 := \mathbf{J}\mathbf{J}$, and

$$\mathbf{J} := \begin{bmatrix} 0 & \frac{1}{2} & 0 & \cdots \\ \frac{1}{2} & 0 & -\frac{1}{2} & 0 & \cdots \\ 0 & \frac{1}{4} & 0 & -\frac{1}{4} & 0 & \cdots \\ 0 & 0 & \frac{1}{6} & 0 & -\frac{1}{6} & 0 & \cdots \\ \vdots & \vdots & & \ddots & \ddots & \ddots \end{bmatrix}. \quad (\text{S1-6})$$

Since $T_0(y) = 1$ and $T_1(y) = y$, we let $c_0 := 2\tilde{c}_0$ and represent integration constants in the basis expansion of u and Du in terms of Chebyshev polynomials,

$$u(y) = \mathbf{t}_y^T \mathbf{J}^2 \mathbf{u} + \begin{bmatrix} \frac{1}{2}T_0(y) & T_1(y) \end{bmatrix} \overbrace{\begin{bmatrix} 1 & 0 \\ 0 & 1 \end{bmatrix}}^{\mathbf{K}^0} \begin{bmatrix} c_0 \\ c_1 \end{bmatrix}, \quad (\text{S1-7})$$

$$Du(y) = \mathbf{t}_y^T \mathbf{J} \mathbf{u} + \begin{bmatrix} \frac{1}{2}T_0(y) & T_1(y) \end{bmatrix} \underbrace{\begin{bmatrix} 0 & 2 \\ 0 & 0 \end{bmatrix}}_{\mathbf{K}^1} \begin{bmatrix} c_0 \\ c_1 \end{bmatrix}. \quad (\text{S1-8})$$

By introducing the vector of integration constants $\mathbf{c} := \begin{bmatrix} c_0 & c_1 \end{bmatrix}^T$, we can represent u , Du , and D^2u as

$$u(y) = \mathbf{t}_y^T (\mathbf{J}^2 \mathbf{u} + \mathbf{R}_2 \mathbf{c}), \quad (\text{S1-9})$$

$$Du(y) = \mathbf{t}_y^T (\mathbf{J}^1 \mathbf{u} + \mathbf{R}_1 \mathbf{c}), \quad (\text{S1-10})$$

$$D^2u(y) = \mathbf{t}_y^T (\mathbf{J}^0 \mathbf{u} + \mathbf{R}_0 \mathbf{c}), \quad (\text{S1-11})$$

where $\mathbf{J}^0 = \mathbf{I}$ is an infinite identity matrix, and

$$\mathbf{R}_i := \begin{bmatrix} \mathbf{K}^{2-i} \\ \mathbf{0} \end{bmatrix}, \quad i = 0, 1, 2,$$

are matrices with an infinite number of rows and two columns, and $\mathbf{K}^2 = \mathbf{K} \mathbf{K}$ results in a 2×2 zero matrix. Thus, in the basis of Chebyshev polynomials, we can express differential equation (S1-1a) without its boundary conditions as

$$\mathbf{t}_y^T ((\mathbf{I} - k^2 \mathbf{J}^2) \mathbf{u} + (\mathbf{R}_0 - k^2 \mathbf{R}_2) \mathbf{c}) = \mathbf{t}_y^T \mathbf{f}, \quad (\text{S1-12})$$

where \mathbf{f} is the vector of spectral coefficients associated with the input f in (S1-1a). Using (S1-9), we can write Dirichlet boundary conditions (S1-1b) as

$$\begin{aligned} \mathbf{t}_{+1}^T \mathbf{J}^2 \mathbf{u} + \mathbf{t}_{+1}^T \mathbf{R}_2 \mathbf{c} &= 0, \\ \mathbf{t}_{-1}^T \mathbf{J}^2 \mathbf{u} + \mathbf{t}_{-1}^T \mathbf{R}_2 \mathbf{c} &= 0, \end{aligned} \quad (\text{S1-13})$$

and the use of (S1-10) brings Neumann boundary conditions (S1-1c) into,

$$\begin{aligned} \mathbf{t}_{+1}^T \mathbf{J} \mathbf{u} + \mathbf{t}_{+1}^T \mathbf{R}_1 \mathbf{c} &= 0, \\ \mathbf{t}_{-1}^T \mathbf{J} \mathbf{u} + \mathbf{t}_{-1}^T \mathbf{R}_1 \mathbf{c} &= 0. \end{aligned} \quad (\text{S1-14})$$

Hence, the infinite-dimensional representation of differential equation (S1-1a) with Dirichlet boundary conditions is given by

$$\begin{bmatrix} \mathbf{I} - k^2 \mathbf{J}^2 & \mathbf{R}_0 - k^2 \mathbf{R}_2 \\ \mathbf{t}_{+1}^T \mathbf{J}^2 & \mathbf{t}_{+1}^T \mathbf{R}_2 \\ \mathbf{t}_{-1}^T \mathbf{J}^2 & \mathbf{t}_{-1}^T \mathbf{R}_2 \end{bmatrix} \begin{bmatrix} \mathbf{u} \\ \mathbf{c} \end{bmatrix} = \begin{bmatrix} \mathbf{f} \\ 0 \\ 0 \end{bmatrix}, \quad (\text{S1-15})$$

and the representation for Neumann boundary conditions is obtained by replacing the last two rows in (S1-15) with those in (S1-14). We obtain the finite-dimensional approximation from (S1-15) by truncating the infinite spectral coefficients to $N + 1$ spectral coefficients using the projection operator [26, Eq. 2.9, also last paragraph of Section 2.4],

$$\mathbf{P} = [\mathbf{I}_{N+1} \ \mathbf{0}], \quad (\text{S1-16})$$

where \mathbf{I}_{N+1} is an identity matrix of dimension $N + 1$, and \mathbf{P} is a matrix with $N + 1$

rows and infinite columns so that

$$\begin{bmatrix} \mathbf{P} & 0 \\ 0 & \mathbf{I}_2 \end{bmatrix} \begin{bmatrix} \mathbf{I} - k^2 \mathbf{J}^2 & \mathbf{R}_0 - k^2 \mathbf{R}_2 \\ \mathbf{t}_{+1}^T \mathbf{J}^2 & \mathbf{t}_{+1}^T \mathbf{R}_2 \\ \mathbf{t}_{-1}^T \mathbf{J}^2 & \mathbf{t}_{-1}^T \mathbf{R}_2 \end{bmatrix} \begin{bmatrix} \mathbf{P}^T & 0 \\ 0 & \mathbf{I}_2 \end{bmatrix} \begin{bmatrix} \mathbf{P} & 0 \\ 0 & \mathbf{I}_2 \end{bmatrix} \begin{bmatrix} \mathbf{u} \\ \mathbf{c} \end{bmatrix} \quad (\text{S1-17})$$

$$= \begin{bmatrix} \mathbf{P} & 0 \\ 0 & \mathbf{I}_2 \end{bmatrix} \begin{bmatrix} \hat{\mathbf{f}} \\ 0 \\ 0 \end{bmatrix} \quad (\text{S1-18})$$

$$\Rightarrow \begin{bmatrix} \mathbf{P} (\mathbf{I} - k^2 \mathbf{J}^2) \mathbf{P}^T & \mathbf{P} (\mathbf{R}_0 - k^2 \mathbf{R}_2) \\ \mathbf{t}_{+1}^T \mathbf{J}^2 \mathbf{P}^T & \mathbf{t}_{+1}^T \mathbf{R}_2 \\ \mathbf{t}_{-1}^T \mathbf{J}^2 \mathbf{P}^T & \mathbf{t}_{-1}^T \mathbf{R}_2 \end{bmatrix} \begin{bmatrix} \hat{\mathbf{u}} \\ \mathbf{c} \end{bmatrix} = \begin{bmatrix} \hat{\mathbf{f}} \\ 0 \\ 0 \end{bmatrix}. \quad (\text{S1-19})$$

The variables with a cap represent the finite-dimensional truncation of spectral coefficients, e.g., $\mathbf{P} \mathbf{u} = \hat{\mathbf{u}}$.

Notice in the left-bottom corner in the matrix in (S1-19) has a matrix multiplication of $\mathbf{t}_{-1}^T \mathbf{J}^2 \mathbf{P}^T$, which is a quantity that involves multiplying matrices of dimensions $(1 \times \infty) \times (\infty \times \infty) \times (\infty \times (N+1))$ which results in a vector of size $1 \times (N+1)$. The product $(1 \times \infty) \times (\infty \times \infty)$ is needed to ensure proper truncation, see [26, last paragraph of Section 2.4]. For a practical implementation some large value greater than $N+1$ works in the place of a matrix dimension of ∞ . In our codes we use $N+1+2n$, where n is the order of the differential equation (e.g., for the reaction-diffusion equation (S1-1a) we use $N+1+4 = N+5$) as the ∞ as we found that results are the same if we use a value greater than $N+1+2n$.

Note on implementation: The routine `Matgen`, i.e., `[J,K,E] = Matgen(n,N)` generates the discretization matrices, here `K{1}` (in Matlab's cell notation) corresponds to \mathbf{K}^0 , `K{2}` to \mathbf{K}^1 and so on in (S1-29). `E{1}` corresponds to the projected versions of $D^2 u(y)$ in (S1-11), `E{2}` to $D u(y)$ in (S1-10) and so on. Finally, `J{1}` stores \mathbf{J}^0 in (S1-6), `J{2}` stores \mathbf{J}^1 , and so on.

Eigenvalues

We now consider the eigenvalues of the transient reaction-diffusion equation with Neumann boundary conditions,

$$D^2 u(y) - k^2 u(y) = \lambda u(y), \quad (\text{S1-20a})$$

$$D u(\pm) = 0. \quad (\text{S1-20b})$$

Using the relations from (S1-9) and (S1-11), the differential equation (S1-20a) is expressed in an infinite Chebyshev basis as,

$$\mathbf{t}_y^T \left((\mathbf{I} - k^2 \mathbf{J}^2) \mathbf{u} + (\mathbf{R}_0 - k^2 \mathbf{R}_2) \mathbf{c} \right) = \lambda \mathbf{t}_y^T (\mathbf{J}^2 \mathbf{u} + \mathbf{R}_2 \mathbf{c}). \quad (\text{S1-21})$$

The boundary conditions are the same as (S1-14). The infinite-dimensional representation from equating terms of the same basis and appending boundary conditions is given by

$$\begin{bmatrix} \mathbf{I} - k^2 \mathbf{J}^2 & \mathbf{R}_0 - k^2 \mathbf{R}_2 \\ \mathbf{t}_{+1}^T \mathbf{J}^1 & \mathbf{t}_{+1}^T \mathbf{R}_1 \\ \mathbf{t}_{-1}^T \mathbf{J}^1 & \mathbf{t}_{-1}^T \mathbf{R}_1 \end{bmatrix} \begin{bmatrix} \mathbf{u} \\ \mathbf{c} \end{bmatrix} = \lambda \begin{bmatrix} \mathbf{J}^2 & \mathbf{R}_2 \\ \mathbf{0} & \mathbf{0} \\ \mathbf{0} & \mathbf{0} \end{bmatrix} \begin{bmatrix} \mathbf{u} \\ \mathbf{c} \end{bmatrix}. \quad (\text{S1-22})$$

The differential equation in (S1-20a) has an eigenvalue λ , but the boundary conditions in (S1-20b) do not. Thus the eigenvalue problem with padded zeros as on the right-hand side of (S1-22) can result in extra eigenvalues that increase in value with an increase in N in certain problems [99]. This zero padding in (S1-22) can be removed by using the procedure described in § 3.3.2. The projection operator (S1-16) is used on (S1-22) to reduce it to a finite dimensional approximation in the same way as (S1-19). Eigenvalues of (S1-22) are computed in Code 7.1.

Frequency responses

The system for frequency responses of the reaction-diffusion equation is given by (see § 3.2.2),

$$(i\omega I - D^2 + \epsilon^2 I) u(y) = d(y), \quad (\text{S1-23a})$$

$$D u(\pm 1) = 0, \quad (\text{S1-23b})$$

and the adjoint system by,

$$(-i\omega I - D^2 + \epsilon^2 I) v(y) = g(y), \quad (\text{S1-23c})$$

$$D v(\pm 1) = 0. \quad (\text{S1-23d})$$

The feedback interconnected system to compute frequency responses is given by (see § 3.3.1),

$$\begin{bmatrix} 0 & I \\ I & 0 \end{bmatrix} \begin{bmatrix} u(y) \\ v(y) \end{bmatrix} = \lambda \begin{bmatrix} (i\omega + \epsilon^2)I - D^2 & 0 \\ 0 & (-i\omega + \epsilon^2)I - D^2 \end{bmatrix} \begin{bmatrix} u(y) \\ v(y) \end{bmatrix}, \quad (\text{S1-24a})$$

with boundary conditions

$$\begin{bmatrix} \mathcal{Q}(+1, D) & 0 \\ \mathcal{Q}(-1, D) & 0 \\ 0 & \mathcal{Q}(+1, D) \\ 0 & \mathcal{Q}(-1, D) \end{bmatrix} \begin{bmatrix} u(y) \\ v(y) \end{bmatrix} = 0, \quad (\text{S1-24b})$$

where $\mathcal{Q}(a, L)$ is an evaluation operator that evaluates the action of the linear operator L on a variable at a point $y = a$, and (S1-24b) specifies homogeneous Neumann boundary conditions on $u(y)$ and $v(y)$ (see (S1-23)).

The expression for the identity operators in (S1-24) is given in (S1-9), and for the second derivative operators in (S1-10). The infinite-dimensional representation for the

differential equation of this system is given by,

$$\begin{bmatrix} \mathbf{0} & \mathbf{0} & \mathbf{J}^2 & \mathbf{R}_2 \\ \mathbf{J}^2 & \mathbf{R}_2 & \mathbf{0} & \mathbf{0} \end{bmatrix} \begin{bmatrix} \mathbf{u} \\ \mathbf{c}^{(u)} \\ \mathbf{v} \\ \mathbf{c}^{(v)} \end{bmatrix} = \lambda \begin{bmatrix} (i\omega + \epsilon^2)\mathbf{J}^2 - \mathbf{I} & \mathbf{0} \\ (i\omega + \epsilon^2)\mathbf{R}_2 - \mathbf{R}_0 & \mathbf{0} \\ \mathbf{0} & (-i\omega + \epsilon^2)\mathbf{J}^2 - \mathbf{I} \\ \mathbf{0} & (-i\omega + \epsilon^2)\mathbf{R}_2 - \mathbf{R}_0 \end{bmatrix}^T \begin{bmatrix} \mathbf{u} \\ \mathbf{c}^{(u)} \\ \mathbf{v} \\ \mathbf{c}^{(v)} \end{bmatrix}, \quad (\text{S1-25a})$$

where $\mathbf{c}^{(u)}$ and $\mathbf{c}^{(v)}$ are the vector of constants of integration corresponding to $u(y)$ and $v(y)$ respectively. The expressions for Neumann boundary conditions follow from (S1-14), and are given by

$$\begin{bmatrix} \mathbf{t}_{+1}^T \mathbf{J} & \mathbf{t}_{+1}^T \mathbf{R}_1 & \mathbf{0} & \mathbf{0} \\ \mathbf{t}_{-1}^T \mathbf{J} & \mathbf{t}_{-1}^T \mathbf{R}_1 & \mathbf{0} & \mathbf{0} \\ \mathbf{0} & \mathbf{0} & \mathbf{t}_{+1}^T \mathbf{J} & \mathbf{t}_{+1}^T \mathbf{R}_1 \\ \mathbf{0} & \mathbf{0} & \mathbf{t}_{-1}^T \mathbf{J} & \mathbf{t}_{-1}^T \mathbf{R}_1 \end{bmatrix} \begin{bmatrix} \mathbf{u} \\ \mathbf{c}^{(u)} \\ \mathbf{v} \\ \mathbf{c}^{(v)} \end{bmatrix} = \mathbf{0}. \quad (\text{S1-25b})$$

The finite-dimensional projection of the infinite-dimensional representation for the differential equation (S1-25a) and boundary conditions (S1-25b) is obtained using (S1-16) in the same manner as (S1-19). The finite-dimensional approximation to (S1-25) is solved to compute $\lambda = \pm\sigma$, and σ_{\max} is the resolvent norm of (S1-23). The last part of Code 7.1 solves for frequency responses of this system.

S1.2 Arbitrary order linear differential equation with non-constant coefficients

In the previous subsection we considered the reaction-diffusion equation, and discussed how spectral integration is used to solve for a forcing, for eigenvalues, and for frequency responses. In this subsection, we illustrate this process for an n th order linear differential equation with non-constant coefficients. Steps that follow are similar to what was

discussed in § S1.1.

Consider a general representation of an n th order linear differential equation with non-constant coefficients,

$$\sum_{k=0}^n a^{(k)}(y) D^k u(y) = f(y), \quad (\text{S1-26a})$$

$$\sum_{k=0}^{n-1} b^{(k, \mathbf{p})} D^k u(\mathbf{p}) = \mathbf{q}, \quad (\text{S1-26b})$$

where $a^{(k)}$ are the non-constant coefficients, and f is an input, $b^{(k, \mathbf{p})}$ are constant coefficients associated with boundary constraints (a general case of mixed boundary conditions), at a vector of evaluation points, \mathbf{p} , and corresponding values at the boundaries, \mathbf{q} .

Differential equation

In the same manner as the second derivative in (S1-2) for the reaction-diffusion equation (S1-1a), the highest derivative of the variable $u(y)$ in (S1-26a) is expressed in a basis of Chebyshev polynomials as

$$D^n u(y) = \sum_{i=0}^{\infty} u_i^{(n)} T_i(y) =: \mathbf{t}_y^T \mathbf{u}, \quad (\text{S1-27})$$

where, $\mathbf{u} = [u_0^{(n)} \ u_1^{(n)} \ \cdots \ u_{\infty}^{(n)}]^T$. The lower derivatives are expressed as,

$$D^i u(y) = \mathbf{t}_y^T (\mathbf{J}^{n-i} \mathbf{u} + \mathbf{R}_{n-i} \mathbf{c}), \quad (\text{S1-28})$$

where, \mathbf{J} is defined in (S1-6), $\mathbf{c} = [c_0 \ c_1 \ \cdots \ c_{n-1}]^T$ are the n constants of integration that result from integrating the highest derivative (S1-27), and

$$\mathbf{R}_i := \begin{bmatrix} \mathbf{K}^{n-i} \\ \mathbf{0} \end{bmatrix},$$

are matrices with n columns and infinite number of rows, where [28, Eq. 10]

$$\mathbf{K} = \begin{bmatrix} 0 & 2 & 0 & 6 & 0 & 10 & \cdots \\ 0 & 0 & 4 & 0 & 8 & 0 & \ddots \\ 0 & 0 & 0 & 6 & 0 & 10 & \ddots \\ \vdots & \ddots & \ddots & \ddots & \ddots & \ddots & \ddots \end{bmatrix}, \quad (\text{S1-29})$$

is a matrix of dimension $n \times n$.

Spatially varying coefficients

The multiplication operator for the product of two Chebyshev series is used to account for non-constant coefficients $a^{(k)}$ in (S1-26a). For a function $a(y)$ in the basis of Chebyshev polynomials,

$$a(y) = \sum_{i=0}^{\infty} a_i T_i(y), \quad (\text{S1-30})$$

the multiplication operator is given by [27, Section 3]

$$\mathcal{M}[a] = \frac{1}{2} \begin{bmatrix} a_0 & a_1 & a_2 & a_3 & \cdots \\ a_1 & a_0 & a_1 & a_2 & \ddots \\ a_2 & a_1 & a_0 & a_1 & \ddots \\ a_3 & a_2 & a_1 & a_0 & \ddots \\ \vdots & \ddots & \ddots & \ddots & \ddots \end{bmatrix} + \frac{1}{2} \begin{bmatrix} 0 & 0 & 0 & 0 & \cdots \\ a_1 & a_2 & a_3 & a_4 & \cdots \\ a_2 & a_3 & a_4 & a_5 & \ddots \\ a_3 & a_4 & a_5 & a_6 & \ddots \\ \vdots & \ddots & \ddots & \ddots & \ddots \end{bmatrix}. \quad (\text{S1-31})$$

Infinite-dimensional representation

The differential equation in (S1-26a) is expressed in a Chebyshev basis using (S1-28) and (S1-31) as

$$\mathbf{t}_y^T \left(\left[\sum_{k=0}^n \mathcal{M}[a^{(k)}] \mathbf{J}^{n-k} \right] \mathbf{u} + \left[\sum_{k=0}^{n-1} \mathcal{M}[a^{(k)}] \mathbf{R}_{n-k} \right] \mathbf{c} \right) = \mathbf{t}_y^T \mathbf{f}, \quad (\text{S1-32})$$

and the boundary conditions (S1-26b) using (S1-28) as

$$\mathbf{t}_{\mathbf{p}}^T \left(\left[\sum_{k=0}^{n-1} b^{(k,\mathbf{p})} \mathbf{J}^{n-k} \right] \mathbf{u} + \left[\sum_{k=0}^{n-1} b^{(k,\mathbf{p})} \mathbf{R}_{n-k} \right] \mathbf{c} \right) = \mathbf{q}. \quad (\text{S1-33})$$

Thus the infinite-dimensional representation based on equating the terms of the same basis for the differential equation (S1-26) using (S1-32) and appending boundary conditions in (S1-33) is given by,

$$\underbrace{\begin{bmatrix} \sum_{k=0}^n \mathcal{M}[a^{(k)}] \mathbf{J}^{n-k} & \sum_{k=0}^{n-1} \mathcal{M}[a^{(k)}] \mathbf{R}_{n-k} \\ \sum_{k=0}^{n-1} b^{(k,\mathbf{p})} \mathbf{t}_{\mathbf{p}}^T \mathbf{J}^{n-k} & \sum_{k=0}^{n-1} b^{(k,\mathbf{p})} \mathbf{t}_{\mathbf{p}}^T \mathbf{R}_{n-k} \end{bmatrix}}_{\mathbf{M}} \begin{bmatrix} \mathbf{u} \\ \mathbf{c} \end{bmatrix} = \begin{bmatrix} \mathbf{f} \\ \mathbf{q} \end{bmatrix}. \quad (\text{S1-34})$$

Finite-dimensional approximation

We use the projection operator (S1-16) to truncate the infinite spectral coefficients in \mathbf{u} and \mathbf{f} in (S1-34) [26, Eq. 2.9, also last paragraph of Section 2.4] in the same way as (S1-19)

$$\begin{bmatrix} \mathbf{P} & \mathbf{0} \\ \mathbf{0} & \mathbf{I}_n \end{bmatrix} \mathbf{M} \begin{bmatrix} \mathbf{P}^T & \mathbf{0} \\ \mathbf{0} & \mathbf{I}_n \end{bmatrix} \begin{bmatrix} \mathbf{P} & \mathbf{0} \\ \mathbf{0} & \mathbf{I}_n \end{bmatrix} \begin{bmatrix} \mathbf{u} \\ \mathbf{c} \end{bmatrix} = \begin{bmatrix} \mathbf{P} & \mathbf{0} \\ \mathbf{0} & \mathbf{I}_n \end{bmatrix} \begin{bmatrix} \mathbf{f} \\ \mathbf{q} \end{bmatrix},$$

to arrive at

$$\begin{bmatrix} \mathbf{P} \sum_{k=0}^n \mathcal{M}[a^{(k)}] \mathbf{J}^{n-k} \mathbf{P}^T & \mathbf{P} \sum_{k=0}^{n-1} \mathcal{M}[a^{(k)}] \mathbf{R}_{n-k} \\ \sum_{k=0}^{n-1} b^{(k,\mathbf{p})} \mathbf{t}_{\mathbf{p}}^T \mathbf{J}^{n-k} \mathbf{P}^T & \sum_{k=0}^{n-1} b^{(k,\mathbf{p})} \mathbf{t}_{\mathbf{p}}^T \mathbf{R}_{n-k} \end{bmatrix} \begin{bmatrix} \hat{\mathbf{u}} \\ \mathbf{c} \end{bmatrix} = \begin{bmatrix} \hat{\mathbf{f}} \\ \mathbf{q} \end{bmatrix}. \quad (\text{S1-35})$$

We represent the two rows of the matrix in (S1-35) separately for the sake of brevity,

$$\mathbf{L} = \begin{bmatrix} \mathbf{P} \sum_{k=0}^n \mathcal{M}[a^{(k)}] \mathbf{J}^{n-k} \mathbf{P}^T & \mathbf{P} \sum_{k=0}^{n-1} \mathcal{M}[a^{(k)}] \mathbf{R}_{n-k} \end{bmatrix}, \quad (\text{S1-36})$$

$$\mathbf{B} = \begin{bmatrix} \sum_{k=0}^{n-1} b^{(k,\mathbf{p})} \mathbf{t}_{\mathbf{p}}^T \mathbf{J}^{n-k} \mathbf{P}^T & \sum_{k=0}^{n-1} b^{(k,\mathbf{p})} \mathbf{t}_{\mathbf{p}}^T \mathbf{R}_{n-k} \end{bmatrix}, \quad (\text{S1-37})$$

where \mathbf{L} is the discrete approximation for the differential equation (S1-26a) and \mathbf{B} is the discrete approximation for the boundary conditions (S1-26b). The final discrete

expression to solve (S1-26) is given by,

$$\begin{bmatrix} \mathbf{L} \\ \mathbf{B} \end{bmatrix} \begin{bmatrix} \hat{\mathbf{u}} \\ \mathbf{c} \end{bmatrix} = \begin{bmatrix} \hat{\mathbf{f}} \\ \mathbf{q} \end{bmatrix}. \quad (\text{S1-38})$$

S1.3 The spectral integration suite

The spectral integration suite is a set of routines to compute the finite-dimensional approximation in (S1-38) to linear operators and block-matrix operators. An example of this is presented in Code 7.1 where we solve (S1-1a) with boundary conditions in (S1-1b) with a forcing and compare our solution with results from Chebfun [31].

In summary, we use the following routines (and these are sufficient for most problems to compute eigenvalues of or solve for inputs to linear differential equations or block-matrix operators):

Note: Our implementation needs that N (where $N + 1$ is the number of basis functions) is an odd number.

- `sety(N)`: Sets points in physical space, $y_i = \cos(\pi(i + 0.5)/(N + 1))$ over $N + 1$ points. These points are such that when we take a discrete cosine transform, we have an array that represents spectral coefficients of a Chebyshev basis [115, Eq. 12.4.16-17].
- `Discretize(n,N,L)`: Produces \mathbf{L} in (S1-38) by taking inputs as the highest differential order of the variable, n , N , and the linear operator L (linear operators are specified using cells in Matlab, e.g., the operator $aD^2 + bD + c$ is represented by a 3×1 cell with values $L\{1\} = a$, $L\{2\} = b$, and $L\{3\} = c$).
- `BcMat(n,N,eval,L)`: Generates a matrix of boundary evaluations (\mathbf{B} in (S1-38)) given the highest order of the linear differential equation, n , N , the evaluation point, `eval`, and the linear operator to be applied at that point (Dirichlet, Neumann or mixed).
- `phys2cheb.m`: Takes points in physical space (we refer to this as phys-space in this text and our codes) and converts them to an array of spectral coefficients in the basis of Chebyshev polynomials of the first kind (we refer to this as cheb-space in this text and our codes) using [115, Eq. 12.4.16-17].

- `cheb2phys.m`: Takes an array of spectral coefficients in the basis of Chebyshev polynomials of the first kind, and converts them to points in phys-space using [115, Eq. 12.4.16-17].
- `Matgen(n,N)`: The solution we solve for, $\hat{\mathbf{u}}$ in (S1-38), is a vector of spectral coefficients of the highest derivatives in the differential equation (S1-27). However, in most cases we need spectral coefficients of the lowest derivative, i.e., the variable itself ((S1-28) with $i = 0$). We use matrices generated from this routine to get to lower derivatives. Suppose we generate $[J,K,E] = \text{Matgen}(n,N)$, then J contains matrices corresponding to (S1-6), K corresponding to (S1-29), and the matrices in E are the ones needed to go to lower derivatives (E uses both J and K). For instance, to integrate n times, we multiply the solution $[\hat{\mathbf{u}}^T \ \mathbf{c}^T]^T$ from (S1-38) with $E\{n+1\}$; see Code 7.1.

In addition to these primary functions, we provide the following auxiliary functions that are useful in certain applications:

- `ChebMat2CellMat` Takes a matrix of size $m \times N \times n$, and returns a cell of arrays of size $m \times n$, each element in the cell is a vector representing a function in y .
- `AdjointFormal` Takes a linear operator or a block matrix operator and returns the formal adjoint.
- `keepConverged` Takes in eigenvalues, eigenvectors, and N , and returns those eigenvalues and eigenvectors that have converged to machine precision.
- `MultOps` Gives the composition of two linear (block) matrix operators of compatible dimensions.
- `integ` Integrates a function in phys-space.
- `ChebEval` Evaluates a function in cheb-space at points in the domain.

Listing 7.1: Problems with the reaction-diffusion equation, solving for a forcing to the system and eigenvalues and frequency responses of the system.

```
% Set problem data
% number of basis functions, differential order, spatial variable, parameters
```

```

N = 63; % N has to be an odd number
m = 2; % order of differential operator
y = sety(N); % spatially-independent variable

% parameter eps in TPBVP
eps = 1; eps2 = eps*eps;

% Represent operator in TPBVP
Delta = cell(m+1,1); % cell array with coefficients
Delta{1} = 1.0; Delta{2} = 1./(y.^2 + 1); Delta{3} = -eps2;

% Input in physical space
d = 1 + y + y.^2;

% Dirichlet BCs
bc1 = BCs(2,1); % two constraints on one variable
% Identity operator
I = cell(1,1); % cell array with coefficients
I{1} = 1.0;

% Dirichlet BCs at y = \pm 1
bc1.Operator = {I; I}; % boundary operator
bc1.Points = [1; -1]; % boundary points
bc1.Values = [1; -1]; % BCs at the boundaries ([0; 0] for homogeneous BCs)

% Neumann BCs
bc2 = BCs(2,1); % two constraints on one variable
% 1st derivative operator: 1.0 Dy + 0.0 I
Dy = cell(2,1); % cell array with coefficients
Dy{1} = 1.0; Dy{2} = 0.0;

% Neumann BCs at y = \pm 1
bc2.Operator = {Dy; Dy};
bc2.Points = [1; -1];
bc2.Values = [2; -2];

% Robin BCs
bc3 = BCs(2,1); % two constraints on one variable
% Operator 4 Dy + 3 I
Op = cell(2,1); % cell array with coefficients
Op{1} = 4; Op{2} = 3;

% Robin BCs at y = \pm 1
bc3.Operator = {Op; Op};
bc3.Points = [1; -1];
bc3.Values = [3; -3];

% Use sisSolves to solve TPBVP
% inputs to sisSolve: differential order m, N, operator, BCs, input forcing d
solution1 = sisSolves(m,N,Delta,bc1,d); % Dirichlet BCs
solution2 = sisSolves(m,N,Delta,bc2,d); % Neumann BCs
solution3 = sisSolves(m,N,Delta,bc3,d); % Robin BCs

% Visualize solution for Dirichlet BCs
plot(y,solution1);

```

```

% Compare with Chebfun
A = chebop([-1 1]);
yc = chebfun('y');
A.op = @(y,u) diff(u,2) + (1/(yc^2 + 1))*diff(u) - eps2*u;
A.lbc = @(u) u + 1;
A.rbc = @(u) u - 1;
solcDir = A\ (1+yc+yc^2);

% Visualize solution for Dirichlet BCs
plot(y,solution1,'-b',yc,solcDir,'--r');
xlabel('$y$');
ylabel('$\phi(y)$');
legend('SISMatlab','Chebfun','location','northwest');
print('-painters','-dsvg','../docs/pics/cod1Dir');

% Visualize solution for Neumann BCs
A.lbc = @(u) diff(u) + 2;
A.rbc = @(u) diff(u) - 2;
solcNeu = A\ (1+yc+yc^2);
plot(y,solution2,'-b',yc,solcNeu,'--r');
xlabel('$y$');
ylabel('$\phi(y)$');
legend('SISMatlab','Chebfun','location','north');
print('-painters','-dsvg','../docs/pics/cod1Neu');

% Visualize solution for Robin BCs
A.lbc = @(u) 4*diff(u) + 3*u + 3;
A.rbc = @(u) 4*diff(u) + 3*u - 3;
solcRob = A\ (1+yc+yc^2);
plot(y,solution3,'-b',yc,solcRob,'--r');
xlabel('$y$');
ylabel('$\phi(y)$');
legend('SISMatlab','Chebfun','location','northwest');
print('-painters','-dsvg','../docs/pics/cod1Rob');

```

Spatially varying coefficients

Spatially varying coefficients are accounted using an expression for product of Chebyshev polynomials detailed in (S1-31) (see [26, Section 2.2]). Spatially varying coefficients are accounted using `MultMat.m`, which generates a matrix for the expression in (S1-31). For example, let us consider the solution of the following system:

$$Du(y) + \frac{1}{y^2 + 1}u(y) = 0, \quad (\text{S1-39a})$$

$$u(-1) = 1. \quad (\text{S1-39b})$$

Analytical solution is given by [26, Eq. 2.12]:

$$u(y) = \exp(-\tan^{-1}(y) - \tan^{-1}(1)). \quad (\text{S1-39c})$$

Code 7.2 solves for $u(y)$ in (S1-39a) and (S1-39b) using spectral integration.

Listing 7.2: Solving (S1-39a) with the boundary condition (S1-39b)

```

y = sety(N); % spatially-independent variable

% parameter eps in reaction-diffusion equation
eps = 1; eps2 = eps*eps;

% Represent operators Delta = D^2 - eps^2 I and I in e-value problem
Delta = cell(m+1,1); % cell array with coefficients
Delta{1} = 1.0; Delta{2} = 0; Delta{3} = -eps2;
I = cell(1,1); % Identity operator
I{1} = 1;

% The first derivative operator 1.0 Dy + 0.0
Dy = cell(2,1); Dy{1} = 1.0; Dy{2} = 0.0;

% Neumann boundary conditions at y = \pm 1
bc = BCs(2,1); % two constraints on one variable
bc.Operator = {Dy; Dy};
bc.Points = [1; -1];

% Use sisEig to conduct the eigenvalue decomposition
[V,lambda] = sisEigs(m,N,Delta,I,bc,10,'Full');

%% Frequency responses
clear;
close all;
clc;

% Set problem data
% number of basis functions, differential order, spatial variable, parameters
N = 63; % N has to be an odd number
m = 2; % order of differential operator
y = sety(N); % spatially-independent variable

% parameter eps in TPBVP
eps = 1; eps2 = eps*eps;
% temporal frequency
omega = 0;

% Represent operators A, B, and C in the frequency response operator
A = cell(m+1,1); % cell array with coefficients
A{1} = -1.0; A{2} = 0; A{3} = 1i*omega + eps2;

% Identity operator
I = cell(1,1); I{1} = 1;

% Input and output operators B and C
B = I; C = I;

```

```

% The first derivative operator 1.0 Dy + 0.0:
Dy = cell(2,1); Dy{1} = 1.0; Dy{2} = 0.0;

% Neumann boundary conditions at y = \pm 1
bc = BCs(2,1); % two constraints on one variable
bc.Operator = {Dy; Dy};
bc.Points = [1; -1];

% Solve
[Phi0Psi0,gamma] = sisSvdfns(2,2,N,A,B,C,bc,bc);
plot(y,Phi0Psi0{1,2}/val_rbc(Phi0Psi0{1,2}));

```

The linearized Navier-Stokes equations in the descriptor form

We consider the eigenvalues of the linearized Navier-Stokes equations (see § 3.2.4 and § 3.3.3). This system is given by,

$$\underbrace{\begin{bmatrix} 1 & 0 & 0 & 0 \\ 0 & 1 & 0 & 0 \\ 0 & 0 & 1 & 0 \\ 0 & 0 & 0 & 0 \end{bmatrix}}_{\mathcal{E}} \partial_t \begin{bmatrix} u \\ v \\ w \\ p \end{bmatrix} = \underbrace{\begin{bmatrix} \frac{\Delta}{Re} - i k_x U & -U' & 0 & -i, k_x \\ 0 & \frac{\Delta}{Re} - i k_x U & 0 & -\partial_y \\ 0 & 0 & \frac{\Delta}{Re} - i k_x U & -i k_z \\ i k_x & \partial_y & i k_z & 0 \end{bmatrix}}_{\mathcal{F}} \begin{bmatrix} u \\ v \\ w \\ p \end{bmatrix}, \quad (\text{S1-40a})$$

$$+ \underbrace{\begin{bmatrix} 1 & 0 & 0 \\ 0 & 1 & 0 \\ 0 & 0 & 1 \\ 0 & 0 & 0 \end{bmatrix}}_{\mathcal{B}} \begin{bmatrix} d_x \\ d_y \\ d_z \end{bmatrix}, \quad (\text{S1-40b})$$

$$\begin{bmatrix} u \\ v \\ w \end{bmatrix} = \underbrace{\begin{bmatrix} 1 & 0 & 0 & 0 \\ 0 & 1 & 0 & 0 \\ 0 & 0 & 1 & 0 \end{bmatrix}}_{\mathcal{C}} \begin{bmatrix} u \\ v \\ w \\ p \end{bmatrix}, \quad (\text{S1-40c})$$

with boundary conditions $u(\pm 1) = v(\pm 1) = w(\pm 1) = v'(\pm 1) = 0$ (the boundary condition $v'(\pm 1) = 0$ is derived in § 3.3.3). Note that pressure is expressed with a highest derivative of 2 as discussed in § 3.3.3. The boundary conditions are expressed

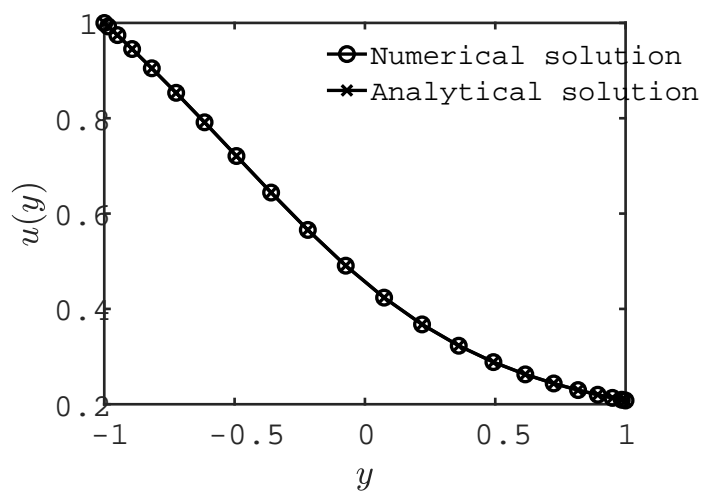


Figure S1: Comparing analytical and numerical solutions to (S1-39) from Code 7.2.

as

$$\begin{bmatrix} \mathcal{Q}(1, I) & \mathcal{Q}(1, Z) & \mathcal{Q}(1, Z) & \mathcal{Q}(1, Z) \\ \mathcal{Q}(1, Z) & \mathcal{Q}(1, I) & \mathcal{Q}(1, Z) & \mathcal{Q}(1, Z) \\ \mathcal{Q}(1, Z) & \mathcal{Q}(1, Z) & \mathcal{Q}(1, I) & \mathcal{Q}(1, Z) \\ \mathcal{Q}(1, Z) & \mathcal{Q}(1, D) & \mathcal{Q}(1, Z) & \mathcal{Q}(1, Z) \\ \mathcal{Q}(-1, I) & \mathcal{Q}(-1, Z) & \mathcal{Q}(-1, Z) & \mathcal{Q}(-1, Z) \\ \mathcal{Q}(-1, Z) & \mathcal{Q}(-1, I) & \mathcal{Q}(-1, Z) & \mathcal{Q}(-1, Z) \\ \mathcal{Q}(-1, Z) & \mathcal{Q}(-1, Z) & \mathcal{Q}(-1, I) & \mathcal{Q}(-1, Z) \\ \mathcal{Q}(-1, Z) & \mathcal{Q}(-1, D) & \mathcal{Q}(-1, Z) & \mathcal{Q}(-1, Z) \end{bmatrix} \begin{bmatrix} u(y) \\ v(y) \\ w(y) \\ p(y) \end{bmatrix} = 0, \quad (\text{S1-40d})$$

where $\mathcal{Q}(a, L)$ is an evaluation operator that evaluates the action of the linear operator L on a variable at a point $y = a$. The generalized eigenvalues of the operators $(\mathcal{F}, \mathcal{E})$ yield eigenvalues of (S1-40). As discussed in § 3.3, the norm of the resolvent operator, $\mathcal{A}^{-1}(\omega) = (i\omega\mathcal{E} - \mathcal{F})^{-1}$ can be computed using a feedback interconnected system,

$$\begin{bmatrix} 0 & \mathcal{B}\mathcal{B}^\dagger \\ \mathcal{C}^\dagger\mathcal{C} & 0 \end{bmatrix} \begin{bmatrix} \phi \\ \psi \end{bmatrix} = \gamma \begin{bmatrix} \mathcal{A} & 0 \\ 0 & \mathcal{A}^\dagger \end{bmatrix} \begin{bmatrix} \phi \\ \psi \end{bmatrix}, \quad (\text{S1-41})$$

where $\gamma = \pm\sigma$ are the singular values and the maximum singular value is the resolvent norm of (S1-40), $\phi = [u \ v \ w \ p]^T$ in (S1-40), and ψ are the adjoint variables corresponding to ϕ .

Finally, the maximum singular value over all $\omega \in \mathbb{R}$ is computed using the fast algorithm by Bruinsma and Steinbuch [78]. The **Matlab** code for these different problems concerning the linearized Navier-Stokes equations is given in Code 7.3.

Figure S2 shows plots generated from Code 7.3. Figure S2a shows the eigenvalues for the case of plane Poiseuille flow with $Re = 2000$, $k_x = k_z = 1$ (also see Figure 3.10a). Figure S2b shows the largest (σ_0) and the second largest (σ_1) singular values calculated from (S1-41). The singular values computed in Figure S2b are in agreement with [6, Figure 4.10].

Listing 7.3: Solving for the eigenvalues, resolvent norms, and the \mathcal{H}_∞ -norm of (S1-40)

% Eigenvalues and frequency responses of LNS

```
%% Eigenvalues
clear;
clc;
```

```

close all;
N = 127;
[~,~,J] = Matgen(2,N);
y = sety(N);

% Set parameters:
Re = 2000;
kx = 1;
kz = 1;
U = 1-y.^2; % Poiseuille flow.
Uy = -2*y;

% Make operators: identity, zero, and first derivative operator:
I = cell(1,1); I{1} = 1; Z = cell(1,1); Z{1} = 0;
Dy = cell(2,1); Dy{1} = 1; Dy{2} = 0;

% Make the diagonal of F:
k2 = kx*kx + kz *kz;
F11 = cell(3,1);
F11{1} = 1/Re;
F11{2} = 0;
F11{3} = (-k2/Re) - 1i*kx*U;

% Make other operators for F12, F14 etc.
F12 = cell(1,1) ; F12{1} = -Uy;
F14 = cell(1,1); F14{1} = -1i*kx;
F24 = cell(2,1); F24{1} = -1; F24{2} = 0;
F34 = cell(1,1); F34{1} = -1i*kz;
F41 = cell(1,1); F41{1} = 1i*kx;
F42 = cell(2,1); F42{1} = 1; F42{2} = 0;
F43 = cell(1,1); F43{1} = 1i*kz;

% Make the operator:
F = {F11, F12, Z, F14;...
     Z, F11, Z, F24;...
     Z, Z, F11, F34;...
     F41, F42, F43, Z};

% Make E:
E = {I, Z, Z, Z;...
     Z, I, Z, Z;...
     Z, Z, I, Z;...
     Z, Z, Z, Z};

% Make boundary conditions matrix:
bcOp = {I,Z,Z,Z;...
        Z,I,Z,Z;...
        Z,Z,I,Z;...
        Z,Dy,Z,Z;
        I,Z,Z,Z;...
        Z,I,Z,Z;...
        Z,Z,I,Z;...
        Z,Dy,Z,Z};
bcPoints = [ones(4,4); % as first 4 rows for bc at y = 1,
            -ones(4,4)]; % next four rows for y = -1.

% Differential orders of u, v, w, and p:

```

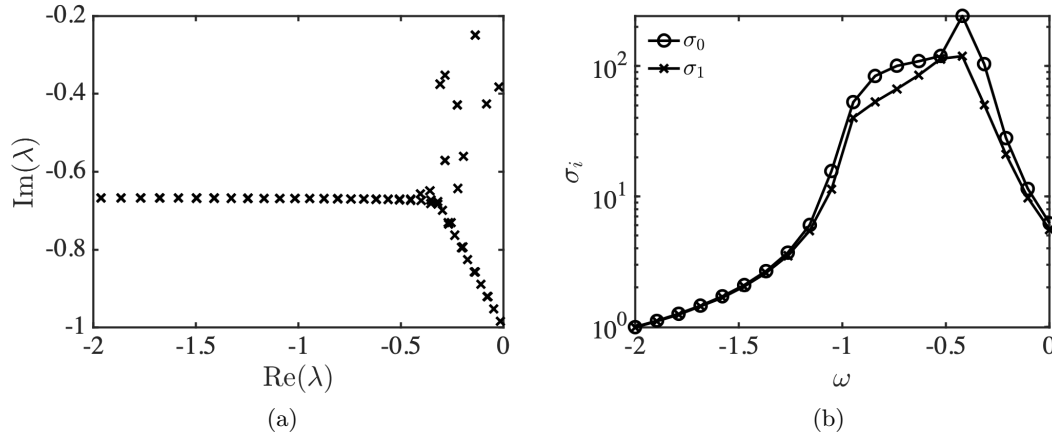


Figure S2: Eigenvalues and frequency responses of the linearized Navier equations in plane Poiseuille flow with $Re = 2000$ and $k_x = k_z = 1$, generated from Code 7.3. The spectral integration method with $N = 91$ basis functions is used. (a) Spectrum resulting from the use of the descriptor formulation, and (b) two largest singular values of the frequency response operator computed using Code 7.3. A reference for this plot is found in [6, Figure 4.10].

```
n = [2,2,2,2];

% Make boundary conditions matrix
M = BcMat(n,N,bcPoints,bcOp);

% Find null space of M:
M_null = null(M);

% Find eigenvalues
F = Discretize(n,N,F)*M_null;
E = Discretize(n,N,E)*M_null;
[~,evals] = eig(F,E);

plot(real(evals),imag(evals),'xk');
ylabel('$\mathrm{Im}(\lambda)$');
xlabel('$\mathrm{Re}(\lambda)$');
ax = gca;
ax.XLim = [-2,0];
ax.YLim = [-1,-0.2];
ax.YTick = [-1 -0.8 -0.6 -0.4 -0.2];
ax.XTick = [-2 -1.5 -1 -0.5 0];
print('-painters','-dsvg','../docs/pics/Code5_1');

%% Frequency responses
```

S1.4 Recurrence relations

Consider the expression for the highest derivative of a second-order differential equation in a Chebyshev basis,

$$D^2 u(y) = u_0^{(2)} \frac{1}{2} T_0(y) + u_1^{(2)} T_1(y) + u_2^{(2)} T_2(y) + u_3^{(2)} T_3(y) + \cdots \quad (\text{S1-42})$$

Relation of Chebyshev polynomials with derivatives is given by [101, Equation 3.25]

$$T_0(y) = T_1'(y), \quad (\text{S1-43a})$$

$$T_1(y) = \frac{1}{4} T_2'(y), \quad (\text{S1-43b})$$

$$T_n(y) = \frac{1}{2} \left(\frac{T_{n+1}'(y)}{n+1} - \frac{T_{n-1}'(y)}{n-1} \right), \quad n > 1. \quad (\text{S1-43c})$$

Substuting (S1-43) in (S1-42) and making an indefinite integration on the resultant expression yields,

$$\begin{aligned} D v(y) = & \frac{u_0^{(2)}}{2} y + \frac{u_1^{(2)}}{2} y^2 + \frac{u_2^{(2)}}{2} \left(\frac{T_3(y)}{3} - \frac{T_1(y)}{1} \right) + \frac{u_3^{(2)}}{2} \left(\frac{T_4(y)}{4} - \frac{T_2(y)}{2} \right) \\ & + \frac{u_4^{(2)}}{2} \left(\frac{T_5(y)}{5} - \frac{T_3(y)}{3} \right) + \cdots + c_0, \end{aligned} \quad (\text{S1-44})$$

where c_0 is the effective integration constant. As $y^2 = (T_0(y) + T_2(y))/2$, (S1-44) takes

the form:

$$\begin{aligned} D v(y) &= \frac{u_0^{(2)}}{2} y + \frac{u_1^{(2)}}{2} \left(\frac{T_0(y) + T_1(y)}{2} \right) + \frac{u_2^{(2)}}{2} \left(\frac{T_3(y)}{3} - \frac{T_1(y)}{1} \right) \\ &\quad + \frac{u_3^{(2)}}{2} \left(\frac{T_4(y)}{4} - \frac{T_2(y)}{2} \right) + \frac{u_4^{(2)}}{2} \left(\frac{T_5(y)}{5} - \frac{T_3(y)}{3} \right) + \cdots + c_0, \end{aligned} \quad (\text{S1-45})$$

$$\begin{aligned} &= T_1(y) \underbrace{\left(\frac{u_0^{(2)}}{2} - \frac{u_2^{(2)}}{2} \right)}_{u_1^{(1)}} + T_2(y) \underbrace{\left(\frac{u_1^{(2)}}{4} - \frac{u_3^{(2)}}{4} \right)}_{u_2^{(1)}} + T_3(y) \underbrace{\left(\frac{u_2^{(2)}}{6} - \frac{u_4^{(2)}}{6} \right)}_{u_3^{(1)}} \\ &\quad + \cdots + \underbrace{\frac{u_1^{(2)}}{4}}_{u_0^{(1)}/2} + c_0. \end{aligned} \quad (\text{S1-46})$$

Hence we have from (S1-46),

$$D v(y) = u_0^{(1)} \frac{1}{2} T_0(y) + u_1^{(1)} T_1(y) + u_2^{(1)} T_2(y) + u_3^{(1)} T_3(y) + \cdots + c_0, \quad (\text{S1-47})$$

where $u_0^{(1)} = u_1^{(2)}/2$ and the remaining coefficients for $u_i^{(1)}$ from the recursive relation in (S1-5).